Optimization of silicon nitride membranes for hybrid superconducting-mechanical circuits

Edouard Ivanov

THÈSE DE DOCTORAT
DE SORBONNE UNIVERSITÉ

Spécialité : Physique
École doctorale : Physique en Île-de-France

réalisée au
Laboratoire Kastler Brossel

présentée par

Edouard Ivanov

pour obtenir le grade de :
DOCTEUR DE SORBONNE UNIVERSITÉ

Sujet de la thèse :

Optimization of silicon nitride membranes for hybrid superconducting-mechanical circuits

devant le jury composé de :

M.	Jack Harris	Rapporteur
M.	Gary Steele	Rapporteur
Mme	Emily Lamour	Examinatrice
M.	Jérémie Viennot	Examinateur
M.	Antoine Heidmann	Directeur de thèse
M.	Samuel Deléglise	Co-directeur de thèse
M.	Thibaut Jacqmin	Co-directeur de thèse

Remerciements

Quand je pense que mon projet aurait pu prendre deux fois autant de temps, ou souffrir d'infiniment plus de complications, je me rends compte à quel point j'ai eu de la chance, finalement. Mais je sais que cette chance ne sort pas du néant, et que je la dois à toutes les personnes qui ont participé à ma thèse, tant professionnellement que personnellement. Sans elles, ce projet n'aurait jamais pu aboutir. Je vois que je ne suis qu'un nom parmi une longue liste, et je dois à tous les autres figurants un grand merci.

Ma thèse s'est déroulée au sein du Laboratoire Kastler-Brossel (LKB), et je remercie Antoine Heidmann, directeur du laboratoire, de m'y avoir accueilli dans la période 2017-2021. Antoine m'a aussi accueilli au sein de son groupe, Optomécanique et Mesures Quantiques. Merci à lui, Samuel Deléglise, et Thibaut Jacqmin de m'avoir co-encadré tout au long de ce projet. Un grand merci à Samuel, qui m'a soutenu tout au long de ses trois années et demi, en dépit de ses autres doctorants et de la naissance de deux enfants, et que je n'ai jamais vu perdre énergie pour ce projet. Son approche osée à la science qui n'hésite pas à reprendre une chose du début si nécessaire, était parfois frustrante, parfois effrayante. Mais il ne l'a jamais fait au hasard, et le pire c'est qu'il avait rarement tort ; le cas contraire, il m'a appris à défendre mes idées avec plus de conviction que je n'avais auparavant. Merci aussi à Thibaut pour ce qu'il m'a appris en fabrication en salle blanche et en optique ainsi que pour la rigueur scientifique qu'il m'a imposé. Je remercie également le reste des membres de notre groupe passés et présents : Thibault Capelle, qui a lancé un travail titanesque et qui a posé les bases de ce projet, rendant ma vie beaucoup plus simple ; à Tristan Briant pour son aide experte en électronique; à Pierre-François Cohadon pour sa bonne humeur constante ; à Ferhat Loubar et Sheon Chua, mes autres compagnons de bureau, pour leurs conversations de bonne humeur après les déjeuners pour reprendre de bon pas ; à Michael Croquette et Rémi Metzdorff avec qui j'ai partagé la salle de manip. De plus, merci à Samuel, Thibaut, et PF pour leurs lectures et relectures de mes textes parfois franchement lourds, et d'en avoir élevé la qualité grandement. Bonne continuation à Luis Najera qui prend en main la manip membranes. Merci à Nicolas Treps et Pierre Cladé, membres de mon jury de thèse, pour leurs conseil et soutien. Merci à Mohammad Haidar pour sa gentillesse, les pauses café, et de m'avoir réappris les jeux de dames et de tennis de table.

Tout ce laboratoire, bien entendu, croulerait sous son propre poids si ce n'est pour un personnel administratif et technique pour le soutenir. Merci à Laetita Morel, Romain Rybka, Thierry Tardieu, Viki Domazet, l'équipe du secrétariat, qui ont toujours la solution magique à tous mes problèmes administratifs. J'ai perdu compte du nombre de fois où je suis allé les embêter, et je leur suis reconnaissant pour leur patience et dur travail. Un grand merci à Stéphanie Dubois pour m'avoir sauvé deux fois d'une soumission prématurée ! Et merci Valérie Revelut pour ta bonne humeur inépuisable et pour les bons moments des fêtes de la science. Cela va de même pour les membres de l'atelier mécanique, en particulier Carounarage Doré et Sébastien Colinot, qui ont fait un travail minutieux sur lequel tout mon travail s'est basé ; pour les membres de l'atelier électronique, Brigitte Delamour, Loïc Garcia, et David Polizzi ; et pour Florence Thibout à l'atelier verreries. Merci à José Palomo et Michael Rosticher de la salle blanche de l'ENS, ainsi qu'à Loïc Becerra et Erwan Dandeu de l'INSP, maîtres de la magie noire qu'est la nanofabrication, pour leur aide, conseils, et bonne humeur dans ces salles fermées et souterraines.

Finalement, merci aux membres du projet OMT pour avoir rendu ces années si enrichissantes. Grand merci à Antonella Ragnelli, une gestionnaire de projet sans pareil, qui fait plus qu'on ne croirait possible pour un seul être humain, avec une énergie inépuisable tout en restant humaine et chaleureuse. A tou.te.s les autres doctorant.e.s de l'OMT, merci pour ces années d'amitié, de conversations stimulantes, et de support mutuel. Merci aussi à Eva Weig pour avoir été mon mentor OMT.

Et puis, finalement, merci à ma famille et à mes amis, qui m'ont rempli d'amour et de joie, qui ont supporté des fluctuations d'humeurs, et qui m'ont remis à ma place dès que nécessaire. Maman et papa, je vous dois tout ce que j'ai et ce que je suis, et merci à vous et à Seb de me donner un lieu chaleureux où je sais que je peux rentrer pour me recharger. Sanda, îţi mulţumesc pentru toate pachetele pe care mi le ai trimis, fiecare umplut cu dragoste, si pentru toate apelurile care mi-au înseninat zilele. Thank you to Bryn, Jom, and Val, my friends from way back, for the laughs, the moral support, and having prevented me from going crazy numerous times. Enfin, merci aux copains de la FBL, à Gaëtan, Lucas, et Bertille d'avoir rendu Paris une ville si merveilleuse, et à Jasmin, Anne, et Farah de m'avoir appris tant de leçons que je m'obstinais à ne pas apprendre. Galia, you make me happy when skies are gray.

Contents

Introduction

Mechanical resonators have played a central role in metrology and precise sensing since the early days of experimental physics. Cavendish for instance has used a torsion balance to measure the elusive gravitational force between two objects of known mass, accurately measuring for the first time, in modern terms, the gravitational constant [1]. Nowadays, the possibility to realize ultralight mechanical resonators has broadly expanded their use. Our ability to measure them with exquisite precision has turned these objects into sensitive probes for physical phenomena occurring down to the nanometric scale. In a landmark experiment performed at IBM in 2004, Dan Rugar and his team have demonstrated that the force exerted by a single electronic spin [2] could be detected by a micrometric cantilever functionalized with a magnetic tip, opening the exciting perspective of Magnetic Resonance Force Microscopy [3–5]. In modern electronics, the comparatively small wavelength of sound can be exploited to realize acoustic filters or delay lines with a much smaller footprint than using purely electromagnetic components. Beyond classical information technologies, mechanical resonators could be used in quantum devices as platforms for coupling otherwise incompatible systems such as microwave and optical photons [6–9], or for storing fragile quantum states in long-lived mechanical oscillations [10].

To leverage the full potential of mechanical systems in quantum computing, their motion must be controlled at the scale of their zero-point fluctuations. This is precisely what is achieved in the field of cavity optomechanics, where a mechanical oscillator is addressed by coupling it to a high-finesse cavity. In such systems, radiation pressure noise exerts a backaction force resulting from the continuous position measurement. In state-of-the-art experiments, the quantum effects of radiation pressure are made the dominant driving force; this has been successfully implemented in a wide variety of platforms, spanning from the 40-kg mirrors used to detect gravitational waves at VIRGO and LIGO, down to femtogram nanophotonic structures or even trapped cold atoms (see fig. 1). This line of research has lead to breakthrough results such as ground-state cooling [11–13], the preparation of single-phonon states [14–16], and entanglement generation [17–19].

Importantly, the control over mechanical motion is limited in most systems by the fact that the optomechanical interaction is linear. To achieve a deeper quantum control, the addition of an extrinsic nonlinear element is required. In this thesis, we

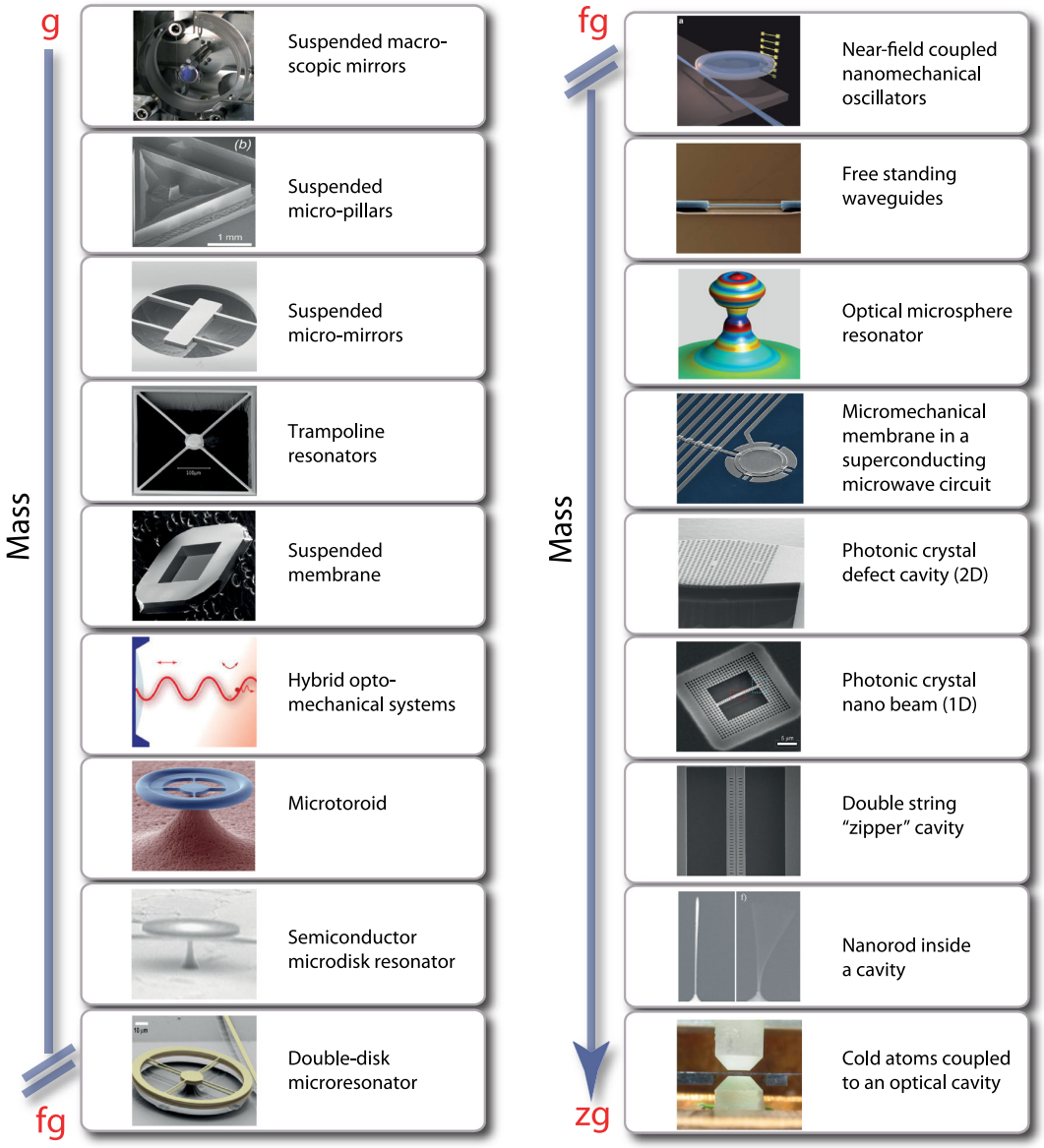

Figure 1: Images or illustrations of a variety of mechanical resonators studied in optomechanics, spanning several order of magnitude of mass. Figure extracted from Ref. [20].

couple a tensioned dielectric nanomembrane [21] to a superconducting microwave cavity. This will allow us to benefit from the rich toolset of circuit quantum electrodynamics, and in particular to make use of the nonlinearities made possible by the Josephson junction. Such a hybrid electromechanical system could for instance serve as an on-chip quantum memory [10] with potential storage times in the second range, or as a quantum-limited force sensor [5].

These possibilities are made possible by having mechanical modes with long coherence times. While this key value is moderately high in the original nanomembrane designs, other mechanical resonators such as crystalline beams [22, 23] significantly outperform them. However, recent developments in phononic engineering [24, 25] have reinstated silicon nitride membranes as one of the leaders in mechanical coherence times, with MHz-frequency mechanical modes and quality factors reaching the billions.

The primary scope of this thesis has been to fabricate and study these resonators in the Optomechanics and Quantum Measurements group at the Laboratoire Kastler-Brossel (LKB), in which silicon nitride membranes had only recently become a subject of research. The scope of this work is to pave the way for quantum electromechanical experiments with such mechanical resonators. The design of the patterned membranes is studied in detail to ensure in particular that a quantum control over its eigenmodes can be achieved. Through numerical simulations and experimental measurements, the necessity for precise mode frequency engineering is demonstrated.

The manuscript is divided into four chapters: chapter 1 provides the theoretical basis for measuring and controlling mechanical motion, which will provide useful tools for describing and interpreting the subsequent experiments; chapter 2 provides details of the first cooling experiment attempted in our group using the original nanomembrane design, yielding promising results but emphasizing the need for state-of-the-art resonators, in particular due to insufficient acoustic isolation; chapter 3 studies the mechanism of loss in membranes, motivating the key design choices we made, and based on which an optimization study was performed; chapter 4 presents the experimental results regarding the patterned nanomembranes designed in this thesis; finally, chapter 5 summarizes the main findings, and discusses the future perspectives enabled by this work.

Chapter 1

Introduction to opto- and electromechanics

Today, opto- and electromechanics are mature fields, and their fundamental theoretical tools have been well developed, understood, and experimentally verified. The coupling between mechanical motion and light, at play in optomechanical systems, gives rise to a variety of concepts and phenomena: it explains for instance the existence of fundamental limits on the precision of interferometric measurements [26], it can be used to cool a mechanical degree of freedom through radiation pressure [27–29], even down to its quantum ground state [30]. It can also be used to generate an effective interaction between two light beams at different frequencies via the effect of Optomechanically Induced Transparency [12].

Nonetheless, several open questions still remain and are the subject of intensive research. Opto-/electromechanical devices are being used to further our understanding of intrinsic mechanical loss mechanisms [24, 25, 31]; to generate and study deep quantum behaviors of mechanical motion [10, 16, 32]; to interface quantum information platforms by converting optical photons into microwave photons [8, 9, 33]; or to try to study the effects of gravitationally-induced quantum decoherence in massive objects [34].

As a result of this research, opto-/electromechanical systems have become excellent platforms for characterizing mechanical resonators and for precisely controlling their motion. Over the following chapters, we will present mechanical resonators in various scenarios: they will be coupled to a resonant microwave circuit and characterized in a Mach-Zehnder interferometer; they will be driven coherently and left to vibrate by thermal fluctuations; their temperature will be gradually reduced as a result of the electromechanical interaction. The scope of this chapter is to equip the reader with the underlying concepts necessary for the interpretation of the data presented subsequently.

In many of the experiments described in this work, the mechanical oscillator is driven solely by a thermal force, and we measure the resulting Brownian motion.

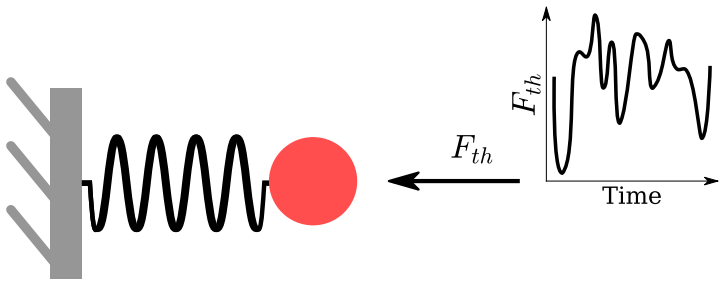

Figure 1.1: A harmonic oscillator mode, represented by a mass on a spring, is driven by a thermal force F_{th} varying randomly with time.

Noise spectra provide a powerful and necessary means to extract useful information from such random motion, and they can be used to determine key parameters such as the mechanical mode frequency, dissipation rate, the electromechanical coupling, and the temperature of the system–which cannot always be assumed to be known a priori (see chapter 2). Section 1.1 introduces the basics of noise spectra and the ever important fluctuation-dissipation theorem.

A simple way to measure mechanical resonators is to probe them by interferometry. In such an experiment, the mechanical motion is transduced into phase fluctuations of a reflected light beam. If the interferometer is sufficiently sensitive, then even the thermal motion of the resonator can be observed. In section 1.2, we apply our description of noise spectra to the light field intensity in a Mach-Zehnder interferometer, and show that the thermal motion can be measured with a high signal-to-noise ratio. Interferometry is thus found to be a convenient method for characterizing mechanical resonators at room temperature, which will be implemented in chapter 4. This scheme does not however enable the control of mechanical motion, which is necessary to prepare the resonator in its ground state.

To achieve such a state preparation, an electromechanical device can be used, where the motion of a mechanical resonator is monitored and controlled through a resonant microwave circuit. Section 1.3, describes such a system, modeled as two coupled harmonic oscillators. The main results for this model are presented, and we show how the coherent interaction between light and mechanics can be applied to reduce the effective temperature of a mechanical mode.

1.1 Thermal motion of a harmonic oscillator

Before describing how to detect and control the motion of a mechanical resonator, let us start by formally describing its dynamics. In this work, the modes of vibration we study are coupled to a thermal environment, and as such are always being driven by a thermal force varying randomly with time, as illustrated in fig. 1.1. The

ensuing Brownian motion contains information both about the environment and the oscillator itself, which can be extracted with the right mathematical tools.

1.1.1 Equation of motion of a mode

We model the resonator as a damped and driven harmonic oscillator, with $x(t)$ describing its time-dependent position. We assume that the oscillator is driven by two forces: a viscous damping term ($\propto \dot{x}$), and an external driving force F_{ext}. The equation of motion for the position of the oscillator reads

$$\ddot{x}(t) + \Gamma_{\mathsf{m}}\dot{x}(t) + \Omega_{\mathsf{m}}^2 x(t) = \frac{F_{\mathsf{ext}}}{m_{\mathsf{eff}}}, \tag{1.1}$$

where Ω_{m} is the mechanical (angular) resonance frequency, and Γ_{m} is the energy dissipation rate. We take into account the distributed nature of the mode by introducing an effective mass m_{eff}, to indicate that the mass which is displaced does not correspond exactly to the full mass of the resonator.

It is simple to solve eq. (1.1) in the frequency domain, and so we define the Fourier transform $A[\Omega]$ of a time-domain variable $\mathcal{A}(t)$ as

$$A[\Omega] \equiv \mathcal{F}\left[\mathcal{A}(t)\right] \equiv \int_{-\infty}^{+\infty} \mathcal{A}(t)\mathsf{e}^{i\Omega t}\mathrm{d}t, \tag{1.2}$$

and the inverse Fourier transform as

$$\mathcal{A}(t) = \int_{-\infty}^{+\infty} A[\Omega]\mathsf{e}^{-i\Omega t}\frac{\mathrm{d}\Omega}{2\pi}. \tag{1.3}$$

We can now rewrite eq. (1.1) in the frequency domain[1]:

$$x[\Omega] = \chi_{\mathsf{m}}(\Omega)F_{\mathsf{ext}}[\Omega], \tag{1.4}$$

where

$$\chi_{\mathsf{m}}(\Omega) \equiv \left[m_{\mathsf{eff}}\left(\Omega_{\mathsf{m}}^2 - \Omega^2\right) - im_{\mathsf{eff}}\Gamma_{\mathsf{m}}\Omega\right]^{-1}. \tag{1.5}$$

$\chi_{\mathsf{m}}[\Omega]$ is the mechanical susceptibility: it represents the mechanical response to a monochromatic force applied at a frequency Ω.

In this work, we will repeatedly find ourselves in cases where there is no monochromatic drive. Then, the resonator only moves in response to random forces, such as the thermal driving force F_{th}, and no explicit expression of either the force or the position can be given. And yet information can still be extracted from the resonator, using another tool: the autocorellation function, which provides a means of

[1] With the definition of the Fourier transform used here, we can apply the identities $\mathcal{F}\left[\dot{x}(t)\right] = -i\Omega x[\Omega]$ and $\mathcal{F}\left[\ddot{x}(t)\right] = -\Omega^2 x[\Omega]$ to obtain this result.

describing correlations lying within random noise.

1.1.2 The autocorrelation function

Noise can be seen as a stochastic process modeled by a continuous complex random variable $z(t)$. It is characterized by its correlation properties, and we can describe them with the autocorrelation function, which encapsulates interesting features of the noise, and is defined as[2]

$$C_{zz}(t,\tau) \equiv \langle z^*(t) z(t+\tau) \rangle, \tag{1.6}$$

where τ is a time delay. The notation $\langle \ldots \rangle$ signifies a time average, defined as

$$\langle \mathcal{A}(t) \rangle = \lim_{\Delta T \to \infty} \frac{1}{\Delta T} \int_{-\Delta T/2}^{\Delta T/2} \mathcal{A}(t+t') \mathrm{d}t', \tag{1.7}$$

where ΔT is an arbitrarily large time increment. Note that the time average of any variable z can always be arranged to be zero by removing its deterministic part. This leaves the first non-zero moment of noise to be the variance.

Consider for instance Gaussian white noise, which is an example of Markovian noise: it is completely random, and has no memory of its previous values, such that $z(t)$ bears no correlation with $z(t+\tau)$, $\forall \tau \in \mathbb{R}$. Then, $C_{zz}(t,\tau) = \delta(t-\tau)$, $\delta(t)$ being the Dirac delta. In more complicated noise forms, some correlations might arise from the randomness. Take weather, for instance, which is chaotic and for almost all intents and purposes random, and yet we know that it follows some predictable patterns: if it is warm today, it will likely be warm tomorrow and a year from now.

To simplify matters, we will restrict this description to stationary processes, such that the properties of the noise do not vary with t. In that case, the autocorrelation only depends on the time lag τ, and $C_{zz}(t, t+\tau) = C_{zz}(0,\tau) \equiv C_{zz}(\tau)$, and reads

$$C_{zz}(\tau) = \langle z^*(0) z(\tau) \rangle. \tag{1.8}$$

Note the identity $C_{zz}(0) = \langle |z(0)^2| \rangle$: $C_{zz}(0)$ is the variance of z. The analysis can be generalized to quantum systems by replacing the variable z with an operator $\hat{z}$ (see e.g. [35]). We will use this approach whenever it is necessary to discuss the quantum mechanics systems studied in this work.

With C_{zz}, we can quantify the thermal force noise driving the mechanical oscillator without needing to give it an explicit expression. Since the equation of motion for x, eq. (1.4), is in the frequency domain, it is more convenient to express the noise

[2]Formally, the autocorrelation function is defined as an ensemble average, but by the ergodic hypothesis this is equivalent to the definition we use here.

correlations in that manner as well.

1.1.3 Noise spectral density

An important quantity is the noise spectral density, which can be used to describe the contribution to the total noise generated in a given frequency interval. It can be immediately calculated from C_{zz}: the Wiener-Khinchin theorem states that the noise spectral density is precisely the Fourier transform of C_{zz}.

The Wiener-Kinchin theorem

The statement above can be readily verified: let S_{zz} denote the Fourier transform of C_{zz}, such that

$$S_{zz}[\Omega] = \int_{-\infty}^{+\infty} C_{zz}(t')\mathsf{e}^{-i\Omega t'}\mathrm{d}t'. \tag{1.9}$$

Conversely, this expression can be inverted, allowing us to re-express C_{zz} as

$$C_{zz}(\tau) = \int_{-\infty}^{+\infty} S_{zz}[\Omega]\mathsf{e}^{i\Omega\tau}\frac{\mathrm{d}\Omega}{2\pi}. \tag{1.10}$$

Then, setting $\tau = 0$ in eq. (1.10), we immediately find that

$$\int_{-\infty}^{+\infty} S_{zz}(\Omega)\frac{\mathrm{d}\Omega}{2\pi} = \langle z^*(0)z(0)\rangle. \tag{1.11}$$

This relation tells us that $S_{zz}(\Omega)d\Omega$ is the contribution to the variance of z in the frequency range $[\Omega, \Omega + \mathrm{d}\Omega]$ [36], i.e. S_{zz} is the noise spectral density (or noise spectrum), as predicted by the Wiener-Kinchin theorem. Note that, the units of the noise spectral density are $[S_{zz}] = [z^2].\mathrm{Hz}^{-1}$.

Let us return to our Gaussian white noise example with $C_{zz}(\tau) = \delta(\tau)$. Its spectral density is perfectly flat, with $S_{zz}(\Omega) = 1$. Note that this means that Gaussian white noise has infinite variance, and is therefore not physically meaningful. Nevertheless, white noise can serve as a useful model if we are only considering small intervals of frequency, as we will below.

Useful identities

1. **Alternative definition**: From eq. (1.9), an alternative definition of the noise spectral density can be derived:

$$2\pi\delta(\Omega - \Omega')S_{zz}[\Omega] = \langle (z[\Omega])^* z[\Omega']\rangle. \tag{1.12}$$

We can deduce from this relation that the noise spectra of uncorrelated sources of noise is the sum of their individual spectra.

2. **Linear filtering**: Suppose there is a variable $y[\Omega] = f(\Omega)z[\Omega]$. It follows from eq. (1.12) that
$$S_{yy}[\Omega] = |f(\Omega)|^2 S_{zz}[\Omega]. \tag{1.13}$$
If the transfer function $f(\Omega)$ from z to y is known and linear, then the spectrum of z can be directly inferred by measuring the spectrum of y.

3. **Symmetric spectra**: In quantum physics, noise spectra can be asymmetric [35] due to the fact that some operators do not commute (e.g. the ladder operators). In such a context (see section 1.3) it can be useful to express noise in terms of symmetrized noise spectra, defined as
$$\bar{S}_{zz}[\Omega] = \frac{S_{zz}[\Omega] + S_{zz}[-\Omega]}{2}. \tag{1.14}$$

1.1.4 The fluctuation-dissipation theorem

Tying in the notion of noise spectra with the Brownian motion of mechanical oscillators, Callen and Welton [37] showed that the channel through which energy is dissipated by a mode is the same as the one through which its random motion, or fluctuations, can be driven. This is the fluctuation-dissipation theorem: the two phenomena are two sides of the same coin. For the damped harmonic oscillator, the symmetric noise spectrum of the thermal driving force reads
$$\bar{S}_{FF}[\Omega] = 2\hbar\Omega \left(n_{\mathsf{th}}(\Omega) + \frac{1}{2} \right) \Gamma_{\mathsf{m}} m_{\mathsf{eff}}, \tag{1.15}$$
where $n_{\mathsf{th}}(\Omega) \equiv 1/\left(\exp\left(\hbar\Omega/k_{\mathsf{B}}T_{\mathsf{env}}\right) - 1\right)$ is the mean number of thermal quanta present in the system. This powerful statement extends beyond the simple harmonic oscillator treated here, and can also apply to fluctuations in the positions of suspended particles (Brownian motion), the electromagnetic field [37], or the current originating from resistors (Johnson noise) [36].

The expression for $\bar{S}_{FF}$ given here is semi-classical. If we were to treat the system in a purely quantum formalism, the commutation relations between the canonical variables would impose an asymmetry in the positive and negative frequency regions of the spectrum [35], which is lost when the spectrum is symmetrized. In section 1.3, where the cooling of the harmonic oscillator to the ground state is derived, we do describe the system in the quantum picture, but only consider linear couplings between harmonic oscillators. In that case, we can satisfy ourselves with the symmetrized noise spectra.

In the regime where $\hbar\Omega \ll k_{\mathsf{B}}T_{\mathsf{env}}$, the thermal force noise becomes a Gaussian

white noise:

$$\bar{S}_{FF}[\Omega \ll k_\mathsf{B} T_\mathsf{env}/\hbar] \approx 2 k_\mathsf{B} T_\mathsf{env} \Gamma_\mathsf{m} m_\mathsf{eff}. \tag{1.16}$$

The force driving the system now being known, we can finally express the noise spectrum of the position x.

1.1.5 Noise spectrum of the harmonic oscillator

Applying the linear filtering property (eq. (1.13)) to the result of the damped driven harmonic oscillator (eq. (1.4)) allows us to find the noise spectrum of the position $\bar{S}_{xx}$:

$$\bar{S}_{xx}[\Omega] = |\chi_\mathsf{m}(\Omega)|^2 2\hbar\Omega \left(n_\mathsf{th}(\Omega) + \frac{1}{2} \right) \Gamma_\mathsf{m} m_\mathsf{eff}. \tag{1.17}$$

The thermal force noise thus becomes filtered by the mechanical response function, giving rise to Lorentzian peaks around $\Omega \pm \Omega_\mathsf{m}$, and out-of-resonance noise tails elsewhere. In fig. 1.2a, we show an example of an experimentally measured spectrum of a mechanical mode (this mode was measured by interferometry, see section 1.2). In general, a given mechanical oscillator may present several modes which are usually uncorrelated, resulting in a series of Lorentzian peaks.

From eq. (1.11), the variance of x reads

$$\langle x^2 \rangle = \frac{\hbar}{m_\mathsf{eff} \Omega_\mathsf{m}} \left(n_\mathsf{th}\left(\Omega_\mathsf{m}\right) + 1/2 \right). \tag{1.18}$$

Note that the variance of x does not have any dependence on the dissipation rate Γ_m, while its spectrum, according eq. (1.17), does. Two effects are at play which balance each other out. Γ_m affects both the height of the response and its width, resulting in a net constant area. This is in agreement with the equipartition theorem, which states that the mean kinetic energy of the system should be $m\langle \dot{x}^2 \rangle \sim k_\mathsf{B} T_\mathsf{env}$. For a harmonic oscillator with low dissipation, $x \approx x_0 \cos(\Omega_\mathsf{m} t)$. It follows that $\langle \dot{x}^2 \rangle = \Omega_\mathsf{m}^2 \langle x^2 \rangle$, resulting in a variance of x which is overall independent of Γ_m.

As $T \to 0$, $n_\mathsf{th} \to 0$, leaving the system with an irreducible background of fluctuations corresponding to the zero-point motion of the oscillator. This is the first truly quantum effect one can observe in a harmonic oscillator–even in its ground state, it still moves with an RMS amplitude of motion $x_\mathsf{ZP} \equiv \sqrt{\hbar/2 m_\mathsf{eff} \Omega_\mathsf{m}}$. That would is not the case in a classical system, and in the limit of low temperatures the two models diverge, as shown in fig. 1.2b.

Equation (1.18) can be read both ways: if we are able to measure the fluctuations of the position of a mode, we can infer the popoulation n_th of the environment that the mode is coupled to. To complicate matters a little, in this chapter and the following, we will study cases where the oscillator is coupled to several baths simultaneously. Then, it will be necessary to talk about the effective resonator

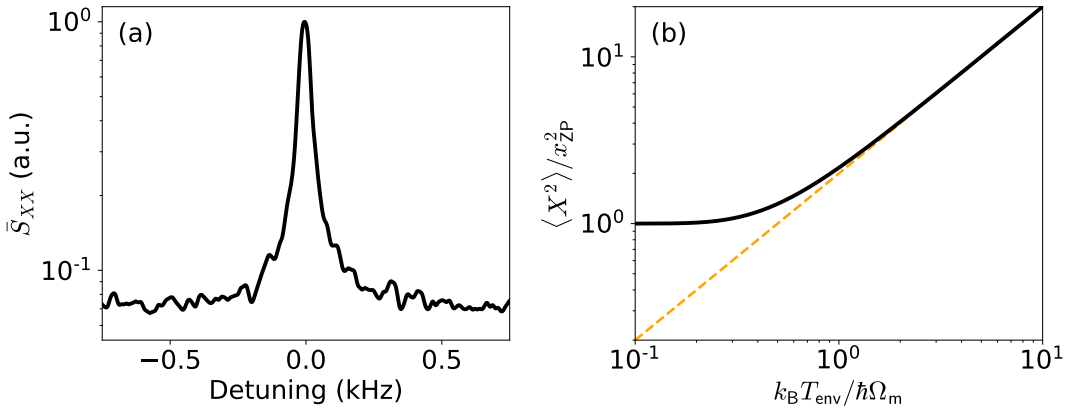

Figure 1.2: **a**, Experimentally measured noise spectrum of the position of a mechanical mode, with a central frequency of 1.47 MHz. The spectrum is plotted against the detuning from the center of the peak. Away from the Lorenztian, the noise floor does not reach zero as additional sources of noise are usually present in a measurement. **b**, Quantum (black) and classical (dashed orange) dependencies of the variance of x with the temperature.

population n_{eff}, defined such that

$$\langle x^2 \rangle = 2x_{\mathrm{ZP}}^2 \left(n_{\mathrm{eff}} + \frac{1}{2} \right). \tag{1.19}$$

The noise spectrum is thus bountiful with information regarding the mode central frequency, mass, dissipation rate, and effective temperature (or population). The latter property will be particularly interesting to know, as n_{eff} is not always known a priori. For instance, in the next chapter, we will see the example of an electromechanical cooling experiment where the mechanical occupation is lowered by coupling the resonator to a microwave circuit, realizing an auxiliary thermodynamical bath at low temperature.

In such experiments a central problem resides in the measurement of the position x, which is in practice measured indirectly. The linear filtering property of the noise spectrum proves useful: if x can be made to affect another directly measurable entity in a linear fashion, then $\bar{S}_{xx}$ can be inferred and the required information extracted. For instance, small mechanical displacements can be determined precisely using light fields. Still, that is not always a trivial task. Interaction between the light field and the mechanical oscillator can arise, and other source of noise can be introduced to the system. In the remaining sections of this chapter we present two different ways to measure the random motion of a mechanical resonator, both of which will be applied in this work (see chapters 2 and 4). In section 1.2 we show how the thermal

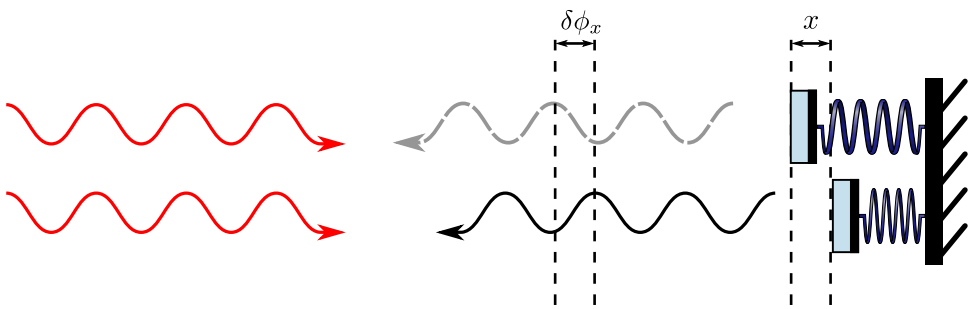

Figure 1.3: Schematic representation of the relative phase shift of a light beam due to the displacement of a reflective surface.

motion of a mechanical mode can be measured by optical interferometry, taking into account the physical limits of such a system.

1.2 Optical measurement of motion

One of the most common ways for measuring the position of a mechanical oscillator precisely is to reflect light off it, inducing a phase shift which can be measured by interferometry. In this section, we verify whether the thermal motion of the typical mechanical oscillator used in this work is sufficiently large to be measured in such a manner. We check this specifically for the case of a Mach-Zehnder interferometer, in correspondence with the experiment presented in chapter 4.

1.2.1 Position-dependent phase shift

If a mechanical resonator is displaced by a small distance x from its original position, then the phase of the reflected beam is correspondingly shifted by $\delta\phi_x$ (see fig. 1.3), with

$$\delta\phi_x = \frac{4\pi}{\lambda}x, \tag{1.20}$$

where λ is the wavelength of the light. In this manner, the information about the position x is now contained in the phase of the light beam, which can be determined by interferometry.

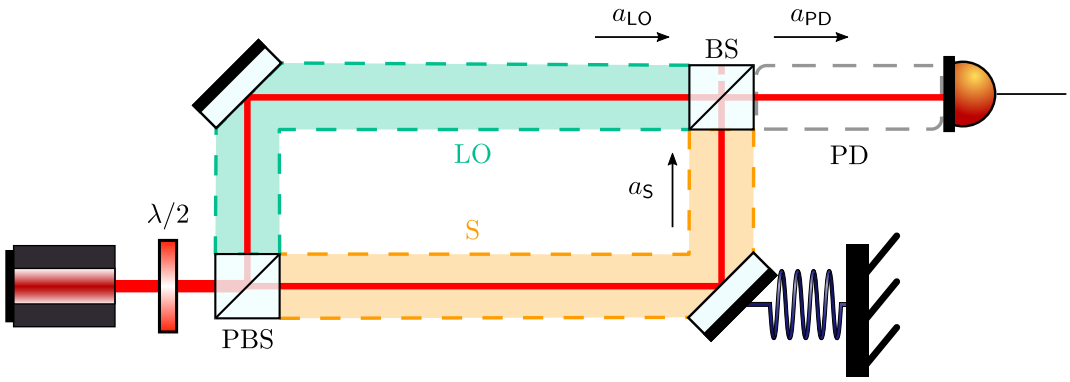

Figure 1.4: Schematic representation of the Mach-Zehnder interferometer. The sample under study is a mechanically compliant reflective surface on the S branch. The phase of the S beam is compared to a reference beam reflected off a mirror in the LO branch. Though a half-wave plate ($\lambda/2$) and a polarizing beamsplitter (PBS), the proportion of power sent into the LO branch with respect to the S branch is set. A second beamsplitter (BS) recombines the beams and partly sends them into the PD branch.

1.2.2 The Mach-Zehnder interferometer

A typical interferomety setup is the Mach-Zehnder interferometer depicted in fig. 1.4. A laser beam is first split into two paths by a beamsplitter (BS). Part of the beam is sent onto a reflective, mechanically compliant sample on the branch denoted "S", and the remainder is sent onto a mirror with fixed but configurable position, called the local oscillator "LO". The beams are then recombined and sent into the "PD" branch by a second BS and finally arrive at a photodiode, which converts the light intensity into a measurable current. This particular scheme is called a homodyne detection, characterized by the fact that the beams in S and LO have the same (*homo*) carrier frequency (*dynamis*, power).

Let a_{S} and a_{LO} respectively describe the propagating light fields coming from the S and LO branches. As they both pass through the beamsplitter, the propagating light field a_{PD} arriving at the photodiode can be expressed as

$$a_{\mathsf{PD}} = \frac{1}{\sqrt{2}}\left(a_{\mathsf{LO}} + a_{\mathsf{S}}e^{i\varphi}\right). \tag{1.21}$$

Here, $\varphi \equiv \phi + \delta\phi_x$ is the accumulated relative phase difference between the sample and the LO, and comprises both a static phase difference ϕ and the mechanically-induced phase fluctuations $\delta\phi_x$. The laser beam injected into the interferometer is assumed to be in a coherent state. We denote its amplitude by the real number α_0. By choosing the first BS to be a polarizing beamsplitter (PBS), the relative amount of light sent into the S and LO branches can be controlled with a half-wave

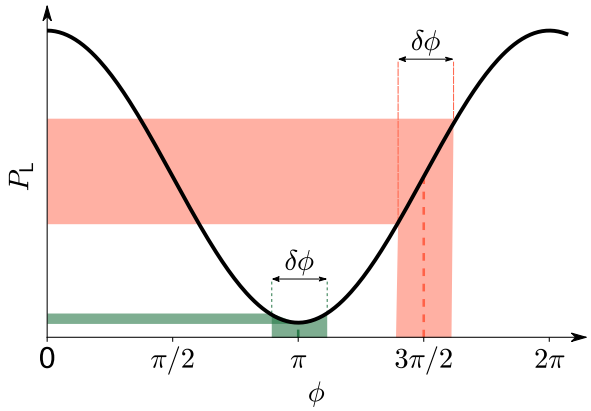

Figure 1.5: Relation between the static phase ϕ and the laser power P_L at the photodiode, considering only the first line of eq. (1.22), with $p_\mathsf{S} p_\mathsf{LO} < 1/2$. By choosing specific values of ϕ, the sensitivity of the interferometer to fluctuations $\delta\phi$ in the phase varies. If ϕ is a multiple of π, the phase fluctuations (green box), such as the ones produced by the small motion of the harmonic oscillator, result in small fluctuations in the field. Conversely, when ϕ is a half-integer multiple of π (red box), the induced fluctuations in P_L are maximal.

plate. Thus, let p_S be the fraction of the light field arriving at the final PBS from S (including losses), and p_LO from LO.

In the interferometer, our ability to discern the mechanical motion will firstly be limited by noise of the light field itself, which might have quantum or classical origins. We express these fluctuations to the first order as $a_\mathsf{S} \approx p_\mathsf{S}\alpha_0 + \delta a_\mathsf{S}$ and $a_\mathsf{LO} \approx p_\mathsf{LO}\alpha_0 + \delta a_\mathsf{LO}$, where $\delta a_{\mathsf{LO,S}} \ll \alpha_0$ represent small fluctuations of the field. We keep here δa_LO and δa_S as two separate terms, but they can be correlated if the noise is classical. δa can be further separated in amplitude noise $\delta a^P \equiv \mathrm{Re}(\delta a)$ and phase noises $\delta a^Q \equiv \mathrm{Im}(\delta a)$.

The laser power at the photodiode $P_\mathsf{L} = \hbar\omega_\mathsf{L}|a_\mathsf{PD}|^2$, where ω_L is the laser angular frequency, reads

$$\begin{aligned}\frac{P_\mathsf{L}(t)}{\hbar\omega_\mathsf{L}} \approx \frac{1}{2}\alpha_0^2\left[1 + \boxed{2p_\mathsf{S}p_\mathsf{LO}\cos\varphi(t)}\right] + \\ \alpha_0\left[p_\mathsf{S}\delta a_\mathsf{S}^P(t) + p_\mathsf{LO}\delta a_\mathsf{LO}^P(t) + \mathrm{Re}\left(\left(p_\mathsf{LO}\delta a_\mathsf{S}(t) + p_\mathsf{S}\delta a_\mathsf{LO}^*(t)\right)\mathrm{e}^{i\varphi(t)}\right)\right],\end{aligned} \tag{1.22}$$

neglecting terms of order δa^2. The term in first line of the above equation (boxed in red) contains the mechanical signal that interests us, while the second line regroups all other noise terms. To recover the influence of the position x, a choice must be made on the working point of the interferometer by choosing a value for ϕ. As shown in fig. 1.5, if $\phi = (2m - 1/2)\,\pi$, with $m \in \mathbb{Z}$, the induced fluctuations $\delta\phi_x$ are transduced maximally to field intensity fluctuations.

Is is typical in such interferometers to have $p_{\mathsf{S}} \gg p_{\mathsf{LO}}$, enabling us to drop the terms of order $(p_{\mathsf{S}}/p_{\mathsf{LO}})$. For $\delta\phi_x \ll 1$ (i.e. $x \ll \lambda$), the fluctuations $\delta P_{\mathsf{L}} = P_{\mathsf{L}} - \langle P_{\mathsf{L}} \rangle$ in the frequency domain read

$$\begin{aligned}\delta P_{\mathsf{L}}[\Omega] \approx & P_0 p_{\mathsf{S}} p_{\mathsf{LO}} \frac{4\pi}{\lambda} x[\Omega] + \\ & \sqrt{\hbar\omega_{\mathsf{L}} P_0}\left[p_{\mathsf{LO}}\delta a^P_{\mathsf{LO}}[\Omega] + \left(p_{\mathsf{S}}\delta a^Q_{\mathsf{LO}}[\Omega] - p_{\mathsf{LO}}\delta a^Q_{\mathsf{S}}[\Omega]\right)\right],\end{aligned} \tag{1.23}$$

where $P_0 \equiv \hbar\omega_{\mathsf{L}}\alpha_0^2$ is the laser power at the input of the interferometer. We note that the term $p_{\mathsf{S}}\delta a^Q_{\mathsf{LO}}$ is not in general of order p_{S}, since in some cases the fluctuations of δa^Q_{LO} vary with p_{LO}, making it a non-negligible contribution; this will be relevant in chapter 4, but we hereafter drop this term for the purposes of this section.

δP_{L} depends on two terms: the variations of the position x (the signal of interest), and a collection of noise terms originating from the fluctuations of the light field itself. With our choice of φ, we have become sensitive to δa^Q_{S}. Irrespective of φ, the amplitude fluctuations of the LO field cause noise in the field.

If we assume all noise terms to be uncorrelated from each other, the noise spectrum $\bar{S}_{PP}$ of the power reads

$$\bar{S}_{PP}[\Omega] \approx P_0^2 p_{\mathsf{S}}^2 p_{\mathsf{LO}}^2 \frac{16\pi^2}{\lambda^2}\bar{S}_{xx}[\Omega] + \hbar\omega_{\mathsf{L}} P_0 p_{\mathsf{LO}}^2 \left(\bar{S}^P_{\mathsf{LO}}[\Omega] + \bar{S}^Q_{\mathsf{LO}}[\Omega]\right), \tag{1.24}$$

where $\bar{S}^P$ and $\bar{S}^Q$ represent the noise spectra of the amplitude and phase quadratures of the fields, respectively.

As a figure of merit, we can define the signal-to-noise ratio *SNR* as the ratio of the height of the mechanical noise peak to the noise floor of $\bar{S}_{PP}$ away from a mechanical resonance. If the laser is shot-noise limited it only carries the vacuum fluctuations of the field, and both $\bar{S}^P$ and $\bar{S}^Q$ are exactly 1/2. From eq. (1.17) the *SNR* reads

$$SNR\,(\mathrm{dB}) \approx 10\log_{10}\left(p_{\mathsf{S}}^2\frac{16\pi}{\hbar c\lambda} \times \frac{k_{\mathsf{B}}T_{\mathsf{env}}}{m_{\mathsf{eff}}\Gamma_{\mathsf{m}}\Omega_{\mathsf{m}}^2}P_0\right), \tag{1.25}$$

for $k_{\mathsf{B}}T \gg \hbar\Omega_{\mathsf{m}}$, and where c is the speed of light. We note that were the laser not shot-noise limited, correlations would arise in the fluctuations of the light-fields in the S and LO branches, complicating matters a little (see chapter 4).

Equation (1.25) shows that to resolve the mechanical motion, low masses and/or dissipation rates are required for a given mode frequency. In this work, we have the advantage of working with relatively light ($m_{\mathsf{eff}} \sim 10$ ng) and low-loss ($\Gamma_{\mathsf{m}}/2\pi \sim 0.1$ Hz) resonators, vibrating around $\Omega_{\mathsf{m}}/2\pi \sim 1$ MHz. We use a Nd:YAG laser with $\lambda \approx 1$ μm , and $P_0 \approx 30$ mW. Typically, we have $p_{\mathsf{S}} \sim 10^{-2}$ (taking into account the finite reflectivity of the sample). In those conditions, at room temperature,

$SNR \sim 45$ dB. The thermal motion of the mechanical resonator can be readily resolved.

In chapter 4 we use this fact to set up an interferometer capable of measuring the thermal motion of nanomechanical samples. We will find however that the laser is not limited by shot-noise, and that a modification to the detection scheme is required to measure the mechanical motion with a high SNR. Optical infererometry, while convenient for precise characterization, does not offer any possibilities for preparing the mechanical mode in its ground state (in principle, one can use radiation pressure to displace or drive the resonator, but nothing beyond that). To do so a reciprocal interaction between the light field and the resonator mode must be set up. In optics, this could be achieved by placing the resonator inside an optical cavity; in our case, we take a similar approach in the microwave domain, for which we need to switch topics to the field of cavity electromechanics.

1.3 Cavity electromechanics

In this section we study the effects of the coupling between a mechanical mode and a microwave resonant circuit. We show that in such a system the effective occupation of a mechanical mode can be reduced to almost 0 when the circuit is pumped strongly and at the correct frequency.

To derive this result we model the entire system as two coupled harmonic oscillators. To begin with we will consider the intracavity field of a "bare" microwave resonator, without any mechanical oscillator, to lay the first stone of our model. We will add the interaction with the mechanical resonator, the effect of a strong pump, and finally the non-negligible dynamics added to the system by the noise in the light field.

1.3.1 The intracavity light field of a bare circuit

Let us consider a simple electronic circuit composed of an inductor and a capacitor in parallel. We know from electronics that, at a specific resonant frequency, the LC loop can hold a mode of the electromagnetic field, as illustrated in fig. 1.6. Such a system is readily modeled as a harmonic oscillator. We adopt a quantum mechanical framework here because it will be necessary later (see section 1.3.5), but we will simplify to classical quantities whenever appropriate.

Let $\hat{\phi}$ and $\hat{q}$ be the canonically conjugate variables of the system, describing the flux and the charge, respectively. The Hamiltonian of the circuit is then

$$\hat{H}_{\mathsf{c}} = \frac{\hat{\phi}^2}{2\mathcal{L}} + \frac{\hat{q}^2}{2\mathcal{C}}, \tag{1.26}$$

where $\mathcal{L}$ is the inductance of the circuit, and $\mathcal{C}$ its capacitance. Since this is a

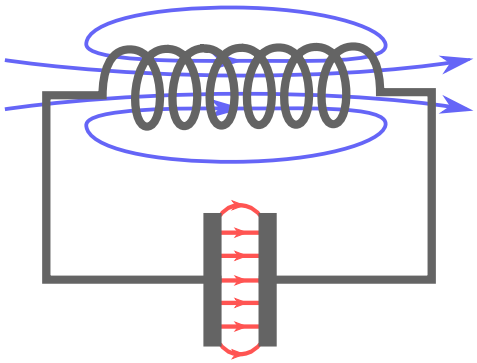

Figure 1.6: Sketch of a microwave resonant circuit, composed of an inductor and a capacitor. In red, the electric field lines are shown and in blue, the magnetic field lines.

harmonic oscillator, we may equivalently model this system using the dimensionless ladder operators $\hat{a}$ and $\hat{a}^\dagger$, defined as

$$\hat{\phi} = \sqrt{\frac{\hbar Z_0}{2}}\left(\hat{a} + \hat{a}^\dagger\right), \tag{1.27}$$

$$\hat{q} = -i\sqrt{\frac{\hbar}{2Z_0}}\left(\hat{a} - \hat{a}^\dagger\right), \tag{1.28}$$

where $Z_0 = \sqrt{\mathcal{L}/\mathcal{C}}$ is the circuit impedance. These ladder operators follow the commutation relation

$$\left[\hat{a}, \hat{a}^\dagger\right] = 1, \tag{1.29}$$

and the Hamiltonian can be rewritten as

$$\hat{H}_\mathsf{c} = \hbar\omega_\mathsf{c}\left(\hat{a}^\dagger\hat{a} + \frac{1}{2}\right), \tag{1.30}$$

where $\omega_\mathsf{c} = 1/\sqrt{\mathcal{L}\mathcal{C}}$ is the circuit resonance frequency. In this work, we describe the dynamics in either the Heisenberg or the interaction pictures, where the operators are the terms that evolve with time and describe the dynamics. As such, $\hat{a}$ describes the intracavity field (formally, the Hamiltonian above is equivalent to a cavity).

If we allow for losses in the system (not included in $\hat{H}_\mathsf{c}$), then the equation of motion for $\hat{a}(t)$ is given by the Heisenberg-Langevin equation [38]:

$$\dot{\hat{a}}(t) = -\frac{i}{\hbar}\left[\hat{a}, \hat{H}_\mathsf{c}\right] - \frac{\kappa}{2}\hat{a} + \sum_{j=0}^{N}\sqrt{\kappa_j}\hat{a}_{\mathsf{in},j}. \tag{1.31}$$

In general, there can be N channels through which the field can dissipate, and

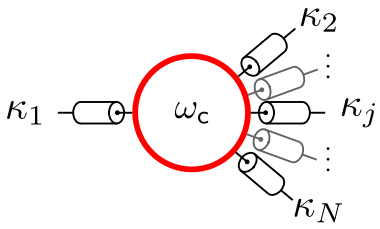

Figure 1.7: Illustration of a resonator of frequency ω_c, coupled to N ports, with a coupling κ_j to the j^{th} port. In most models, one or two ports are chosen as the input/output ports, and all others are grouped together as a single effective port through which information is irreversibly lost.

through which noise or coherent driving terms can enter the system. They are grouped into the final term of the equation, where κ_j is the decay rate for the j^{th} port (see fig. 1.7), and $\hat{a}_{in,j}$ in the corresponding input field operator. Let κ be the total loss rate, such that $\kappa \equiv \sum_j \kappa_j$.

In this work, the circuit is in reflection, i.e. the input and the output of the signal pass through the same port. We note that there are several ways in which the circuit can be read in reflection, detailed in section 1.3.2. Let κ_c be the coupling rate at which the signal passes through the readout port, with the associated input field $\hat{a}_{in,c}$. Information exiting through all other ports is considered lost, and we group all of them as one port with a net internal loss rate κ_i and an associated input light field $\hat{a}_{in,i}$. Overall, $\kappa = \kappa_c + \kappa_i$, and the equation of motion reads

$$\dot{\hat{a}}(t) = \left(-i\omega_c - \frac{\kappa}{2}\right)\hat{a}(t) + \sqrt{\kappa_c}\hat{a}_{in,c} + \sqrt{\kappa_i}\hat{a}_{in,i}. \tag{1.32}$$

In practice, $\hat{a}_{in,i}$ will only introduce noise into the system, whereas $\hat{a}_{in,c}$ may contain coherent drives sent into the circuit.

We can derive the classical behavior of the circuit by assuming that a strong drive of frequency ω_d is sent into the circuit, i.e. we let $\hat{a}_{in,c} = \alpha_{in}e^{-i\omega_d}\hat{1}$, where $\hat{1}$ is the identity operator. Switching to a frame rotating with ω_d, the equation of motion for the average amplitude of the field $\alpha = \langle\hat{a}\rangle$ reads

$$\dot{\alpha} = \left(i\Delta - \frac{\kappa}{2}\right)\alpha + \sqrt{\kappa_c}\alpha_{in,c}, \tag{1.33}$$

where we have introduced $\Delta = \omega_d - \omega_c$ as the detuning of the drive from the circuit resonance. In the steady state ($\dot{\alpha} = 0$), the intracavity field amplitude is

$$\alpha = \chi_e(\Delta)\sqrt{\kappa_c}\alpha_{in,c}, \tag{1.34}$$

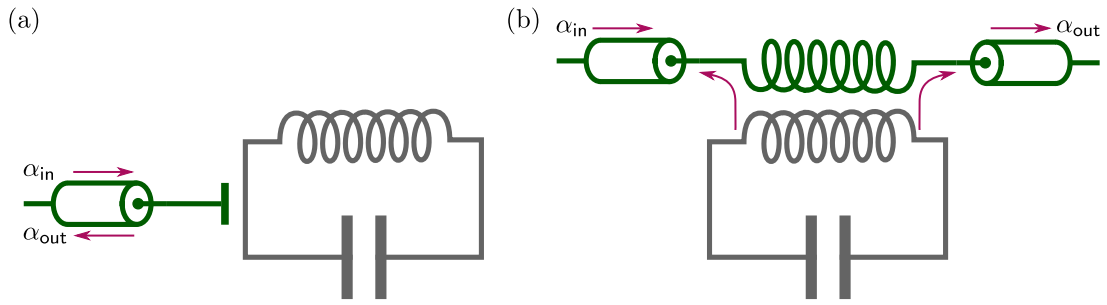

Figure 1.8: **a-b**, Two configuration cases for a microwave circuit readout. In **(a)**, we show the reflection conifguration. A transmission line (green) is capacitively coupled to the resonant microwave circuit. The input field and the output field are connected to the same port. In **(b)**, the circuit is in a hanger configuration. A transmission line (green) is inductively coupled to the circuit, with the input and output fields being connected to two separate ports. We note that the circuit radiates the field symmetrically into both directions of the transmission line–in principle, the output field can be therefore recovered from either port.

where χ_e is the electric susceptibility, defined as

$$\chi_e(\omega) \equiv [-i\omega + \kappa/2]^{-1}\,. \tag{1.35}$$

1.3.2 Input-output formalism

As the field leaks into the readout port a measurable current is generated. The output of the circuit can be predicted by the input-output relation [35], giving the output field α_{out} in terms of α and α_{in}. This relation depends on the readout scheme [20]. Within the context of this work, two main configurations will be presented: the reflection and the hanger configurations. In both cases the input and output fields pass through the same circuit port.

The reflection configuration simply consists of a transmission line which capacitively couples to the circuit–see fig. 1.8a. This line carries the input field and the output circuit signal; its behavior is analogous to that of an optical circuit measured in reflection, and will have the same sort of response. In this configuration the input-output relation reads

$$\alpha_{out} = -\alpha_{in,c} + \sqrt{\kappa_c}\alpha. \tag{1.36}$$

In the hanger configuration, the circuit is inductively coupled to a transmission line which carries the information, as shown in figure fig. 1.8b. This is almost equivalent to reading the reflection of a circuit, except that the output signal radiates symmetrically in both directions of the transmission line, meaning half of the infor-

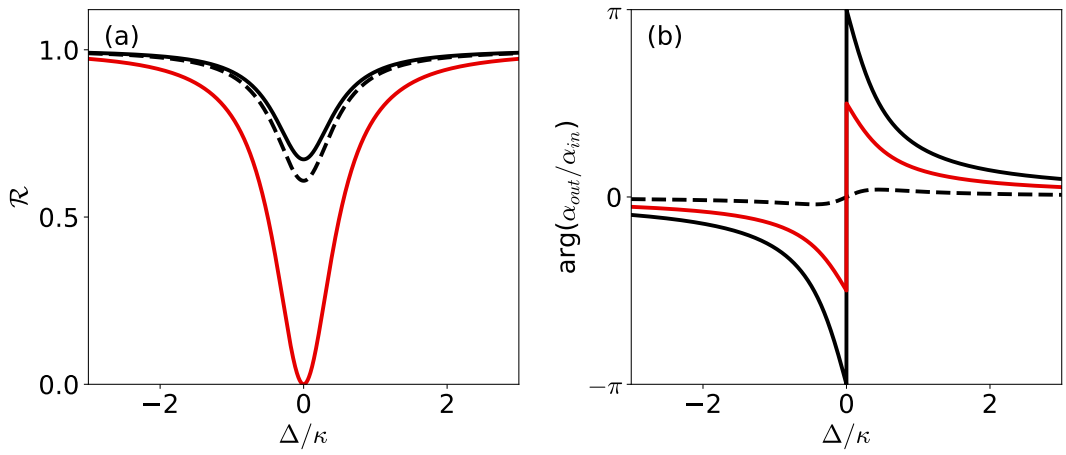

Figure 1.9: **a-b**, The response of a bare harmonic circuit in the reflection configuration, for fixed κ. The reflection coefficient is shown in **(a)**, and the phase of the reflected signal is shown in **(b)**. Three different cases are considered: $\eta = 0.91$, the undercoupled case depicted by the dashed black line, $\eta = 0.11$, the overcoupled case depicted by the solid black line, and $\eta = 0.5$, the critically coupled case depicted by the solid red line.

mation put out by the circuit is lost. This configuration is nevertheless practical for measuring several cavities in a series, and is used in this work. For this configuration the input-output relation reads

$$\alpha_{\mathsf{out}} = -\alpha_{\mathsf{in,c}} + \sqrt{\frac{\kappa_{\mathsf{c}}}{2}}\alpha. \tag{1.37}$$

As an example, let us analyze the output signal of a circuit measured in a reflection configuration. Substituting our result from eq. (1.34), we find that the reflected power $\mathcal{R} \equiv |\alpha_{\mathsf{out}}/\alpha_{\mathsf{in}}|^2$ reads

$$\mathcal{R} = \left| 1 - \frac{\eta}{i\Delta/\kappa + 1/2} \right|^2, \tag{1.38}$$

where $\eta = \kappa_{\mathsf{c}}/\kappa$. The reflected power follows a Lorentzian dip, shown in fig. 1.9a. The form of the reflected spectrum depends on the newly introduced coupling ratio η, which compares how much of the intracavity field leaks into the loss ports compared to the readout port. We can distinguish three cases:

- *critical coupling*, $\eta = 1/2$: in this optimal case, $\mathcal{R} = 0$ on resonance, accompanied by a phase flip of π.

- *overcoupled*, $\eta < 1/2$: the dip in the reflected intensity is shallower than in the critical coupling case, and in the limit of small η essentially no information can be obtained by measuring the intensity of the reflected signal. The phase of the reflected signal on the other hand varies maximally, see fig. 1.9b.
- *undercoupled* $\eta > 1/2$: in that case, most of the intracavity field is dissipated into the loss port. Note from fig. 1.9 that the undercoupled and overcoupled cases can produce identical intensity reflection spectra, but with significantly different behaviors in phase.

In practice it is always better to be a little overcoupled than undercoupled: although in both cases the variation in the reflected power is reduced compared to the critically coupled case, more signal leaks into the readout port in the overcoupled case.

This simple and well-known circuit can be to a harmonic oscillator, which gives rise to rich dynamics. In opto-/electromechanics, the paradigmatic way to induce this coupling is to fabricate a system where the motion of the mechanical resonator shifts the resonance frequency of the circuit. This is called dispersive coupling, and is precisely the scenario studied in this work.

1.3.3 Dispersive coupling

General description

One way to introduce dispersive coupling is to allow one of the capacitor plates of the microwave circuit to move, thereby varying the circuit frequency inversely with the plate displacement, as illustrated in fig. 1.10. For a small displacement x from equilibrium, we can take a perturbative approach, and express ω_c as

$$\omega_\mathsf{c}(x) \approx \omega_\mathsf{c}(0) - Gx + \mathcal{O}(x), \tag{1.39}$$

where $G \equiv -\partial\omega_\mathsf{c}(x)/\partial x$. Note the sign convention: G is chosen to always be positive, following [20], and x must therefore be defined accordingly–here, an increase in the distance between the capacitor plates represents a decrease in x[3]. In a quantum framework, replacing x with the operator $\hat{x}$, the Hamiltonian of the entire system reads

$$\hat{H}_\mathsf{em} = \hat{H}_\mathsf{c} - \hbar G\hat{x}\hat{a}^\dagger\hat{a} + \hat{H}_\mathsf{m}, \tag{1.40}$$

with

$$\hat{H}_\mathsf{m} \equiv \frac{\hat{p}^2}{2m_\mathsf{eff}} + \frac{1}{2}m_\mathsf{eff}\Omega_\mathsf{m}^2\hat{x}^2, \tag{1.41}$$

[3]Several other dynamics may be present in optomechanical systems: nonlinear terms may play a relevant role in the dynamics of the system if the fluctuations or the coupling rate are large; dissipative coupling is also a possibility to induce an interaction between phonons and photons, wherein the dissipation of the system is dependent on the position of the oscillator [39]. Such cases are not relevant to this work, and will not be mentioned further.

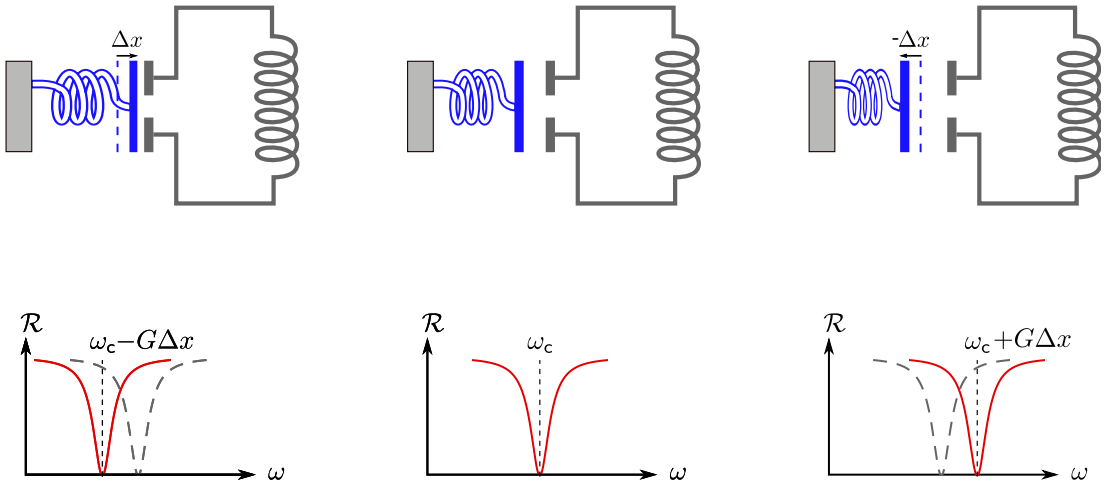

Figure 1.10: **(Center)** Illustration of a dispersively coupled electromechanical system with a mechanically compliant capacitor. Below, the typical reflection of the circuit is shown. If the mobile capacitor plate moves closer to **(left)** or farther away from **(right)** the static capacitor plate by a small distance Δx, the frequency of the circuit decreases or increases by $G\Delta x$. The drawing is not to scale.

and where $\hat{p}$ is the momentum operator.

From the Heisenberg-Langevin equations, transforming as before to the frame rotating with the drive, the equations of motion of the system can be derived to be

$$\dot{\hat{a}}(t) = \left(i\Delta + iG\hat{X}(t) - \frac{\kappa}{2}\right)\hat{a}(t) + \sqrt{\kappa_\mathsf{c}}\hat{a}_{\mathsf{in,c}}(t) + \sqrt{\kappa_\mathsf{i}}\hat{a}_{\mathsf{in,i}}(t), \tag{1.42}$$

$$\ddot{\hat{x}}(t) + \Gamma_\mathsf{m}\dot{\hat{x}}(t) + \Omega_\mathsf{m}^2\hat{x}(t) = \frac{1}{m_\mathsf{eff}}\left(\hat{F}_\mathsf{th}(t) + \hbar G\hat{a}^\dagger(t)\hat{a}(t)\right). \tag{1.43}$$

In the steady state, the pumping of the circuit shifts the oscillator's equilibrium position from 0 to $\bar{x} \equiv \langle\hat{x}(t)\rangle$. Reciprocally, this displacement results in a shift in the circuit's resonance frequency, which we take into account by a corrected detuning $\bar{\Delta} \equiv \Delta - g_0^2|\alpha|^2/2\Omega_\mathsf{m}$. Here, g_0 is the vacuum electromechanical coupling rate, with

$$g_0 \equiv Gx_\mathsf{ZP}, \tag{1.44}$$

and corresponds to the frequency shift of the circuit if the resonator is displaced by x_ZP. This often-recurring term is sometimes preferred to G for quantifying the coupling, as g_0 allows a more direct comparison between different electromechanical systems with distinct geometries.

Assuming that $\hat{a}_{\mathsf{in,i}}$ is purely a noise term, the steady-state solutions read

$$\bar{x} = 2x_{\mathsf{ZP}}\frac{g_0}{\Omega_{\mathsf{m}}}|\alpha|^2, \tag{1.45}$$

$$\alpha = \chi_{\mathsf{e}}\left(\bar{\Delta}\right)\sqrt{\kappa_{\mathsf{c}}}\alpha_{\mathsf{in,c}}. \tag{1.46}$$

Linearized interaction

Many of the interesting dynamics in an electromechanical circuit occur in the fluctuations around these steady states of the system. To study them, the system must be strongly pumped. We hence shift our reference frame to the equilibrium of the mechanical mode, transforming $\hat{x} \to \bar{x}\hat{1} + \hat{x}$, where $\hat{1}$ is the identity operator, and $|\hat{x}| \ll \bar{x}$. The fluctuations of the mechanical resonator cause small variations in the field, such that we can write $\hat{a}(t) = \alpha\hat{1} + \delta\hat{a}(t)$, with $|\delta\hat{a}| \ll \alpha$.

Keeping only the dominant terms in $\hat{x}$ and $\delta\hat{a}$, eqs. (1.42) and (1.43) become

$$\delta\dot{\hat{a}}(t) = \left(-i\bar{\Delta} - \frac{\kappa}{2}\right)\delta\hat{a}(t) + iGx(t)\alpha + \sqrt{\kappa_{\mathsf{c}}}\delta\hat{a}_{\mathsf{in,c}}(t) + \sqrt{\kappa_{\mathsf{i}}}\delta\hat{a}_{\mathsf{in,i}}(t), \tag{1.47}$$

$$\delta\dot{\hat{a}}^{\dagger}(t) = \left(i\bar{\Delta} - \frac{\kappa}{2}\right)\delta\hat{a}(t) - iG\hat{x}(t)\alpha^* + \sqrt{\kappa_{\mathsf{c}}}\delta\hat{a}^{\dagger}_{\mathsf{in,c}}(t) + \sqrt{\kappa_{\mathsf{i}}}\delta\hat{a}^{\dagger}_{\mathsf{in,i}}(t), \tag{1.48}$$

$$\ddot{\hat{x}}(t) + \Gamma_{\mathsf{m}}\dot{\hat{x}}(t) + \Omega_{\mathsf{m}}^2\hat{x}(t) = \frac{1}{m_{\mathsf{eff}}}\left[\hat{F}_{\mathsf{th}}(t) + \hbar G\left(\alpha^*\delta\hat{a}^{\dagger}(t) + \alpha\delta\hat{a}(t)\right)\right], \tag{1.49}$$

where we have included the dynamics of $\delta\hat{a}^{\dagger}$. In the frequency domain, we find a set of equations of which we will make consistent use hereafter:

$$\chi_{\mathsf{e}}^{-1}\left(\bar{\Delta} + \Omega\right)\delta\hat{a}[\Omega] = i\alpha G\hat{x}[\Omega] + \sqrt{\kappa_{\mathsf{c}}}\delta\hat{a}_{\mathsf{in,c}}[\Omega] + \sqrt{\kappa_{\mathsf{i}}}\delta\hat{a}_{\mathsf{in,i}}[\Omega], \tag{1.50}$$

$$\chi_{\mathsf{e}}^{-1^*}\left(\bar{\Delta} - \Omega\right)\delta\hat{a}^{\dagger}[\Omega] = -i\alpha^* G\hat{x}[\Omega] + \sqrt{\kappa_{\mathsf{c}}}\delta\hat{a}^{\dagger}_{\mathsf{in}}[\Omega] + \sqrt{\kappa_{\mathsf{i}}}\delta\hat{a}^{\dagger}_{\mathsf{in,i}}[\Omega], \tag{1.51}$$

$$\chi_{\mathsf{m}}^{-1}(\Omega)\hat{x}[\Omega] = \hbar G\left(\alpha\delta\hat{a}^{\dagger}[\Omega] + \alpha^*\delta\hat{a}[\Omega]\right) + \hat{F}_{\mathsf{th}}[\Omega]. \tag{1.52}$$

In this set of equations where we only consider small variations around larger averages, we are left with a linearly interacting system. Crucially, the electromechanical coupling G is now dressed by the circuit field α: the coupling is enhanced and linearized by the strong pumping of the circuit.

From eq. (1.52), the mechanical oscillator is driven both by the electrostatic force and by the thermal Langevin force. As for the fluctuations in the circuit field, they are driven both by $\delta\hat{a}_{\mathsf{in}}$ and the motion of the oscillator. Depending on the experiment, $\delta\hat{a}_{\mathsf{in}}$ may simply be noise entering the circuit or an additional weak drive sent into the system. Both of these options will be explored in the following subsections.

We see that the interaction is two-sided: the motion of the mode causes fluctuations in the field, which in turn induce fluctuations in the motion. This backaction

effect modifies the dynamics of the resonator, which is at the core of the phenomenon of electromechanical cooling.

1.3.4 Dynamical backaction

The main result that we derive from eqs. (1.50) to (1.52) is that the response of the mechanical resonator itself becomes modified as a result of the interaction between the light and motion. To find the effective response of the resonator we first solve for $\hat{x}$ in eqs. (1.50) and (1.51). For simplicity we drop the input field terms $\delta\hat{a}_{\mathsf{in}}$, which do not affect the results of this derivation. Then, the equations of motion for the intracavity field read

$$\delta\hat{a}[\Omega] = iG\chi_{\mathsf{e}}(\bar{\Delta}+\Omega)\alpha\hat{x}[\Omega], \tag{1.53}$$

$$\delta\hat{a}^{\dagger}[\Omega] = -iG\chi_{\mathsf{e}}^{*}(\bar{\Delta}-\Omega)\alpha^{*}\hat{x}[\Omega]. \tag{1.54}$$

Plugging these terms into eq. (1.52), we find that the equation of motion for the position can be written in the form

$$\hat{x}[\Omega] = \chi_{\mathsf{eff}}(\Omega)^{-1}\hat{F}_{\mathsf{th}}[\Omega], \tag{1.55}$$

where χ_{eff} is an effective susceptibility which we can approximate as

$$\chi_{\mathsf{eff}}^{-1}(\Omega) \approx m_{\mathsf{eff}}\left[-\left(\Omega^2-(\Omega_{\mathsf{m}}+\delta\Omega_{\mathsf{m}})^2\right)-i\Omega\left(\Gamma_{\mathsf{m}}+\Gamma_{\mathsf{em}}\right)\right], \tag{1.56}$$

where $\delta\Omega_{\mathsf{m}}$ is the electromechanically induced frequency shift and Γ_{em} the electromechanical damping rate. We note that this expression for χ_{eff} is only valid when $\delta\Omega_{\mathsf{m}}$ and $(\Gamma_{\mathsf{m}}+\Gamma_{\mathsf{em}})$ are both much smaller than Ω_{m} and κ.

The newly introduced terms $\delta\Omega_{\mathsf{m}}$ and Γ_{m} read

$$\delta\Omega_{\mathsf{m}} \equiv g^2\times\left[(\bar{\Delta}+\Omega_{\mathsf{m}})|\chi_{\mathsf{e}}(\bar{\Delta}+\Omega_{\mathsf{m}})|^2+(\bar{\Delta}-\Omega_{\mathsf{m}})|\chi_{\mathsf{e}}(\bar{\Delta}-\Omega_{\mathsf{m}})|^2\right], \tag{1.57}$$

$$\Gamma_{\mathsf{em}} \equiv C\Gamma_{\mathsf{m}}\left(\frac{\kappa}{2}\right)^2\left[|\chi_{\mathsf{e}}(\bar{\Delta}+\Omega_{\mathsf{m}})|^2-|\chi_{\mathsf{e}}(\bar{\Delta}-\Omega_{\mathsf{m}})|^2\right], \tag{1.58}$$

where we have introduced the dressed electromechanical coupling rate $g = g_0\alpha$, and the cooperativity $C \equiv 4g^2/\kappa\Gamma_{\mathsf{m}}$. This cooperativity compares the electromechanical coupling rate both to the mechanical and the electrical dissipation rate. As such, it essentially serves as a measure for the average number of coherent interactions that can occur in the system. C is an important parameter which will often appear in key equations of the electromechanical interaction.

The net result is that the motion of the membrane, causing fluctuations of the field, can become driven by these very fluctuations. This backaction effect can be perceived as a modified response to external forces, adding both an in-phase and a quadrature component. The in-phase term modifies the restoring force acting on

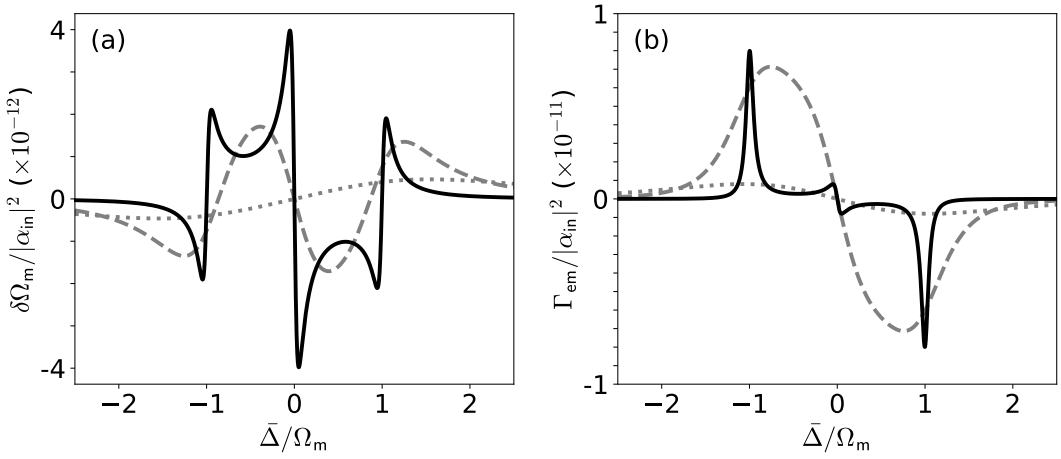

Figure 1.11: **a-b**, Shift in **(a)** the mechanical resonance frequency and **(b)** the electromechanical damping rate, for various pumping frequencies $\bar{\Delta}$. For both figures, various values of κ/Ω_m are taken, namely: 0.1 (black), 1 (gray, dashed) and 4 (gray, dotted). The black curve is representative of the electromechanical device parameters presented in chapter 2, with typical values $g_0 = 1$ Hz, $\Omega_m = 500$ kHz, and $\eta = 1/2$.

the oscillator, changing its response frequency, effectively softening or hardening the mechanical "spring"–note that the sign of the change depends on the laser detuning $\bar{\Delta}$. For this reason, this effect has been dubbed the optical spring, shown in fig. 1.11a. Similarly, the quadrature term given in eq. (1.58) describes the modification to the mechanical linewidth which can be either positive or negative , as shown in fig. 1.11b. This term, resulting from the retarded nature of the circuit response, is in phase with the velocity, and induces an amplification or a damping of the mechanical motion, as we will see below.

The dynamical backaction is strongly dependent on the ratio κ/Γ_m. In the so-called "bad cavity limit", $\kappa \gg \Gamma_m$, the electromechanically induced damping/anti-damping effects essentially vanish. The intracavity field responds perfectly in-phase to the mechanical motion. In the opposite regime, called the "resolved sideband regime" where $\kappa \ll \Gamma_m$, the extrema of Γ_m and all interesting dynamics occur on the mechanical sidebands of the circuit, around $\bar{\Delta} = \pm\Omega_m$. At those special points, it can in general be shown that

$$\Gamma_{em}\big|_{\bar{\Delta}=\pm\Omega_m} = \mp C\Gamma_m \left(1 - \frac{1}{\eta_{rsf} + 1}\right), \tag{1.59}$$

where $\eta_{rsf} \equiv (4\Omega_m/\kappa)^2$ is the resolved sideband factor.

When pumping (i.e. increasing C) on the blue sideband, the effective damping rate $\Gamma_{\mathsf{eff}} \equiv \Gamma_{\mathsf{em}} + \Gamma_{\mathsf{m}}$ eventually becomes negative, resulting in self-sustaining oscillations, leading to parametric instabilities and chaotic motion [40]. Conversely, pumping on the red sideband increases the net dissipation rate Γ_{eff}. This is particularly interesting for this work: from the fluctuation-dissipation theorem we know that inducing dissipation leads to fluctuations of the mechanical motion, and by extension, as seen in section 1.1.5, on the occupancy of the mechanical mode. As we will see, the consequence of this dynamical interaction is that the temperature of the mode can be reduced by pumping the red sideband of the circuit.

1.3.5 Electromechanical cooling

As one might expect from the fluctuation-dissipation theorem, the modification in the damping rate has consequences for the motion spectrum of the mechanical resonator. Interestingly, although we have previously found that the dissipation rate played no role in the RMS fluctuations of the resonator (i.e. did not affect its temperature), the situation is now different.

To show this, we solve for $\hat{x}$ in eqs. (1.50) to (1.52), and find

$$x[\Omega] = \chi_{\mathsf{eff}}^{-1}(\Omega)\left(\hat{F}_{\mathsf{th}}[\Omega] + \hat{F}_{\mathsf{cav}}[\Omega]\right), \tag{1.60}$$

with

$$\begin{aligned}\hat{F}_{\mathsf{cav}}[\Omega] \equiv &\hbar G\alpha^* \chi_{\mathsf{e}}(\bar{\Delta}+\Omega)(\sqrt{\kappa_{\mathsf{c}}}\delta\hat{a}_{\mathsf{in,c}}[\Omega] + \sqrt{\kappa_{\mathsf{i}}}\delta\hat{a}_{\mathsf{in,i}}[\Omega]) + \\ &\hbar G\alpha \chi_{\mathsf{e}}^*(\bar{\Delta}-\Omega)(\sqrt{\kappa_{\mathsf{c}}}\delta\hat{a}_{\mathsf{in,c}}^\dagger[\Omega] + \sqrt{\kappa_{\mathsf{i}}}\delta\hat{a}_{\mathsf{in,i}}^\dagger[\Omega]).\end{aligned} \tag{1.61}$$

In a quantum picture, this can be interpreted as photons from the upper and lower mechanical sidebands being scattered to the circuit resonance frequency by Stokes resp. anti-Stokes processes. As a result, in addition to the thermal force, the mechanical mode is also being driven by a cavity force $\hat{F}_{\mathsf{cav}}$, which heats the mode up. On the other hand, we found in eq. (1.55) that the dissipation rate of the mode is also modified by the backaction. Let us verify the net effect of the electromechanical interaction by computing $S_{\hat{x}\hat{x}}$, the noise spectrum of $\hat{x}$, which we can determine from the linear filtering property (eq. (1.13)).

We recall the spectrum of the thermal force noise given in eq. (1.15). The spectrum of the cavity force can be determined from the definition of $\hat{F}_{\mathsf{cav}}$. We assume that the two input field noise terms, $\delta\hat{a}_{\mathsf{in,c}}$ and $\delta\hat{a}_{\mathsf{in,i}}$, are uncorrelated and Markovian, with a thermal population $\bar{n} \equiv n_{\mathsf{B}}(\omega_{\mathsf{c}})$. For both terms, the spectral autocorrelation has the form [35]

$$\left\langle (\hat{a}_{\mathsf{in}}[\Omega])^\dagger \hat{a}_{\mathsf{in}}[\Omega']\right\rangle = 2\pi\bar{n}\delta(\Omega-\Omega'), \tag{1.62}$$

$$\left\langle \hat{a}_{\mathsf{in}}[\Omega]\,(\hat{a}_{\mathsf{in}}[\Omega'])^\dagger\right\rangle = 2\pi(\bar{n}+1)\delta(\Omega-\Omega'). \tag{1.63}$$

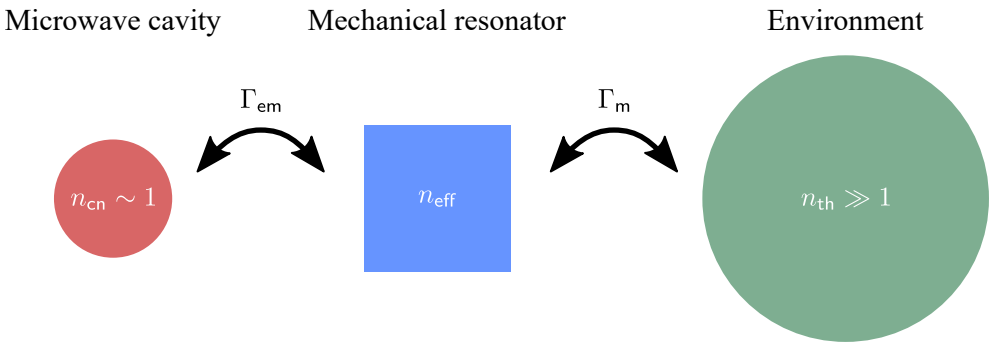

Figure 1.12: Illustration of the mechanical resonator (shown as a square), of population n_{eff}, in an electromechanical cooling experiment. It is coupled to two baths (shown as circles): the thermal environment, with a population $n_{\mathsf{th}} \gg 1$, at a rate Γ_{m}, and to the microwave resonator, with an effective population $n_{\mathsf{cn}} \sim 1$ (derived below), at a rate Γ_{em}.

By evaluating the autocorrelation of the cavity force[4] $\langle F_{\mathsf{cav}}[-\Omega] F_{\mathsf{cav}}[\Omega'] \rangle$, we find that the symmetric cavity noise spectrum reads

$$\bar{S}_{\mathsf{cav}}[\Omega] = \hbar^2 G^2 |\alpha|^2 \kappa \left(\bar{n} + \frac{1}{2} \right) \left[|\chi_{\mathsf{e}}(\bar{\Delta} - \Omega)|^2 + |\chi_{\mathsf{e}}(\bar{\Delta} + \Omega)|^2 \right] . \tag{1.64}$$

From the linear filtering of noise spectra, the symmetric motion spectrum thus reads

$$\bar{S}_{\hat{x}\hat{x}}[\Omega] = |\chi_{\mathsf{eff}}(\Omega)|^2 \left(\bar{S}_{\hat{F}\hat{F}}[\Omega] + \bar{S}_{\mathsf{cav}}[\Omega] \right) , \tag{1.65}$$

In the following, we will show that the resulting system is equivalent to fig. 1.12 where the mechanical resonator is coupled to two baths simultaneously. Firstly, as we have seen up to now, it is coupled to a thermal bath of population n_{th} at a rate Γ_{m}. But the microwave resonator now plays the role of a second bath, of effective population n_{cn} (different from $\bar{n}$, and shown below to be of order 1 for our device parameters), at a rate Γ_{em}.

Thermal force noise

From eq. (1.15), based on the fluctuation-dissipation theorem, the thermal force noise reads:

$$\bar{S}_{\hat{\mathsf{F}}\hat{\mathsf{F}}}[\Omega] = 2\hbar\Omega \left(n_{\mathsf{th}} + \frac{1}{2} \right) \Gamma_{\mathsf{m}} m_{\mathsf{eff}} . \tag{1.66}$$

[4] For a Hermitian operator $\hat{O}$, $\left(\hat{O}[\Omega]\right)^\dagger \equiv \hat{O}[-\Omega]$

Its contribution to the fluctuations in position, denoted as $\langle x^2 \rangle_{\mathsf{th}}$, can be shown to read[5]

$$\langle x^2 \rangle_{\mathsf{th}} = 2x_{\mathsf{ZP}} \frac{\Gamma_{\mathsf{m}}}{\Gamma_{\mathsf{eff}}} \left(n_{\mathsf{th}} + \frac{1}{2} \right). \tag{1.67}$$

Due to the modified susceptibility, we find a different expression for the thermal mode population $n_{\mathsf{eff,th}}$ than previously derived: a dependence on the ratio $\Gamma_{\mathsf{m}}/\Gamma_{\mathsf{eff}}$ has been acquired. If the pump is on the blue sideband of the circuit ($\bar{\Delta} = \Omega_{\mathsf{m}}$), then the mechanical linewidth decreases and the mechanical resonator is heated up, increasing the thermal population. On the other hand, if the pump is on the red sideband ($\bar{\Delta} = -\Omega_{\mathsf{m}}$), $n_{\mathsf{eff,th}} < n_{\mathsf{th}}$. In the latter case, the effective thermal population reads

$$n_{\mathsf{eff,th}} = n_{\mathsf{th}} \times \left(\frac{1 + \eta_{\mathsf{rsf}}^{-1}}{1 + C + \eta_{\mathsf{rsf}}^{-1}} \right). \tag{1.68}$$

In this context, eq. (1.68) allows us to interpret C as a measure for the cooling power. As C becomes large, the thermal population tends to zero. This classical cooling scheme is a well-established result in the field of optomechanics, and has been demonstrated experimentally by Arcizet et al. [27] some fifteen years ago.

Conventionally, the ground state is defined as having an effective resonator population n_{eff} well below 1. Achieving this is therefore conditional on having a sufficiently high cooperativity, specifically $C \gg n_{\mathsf{th}}$ (here, $\eta_{\mathsf{rsf}} \sim 1$). In practice, it can be challenging to achieve ground-state cooling for low-frequency (below megahertz) modes at room temperature, and this has only been achieved recently [34]. Most experiments, those presented in this work included, pre-cool the electromechanical device to cryogenic temperatures to reduce n_{th}, and ease the requirement for strong pumping.

Interestingly, as C becomes large, all fluctuations in eq. (1.67) vanish. This is not a violation of the Heisenberg uncertainty principle however, as the electromechanical coupling induces an additional noise source to the mechanical system, which adds fluctuations. This additional term also imposes another requirement for the system to reach the ground state which must be taken into account.

Cavity backaction noise

From eq. (1.64) we derive the resonator fluctuations induced by the cavity noise, $\langle x^2 \rangle_{\mathsf{cav}}$:

$$\langle x^2 \rangle_{\mathsf{cav}} = 2x_{\mathsf{ZP}} \frac{\Gamma_{\mathsf{em}}}{\Gamma_{\mathsf{eff}}} \left(\bar{n}(1 + 2\eta_{\mathsf{rsf}}^{-1}) + \eta_{\mathsf{rsf}}^{-1} + \frac{1}{2} \right), \tag{1.69}$$

where we have already assumed that the pump is placed on the red sideband.

[5] For simplicity, we assume that the coupling is weak compared to the mechanical frequency, such that the optical spring effect is negligible, and $\delta\Omega_{\mathsf{m}} \ll \Omega_{\mathsf{m}}$.

For an optical field, $\bar{n} \ll 1$ even at room temperature. More attention is required when dealing with microwave photons, with a typical frequency here on the order of 5 GHz. At room temperature, $\bar{n} \approx 8000$, making it impossible to study quantum electromechanics with microwave photons at room temperature. To ensure that $\bar{n} < 1$, quantum electromechanical experiments are performed at temperatures of about 20 mK.

From eq. (1.69) we can treat the circuit as a thermal bath, coupled to the mechanical oscillator at a rate Γ_{em}, with an effective population n_{cn}, which reads

$$n_{\mathsf{cn}} \approx \eta_{\mathsf{rsf}}^{-1}. \tag{1.70}$$

Note that the final term 1/2 in eq. (1.69) does not enter in our definition of the effective population, as seen below.

Effective resonator population

Overall, the fluctuations of the mechanical resonator position read

$$\langle x^2 \rangle \equiv \langle x^2 \rangle_{\mathsf{th}} + \langle x^2 \rangle_{\mathsf{cav}} = 2x_{\mathsf{ZP}} \left(n_{\mathsf{eff}} + \frac{1}{2} \right), \tag{1.71}$$

where

$$n_{\mathsf{eff}} = \frac{\Gamma_{\mathsf{m}} n_{\mathsf{th}} + \Gamma_{\mathsf{em}} n_{\mathsf{cn}}}{\Gamma_{\mathsf{eff}}}. \tag{1.72}$$

This expression confirms our original assertion: the mechanical resonator is coupled to two baths, at different rates. The evolution of the effective resonator population is summarized in fig. 1.13. In the limit of strong pumping $\Gamma_{\mathsf{eff}} \to \Gamma_{\mathsf{em}}$, and the mechanical resonator thermalizes fully with the microwave resonator.

From eq. (1.72) we find that the sideband resolved factor plays a limiting role on the minimal value of n_{eff}: as $C \to \text{inf}$, $n_{\mathsf{eff}} \to \eta_{\mathsf{rsf}}^{-1}$. This highlights a second requirement for an electromechanical device: if it is to be cooled to the ground state, in addition to reaching $C \gg n_{\mathsf{th}}$, the system needs to be deeply in the resolved sideband regime. If $\eta_{\mathsf{rsf}} \leqslant 1$, the ground state cannot be reached, independent of the pumping strength[6]–for instance, in fig. 1.13, $\eta_{\mathsf{rsf}} = 1$, and $n_{\mathsf{eff}} > 1$ for any C.

1.4 Summary

In summary, we have presented the reader with the basic tools which can be used to determine the position of a mechanical oscillator by means of a probing system.

[6]Other methods exist to achieving the ground state if this condition is not met, see e.g Refs. [41, 42]. However, these usually require high measurement efficiency, or multiple cavities, and could not be applied in this work.

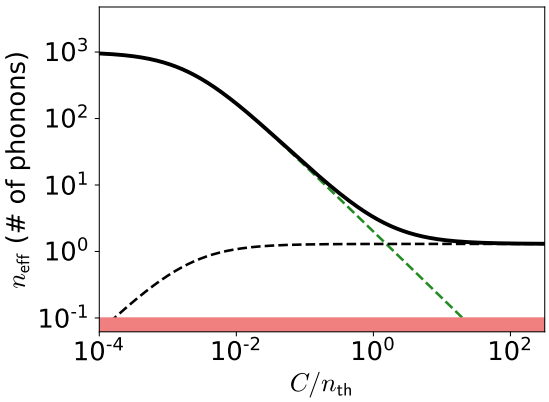

Figure 1.13: Electromechanical cooling of a mechanical resonator coupled to a microwave resonator which is pumped on its red sideband. For this figure it was assumed that $\eta_{\mathsf{rsf}} = 1$, representative of the experiments in the following chapter. Represented are the effective population of the resonator (black), and contributions $n_{\mathsf{eff,th}}$ added to it by the thermal environment (green, dashed) and the circuit n_{cn} (black, dashed). For illustrative purposes, $\bar{n} = 10^{-1}$ (represented by the red rectangle), although this value is typically even lower in physical experiments.

We have introduced the concept of noise spectra, and described how these can be used to extract information from a randomly fluctuating mechanical oscillator. To experimentally obtain this information, we have proposed two schemes. First, we considered the Mach-Zehnder interferometer, which transduces the position of a mechanical oscillator into phase fluctuation of a probing laser beam. By analyzing the various noise sources in such a system, we found that, for a shot-noise limited laser beam, a signal-to-noise ratio of up to 45 dB could be attained.

To push the accuracy of the detection further and allow a finer control over the mechanical motion, an electromechanical device, where the mechanical oscillator is dispersively coupled to a microwave circuit, was then considered. We found that the interplay between the two resonators causes a backaction effect on the mechanical oscillator which modifies its response to external forces. As a result, the effective thermal environment of the oscillator becomes modified. We described how its average population could brought close to 0 in a sideband cooling experiment. Two conditions are necessary to achieve this: the cooperativity of the system must be higher than the thermal population, and the system must be in the resolved sideband regime. In the following chapter we present an electromechanical device fabricated and characterized in our group at the beginning of this thesis. The results covered in this chapter are applied to verify the figures of merit of that device, and a sideband cooling experiment is presented.

Chapter 2

First electromechanical experiments

All the necessary theoretical background having been introduced in the previous chapter, we now turn our attention to the first set of results obtained in our group with an electromechanical cavity. This chapter summarizes the work done at the beginning of this thesis, and which forms the essential part of the work of T. Capelle who defended his thesis in 2020 [43]. These experiments introduce the physical system that we work with Their results will serve to motivate the subsequent work pursued by the author, presented in the following chapters.

We aim to leverage the tools of circuit quantum electrodynamics to achieve a deep quantum control over a mechanical mode. In the short term, the first milestone is to initialize the mechanical mode in its ground state through a sideband cooling process. As discussed in chapter 1 the ability to do so is defined by two parameters: the cooperativity C and the sideband resolution factor η_{rsf}. For the mechanical resonator its mass, frequency, quality factor, and temperature all play a role; as for the microwave circuit a low dissipation κ and a thermal population $\bar{n} \ll 1$ are required.

The emphasis placed on these different parameters varies from experiment to experiment in the literature, producing a veritable zoo of electromechanical devices, each with their own specialization. A brief overview of the state of the art of these electromechanical cavities is given in section 2.1. Based on this, we present our choice of device: it consists of a 100-nm thick silicon nitride membrane, coupled by electrostatic interaction to a planar LC circuit.

Section 2.2 presents the experiments through which principal parameters of this electromechanical cavity are extracted. The mechanical resonator is probed by measuring its thermal spectrum and inducing a coherent response via the effect of optomechanically induced transparency. We thus find that the mechanical resonator has a Qf-product of 4.8×10^{13} Hz, and that the vacuum coupling rate is $g_0/2\pi = 0.62 \pm 0.8$ Hz. Section 2.3 then presents a sideband cooling experiment in which

a reduction in the phonon population by several orders of magnitude is achieved. However, the minimal occupation of the mechanical resonator is only reduce to approximately 100, relatively far from the ground state.

Section 2.4 discusses the significance of these results. It analyzes in particular the main limitations to the presented device, and why the ground state could not be reached. Upon this basis, the improvements on this device that were made by the author are introduced.

2.1 Silicon-nitride membrane electromechanics

Owing to the generic nature of the dispersive interaction, no fundamental constraint is imposed either on the shape, size, or frequency of the mechanical resonator. As a result, a plethora of resonators can be found in the literature of cavity electromechanics. In this section we briefly review the various possible options, and show the advantages of the system we ultimately opted for: a device based on silicon nitride (SiN) membranes.

First and foremost, to have the capacity to prepare quantum states of mechanical motion, the resonator must be in its ground state. If it must be cooled by the opto- or electromechanical interaction, a necessary (but insufficient) condition is that the mechanical frequency $f \equiv \Omega_{\mathsf{m}}/2\pi$ must be larger than the thermal decoherence rate [44]. This can be expressed in terms of the so-called Qf-product, which must satisfy

$$Qf > \frac{k_{\mathsf{B}} T_{\mathsf{env}}}{h}. \tag{2.1}$$

Note that higher temperatures also result in low coherence times. Experiments are therefore often performed in cryogenic environments to ease the requirements on the device parameters. For cooling at $T_{\mathsf{env}} = 20$ mK as in this work, $Qf \gtrsim 10^9$ Hz is theoretically required. This is in fact readily achievable but the Qf-product still serves as a good figure of merit for the mechanical resonator, and we will base our choice on this factor. Having long coherence times is conditional for highly perfomant in quantum memories [10], for coupling incompatible quantum systems such as for optical-to-microwave photon conversion [6–9], or for studying non-classical states of motion [16, 45, 46]. Maximizing this product starts with the right choice of material.

2.1.1 Choosing the mechanical resonator

Crystalline materials are an intuitive choice for obtaining high Q: they can be almost perfectly cleaved or etched along their flat faces, resulting in low surface roughness and low loss [49]. Many ground-breaking experiments have been pursued using for instance quartz [40, 50] ($Qf \approx 10^{10}$ Hz in [40]) or silicon [12, 22, 51,

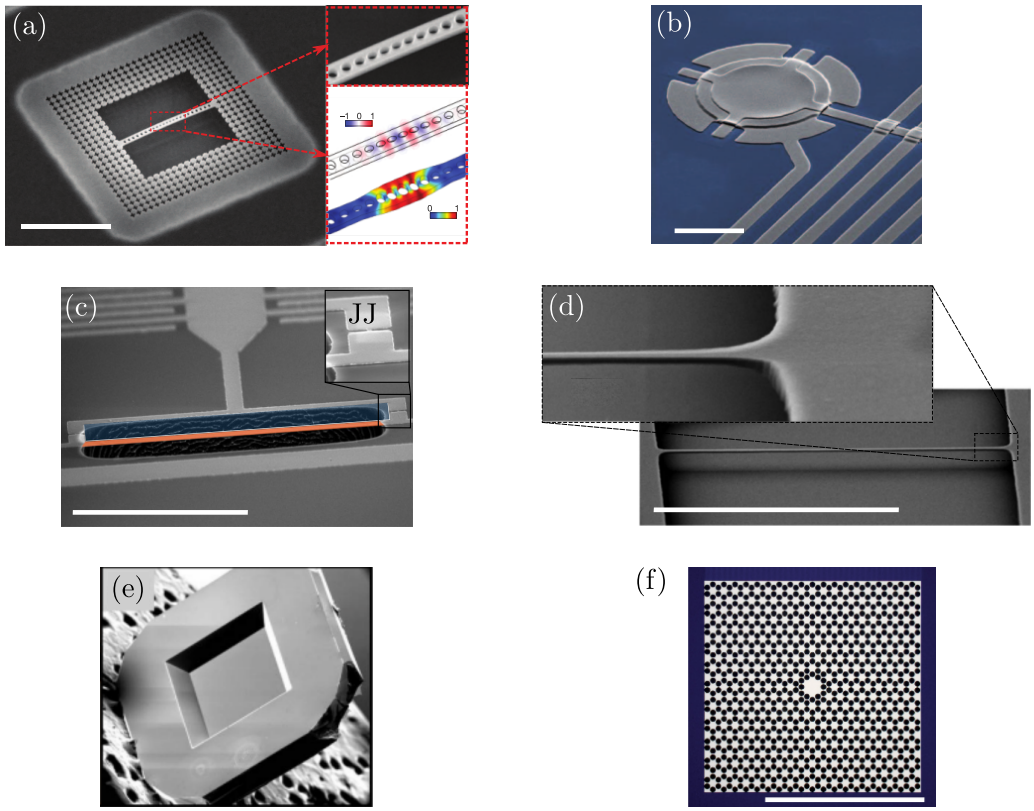

Figure 2.1: Examples of mechanical resonators. **a-d**, The scale bars represent 10 μm. **(a)** Scanning electron microscope (SEM) image of a silicon nanobeam where the mechanical and electromagnetic modes are colocalized. The uppermost inset picture is a zoom of the area in which the fields are localized. The lower inset illustrates the profiles of the the electromagnetic mode (top) and the mechanical mode (bottom), respectively. **(b)** False-colored SEM image of an aluminium plate serving as a mechanically compliant capacitor in a resonant LC circuit. **(c)** SEM image of a mechanically compliant wire (colored in orange), resulting in a variable coupling to a flux line in a superconducting quantum interference device. Inset is a zoom into one of the Josephson junctions (JJ) of the circuit. **(d)** SEM image of a SiN nanobeam. Inset is a zoom into the clamping point. **e**, SEM image of a SiN nanomembrane. The membrane, seen in the center, has dimensions of 1 x 1 mm^2. **f**, Optical micrograph of a patterned SiN membrane. The white scale bar represents 3 mm. Images extracted from: **(a)** Chan et al. [12], **(b)** Teufel et al. [13], **(c)** Rodrigues et al. [47] **(d)** Verbridge et al. [48], **(e)** Zwickl et al. [21] **(f)** Tsaturyan et al. [24].

52] ($Qf \approx 10^{15}$ Hz in [22] at 25 mK)–an example of a Si resonator is shown in fig. 2.1a. Amongst crystalline materials those exhibiting piezoelectric properties are interesting [9, 53] ($Qf \approx 10^{13}$ Hz in [9]) because they are intrinsically coupled to electromagnetic fields, which allows for integrated designs. For this reason, metals are also an interesting materials to make mechanical resonators out of [13, 17, 47, 54] ($Qf \approx 10^{12}$ Hz in [54]). Figure 2.1b shows a microwave cavity where the capacitance is made of a mechanically compliant aluminium plate; in fig. 2.1c a nonlinear cavity is shown where the frequency is shifted by mechanically varying the coupling to a flux line. Other kinds of materials such as carbon nanotubes [55, 56], graphene [57], or superfluid helium [58] have also demonstrated promising features.

Among the numerous possible platforms the current record holder for the best Qf-product is, perhaps surprisingly, made from an amorphous dielectric: SiN. The typical geometries for SiN resonators are thin beams (fig. 2.1d) or membranes (fig. 2.1e), which can yield moderate Qf-products (for their fundamental modes, $Qf \leq 10^{13}$ Hz [44] at room temperature). Yet in recent years engineered SiN resonators have demonstrated quality factors approaching the billions [24], and even at room temperature $Qf > 10^{14}$ Hz [31][1]; an example of such an engineered resonator is shown in fig. 2.1f. So far, these engineered resonators have mainly been employed in the optical domain [59, 60], and no experiments have demonstrated quantum behaviors in an electromechanical system. Nevertheless, promising results regarding the implementation of SiN resonators in microwave circuits have been obtained [6, 61].

Furthermore, it it well understood that mechanical quality factors of systems limited by two-level-system losses, as is the case for SiN, increase at cryogenic temperatures [9, 62–65]. This suggests that the new generation of engineered SiN resonators could significantly exceed the performance of the best crystalline silicon resonators once cooled to cryogenic temperatures.

SiN resonators can only be found in the form of beams or membranes, due to the fact that the mechanical properties of SiN only excel when it is clamped and highly stressed [48, 67, 68] (see chapter 3 for a more detailed discussion). As a general rule, beams are often used for compact, integrated designs; devices with membranes on the other hand are larger but modular: their components can be fabricated and characterized separately before being coupled, allowing each element to be characterized individually before being implemented. In this work the latter approach was preferred. We employ membranes, thin square sheets of SiN, with a typical side length of a millimeter and a thickness of approximately 100-200 nm. An example of the membranes fabricated for this work is shown in fig. 2.2.

[1] With such a Qf-product, quantum optomechanics could in principle be studied even at room temperature, although that has yet to be demonstrated.

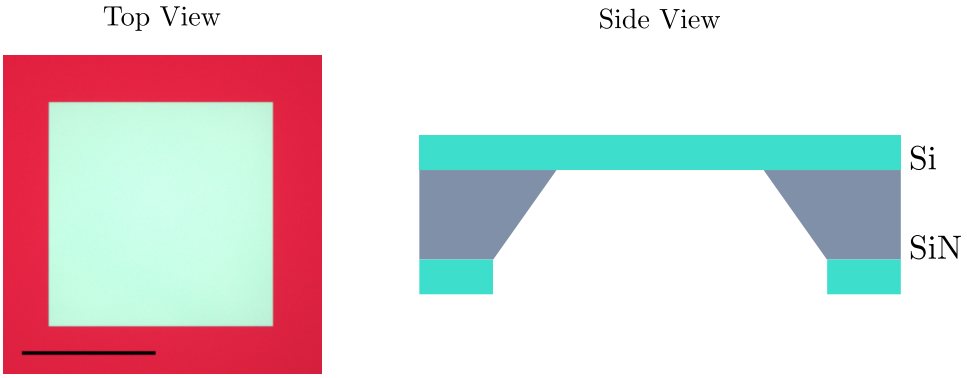

Figure 2.2: **(left)** Optical micrograph of a SiN membrane fabricated by the optomechanics group of the LKB. Suspended SiN is seen in light blue, and SiN above Si is seen in magenta. The membrane has a thickness of 200 nm. The black scale bar represents 0.5 mm. **(right)** Side view of the mechanical resonator, not to scale. The Si substrate is about 500-μm thick, whereas the SiN thickness is approximately 100 nm.

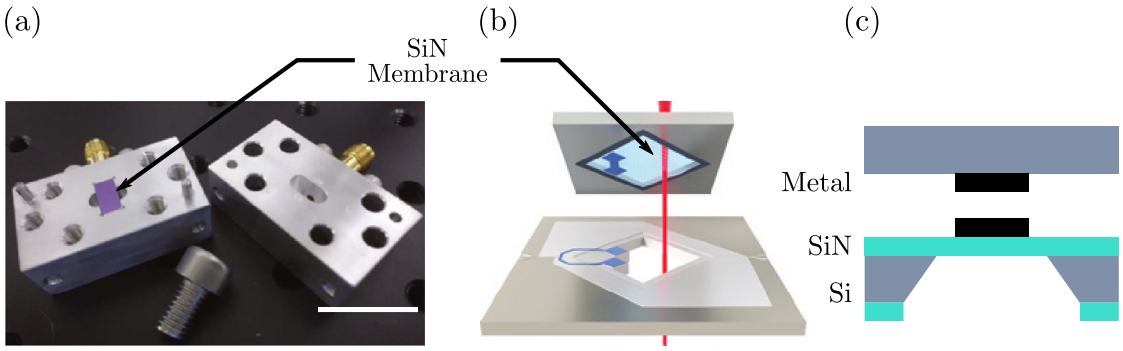

Figure 2.3: **a**, Picture of a SiN membrane within an aluminium box. The membrane is coupled to the box via a nearby antenna chip. The white scale bar represents 10 mm. Image exctracted from Yuan et al. [66]. **b**, Illustration of a SiN membrane coupled to a resonant microwave circuit. Metal is shown in blue. The red beam indicates a laser beam which simultaneously couples to the membrane, but this is beyond the scope of this chapter. Image extracted from Andrews et al. [6]. **c**, Simplified view of a SiN-membrane based electromechanical cavity, in a "flip-chip" geometry. The metal (in black) on the membrane chip (on the bottom) directly faces the metal on the separate microwave chip.

Table 2.1: Summary of various device parameters coupled to SiN membranes. All cavities in these works were measured below 40 mK. For Refs. [33, 69], we estimate G by assuming $x_{\mathsf{ZP}} \sim 1$ fm (based on similar systems [66]). In Yuan et al. [66] only the "loaded" cavity dissipation rate was given, in which loss channels are saturated by a strong pump. We assume that the unloaded dissipation rate quoted here is an order of magnitude higher, in accordance with similar works [69].

	Microwaves	**Mechanics**	**Electromechanical device**
	$\kappa/2\pi$ (MHz)	$\Gamma_{\mathsf{m}}/2\pi$ (Hz)	G (MHz.nm^{-1})
2D circuits			
Andrews et al. [6]	1.6	0.42	4
Higginbotham et al. [33]	2.7	11	4
3D cavities			
Yuan et al. [66]	0.5	3.5×10^{-3}	0.6
Noguchi et al. [69]	0.3	1	7

2.1.2 Electromechanical devices with SiN membranes

To couple a SiN membrane to an electromechanical cavity, essentially two approaches have been taken in the past, differing in the way in which the microwave cavity is created. One option is to fabricate it from a superconducting metal box (fig. 2.3a). Inside of it the electromagnetic field can resonate at specific frequencies. The mode is coupled to an antenna which can address the membrane motion. Alternatively, the cavity can made of a planar superconducting circuit fabricated on-chip, as illustrated in fig. 2.3b. In both cases the membrane is fabricated on its own separate chip, and can be functionalized by the deposition of metal on its surface. The functionalized area is aligned to the metal plate of a separate chip, which is either the antenna of the 3D cavity or the capacive plate of the 2D circuit. thereby forming a capacitor whose capacitance varies with the position of the membrane (for a 3D cavity, that chip contains the antenna; in the 2D case, it contains the resonant circuit). This assembly is called a "flip-chip" and is illustrated in fig. 2.3c.

Since the mechanical resonator remains the same in both cases, we can compare them based on the mechanical loss Γ_{m}, the microwave loss κ, and the cavity frequency shift per mechanical displacement[2] G. The values of these parameters

[2]To compare different resonator geometries g_0 is in general preferable, but since we only consider membranes, G is suitable.

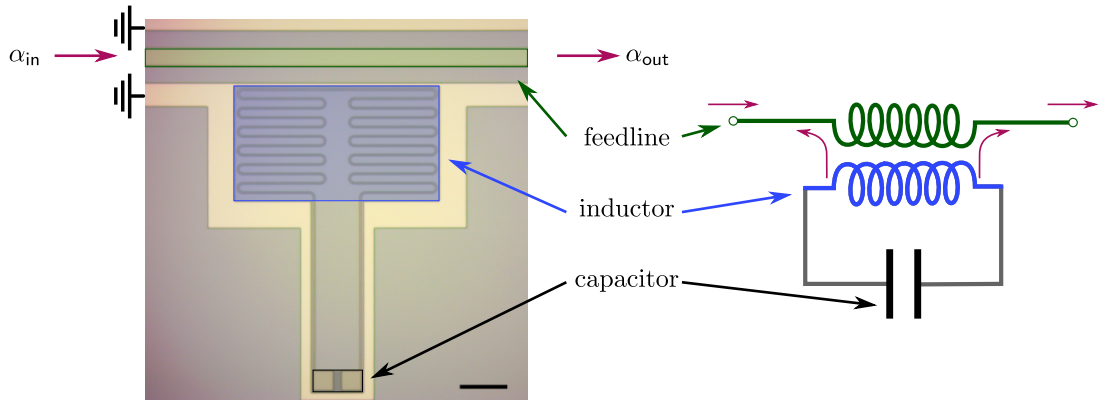

Figure 2.4: **(left)** Optical micrograph of a lumped-element microwave cavity, from the sample labelled BM2. Nb is shown in yellow, and the Si substrate in gray. The feedline is highlighted in green, the inductance in blue, and the capacitor pads in black. The scale bar represents 150 μm. **(right)** Equivalent circuit to the cavity, with the circuit elements colored following the same code as in the image.

for devices found in the literature, for both 2D and 3D systems, are reported in table 2.1. We find that overall, the 2D and the 3D approaches yield comparable devices, with one exception: in Ref. [66], an exceptionally low mechanical dissipation is found. That that is not unique to 3D cavities however, and we show below that a low mechanical dissipation rate can be obtained in 2D circuits as well.

This being said the 2D approach presents the advantage of being more streamlined in design, as it does not require an intermediary antenna to couple microwaves and mechanics. Furthermore, it was expected that using 2D circuits would ultimately yield lower κ, as the field is more strongly confined than 3D cavities, reducing the participation ratio of the amorphous SiN in microwave losses.

2.1.3 Fabricating the electromechanical device

The design of our microwave circuit is based on the optimized designs of Geerlings et al. [70]. It is a lumped-element circuit, meaning the inductor and the capacitor are discrete entities (see fig. 2.4), and the sizes of the individual elements are well below the microwave photon wavelength. The cavity is addressed through a coplanar waveguide (CPW) feedline: a metallic strip surrounded by two planes connected to the ground conducts the signal,. Note that placing the circuit in this manner with respect to the feedline places it in a hanger configuration.

We fabricate such circuits by evaporating a uniform niobium (Nb) layer on a bare Si substrate, and patterning the metal by UV lithography–see Ref. [43] for further details. To ensure that κ to be low the superconducting metal Nb is used, with a transition temperature of 9.3 K. It is used for instance in Ref. [6] and shown

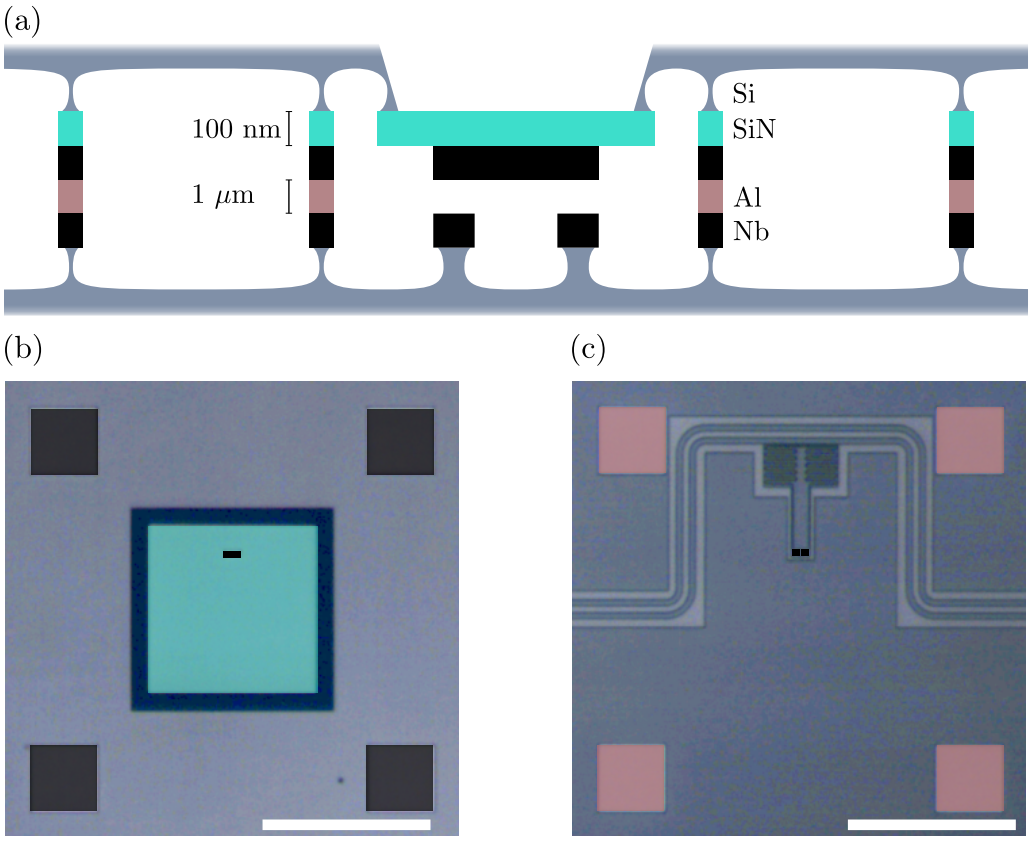

Figure 2.5: **a**, Schematic representation of the electromechanical device, seen through a cut plane normal to the surface. The diagram is not to scale, and the ground planes have been omitted for clarity. **b-c**, Optical micrographs of a metallized SiN membrane **(b)** and the LC cavity circuit **(c)** from the sample labeled BM2. The relevant areas have been colored to correspond to the material color-coding set by **(a)**. The white scale bars represent 1 mm.

to allow for high coherence times [71]. The substrate used here is high-resistivity Si ($\rho > 10$ kΩ.cm).

The electromechanical device is then fabricated with a flip-chip design: the microwave circuit chip and the membrane chip are aligned and stacked, giving the overall structure shown in fig. 2.5a. The alignment of the chips is done using a mask aligner, such that the metallic pad on the membrane faced (fig. 2.5b) the capacitive plates of the circuit. They are then fixed together with two drops of epoxy on diagonally opposite corners of the chips. Aluminium pillars approximately 300-nm thick serve the role of spacers (fig. 2.5c).

As mentioned in the previous section the two main figures of merit for the system are the electromechanical coupling G and the Qf-product. To estimate these parameters Ω_m, Γ_m, κ, and g_0 are measured, and the results are given below. The measurements are taken in a wet Helium-3 cryostat, at a temperature of approximately 400 mK, unless stated otherwise.

Although the experiments presented below were mainly conducted by T. Capelle during his PhD thesis, the following sections contain a summary of the main experimental results together with an independent data analysis. The interested reader is referred to T. Capelle's PhD thesis for a more detailed description of this work [43].

2.2 Characterization experiments

Since an electromechanical device cannot be characterized prior to being cooled in a cryostat, is it difficult to be sure that a coupling between the mechanics and microwaves has been successfully engineered. A series of characterization measurements checks that the device functions as expected. Firstly, we measure the frequency and dissipation rate of the microwave cavity. Once this has been done, further measurements are performed to quantify the electromechanical couplings and the parameters of the mechanical mode.

2.2.1 Characterizing the cavity resonance

The cavity response is measured using a vector network analyzer (VNA), which sends a signal into the cavity and measures the reflected field. The spectrum of the reflected power is shown in fig. 2.6: its presents a series of resonances, characterized by dips of more than 10 dB. We know from finite element simulations that the microwave circuit only has one resonance frequency in the measured range; all other measured dips in the signal are attributed to parasitic effects, originating for instance from standing waves created by impedance mismatches at wire junctions. To distinguish the circuit resonance from the other parasitic ones, we search for the

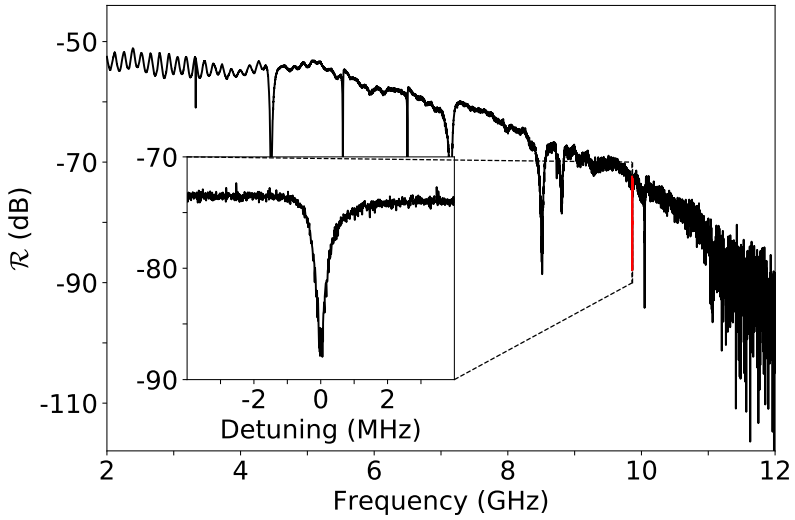

Figure 2.6: Reflection spectrum $\mathcal{R}$ of the sample labeled BM2. Several resonance peaks are present, with the cavity resonance highlighted in red. Inset is a close-up on the cavity resonance.

one which is coupled to a mechanical mode (section 2.2.2), and we indicate it in red in fig. 2.6.

In chapter 1 we showed that the reflected power $\mathcal{R}$ follows a Lorentzian dip around the microwave resonance (eq. (1.38)), as shown in the inset of fig. 2.6. We find a circuit resonance frequency $\omega_c/2\pi = 9.8$ GHz and a linewidth of $\kappa/2\pi = 2.0$ MHz. This corresponds to the frequency around which the cavity was designed to resonate, although the high number of parasitic neighboring modes prevents us form affirming this conclusively. This measurement is therefore completed with another, which searches for the typical mechanical response and ensures that the considered microwave mode is indeed coupled to the mechanical resonator.

2.2.2 Optomechanically Induced Transparency (determining Ω_m)

To verify the existence of a coupling between the microwaves and the mechanical mode, we induce a response characteristic of electromechanical cavities called optomechanically induced transparency (OMIT). This is a phenomenon which can arise when two tones are sent into the circuit. It is formally equivalent to electromagnetically induced transparency, where a three-level system can be made perfectly transparent to a readout probe [72]. Here, we give the basic principles and main predictions of OMIT, and more details can be found e.g. in Refs. [20, 30, 38].

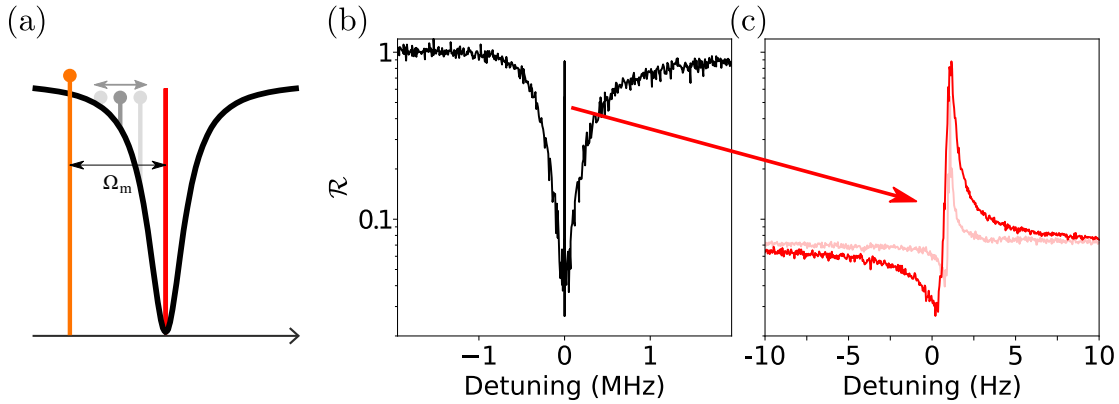

Figure 2.7: **a**, Illustration of the OMIT scheme: a strong pump (orange) is placed on the mechanical sideband of the cavity, while a weak tone (dark and light gray) is swept in frequency to probe the cavity response (black). When the two tones are detuned by the mechanical frequency, a transparency window opens (red). **b**, Response of a weak probe around the circuit resonance. The circuit is pumped at -776 kHz, corresponding to a mechanical mode. A transparency window opens when the probe is resonance with the circuit. The reflection is normalized such that it equals 1 far from resonance. **c**, Close-up on the central transparency peak from **(b)**, for two different pump powers. The power is smaller for the light red curve.

In OMIT a strong tone is sent into the red mechanical sideband[3] of the circuit (detuned from resonance by $-\Omega_\mathsf{m}$), while its response is probed by a weak probe, as illustrated in fig. 2.7a. If the two tones are detuned by exactly Ω_m, a beat note is created which drives the mechanical mode. This results in a backaction effect: the driven motion of the oscillator generates mechanical sidebands of the strong tone, one of which is resonant with the readout probe. This finally results in destructive interference for the intracavity field at the probe frequency, which is observed by a complete reflection of the probe from the cavity. It appears as the transparency window shown in fig. 2.7b.

More precisely, provided $\Gamma_\mathsf{m} \ll \Gamma_\mathsf{m} C \ll \kappa$ and the pump is placed on a mechanical sideband, it can be shown that the reflected power $\mathcal{R}$ around the cavity resonance reads

$$\mathcal{R}(\Delta) \approx \left|\frac{C}{1+C}\right|^2 \times \left|\frac{1}{1+\frac{2i\Delta}{(1+C)\Gamma_\mathsf{m}}}\right|^2, \tag{2.2}$$

where Δ is the detuning from the cavity resonance. We see that this gives rise to a Lorentzian peak whose height and width both increase with C. To verify that we are indeed observing mechanical modes we vary the pump power, from which

[3]Pumping on the blue sideband is also possible, and results in optomechanically induced amplification [20, 73].

we observe the dependency of the peak width and height on C (fig. 2.7c). The mode characterized here oscillates at $\Omega_{\mathsf{m}}/2\pi = 776$ kHz. Several other mechanical modes were found in this manner, and the frequencies were in good agreement with numerical simulations. Here, the most interesting mode is at $\Omega_{\mathsf{m}}/2\pi = 480$ kHz, as it has the highest coupling rate to the cavity–we note that this is not the fundamental mode, which vibrates at a lower frequency still.

2.2.3 Measuring g_0

The single-photon coupling rate g_0 can be a tricky parameter to measure experimentally, since it is usually dressed by the intracavity field amplitude α, requiring a careful calibration of the electrical circuit from the circuit to the detector. A more straightforward and self-calibrating procedure for determining g_0 has been proposed by Gorodestky et al. [74], and we give a brief outline of its principal ideas here.

In an electromechanical cavity the thermal fluctuations in the position of the resonator result in fluctuations of the circuit resonance frequency ω_{c}. The variance of ω_{c} reads $\langle\omega_{\mathsf{c}}^2\rangle = 2g_0^2 n_{\mathsf{th}}$, where n_{th} is the average thermal phonon population of the mechanical resonator. We can thus gain direct access to the vacuum coupling rate by measuring these frequency fluctuations. To do so we send a probe into the circuit, causing it to acquire a phase noise sideband with a spectrum $\bar{S}_{\phi\phi} \propto g_0^2 \bar{S}_{xx}$. The challenge comes from the fact that we do not measure $\bar{S}_{\phi\phi}$ directly, but a current noise $\bar{S}_{ii}$ related to the phase noise by some (generally not accurately known) transfer function. This transfer function depends, among other things, on the resolved sideband factor η_{rsf}, the coupling ratio to the cavity η, and the total amplification of the signal from the cavity to the measurement apparatus.

The principle of the experiment demonstrated in Ref. [74] is to modulate the phase of the probe such that its spectrum $\bar{S}_{\phi\phi,\mathsf{cal}}$ acquires a modulation sideband at a frequency Ω_{cal} near Ω_{m}. In this manner the calibration tone becomes converted into a current noise $\bar{S}_{\mathsf{ii,cal}}$ by the same transfer function as the mechanical sideband, and $\bar{S}_{ii}/\bar{S}_{ii,\mathsf{cal}} \approx \bar{S}_{\phi\phi}/\bar{S}_{\phi\phi,\mathsf{cal}}$[4]. The phase noise terms can be derived analytically, and it can be shown that

$$g_0^2 = \frac{\Omega_{\mathsf{m}}^2 \phi_0^2 \langle i^2\rangle}{2 n_{\mathsf{th}} \langle i_{\mathsf{cal}}^2\rangle}, \tag{2.3}$$

where ϕ_0 is the amplitude of the phase modulation. We note that for this procedure to work, the two peaks must not overlap, such that their integrals can be evaluated independently.

[4]For the transfer functions of the mechanical and calibration spectra to be identical, the output current from the cavity must be measured either by direct detection or by homodyne detection. This allows us demodulate the field and to extract a specific quadrature at the Fourier frequencies Ω_{cal} and Ω_{m}. Here, we use the analog demodulation function of a vector spectrum analyzer to

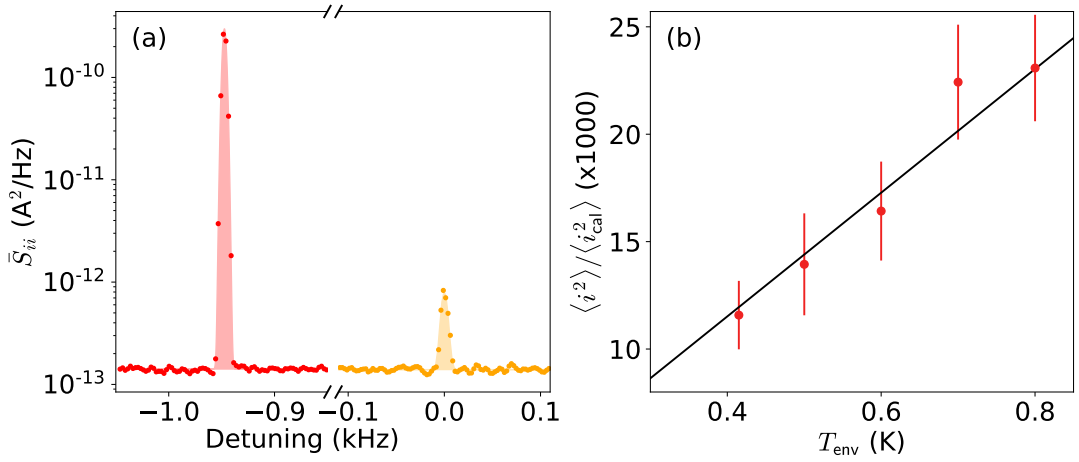

Figure 2.8: **a**, Calibration (red) and mechanical (yellow) sidebands of the probe. The filled areas are Gaussian fits. **b**, Repetition of the spectrum acquisition of **(a)** for various cryostat temperatures. The solid black line is a linear fit.

A weak probing tone is thus sent through the electromechanical cavity (slightly detuned from the red sideband of the cavity), with a phase modulation amplitude of ϕ_0, at a frequency $\Omega_{\mathsf{cal}} \approx \Omega_{\mathsf{m}}$. The experimentally measured current noise spectra of $\bar{S}_{ii}$ and $\bar{S}_{ii,\mathsf{cal}}$ are shown in fig. 2.8a. We note that the direct detection scheme for a microwave experiment requires a specific setting on the vector spectrum analyzer (VSA), setting a lower limit to the measurement bandwidth to 1 Hz, much above the mechanical linewidth. For this reason, the peaks appear as Gaussian instead of a Lorentzian.

Although g_0 could in principle be extracted directly from fig. 2.8a, eq. (2.3) involves the population of the mechanical oscillator, which we cannot assume to be know a priori (c.f. section 2.3). To increase the accuracy of our estimate in g_0 we vary the base cryostat temperature T_{env} and measure the ratio of the peak areas several times (fig. 2.8b). As those temperatures n_{th} varies linearly with T_{env}, which we leave as a fitting parameter. The error at each data point is estimated using a bootstrap method. From this dataset we determine that $g_0/2\pi = 0.62 \pm 0.8$ Hz.

To cool the resonator to its ground state with sideband pupming, the lowest base temperature possible is desirable so minimize n_{th}. The following measurements are therefore done in a different cryostat with $T_{\mathsf{env}} \approx 20$ mK. We performed the final characterization measurement, the measurement of Q, in this environment, since it strongly depends on T_{env}. We assume this does not affect g_0 significantly.

extract the intensity modulation component of the signal around the carrier.

2.2.4 Ringdown measurement of Γ_{m}

The mechanical dissipation rate Γ_{m} is determined by ringdown measurement, consisting of two phases. In the "driving phase" the membrane motion is driven strongly at a frequency resonant with the mode of interest. This can be done with a scheme similar to the OMIT measurement: a pump is set on the mechanical sideband and a second, weaker tone is placed on resonance with the cavity, generating a beat note at the mechanical frequency and driving the mode. After a few seconds the weaker tone is abruptly turned off; during this second "readout phase" the evolution of the mechanical amplitude is recorded. The height of the measured sideband is proportional to the displacement amplitude $x(t)$, The measurement scheme is summarized in fig. 2.9a. During the readout phase the amplitude of motion decays exponentially as $x(t) = x(0)\exp\left[-\Gamma_{\mathsf{eff}}t/2\right]$, which can be fit to the data to extract the effective mechanical dissipation Γ_{eff}.

There is a caveat: since the electromechanical cavity is probed on its red sideband, Γ_{eff} depends on the sideband tone power due to electromechanical damping. In section 1.3.4 (eq. (1.59)) we derived the expression for the effective mechanical dissipation rate in the presence of a red sideband tone, and found that it varied with the electromechanical cooperativity C. In principle C is not known a priori, but it can be determined from the fact that C is proportional to the pump tone power P_{in}. Letting $K_{P\to C}$ be the proportionality constant, Γ_{eff} can empirically be expressed as

$$\Gamma_{\mathsf{eff}} = \Gamma_{\mathsf{m}}\left[1 + K_{P\to C}P_{\mathsf{in}}\left(1 - \frac{1}{\eta_{\mathsf{rsf}}+1}\right)\right]. \tag{2.4}$$

Γ_{m}, which is the ordinate of the asymptote for $C \ll 1$, can be robustly extracted with this method. In addition if Γ_{eff} is measured as a function of P_{in}, C can be determined as well.

Here, we investigate the mode at $\Omega_{\mathsf{m}}/2\pi = 480$ kHz. We first carry out a series of ringdown measurements with different pump powers. Three examples of ringdown curves are given in fig. 2.9b for increasing C, and they are found to be in good agreement with an exponential decay. As predicted by eq. (2.4), the attenuation of the mechanical amplitude is stronger for higher C. The extracted Γ_{eff} from all ringdowns are compiled in fig. 2.9c, which we fit with eq. (2.4) to extract Γ_{m}. We found that $\Gamma_{\mathsf{m}}/2\pi = 54$ mHz, corresponding to $Q_{\mathsf{m}} = 1\times10^8$ or a Qf-product of $Qf = 4.8\times10^{13}$ Hz. This is sufficient according to condition (2.1) to reach the ground state. However, as we show in the following, this is not the only constraint placed on our system. Despite this extremely low dissipation rate a ground-state cooling experiment was still far from trivial.

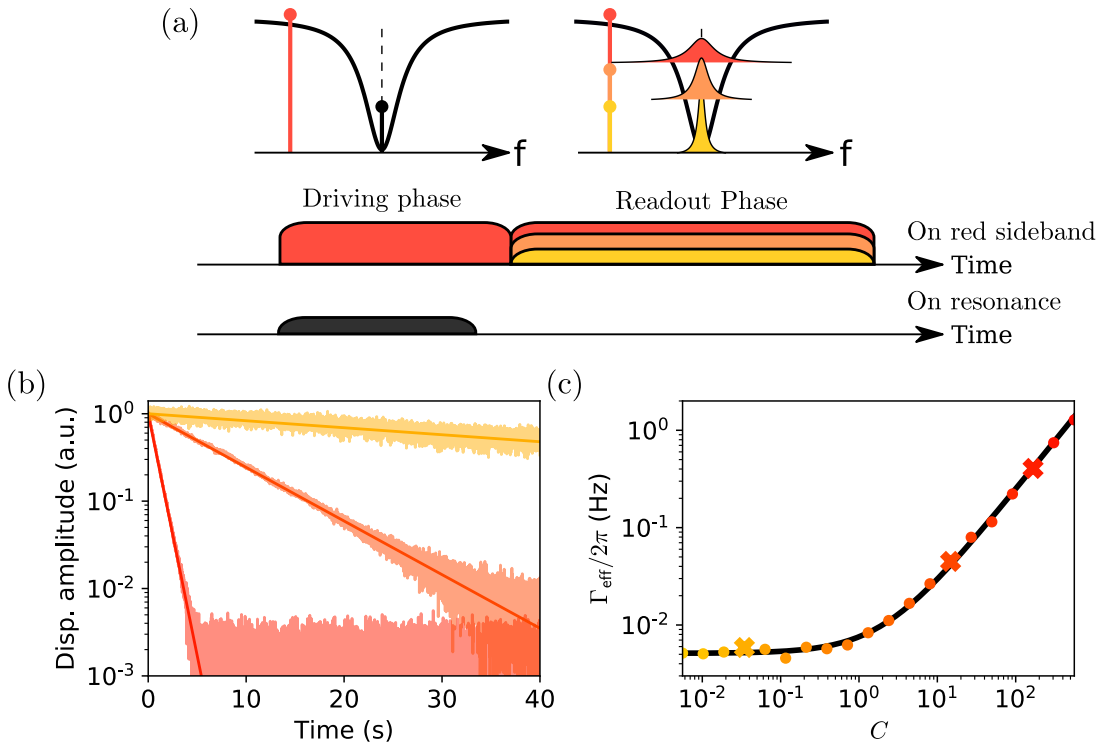

Figure 2.9: **a**, Schematic of the two phases of a ringdown sequence. In the "driving phase" the motion of the mechanical resonator is amplified by sending a pump tone (red) on the red mechanical sideband of the cavity, with a weaker tone (black) on its resonance. In the "readout phase" the weak tone is turned off, and the mechanical amplitude is measured. From yellow to red the pump power increases. **b**, Examples of ringdown curves showing the normalized displacement (Disp.) amplitude for $C = 3.3 \times 10^{-2}, 14, 1.2 \times 10^{2}$, from yellow to red. The straight lines represent the theoretically predicted decay of the amplitude $\exp\left[-\Gamma_{\mathrm{eff}} t/2\right]$. **c**, Extracted Γ_{eff} for various cooperativities C. The continuous black line represents the fit with eq. (2.4).

Table 2.2: Summary of the device parameters of BM2. The mechanical mode parameters are given for the mode with the highest measured g_0. Here, $T = 20$ mK. G is computed assuming $x_{\mathsf{ZP}} \approx 1$ fm.

Microwaves		
$\omega_{\mathsf{c}}/2\pi$	(GHz)	9.8
$\kappa/2\pi$	(MHz)	2.0
Mechanics		
$\Omega_{\mathsf{m}}/2\pi$	(kHz)	480
$\Gamma_{\mathsf{m}}/2\pi$	(mHz)	54
Q		1×10^8
$Qf/\left(k_{\mathsf{B}}T_{\mathsf{env}}/\hbar\right)$		$1.8 \times 10^4 \gg 1$
Electromechanical device		
η_{rsf}		0.88
$g_0/2\pi$	(Hz)	0.62
G	(MHz.nm^{-1})	0.62

2.2.5 Summary

The measured values for the BM2 device are summarized in table 2.2. In particular, we verify that the first ground-state cooling condition for the Qf-product (eq. (2.1)) is satisfied–here, we take $T_{\mathsf{env}} = 20$ mK which is the typical temperature of a dilution cryostat. Since the inequality is well verified it is in principle possible to achieve ground-state cooling with the mechanical modes of SiN membranes. Furthermore, the electromechanical coupling G is close to the ones reviewed in the literature, and a cooling experiment can be attempted. However, there already is a conspicuous complication: $\kappa > \Omega_{\mathsf{m}}$. Thus, the cavity is not in the resolved sideband regime, and so the minimal possible population that can be achieved is $\eta_{\mathsf{rsf}}^{-1} \approx 1.1$ quanta, as derived in section 1.3.5.

Nevertheless, cooling the mechanical resonator down to one phonon is already a promising result and worth attempting. In the following section we present a sideband cooling experiment where we reduce the temperature of a mechanical mode by thermalizing it with the microwave circuit.

2.3 Cooling experiments

In chapter 1 we present the theory of how the average population of a mechanical mode can be reduced, even for high n_{th}. When a strong pump is sent on the red

sideband of the circuit, the latter acts as an effective cold bath of average population $n_{\mathsf{cn}} \approx \eta_{\mathsf{rsf}}^{-1}$ to which the mechanical mode thermalizes. Here, we consider the mode of the oscillator at $\Omega_{\mathsf{m}}/2\pi = 480$ kHz.

Cooling can be observed when measuring the noise spectrum of the mechanical mode for varying cooling powers, i.e. for increasing C. The experimental current noise spectrum $\bar{S}_{ii}$, measured in $\mathrm{A}^2.\mathrm{Hz}^{-1}$, can be converted to the mechanical noise spectrum $\bar{S}_{\hat{x}\hat{x}}$ provided the measurement chain is well calibrated. In principle this can be done similarly to the measurement scheme presented in section 2.2.3.

Here a different approach is taken where the noise floor of the signal is used as a reference. The signal at the output of the device is amplified in a phase-insensitive manner, allowing us to measure the intensity of the field. The amplification chain adds a constant amount of noise to the signal, which we express in terms of noise quanta n_{ampl}. This known noise floor can be used to convert the signal from a current noise back to a mechanical noise spectrum. Appendix A shows how this conversion can be done; we note that the derivation neglects all the quantum noises in the mechanical resonator caused by the cavity backaction, as they are assumed negligible compared to the noise level n_{ampl} of the amplification chain. The mechanical noise spectrum can be written as

$$\frac{\bar{S}_{\hat{x}\hat{x}}[\Omega]}{2x_{\mathsf{ZP}}^2} + \bar{S}_{\mathsf{noise}} = \frac{2}{\mathcal{A}\eta\Gamma_{\mathsf{m}}C}\frac{\bar{S}_{ii}[\Omega]}{\bar{S}_{ii}[\Omega_{\mathsf{ref}}]}n_{\mathsf{ampl}}, \tag{2.5}$$

where $\mathcal{A}$ is the attenuation of the signal between the device and the amplifier, $\eta \equiv \kappa_{\mathsf{i}}/\kappa \approx 0.79$, and $\bar{S}_{\mathsf{noise}}$ is a residual noise floor.

A high-electron mobility transistor was used to amplify the signal with a measured added noise of $n_{\mathsf{ampl}} = 13$ quanta, corresponding to a temperature noise of 4.4 K. The attenuation $\mathcal{A}$ is estimated to be approximately 10 dB. The calibrated noise spectra are shown in fig. 2.10a. With increasing C the integral of these curves (minus the noise floor) decreases.

In section 1.3.5 we showed that the effective population could be written as

$$n_{\mathsf{eff}} = n_{\mathsf{th}} \times \left(\frac{1+\eta_{\mathsf{rsf}}^{-1}}{1+C+\eta_{\mathsf{rsf}}^{-1}}\right) + \eta_{\mathsf{rsf}}^{-1}. \tag{2.6}$$

Figure 2.10b shows the extracted phonon population n_{eff} of the mode. We find it to be in good agreement with this equation. In particular, we report a reduction of the mode temperature by a factor of approximately 500. However, the ground state is not reached and the minimal value of n_{eff} is approximately 100. The theoretical fit shows that the pump power should be increased by another factor 100 to approach the minimal value of $n_{\mathsf{eff}} \approx \eta_{\mathsf{rsf}}^{-1}$.

There is another glaring problem: for $C \ll 1$, $n_{\mathsf{eff}} \approx 6 \times 10^4$, corresponding to $T_{\mathsf{env}} \approx 1.4$ K, significantly above the base cryostat temperature of 20 mK. This

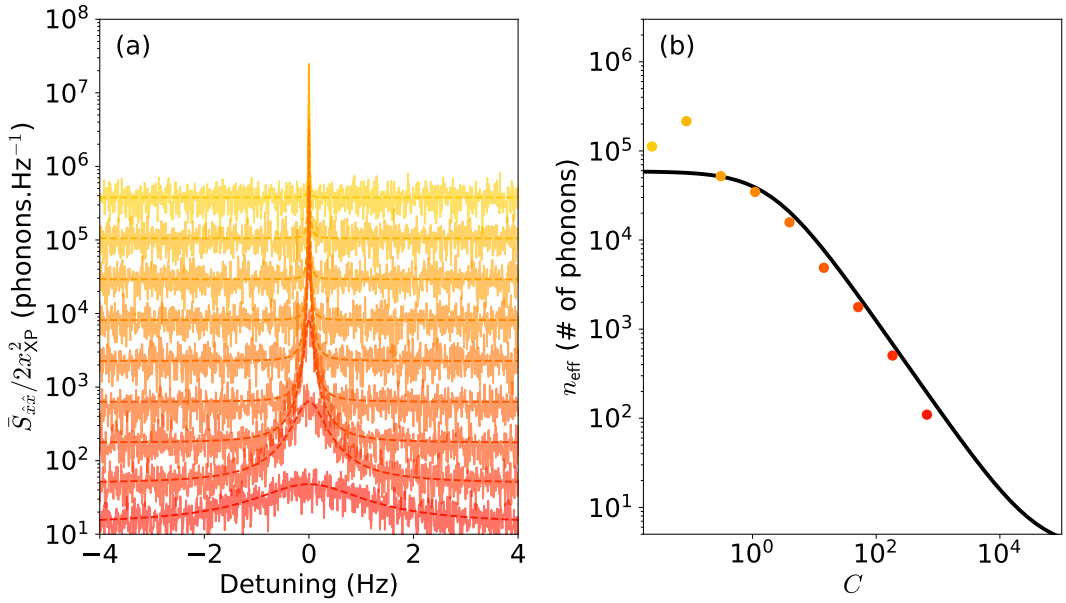

Figure 2.10: **a**, Phonon noise spectra in an electromechanical cooling experiment. The centers of the peaks are shifted to be centered around 0. The full lines represent experimental data and the dashed lines are Lorentzian fits to the peaks. From orange to red we show the spectra for increasing cooperativities C, following the colors of the data points in **(b)**. **b**, The data points represent the extracted phonon population. The full line represents a fit to the data of eq. (2.6).

effective bath temperature is attributed to mechanical noises in the cryostat itself. They drive the mechanical mode and constitute a significant challenge for preparing the mode in its ground state. Its potential resolution is discussed in more detail in Ref. [43], and is beyond the scope of this work. Here, we use these partial results as a guide to motivate the improvements on the electromechanical device itself, and discuss the main points below.

2.4 Discussion

Although the quantum ground state of the mechanical resonator was not reached, several insights into the requirements for doing so were gained. By the modular nature of this device, we can discuss most of the properties of the microwave circuit and of the nanomembrane separately. This section aims to clarify which points can most readily be improved upon in this system, and to present the direction in which the project was carried further.

2.4.1 The microwave cavity

The design for the lumped-element microwave cavity was focused on minimizing κ (or more specifically κ_{i}) in a compact resonator; reducing κ increases both η_{rsf} and C. Here this might have been a counter-productive approach. Indeed, the meandering inductance also acts as a parasitic capacitance due to its parallel metal lines lying close to each other. The equivalent circuit to the cavity may be drawn as in fig. 2.11. With such a model the effective capacitance of the circuit can be seen as the summed contribution of a position-dependent capacitance $\mathcal{C}(x)$ (where x is the height of the membrane), and a parasitic capacitance $\mathcal{C}_{\mathsf{par}}$. If we model $\mathcal{C}(x)$ as a parallel plate capacitor we can write

$$\mathcal{C}(x) = \frac{\varepsilon_0 A_{\mathsf{pad}}}{x}, \tag{2.7}$$

where ε_0 is the vacuum permittivity, and A_{pad} is the area of the capacitor pads. Then, the electromechanical coupling reads

$$G = \frac{\mathcal{L}\varepsilon_0 A_{\mathsf{pad}}}{2x^2 \left[\mathcal{L}\left(\varepsilon_0 A_{\mathsf{pad}}/x + \mathcal{C}_{\mathsf{par}}\right)\right]^{3/2}}. \tag{2.8}$$

From finite-element simulations [43] the parameters for BM2 are: $\mathcal{L} = 2.9$ nH, $A_{\mathsf{pad}} \approx 6000\ \mu\mathrm{m}^2$, $\mathcal{C}_{\mathsf{par}} \approx 0.8$ fF. With these values the variation of the coupling with the membrane height is plotted in fig. 2.12a. We can distinguish two regimes: the parasitic capacitance dominates for distances greater than about 1 μm. In this regime the scaling of G with x becomes is less favorable than for $\epsilon_0 A_{\mathsf{pad}}/x > \mathcal{C}_{\mathsf{par}}$.

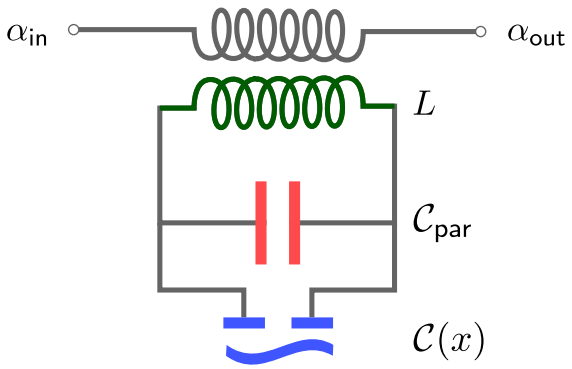

Figure 2.11: Equivalent circuit to an electromechanical device with an inductance (green), and capacitance varying with position (blue), and a parasitic capacitance in parallel (red).

With the device presented in this chapter, we are deeply in the regime where $\mathcal{C}_{\text{par}}$ dominates.

This problem is partially resolved by reducing the height of the membrane with a spring mechanism in the chip box. As shown in fig. 2.12b a set of screws is used to physically push the membrane chip further down. With this method dubbed the "pushing top", G was increased tenfold to 6 MHz.nm^{-1}, as can be seen in fig. 2.12a. This improvement notwithstanding, we remain in the regime where $\mathcal{C}_{\text{par}}$ dominates.

Work was also undertaken to reduce $\mathcal{C}_{\text{par}}$ with optimized inductances but this is beyond the scope of this work: see [43] (p. 107) for further detail. Here, we turn our attention specifically to the mechanical resonator. As we will see in the following chapters significant improvements can be made to the membrane geometry. We introduce them below.

2.4.2 The mechanical resonator

In addition to the improvements to the microwave cavity, ground state cooling can be rendered much easier by improving on the mechanical resonator. Importantly, we found two major obstacles: firstly, the fact that the mode is not thermalized to the base temperature of the cryostat but to a much higher value of approximately 1.4 K; secondly $\eta_{\text{rsf}} < 1$, making it impossible to reach the ground state even in the limit $C \gg n_{\text{th}}$. The central concept that is introduced to address these issues is that of phononic engineering, in the form first introduced in the Schliesser group [24]. The principle of this engineering is to isolate a mechanical mode in the center of the membrane, and to surround it with a phononic shielding.

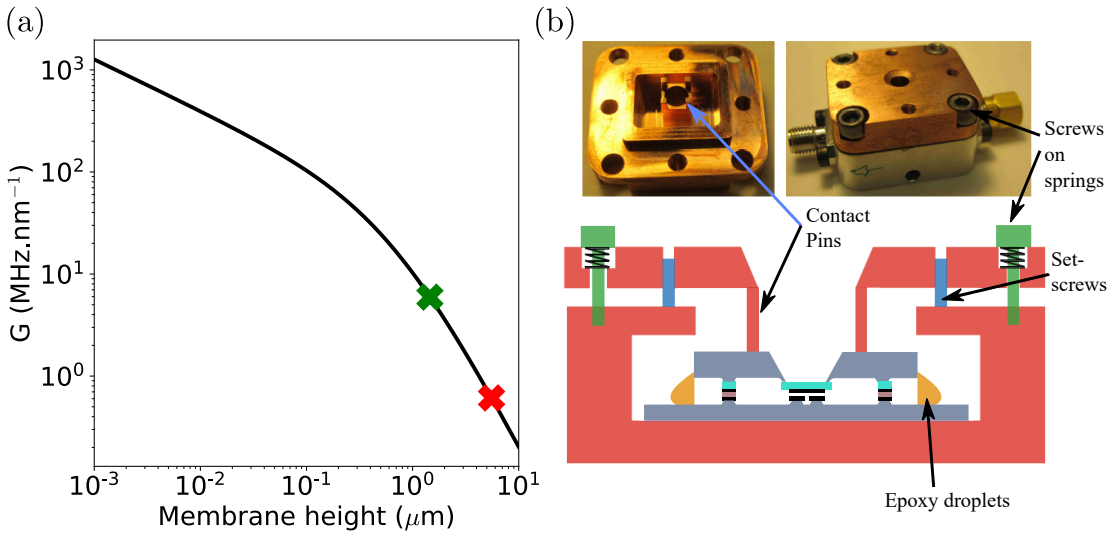

Figure 2.12: **a**, Electromechanical coupling G as a function of the membrane-to-circuit distance, based on eq. (2.8) for the estimated values of the BM2 device. The red cross indicates the measured value, and the green cross indicates the measured value with the improvement described in **(b)**. **b**, Images of the pushing top, with the sample box opened (top left) and closed (top right). Four setscrews limit the maximal pushing strength and the chip is mechanically pushed down by four contact pins. (Below) Cut-plane sketch of the pushing top. Figure **(b)** extracted from Ref. [43].

Acoustic noise isolation with a phononic crystal

We expect firstly that such designs could help thermalize to lower temperatures and significantly reduce n_{th}. Although the author could find no report of this in the literature, the consistent discrepancy between the effective mode temperature and the croystat temperature has been observed in other research groups as well for sub-MHz mechanical resonators–with some exceptions for wet, vibration-less cryostats. We hypothesize that this spurious heating arises from a combination of several uncontrolled noise sources in a laboratory (e.g. vacuum pumps) and mechanical noise of the cryostat itself. A Bluefors pulse-tube cryostat was used for the cooling experiment presented here, in which a mechanical element drives the croygenic fluid through the system, generating audible noise. We expect that this noise is up-converted through nonlinear effects to the MHz range, driving the membrane. Phononic shielding [24, 75, 76] could be a potential solution to protect the mechanical modes from such noises.

High frequency softly-clamped mechanical modes

To increase η_{rsf} the mechanical frequency can be increased. For the nanomembranes presented here Ω_{m} can be increased by reducing the side length. However this comes at the cost of an increased dissipation, linked to the curvature of the mode profile [77], reducing the vacuum cooperativity $C_0 = C/\alpha$. The phononic engineering method grants a control over this profile, and can give rise to modes confined to a small area while maintaining a high Q. This method dubbed "soft clamping" (for reasons described in the following chapter) gives rise to modes with an overall higher Qf-product, making it possible to attain high η_{rsf} without compromising C.

2.5 Summary

In summary, we have presented an electromechanical device comprising a nanomechanical silicon-nitride membrane and an on-chip LC circuit. The choice of this design was based on a brief review of the literature. It was found that silicon-nitride based resonators could result in some of the highest Qf-products ever measured in mechanical resonators. Such a property is particularly desirable for high coherence times in quantum states.

This device was characterized in four experiments aiming to determine its main parameters: the circuit was probed to determine its response; OMIT and ringdown measurements were performed to measure the mechanical response; a calibrated probing of the thermal mechanical motion was performed to determine the electromechanical coupling rate. They were found to be comparable to similar devices, with Qf-product of approximately 5×10^{13} Hz and $G \approx 0.6$ MHz.nm^{-1}. Finally, an electromechanical cooling experiment was performed by pumping the cavity on the

red sideband. The temperature of one of the membrane modes was reduced by a factor 500 using a sideband cooling experiment, but $n_{\mathsf{eff}} < 1$ could not be reached.

Several shortcomings of this first device iteration were discussed. In particular, we mention a significant improvement which can be added to the mechanical resonator: phononic engineering, which has been shown to significantly increase the Qf-product. This could result in a decrease in n_{eff} as well. The bulk of the work pursued in this thesis has been to design, fabricate, and characterize these engineered resonators. The remainder of this manuscript focuses on this aspect. In the following chapter we present the theoretical background to losses in nanomechanical oscillators. We detail how phononic engineering improves the quality of mechanical modes in silicon-nitride membranes; following that, the design of the improved membranes is given, and critical considerations to their optimal functioning are discussed.

Chapter 3

Membrane design and simulations

In the previous chapter we found two main limitations to the sideband cooling experiment: the thermal population n_{th} of the mode was too high (or, reciprocally, the sideband pump power could not be sufficiently increased), and the system was not in the sideband resolved regime, making it impossible to reach the ground state even if the limit $C \gg n_{\mathsf{th}}$ had been achieved. To overcome this higher mechanical frequencies Ω_{m} can be considered, all other things being equal, thereby both increasing η_{rsf} and decreasing n_{th}.

This being said, we must ensure that an increase in Ω_{m} does not adversely affect the other device parameters, in particular the Qf-product and the minimal achievable value for the effective mode population n_{eff}. Section 3.1 reviews in detail the dependence of losses on the membrane geometry, and discusses their origin. Crucially, we find that Q is limited by the strong bending of the membrane at its contact points with the substrate. Because of this we show that neither the Qf-product nor n_{eff} can be significantly improved beyond the experiment shown in the previous chapter, for a plain membrane.

Section 3.2 demonstrates how this issue can be overcome by phononic engineering of SiN membranes. By patterning the resonators with a phononic crystal, we are able to engineer mechanical modes localized close to a central defect, avoiding the dominant loss source in membranes. We give the key design elements of such patterned membranes which give rise to mechanical modes with utrahigh quality factors first demonstrated by the K-Labs [24]. We describe the rich dynamics that develop from this patterning, and how these enable a high degree of control over the mechanical mode shape. We show that finite-size effects significantly degrade the reproducibility of the quality factor.

Indeed, section 3.3 finds that these finite-size effects result in a coupling between the localized modes of interest and lossy parasitic modes. We derive a model of coupled modes to quantify this coupling. To bypass this problem we suggest a modified design of the engineered membranes, which are made robust to these kinds of finite-size effects. Finally, section 3.3 studies how this coupling can be used

to deliberately create symmetric and anti-symmetric normal modes, separated by several millimeters and with high quality factors.

3.1 Key parameters of SiN nanomembranes

In this section we solve the equations of motion for square SiN membranes, which we will refer to as "plain membranes", in contrast to the engineered resonators introduced subsequently. In doing so we derive the dependence of key parameters, the Qf-product and the minimal effective population n_{eff}, on the resonator geometry. This analysis will serve as a demonstration that the electromechanical device presented in the previous chapter cannot be significantly improved by changing the geometry of the plain membrane (i.e. its thickness, length, or tensile stress). Instead, other solutions are introduced in the following section.

3.1.1 Quality factor of a harmonic oscillator

For a harmonic oscillator the quality factor Q is defined as

$$Q \equiv 2\pi \frac{\mathcal{U}}{\Delta\mathcal{U}}, \tag{3.1}$$

where $\mathcal{U}$ is the total energy stored in the mode and $\Delta\mathcal{U}$ is the energy dissipated in one oscillation cycle. If various loss channels contribute incoherently to the total loss, then the overall quality factor can be expressed as

$$Q_{\mathsf{tot}}^{-1} = Q_1^{-1} + Q_2^{-1} + ..., \tag{3.2}$$

where $Q_i \equiv 2\pi\mathcal{U}/\Delta\mathcal{U}_i$ is the quality factor associated to the i^{th} loss channel, and $\Delta\mathcal{U}_i$ the corresponding amount of energy lost per cycle. In a plain membrane there are several loss channels which need to be considered in order to obtain an accurate estimate of Q. We give an overview of the main sources of loss below.

3.1.2 Mode profile of a vibrating plate

One of the dominant channels of loss depends on the boundary conditions of the membrane. To estimate the associated quality factor, we start by deriving the mode profiles of a plain membrane. We model it as a square vibrating plate with a thickness h and a side length l, such that $h \ll l$. We assume that the plate has an isotropic tensile stress σ_0, is infinite, and is clamped by the anchoring substrate as shown in fig. 3.1. The out-of-plane displacement u of the plate, for $u \ll h$, follows

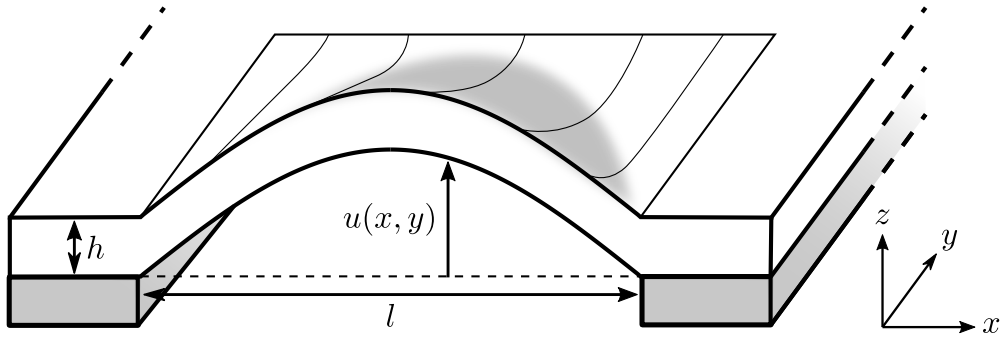

Figure 3.1: Schematic representation of the middle cross-section of a "hard-clamped" vibrating plate. The anchoring substrate is represented in dark gray.

the equation of motion (see chapter 10 of Ref. [78] and its corresponding appendix)

$$\left[\frac{D}{\rho h}\left(\frac{\partial^4}{\partial x^4}+\frac{\partial^4}{\partial y^4}+2\frac{\partial^4}{\partial x^2\partial y^2}\right)-\frac{\sigma_0}{\rho}\left(\frac{\partial^2}{\partial x^2}+\frac{\partial^2}{\partial y^2}\right)\right]u(x,y)=\Omega_m^2 u(x,y), \quad (3.3)$$

where $D = Eh^3/12\,(1-\nu^2)$ is the flexural rigidity of the membrane, E is Young's modulus, ν is Poisson's ratio, and ρ is the mass density. We assume that the displacement of the membrane is sufficiently small to allow us to neglect nonlinear terms such as the Duffing term.

Such a system has a "hard-clamped" boundary condition: the displacement at the border of the plate ($x = 0$, $x = l$, $y = 0$, and $y = l$) must be zero; furthermore, the plate at the border must be parallel to the thin film anchored to the substrate. Formally, these conditions read

$$u(x,y)|_{\mathsf{border}} = 0 \quad (3.4)$$

$$\mathbf{n}\cdot\boldsymbol{\nabla}u(x,y)|_{\mathsf{border}} = 0, \quad (3.5)$$

where $\mathbf{n}$ is a vector of unit length normal to the border. The condition (3.5) is the hard clamping of the plate.

The exact solution to these equations can be calculated analytically. The interested reader is referred e.g. to the Appendix of [77] for its full derivation. The solutions of u for $x \in [0, l/2]$ read

$$u(0\le x\le l/2,0)\sim \underbrace{\frac{m\pi\Lambda}{2}\left[\mathsf{e}^{-2x/\Lambda l}-\cos\!\left(\frac{m\pi}{l}x\right)\right]}_{\text{From eq. (3.5)}}+\underbrace{\sin\!\left(\frac{\pi m}{l}x\right)}_{\text{From eq. (3.4)}}, \quad (3.6)$$

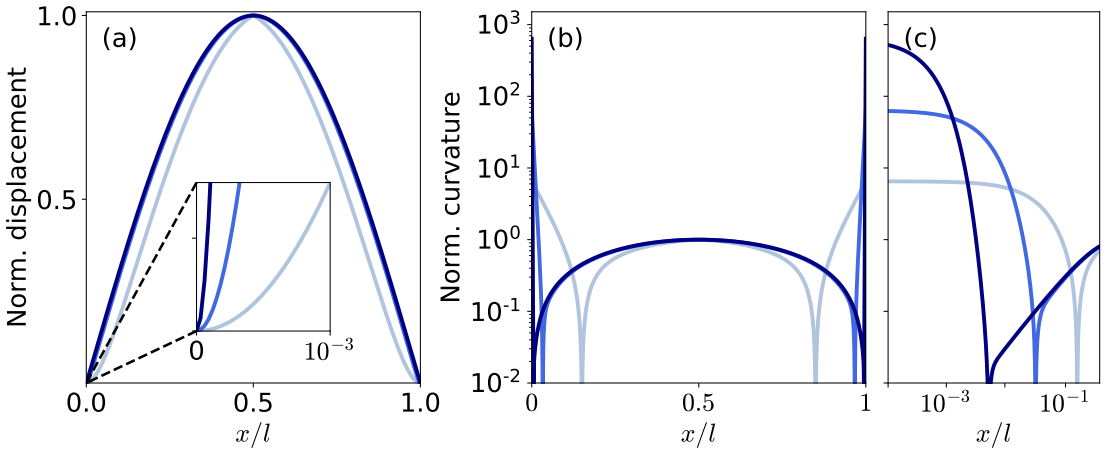

Figure 3.2: **a**, Displacement profile of the fundamental mode of a plate normalized (Norm.) by the displacement at $x = l/2$. **b**, Absolute value of the curvature of the mode, normalized by the curvature at $x = l/2$. The cancellation of the curvature corresponds to a sign change. The values are plotted along the $y = 0$ line. **c**, Normalized curvature of the fundamental mode near the border of the membrane. The curves were calculated for $\Lambda = 10^{-1}$, 10^{-2}, 10^{-3}, from light blue to dark blue.

where m is the number of antinodes, and

$$\Lambda \equiv \sqrt{\frac{Eh^2}{3\sigma_0 l^2 \left(1-\nu^2\right)}} \ll 1 \tag{3.7}$$

is a dimensionless parameter which we discuss in more detail in the following section[1]. For typical sample parameters, $\Lambda \approx 10^{-3}$. The solution is symmetric for $x \in [l/2, l]$ such that $u(x + 1/2) = u(1/2 - x)$.

It can be shown (see the Appendix of [77]) that the frequency of the $(m, n)^{\text{th}}$ mode reads:

$$\Omega_{\mathsf{m}} = \pi \sqrt{\frac{\sigma_0 (m^2 + n^2)}{\rho l^2}}. \tag{3.8}$$

With the fixed constraint on the derivative an exponential term of characteristic length Λl appears, underlined in red in eq. (3.6). This tail at the border of the membrane is shown in fig. 3.2a where the full solution to the plate equation is plotted. In the limit of $\Lambda l \to 0$ the profile converges uniformly to a simple sinusoidal function. This is not the case for the second derivative of the mode shown in fig. 3.2b: it is shown in fig. 3.2c that the peaks in the curvature at the borders only converge

[1]We note that this parameter is conventionally denoted λ in the literature, but the uppercase was taken here to prevent confusion with the optical wavelength.

pointwise as $\Lambda l \to 0$, i.e. the peak width reduces while its height increases. This difference in convergence between the mode profile and its curvature has significant repercussions on the dissipation of the energy of the mode.

3.1.3 Bending losses

The main contributors to dissipation are losses intrinsic to the membrane material [79], and depend on the mode's second derivative; they are referred to as bending losses. Understanding these losses is key to the rest of this thesis, and we therefore describe them here in detail. The analysis below follows the derivation of Ref. [77].

The bending quality factor

In high aspect-ratio, high-stress resonators (such as the one described above), most of the elastic energy of their modes is used to elongate the material, which is a lossless process [80]. However, the small remaining fraction of the total energy goes into bending the material, which does cause dissipation. The energy lost per oscillation cycle is

$$\Delta\mathcal{U} = \frac{2\pi}{Q_{\mathsf{intr}}}\mathcal{U}_{\mathsf{bend}}, \tag{3.9}$$

where Q_{intr} is the intrinsic quality factor of the material and $\mathcal{U}_{\mathsf{bend}}$ is the energy stored in bending. The total stored bending energy density $d\mathcal{U}_{\mathsf{bend}}$ is the integral of the local work done during a quarter of an oscillation cycle (i.e. until the plate bends maximally), and reads

$$d\mathcal{U}_{\mathsf{bend}}(\mathbf{r}) = \int_0^{\pi/2\Omega_{\mathsf{m}}} \mathrm{Re}\left[\boldsymbol{\sigma}(\mathbf{r},t)\right] \cdot \mathrm{Re}\left[\dot{\boldsymbol{\epsilon}}(\mathbf{r},t)\right] dt, \tag{3.10}$$

where $\boldsymbol{\sigma}$ is the local tensile stress, $\boldsymbol{\epsilon}$ is the local strain, and $\mathbf{r} = (x,y,z)^T$ denotes a point on the plate.

For small displacements the strain is given to the first order[2] by [81]

$$\boldsymbol{\epsilon}(\mathbf{r},t) \approx (-z)\begin{pmatrix}\partial^2_{xx}\\ \partial^2_{yy}\\ 2\partial^2_{xy}\end{pmatrix} u(x,y)\mathsf{e}^{-i\Omega_{\mathsf{m}}t}. \tag{3.11}$$

$\boldsymbol{\sigma}$ relates to $\boldsymbol{\epsilon}$ by

$$\boldsymbol{\sigma}(\mathbf{r},t) = \tilde{E}\begin{pmatrix}1 & \nu & 0\\ \nu & 1 & 0\\ 0 & 0 & (1-\nu)/2\end{pmatrix}\boldsymbol{\epsilon}(\mathbf{r},t), \tag{3.12}$$

[2]This term corresponds to the strain due to bending only. The strain due to elongation, which is to the second order of u, was neglected.

where we have introduced the generalized Young's modulus $\tilde{E}$.

$\tilde{E}$ was introduced by Zener [79] to semi-empirically model losses in elastic media resulting from internal friction. It has been verified by several experiments [44, 77, 80] to accurately describe the behavior of high aspect-ratio oscillators. We define $\tilde{E} \equiv E - iE_2$, where $E_2 \in \mathbb{R}_+$. Typically, $E_2 \ll E$, and so its effect is to add a small component to the stress that oscillates with a $\pi/2$ phase lag compared to the strain, inducing a net energy loss. This may be seen as elastic energy being irreversibly converted into heat and can be interpreted as an internal friction process. We note that the intrinsic quality factor of the membrane derives from this model, with $Q_{\mathsf{intr}} \equiv E/E_2$.

From eqs. (3.10) to (3.12) the bending energy $\mathcal{U}_{\mathsf{bend}}$ reads

$$\mathcal{U}_{\mathsf{bend}} = \frac{Eh^3}{24\,(1-\nu^2)} \int_0^l \int_0^l \left(\frac{\partial^2 u}{\partial x^2} + \frac{\partial^2 u}{\partial y^2} \right)^2 dxdy, \tag{3.13}$$

$$= \Lambda \sigma_0 h \times \frac{\pi^2 (m^2+n^2)}{2} \left(\boxed{1} + \boxed{\Lambda \frac{(m^2+n^2)\pi^2}{4}} \right) \times A^2, \tag{3.14}$$

where A is the amplitude of the mode[3]. The losses in the system $\Delta\mathcal{U} = 2\pi\mathcal{U}_{\mathsf{bend}}/Q_{\mathsf{intr}}$, as seen in eq. (3.13), are thus proportional to the square of the mode's mean curvature. This results in two distinct terms which were boxed in eq. (3.14): the term in red, which we will refer to as "edge loss", originates from the hard clamping condition (3.5), while the one in blue comes from the condition (3.4). Crucially, edge loss is the dominant term and varies as $\Lambda\sigma_0 \propto \sqrt{\sigma_0}$: although the curvature peaks become thinner with increasing σ_0 the induced losses still increase. On the other hand, the remaining term varies as $\Lambda^2\sigma_0$ which does not depend on σ_0. This is to be expected: a mode subject only to the condition (3.4) has a profile resembling a simple sine function (see eq. (3.6)) which only varies with l.

From eq. (3.1) the total energy of the system must be evaluated to evaluate Q. By conservation of energy $\mathcal{U} = \mathcal{U}_{\mathsf{elong}} + \mathcal{U}_{\mathsf{bend}}$, where $\mathcal{U}_{\mathsf{elong}}$ is the elongation energy which reads

$$\begin{aligned} \mathcal{U}_{\mathsf{elong}} &= \frac{\sigma_0 h}{2} \int_0^l \int_0^l \left(\left(\frac{\partial u}{\partial x} \right)^2 + \left(\frac{\partial u}{\partial y} \right)^2 \right) dxdy, \\ &= \sigma_0 h \times \frac{(m^2+n^2)\pi^2}{2} \times A^2. \end{aligned} \tag{3.15}$$

From eqs. (3.14) and (3.15) $\mathcal{U}_{\mathsf{bend}}/\mathcal{U}_{\mathsf{elong}}$ is of order Λ, and so $\mathcal{U} \approx \mathcal{U}_{\mathsf{elong}}$. The quality factor associated to the bending loss Q_{b} of the $(m,n)^{\mathsf{th}}$ mode can thus be calculated

[3] The reader may notice that several terms are missing from eq. (3.13), namely $\partial^2_{xx}u\partial^2_{yy}u - (\partial^2_{xy}u)^2$. These correspond to the Gaussian curvature of the mode, and from Green's theorem their integral is exactly zero [77].

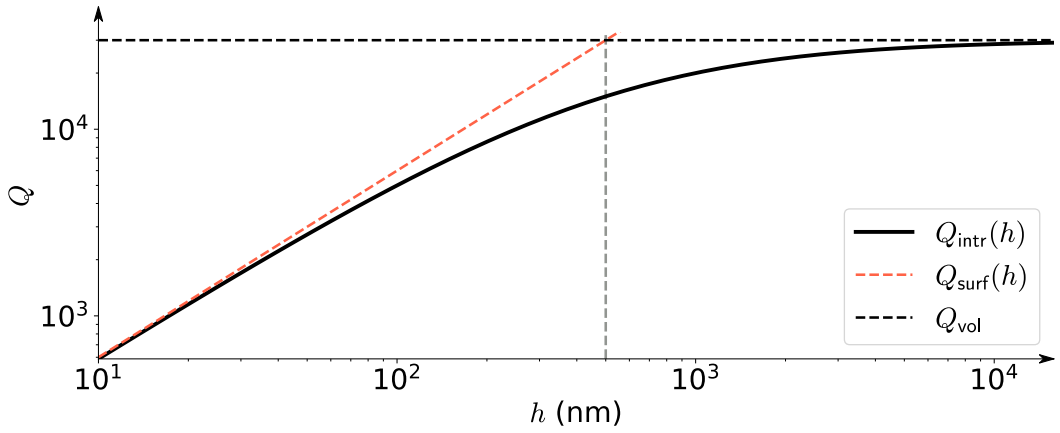

Figure 3.3: Variation of Q_{intr} with the thickness for SiN membranes. The gray dashed line represents the thickness for which surface and volume losses contribute equally to the Q_{intr}.

from eqs. (3.1), (3.14) and (3.15). It reads

$$Q_{\text{b}} = \frac{Q_{\text{intr}}}{\Lambda}\left(1 + \Lambda\frac{(m^2+n^2)\pi^2}{4}\right)^{-1}. \tag{3.16}$$

For low mode orders the red term is dominant, and $Q_{\text{b}} \approx Q_{\text{intr}}/\Lambda$. This can be taken advantage of to fabricate high-Q resonators even if Q_{intr} is low. To maximize Q_{b} it is thus desirable to increase the aspect ratio of the resonator as much as possible, and to push σ_0 to its limit[4]. We note that $\Lambda \approx \mathcal{U}_{\text{bend}}/\mathcal{U}_{\text{elong}}$, and therefore represents "the ratio of the bending energy to the elongation energy for the fundamental mode" [77]. It quantifies how much more energy is stored in lossless elongation rather than dissipative bending–Λ is often referred to as the "dissipation dilution factor".

However, this equation does not tell the whole picture and a more detailed description of Q_{intr} is required. Indeed, this term was treated up to here as a constant but it has been shown to depend on the membrane thickness as well, modifying the scaling of Q_{b}.

Thickness dependence of Q_{intr}

Q_{intr} can be modeled as an incoherent sum of losses arising both from the surface (with a quality factor Q_{surf}) of the resonator and from its bulk (Q_{vol}) [44, 82]. Q_{intr}

[4]In practice, SiN can be deposited with σ_0 up to 1.4 GPa. This value can be pushed close to the ultimate yield limit of approximately 6 GPa by stress engineering [76], but cannot be applied in this work as it can only be implemented in string resonators.

then reads

$$Q_{\mathsf{intr}}^{-1} = Q_{\mathsf{vol}}^{-1} + Q_{\mathsf{surf}}^{-1}. \tag{3.17}$$

Yasumura et al. [82] found that in thin SiN beams Q_{surf} could be well described by $Q_{\mathsf{surf}}(h) = \beta h$, where $\beta \in \mathbb{R}_+$. The meta-analysis by Villanueva and Schmid [44] found that this description applied to plain SiN membranes as well, and estimated that $\beta = 60 \pm 40$ nm^{-1} at room temperature. Conversely, Q_{vol} was found to be constant with $Q_{\mathsf{vol}} = (2.8 \pm 0.2) \times 10^4$. The overall behavior of Q_{intr} for SiN membranes is summarized in fig. 3.3.

For the thin membranes ($h < 100$ nm) considered in this work, surface losses dominate and $Q_{\mathsf{intr}} \approx \beta h$. In that regime the dependence Q_{b} on h is removed, and we remain with

$$Q_{\mathsf{b}} \propto l\sqrt{\sigma_0}. \tag{3.18}$$

We note that although fig. 3.3 seems to indicate that higher membrane thicknesses are desirable to increase Q_{intr}, overall $\partial Q_{\mathsf{b}}/\partial h \leq 0$. Being in the surface-loss dominated regime remains preferable.

In sections 3.2 and 3.3 we employ numerical simulations to determine the displacement and curvature profiles of various mechanical modes, from which we can extract Q_{b}. We first apply them to a plain membrane to verify the accuracy of such simulations. This allows us to to compare the numerical results with the theoretical predictions from above.

Numerically computing Q_{b}

The numerical calculations in this work are done using the finite-element solver COMSOL Multiphysics. The file used to the simulations presented below can be accessed in the Zenodo repository of Ref. [83][5].

To compute $\Delta\mathcal{U}$, from eq. (3.14), the curvature of a mode must be precisely determined. This is particularly challenging due to the sharp features that arise near the borders. For numerical efficiency we assume that the system has two lines of symmetry, and only model a quarter of the membrane shown in fig. 3.4a. Also shown is a further division of the membrane into a "border region" and an "inner region". This distinction is made to ensure that the sharp curvature features are well resolved; we define the boundary between the two regions to lie at a distance $3\Lambda l$ away from the border, slightly larger than the typical peak width Λl. The purpose of such a distinction is to enable us to mesh the border region with a much finer resolution than the inner region. We thus mesh the border region with a dense regular square mesh and leave COMSOL to mesh the inner region adaptively, setting only the maximal size limit–the minimal size corresponding to the border mesh size.

The quality factor is evaluated using eq. (3.1). We compute $\mathcal{U}$ from the maximal kinetic energy, which is simpler to compute than the elongation energy (by

[5] Found under the filename "SiN_membrane_opt_dimless.m".

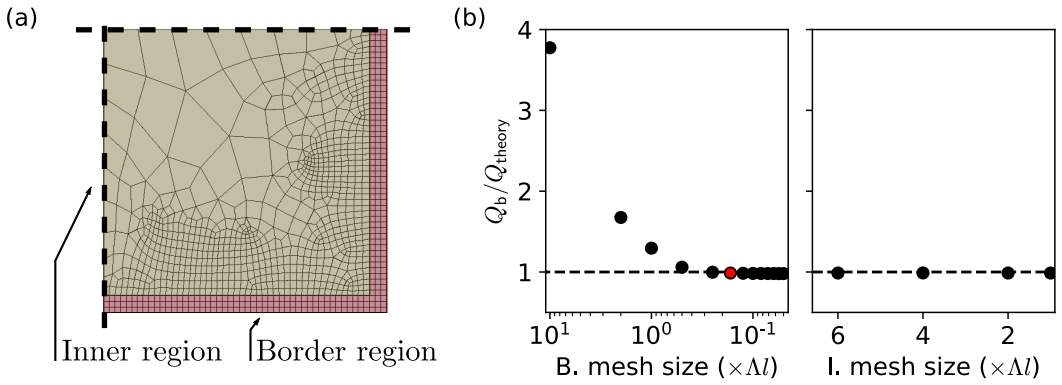

Figure 3.4: **a**, Typical meshing for a plain membrane geometry, highlighting the definition of the inner region (yellow), and the outer region (red). The dashed lines indicate the reflection symmetry axes assumed for the model. **b**, We compare the error in our estimation of Q_b relative to the theoretical Q_theory calculated from eq. (3.16) for different border (B.) and inner (I.) mesh sizes. The inner mesh size corresponds to the maximal mesh size allowed, while the border mesh size is the universal size of all squares in that region. The red point corresponds to the border mesh size value while the inner mesh size is varied. The dashed lines indicate $Q_\mathsf{b} = Q_\mathsf{theory}$. For this simulation $\Lambda l = 30$ μm was taken.

conservation of energy, the two are the same). We thus take

$$\mathcal{U} = \frac{1}{2}\rho h \Omega_\mathsf{m}^2 \int_0^l \int_0^l u^2(x,y)dxdy. \tag{3.19}$$

We made the following convergence test: we progressively reduce first the border mesh size then the maximal inner mesh size, to verify that the computed value for Q_b converges. In fig. 3.4b we find that the simulated value of Q_b arrives to within less than 2% of the theoretically predicted value for border mesh sizes below $\Lambda l/10$. The inner mesh size could be left relatively large (above $6\Lambda l$) with little influence on the convergence of Q_b.

Applying such a technique for realistic parameters such as a stress $\sigma_0 = 1$ GPa and an aspect ratio $l/h = (1\text{ mm}/100\text{ nm})$ would be highly challenging, since the width of the curvature peak $\Lambda l \approx 1$ μm is very hard to resolve in a finite element simulation. However, assuming that a $Q_{\mathsf{b,ref}}$ has been computed at a reference Λ_ref (maintaining $\Lambda_\mathsf{ref} \ll 1$), we can use the known scaling of Q_b with Λ given by eq. (3.16) to express it as

$$Q_\mathsf{b} = Q_{\mathsf{b,ref}} \frac{\Lambda_\mathsf{ref}}{\Lambda}. \tag{3.20}$$

We expect this method to be of use for calculating the quality factor of low-Λl mechanical resonators which meet the following criteria: their modes are subject to

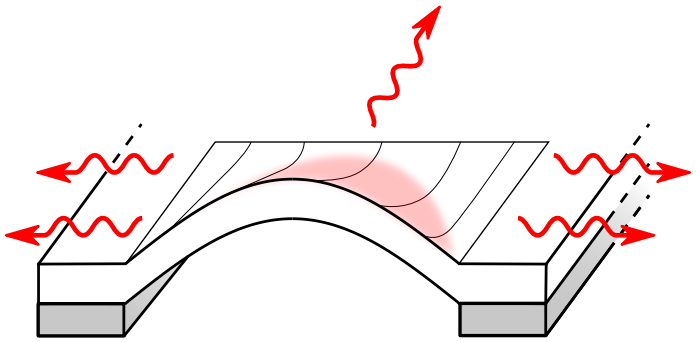

Figure 3.5: Schematic illustration of phonons "leaking" from the mode (the energy density is depicted in red) into the surrounding substrate. Shown here is a cross-section of a vibrating plate similar to the one in fig. 3.1.

the boundary condition (3.5) and the mode profile can be assumed independent of Λl.

3.1.4 Radiation losses

A separate but coequal contribution to mechanical losses is attributed to acoustic radiation into the substrate. We will refer to it as "radiation loss", in keeping with the nomenclature from Ref. [44], although they have equivalently been labeled clamping losses, anchor losses, or tunneling losses. These arise from a finite acoustic impedance mismatch between the membrane and the surrounding substrate, which is in practice not infinite and possesses a finite mass. Thus, energy can be irreversibly transferred away from the resonator, reducing Q_{tot}.

Radiation losses have been studied actively in SiN resonators, and several complementary descriptions have been offered as to their origin:

- Jöckel et al. [84] showed that strong losses appear when the membrane modes are resonant with substrate modes, indicating that they become coupled and share their loss channels.
- Radiation losses were modeled by Wilson-Rae as phonons tunneling into the bulk of the surrounding substrate [85], depicted in fig. 3.5.
- It was later verified that the rate of this tunneling depends on the "overlaps between the resonator mode and the free modes of the substrate" [86].

For a plain membrane the associated quality factor Q_{rad} can be approximated as [44]

$$Q_{\mathsf{rad}} \approx \zeta \frac{\rho_S}{\rho} 1.5\varsigma^3 \frac{n^2 m^2}{(n^2+m^2)^{3/2}} \frac{l}{h}, \tag{3.21}$$

where $\varsigma = \sqrt{(E_S/\sigma_0)(\rho/\rho_S)}$ is the ratio of the phase velocities ("acoustic mismatch") and ρ_S and E_S are the density and Young's modulus of the substrate, respectively. $\zeta \in [0, 1]$ is a phenomelogical term that accounts for the mounting conditions of the substrate in the experiment. Equation (3.21) predicts that higher-order modes are less affected by radiation losses than the lower-order modes, which was confirmed by the measurements of [44].

The parameter ζ merits further discussion as it has been shown to vary strongly under different experimental conditions. If the chip mounting conditions are not systematically controlled, ζ is left to vary freely and eq. (3.21) becomes a fruitless approach to quantifying radiation losses. It has been shown that ζ is maximal if the sample was resting freely on the experimental table, held in place only by gravity [87]. In comparison, a factor 10 reduction in ζ was observed when the sample is fixed in place by double-sided tape. We assume that these results, measured for SiN beams, similarly apply to SiN membranes, as these variations in ζ relate more to the condition of the substrate rather than the resonator shape–although we note that the precise value of ζ depends on the mode shape. Thus, we consider that ζ can be held constant for constant chip mounting conditions. More sophisticated phononic shielding schemes [76, 88] can make radiation losses negligible, and in subsequent SiN designs, discussed in section 3.2, Q_{rad} will not be a limiting factor to Q_{tot}.

The radiation and bending losses are the only two main sources of loss considered in this chapter. Further dissipation can occur by gas damping, due to elastic collisions with gaseous molecules. That case is treated empirically in the following chapter, but it is beyond the scope of the present analysis, as it is almost always negligible in typical experimental conditions. Thus, the total quality factor Q_{tot} can be evaluated and we can verify how the Qf-product and the minimal n_{eff} vary with the membrane geometry.

3.1.5 Scaling of the parameters with the membrane geometry

To summarize, the dominating losses in a plain SiN membrane can be described by

$$(Q_{\mathsf{tot}})^{-1} = (Q_{\mathsf{b}})^{-1} + (Q_{\mathsf{rad}})^{-1}\,. \tag{3.22}$$

The scaling of the various quality factors is summarized in table 3.1, as well as their values for typical parameters. We estimate that under ideal clamping conditions and for typical sample parameters, $Q_{\mathsf{rad}} > 2Q_{\mathsf{b}}$, and

$$Qf \approx 1.5 \times 10^{12}\ \text{Hz}. \tag{3.23}$$

We note that the value for Q_{tot} measured for a plain membrane at cryogenic temperatures (section 2.2.4) exceeds the room-temperature Qf-product by a factor 50,

Table 3.1: Summary of the scaling of the various quality factors for the fundamental mode, $m = n = 1$. Estimated values are given for typical sample parameters: $h = 100$ nm, $l = 1$ mm, $\sigma_0 = 1$ GPa, $\rho = 3200$ kg.m^{-3}, and $E = 270$ GPa. The Si parameters are taken to be $\rho_{\mathsf{S}} = 2300$ kg.m^{-3}, and $E_{\mathsf{S}} = 170$ GPa. Q_{b} is determined from eqs. (3.16) and (3.17) and Q_{rad} from eq. (3.21).

Quality factor	Scaling	Estimated value ($\times 10^6$)
Q_{b}	$l\sqrt{\sigma_0}$	6 ± 4
Q_{rad}	$l/\left(h\sqrt{\sigma_0^3}\right)$	14 ($\zeta = 1$)
Q_{tot}	-	4 ± 2

in agreement with similar experiments [66, 89].

In the limit of thin membranes where Q_{rad} is higher, $Q_{\mathsf{tot}} \sim Q_{\mathsf{b}}$. We then find that the Qf-product of the fundamental mode cannot be increased by varying the resonator parameters (h or l). It could still be increased with higher σ_0, but a tensile stress significantly beyond 1 GPa cannot be achieved in SiN nanomembranes. This sets an upper limit to the room-temperature Qf-product for such resonators to $Qf \approx 2 \times 10^{12}$ Hz.

Another parameter remains to be described, namely the mean population of a mechanical mode in a sideband cooling experiment n_{eff}. The expression for this term was derived in chapter 1, and for $n_{\mathsf{th}} > C \gg \eta_{\mathsf{rsf}}$ (representative of the experiment described in section 2.3) we find

$$n_{\mathsf{eff}} \approx \frac{n_{\mathsf{th}}}{C}. \tag{3.24}$$

Both n_{th} and C depend on the resonator geometry, and we show in Appendix B that in the ideal case where $Q_{\mathsf{rad}} \gg Q_{\mathsf{b}}$ and the parasitic capacitance of the microwave circuit can be neglected,

$$n_{\mathsf{eff}} \propto h. \tag{3.25}$$

In practice, h can be made a factor 10 lower than the 100 nm used here. While the ensuing reduction in n_{eff} is significant is it ultimately insufficient to reach the ground state (in chapter 2, the minimal achieve value for n_{eff} was 100). From this study we find that none of the key parameters of a plain SiN membrane can be sufficiently improved, and the ground state in the experimental conditions of chapter 2 cannot be reached.

Several solutions have been suggested to overcome the present impasse, and at their core lies the idea of mode shape engineering. We found that both sources of loss (bending and radiation), although they have different origins, are both related

to the clamping condition of the membrane to its anchoring substrate. In particular, Q_{b}, given in eq. (3.16), is dominated by edge losses (the red term) which results in the scaling $Q_{\mathsf{b}} \propto \Lambda^{-1}$. If the hard clamping condition were absent the remaining term would result in the more favorable scaling $Q_{\mathsf{b}} \propto \Lambda^{-2}$. In the following, we show how phononic engineering techniques can be applied to remove the hard clamping boundary condition (3.5) altogether, and render both edge losses and radiation losses negligible.

3.2 Phononic crystal membrane design

Several approaches have been taken in the past to reduce either or both of the main loss channels discussed above. For instance, a proposed solution has been to attach a resonator to the substrate by means of thin tethers, instead of clamping it directly. The so-called "free-free" resonator [90] or the trampoline resonator [91, 92] are instances of such an implementation–they are shown in fig. 3.6a and b. If the tethers are judiciously positioned and shaped the quality factor of the resonator is increased. Another approach has been to implement phononic shielding in the substrate, as shown in fig. 3.6c. This limits radiation losses by engineering a spectral stop-band at the relevant frequency range [75].

The most successful approaches to date have combined both of the ideas discussed above. In many modern approaches a phononic crystal structure is directly embedded within the beams [76] or the membranes [24] themselves–examples of such resonators are shown in fig. 3.6d and e. In those cases, similarly to a photonic crystal, a periodic modulation of the material density is introduced by means of which a localized state of motion can be created close to a central defect of the structure. This ensures that the displacement is minimal at the border of the resonator, thereby suppressing bending losses. Furthermore, Ghadimi et al. [76] have shown for 1D resonators that this patterning also fulfills its role as a phononic shield, simultaneously reducing radiation losses.

Owing to their strong localization, the frequencies of the modes of interest are increased. In addition, the quality factors that can be obtained with such resonators approach 10^9 at room temperature [24, 31], and have exceeded this value even in modest cryogenic environments [93]. Such ultracoherent phononic crystal membranes were therefore chosen as a replacement for the plain membranes in our electromechanical device. We note that such membranes have yet to be measured at sub-kelvin temperatures. Their properties in such environments are still to be determined, making such a study valuable beyond ground-state cooling experiments. From the predicted increase of Q at cryogenic temperatures, it can be anticipated that these new resonators will significantly outperform plain membranes. The phononic shield is further expected to act as an attenuator for noise sources originating from the laboratory environment. In this section, we present the working

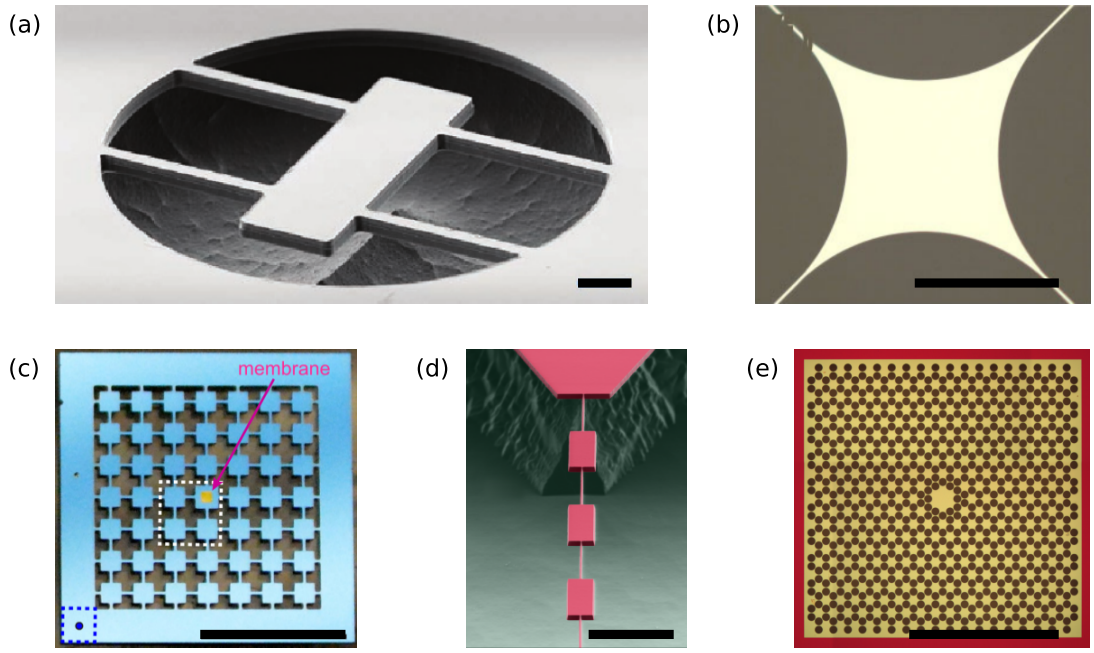

Figure 3.6: Optical micrographs of engineered resonators. **a**, "Free-free" resonator which minimizes the coupling of the resonator mode to the substrate modes. A central oscillating slab is anchored to the substrate by 4 tethers placed near the nodes of the oscillation mode. The scale bar represents 20 μm. Image extracted from [90]. **b**, Trampoline resonator. A central membrane, oscillating out of plane, is anchored to the substrate by four thin tethers. The scale bar represents 100 μm. Image extracted from [91]. **c**, A phononic crystal structure in the substrate which reduces the radiation loss of a central membrane. The scale bar represents 0.5 cm. Image extracted from [75]. **d**, A phononic shield integrated within a SiN nanobeam, suppressing radiation losses. The scale bar represents 5 μm. Image extracted from [76]. **e**, Micrograph of a phononic shield SiN membrane fabricated by the author, based on the design from [24]. The scale bar represents 1 mm.

principles of these membranes, and list the key design considerations necessary to achieve ultrahigh quality factors.

3.2.1 Engineering bandgaps in periodic structures

A cornerstone discovery in wave engineering was the appreciation that the properties of waves could be altered by introducing modulations in the propagation medium. Non-interacting waves propagating through a medium can be described by their direction and their wavenumber, summarized by the wavevector $\mathbf{k}$. In infinite homogeneous media the frequency ω of a wave is given by the linear relationship $\omega = c|\mathbf{k}|$, where c is the speed of the wave. Crucially, c depends both on the type of wave and on the properties of the propagation medium itself. For electromagnetic waves c depends on the refractive index, and for mechanical waves $c \propto 1/\sqrt{\rho}$ [94].

The dispersion relation becomes more complex when the speed of the wave is not constant throughout the propagation medium, for instance due to local variations in ρ for mechanical waves. In the special case where the wave velocity is modulated periodically, several eigenenfrequencies can exist for a given wavevector. This gives rise to the well-known concept of band diagrams. In analogy to the periodic arrangement of atoms in solids, such periodic materials are also called crystals. For electromagnetic waves a periodic modulation of the refractive index results in a photonic crystal (PhC); for mechanical waves modifying the density of the material gives rise to a phononic crystal (PnC). The solutions to the motion of a wave in such a medium can be found with the Bloch theorem. It states that any solution to the wave equation must follow the periodicity of the medium. This theorem was originally developed to describe the behavior of charge carriers in semiconductor crystals, where the periodic modulation of the electric potential leads to band structures for the charge carriers. It has since then been fruitfully applied to periodic media for electromagnetic [95, 96] and acoustic [97] waves, but also to systems like ultracold atom lattices [98] or lattices for polaritons [99]. A major source of interest of PhCs or PnCs is the fact that for specific crystal structures, intervals of frequency can exist where no solution is allowed: these are called bandgaps, and they can be employed to engineer localized states of motions whose properties can be finely tailored.

For mechanical vibrations a simple way to generate the required periodicity in the propagation constant is to modulate ρ. Here, we restrict our analysis to two-dimensional systems as these are a good approximation to the high aspect-ratio resonators used in this work. We thus consider a uniform sheet of material into which a periodic array of holes has been punched, resulting in a honeycomb array of pads bound together by thin tethers, shown in fig. 3.7.

Interestingly, if a defect is introduced in the periodic structure, localized states of motion can arise, which are of particular interest here. In 2D, there are 5 different periodic lattice structures to choose from: square, hexagonal, oblique, rhombic, and

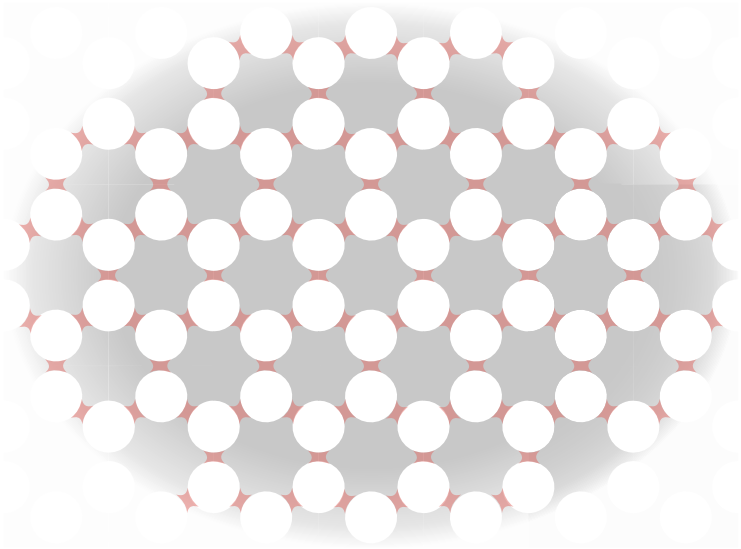

Figure 3.7: Illustration of a a few cells of an infinite 2D hexagonal PnC. The material is represented in gray and red, and is patterned with circular holes. The resulting structure is an array of pads connected by thin tethers (colored in red).

rectangular[6]. An imperative of the PnC lattice is that it must present a bandgap; if this condition is not met, localized states of motion cannot be generated. Square and hexagonal lattices are common structures for PnCs, and it has been shown that both of these structures can give rise to large bandgaps [101]. Rhombic lattices have also been predicted to exhibit bandgaps [102], although such structures have, to the author's knowledge, not been studied experimentally. Since hexagonal lattices have been predicted to exhibit larger bandgaps than square lattices [101] and have been extensively studied in SiN membranes [24, 25, 103], this lattice type will be studied in this work as well. The hexagonal lattice can be described fully by a lattice constant b and a hole radius r, and we show its primitive unit cell in fig. 3.8a. Note that the rectangular cell shown here is not the primitive cell of the lattice, and was introduced for numerical convenience.

We numerically compute the band diagram for this structure using COMSOL. The simulation is run in two steps to encompass all effects of the holes in the plane. First, the in-plane stress and material deformation are left to reach a steady state from a uniform distribution of the tensile stress, with $\sigma_0 = 1$ GPa. This stationary study step is important, as the resulting non-uniform redistribution of stress and the deformation of the material affects the propagation of the wave. Shown in fig. 3.8b is the result of the stationary study, showing the stress distribution in a PnC cell: the stress is more than twice as high in the tether regions than in the pads.

[6]Other arrangements, such as fractal-like structures [100], have been proposed, but they are beyond the scope of this work

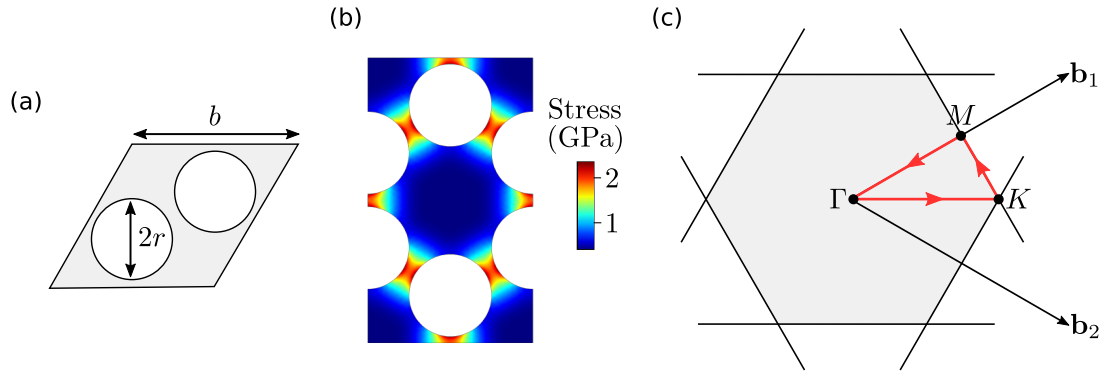

Figure 3.8: **a**, Primitive unit cell of a hexagonal lattice. **b**, Von Mises stress distribution for one unit cell of the PnC, with an initial isotropic stress $\sigma_0 = 1$ GPa, and where the material deformation has been allowed to reach the steady state. A rectangular unit cell is used in the computations. **c**, The irreducible Brillouin zone of a hexagonal lattice, where $\mathbf{b}_1$ and $\mathbf{b}_2$ are the primitive reciprocal lattice vectors. The points of high symmetry Γ, K, and M are indicated, with the red path representing the sweep in $\mathbf{k}$ followed for numerical simulation of band diagrams.

Afterwards, the eigenfrequencies of the structure are calculated, using the periodicity condition for the displacement vector $\mathbf{u}(\mathbf{r})$

$$\mathbf{u}(\mathbf{r}) = \mathbf{u}_\mathbf{k} e^{i\mathbf{k}\cdot\mathbf{r}}, \tag{3.26}$$

where $\mathbf{u}_\mathbf{k}$ is the displacement profile within a single unit cell. The periodicity is defined by the wavevector $\mathbf{k}$ which is set by the user. The simulation finds all the eigenfrequencies corresponding to a user-specified value of $\mathbf{k}$. To obtain a band diagram a sweep over several values of $\mathbf{k}$ is made. It must be ensured that specific points in phase space are crossed to encompass all the relevant features of the bandgap. The information that is sought is the width of the bandgap, defined as the frequency difference between the minimum of the upper band and the maximum of the lower band. We know that all extrema are found by including the points of high symmetry of the reciprocal lattice in our sweep, which are:

$$\Gamma : (0, 0), \tag{3.27}$$
$$K : (4\pi/3b, 0), \tag{3.28}$$
$$M : (\pi/a, \pi/\sqrt{3}b). \tag{3.29}$$

At these points the energy eigenstates become degenerate and avoided crossings appear, and the band-gap is minimal. The irreducible Brillouin zone as well as the high-symmetry points are represented in fig. 3.8c.

The set of eigenfrequencies are grouped in the band diagram shown in fig. 3.9a.

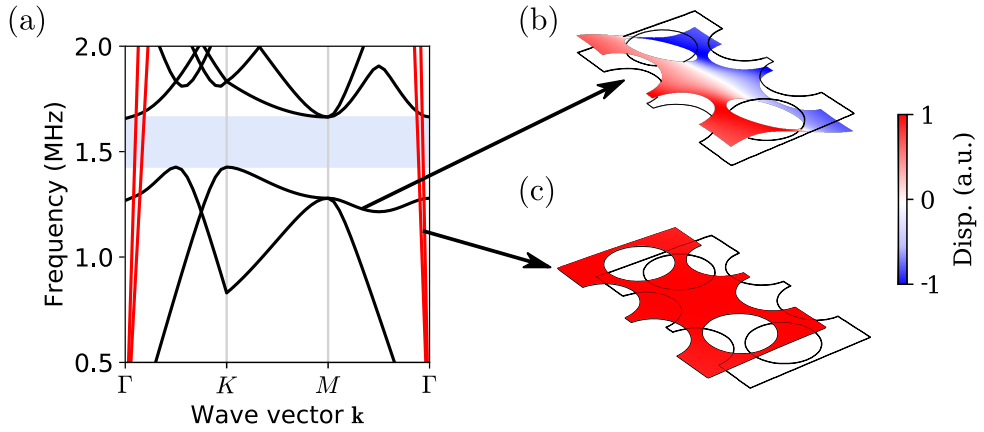

Figure 3.9: **a**, Simulated band diagram for a PnC with a hexagonal unit cell with $b = 160$ μm, $r = b/4$ μm, and $\sigma_0 = 1$ GPa. The modes highlighted in red are in-plane modes with high velocities. The area highlighted in blue is the inferred quasi-bandgap. **b-c**, Displacement (Disp.) profile of a single unit cell, for: **(b)** an out-of-plane crystal mode, and **(c)** an in-plane crystal mode. The unit cell at rest is shown as a black contour.

For the simulation that is reported here, $b = 160$ μm and $r = 40$ μm were chosen to ensure the appearance of a band gap in the MHz range, as in [24]. The Matlab script used for running this COMSOL simulation can be found in Ref. [83][7]. For clarity, we will refer to all of the modes that appear in this diagram as "crystal modes", as they represent the frequencies at which the PnC membrane can vibrate.

A striking feature of this diagram is that it is not fully open: there are, for wavevectors close to the Γ point, modes of high dispersion velocity that can propagate in the entire frequency range. This is in agreement with the simulations of [101], where it was demonstrated that a full bandgap can only be opened if the radius r of the holes is of the same order as the thickness h of the membrane. Here, we have $r/h = 4 \times 10^4$. These modes have no impact on the relevant dynamics of our systems however, as we will only consider transverse vibrations akin to the membrane mode shown in fig. 3.9b. In fact, all modes highlighted in black in fig. 3.9a vibrate out-of-plane, whereas the high-dispersion crystal modes shown in red oscillate entirely in-plane. A typical mode profile for an in-plane mode is shown in fig. 3.9c. For all intents and purposes, the PnC possesses a quasi bandgap to all transverse oscillations, which we infer to be centered at 1.55 MHz with an opening of 15% of the bandgap's central frequency.

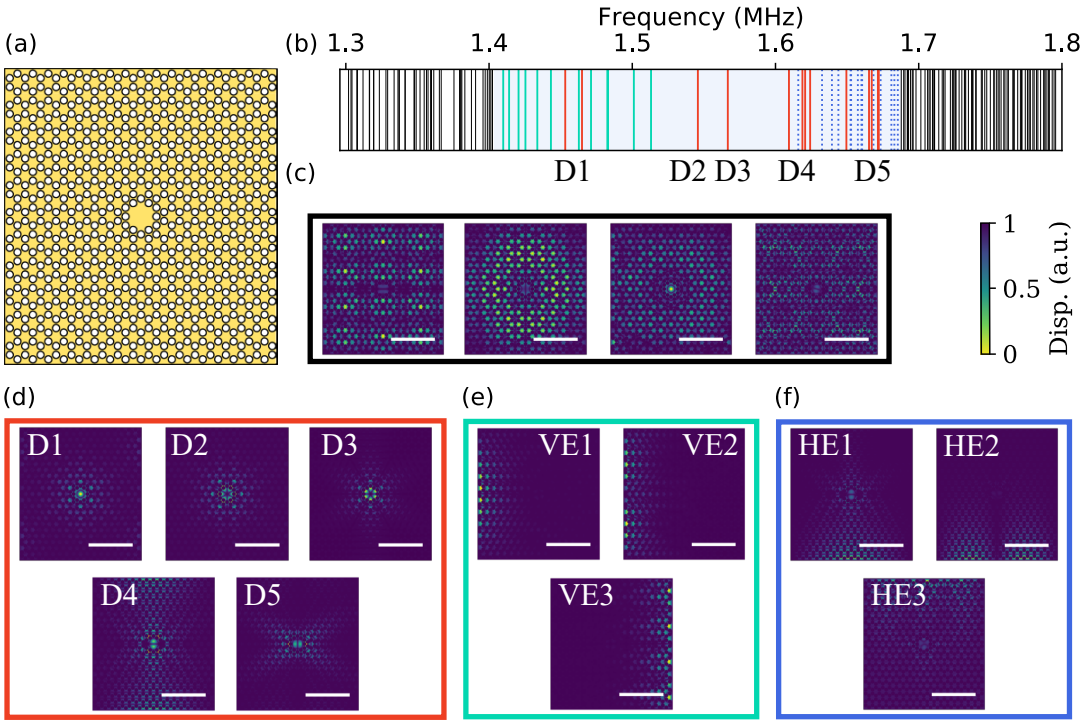

Figure 3.10: **a**, Illustration of a PnC membrane used in simulations, possessing a central defect. SiN is depicted in yellow. **b**, Frequency spectrum of the PnC membrane, with $b = 160$ μm, $r = 40$ μm, and $\Lambda l \approx 1.6$ μm. Each vertical line represents a mode found in COMSOL. We distinguish four types of modes, namely: crystal modes (black), defect modes (red), vertical edge modes (cyan), and horizontal edge modes (dashed, dark blue). **c-f**, Selected examples of displacement (Disp.) profiles for: **(c)** crystal modes, **(d)** defect modes, **(e)** vertical edge modes, and **(f)** horizontal edge modes. The white scale bars represent 1 mm. This figure is adapted from Ref. [104].

3.2.2 Localized defect states in PnC membranes

Through this bandgap for out-of-plane motion the PnC can be exploited to engineer localized states. Indeed, any defect introduced to the PnC will break its periodicity and support a unique set of modes. If the geometry of the defect is such that some of its eigenfrequencies lie within the bandgap, then the resulting "defect modes" will be confined to that region. To study these defect modes, a SiN membrane is structured with a hexagonal lattice of holes, following the design first introduced by Tsaturyan et al. [24], and shown in fig. 3.10a. In the center of the membrane the holes are displaced, creating a defect in the PnC.

The defect modes of a PnC membrane are found by numerical simulation with COMSOL. We take as before $b = 160$ μm and $r = 40$ μm, with a membrane side length of approximately 2.8 mm $\times$ 3.1 mm as in our physical samples. The value for b that we choose is consistent with the fact that a Nb pad deposited on the defect should have approximately the same area as in chapter 2. The process for choosing the side length of the membrane is discussed in section 3.3.

To obtain the spectrum of the membrane we run a two-stage simulation as before. The file used for these simulations can be found in Ref. [83][8]. For this simulation the curvature peaks do not need to be resolved since we are only looking for the mode spectra and approximate profiles. We can take $\sigma_0 = 1$ GPa ($\Lambda l \approx 1.6$ μm), representative of our samples.

It was a priori expected that the spectrum would have an overall high mode density with a clearly distinguishable region of low mode density, populated only by defect modes. The resulting spectrum of the membrane, shown in fig. 3.10b, fails to match these expectations. Indeed, it presents a complex distribution of modes, and it is not immediately obvious where the bandgap should be located, judging solely from the mode density. The spectrum only becomes tractable when the mode profiles are analyzed and categorized in detail. The rich dynamics hidden behind this spectrum, studied throughout this section, will reveal some crucial considerations to which one must pay particular attention when designing a PnC membrane.

In fig. 3.10b we have highlighted a region of the spectrum in blue for further reference. Outside of this region, the simulated mode profiles are delocalized over the entire membrane, which we therefore infer to be crystal modes, with selected examples shown in fig. 3.10c. This behavior is distinct from that of the modes within the blue region, which are strongly localized to a specific area of the membrane. As expected we find the defect modes localized to the central defect area of the membrane, as shown in fig. 3.10d–we have labeled the first few modes D1 to D5. However, two other types of modes appear localized near the borders of the membrane: first, we find modes localized to the vertical borders of the membrane shown in fig. 3.10e, which we refer to as vertical edge modes (VEMs); similarly, we

[7]Found under the filename "SiN_PnC_Honeycomb_A_hexagonal_recip_space".
[8]Found under the filename "SiN_PnC_membrane_asym_spectum.m".

find a set of modes confined to the horizontal borders of the membrane, and such horizontal edge modes (HEMs) are shown in fig. 3.10f.[9]

We explicitly distinguish VEMs ans HEMs as they are both spectrally and spatially distinct. These edge modes arise from finite-size effects, due to the sudden break in the crystal pattern near the borders. Note that the VEMs and HEMs shown here do not respect a mirror symmetry; that is a deliberate choice intended to produce a realistic spectrum, because the PnC structure in physical systems is never perfectly centered with respect to the membrane. Here, the PnC structure is shifted away from the center by 5 μm in both the x- and y-directions, corresponding to the approximate off-centering we measure in physical systems (see chapter 4 for more details).

Importantly, all of the modes within the blue region are localized states of motion. We therefore conclude that region to be the bandgap of the PnC. It is centered around 1.5 MHz and spans approximately 17% of the central frequency, in good agreement with the simulated band diagram for an infinite PnC.

We note a further crucial point, which is that in fig. 3.10b some of the labels for defect modes (namely, D1, D4, and D5) are not placed below a single mode line. That is because at those frequencies, it is impossible to uniquely identify the defect modes; due to the fact that edge modes exist at similar frequencies to those defect modes, the latter hybridize with the former, resulting in normal modes. For the normal modes the vibration is no longer localized to the central defect of the membrane, but "leaks" towards its edges. This feature is discussed further in section 3.2.5.

This preliminary simulation helps us to understand the behavior of the membrane in more detail. Ultimately, we wish to obtain a value for the quality factor of the defect modes, and in particular of the one with the lowest frequency D1, by virtue of its resemblance to the (1, 1) mode of a plain membrane. It is furthermore the mode being primarily studied in contemporary applications of PnC membranes [4, 19, 25, 32, 60, 93]. To estimate the losses of D1, the curvature profile needs to be simulated in detail.

3.2.3 The curvature profile of defect and edge modes

As we have done in section 3.1.3 only a quarter of the membrane is simulated, for numerical efficiency. An example of a cut of its displacement profile is shown in fig. 3.11a, with a typical curvature peak width taken as $\Lambda l \approx 16$ μm for illustration purposes. In stark contrast to the (1, 1) mode of similar frequency, the displacement amplitude of D1 is attenuated by the PnC. The profile envelope is well fitted by an exponential function of characteristic decay length 0.2 mm We also compare D1 to

[9]The denomination "edge mode" is only related to the position at which they are localized, as is not meant to be a reference to topological transport. The PnC structure studied here does not fulfill the specific conditions required for the edge modes to propagate directionally [105, 106].

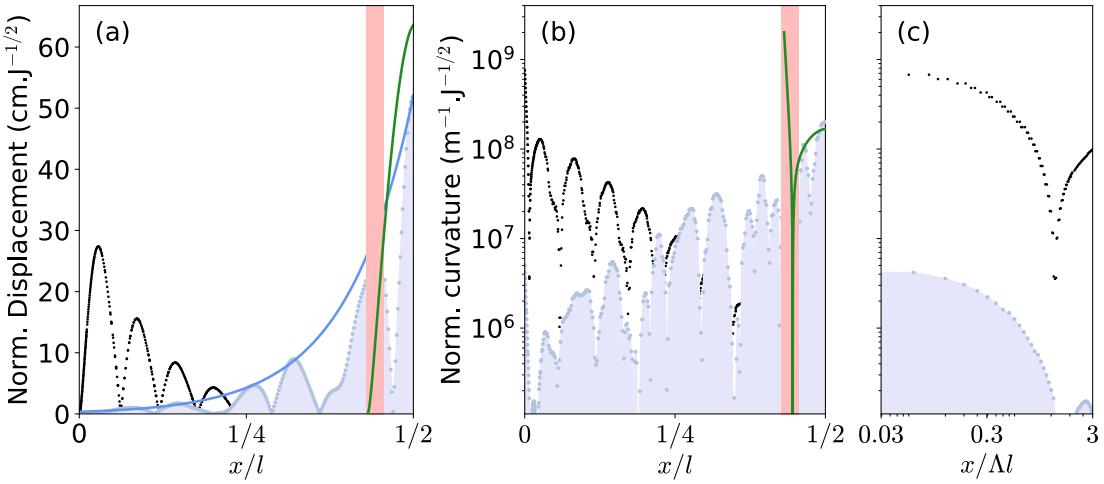

Figure 3.11: **a-b**, Displacement **(a)** and curvature **(b)** of the D1 mode (filled light blue) and the (1, 1) mode of a plain membrane with the same frequency (green), along the $y = 0$ line. The red region represents a hole in the PnC along that line, in which no data for D1 can be obtained. In black, the VE1 mode of the PnC membrane is plotted along the $y = 2.5 \times (\sqrt{3}b/2)$ line, where it possesses an anti-node. The data are normalized (Norm.) by the square root of the corresponding mode energy. The data is acquired for $\Lambda l \approx 16$ μm, with $b = 160$ μm and $r = b/4$. In **(a)**, serving as a guide to the eye, the dark blue line represents an exponential decay. **c**, Curvature of D1 and VE1 near the border of the membrane.

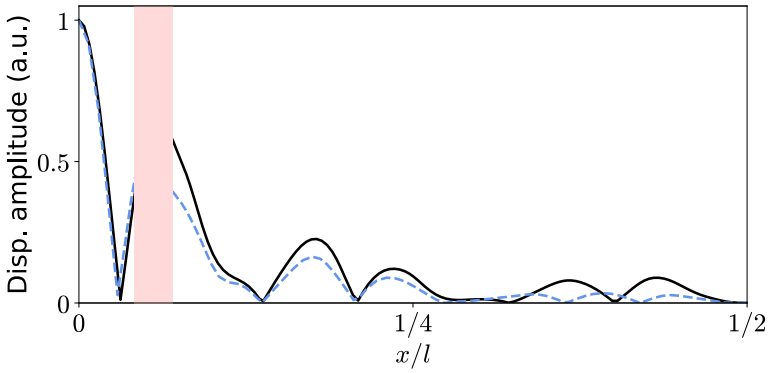

Figure 3.12: Displacement (Disp.) amplitude of D1 for $\Lambda l \approx 30$ μm (black) and for $\Lambda l \approx 1$ μm (blue, dashed). For these plots, all parameters were kept fixed except for σ_0, which was taken as 1 MPa and 1 GPa, respectively. The red region represents a hole in which no data can be acquired.

VE1, which we find to have a similar attenuation through the PnC. For simplicity, the geometry of the membrane was chosen such that no coupling could occur between D1 and VE1 in this simulation, nor in the one described in section 3.2.4. The manner in which this is done is described in section 3.3.2.

We computed from these profiles the curvature of D1, VE1, and the (1, 1) mode, which we show in fig. 3.11b. For DM1, the curvature is not maximal at the borders as is the case for a plain membrane, but peaks at the center of the membrane and steadily diminishes towards the borders. Note that there still remains a peak in curvature at the edges even for the defect mode, although it is several orders of magnitude smaller than the curvature maximum. For this reason, this sort of membrane patterning has been nicknamed "soft clamping" [24], since the hard clamping condition (3.5) has been removed. In the section below, we verify the advantages of this technique by numerically simulating Q for D1 and VE1 based on the displacement and curvature profiles.

3.2.4 Computing Q_b of D1 and VE1

To compute Q_b for a PnC membrane mode a similar approach to the one described in section 3.1.3 could be taken: the mode profile and curvature can be computed at high Λl and then, to obtain its value for real parameters, Q could then be scaled accordingly[10]. This would allows us to resolve the peaks in the curvature profile and accurately compute Q for VE1. For a plain membrane this technique works because the mode profile is independent of Λl, for sufficiently small values of Λ. It is not the case for PnC membranes however, owing to the fact that when Λl is scaled up,

[10]The conversion equation would be slightly more complicated than eq. (3.18), since we could no longer assume edge losses to be dominant.

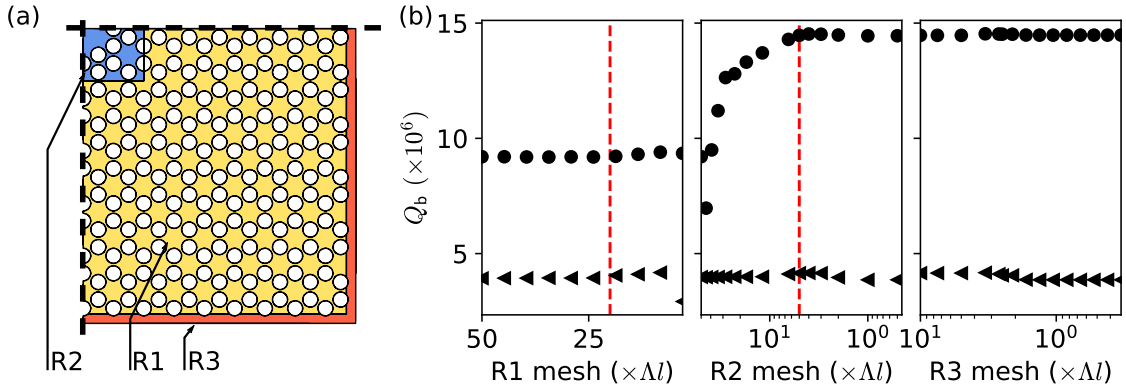

Figure 3.13: **a**, Geometry of the COMSOL model of a PnC membrane. We divide it into three regions. The border region is shown here as the R3 region. We split the inner region into two, shown as the R1 and R2 regions. The width of the border region is greatly exaggerated, for clarity. **b**, Computed Q with respect to the mesh size. The mesh size is progressively reduced first in R1, then R2, and finally R3. Q_b is computed for D1 (dots) and for VE1 (triangles). The dashed red lines indicate the values for the mesh size which were taken in one region, when meshing the next one.

which can in practice only be done by lowering σ_0[11], the non-uniform distribution of stress resulting from the PnC structure causes the mode profile to vary, as shown in fig. 3.12. This poses a conundrum: the profile of PnC membrane modes can only be accurately computed if $\Lambda l \approx 1$ μm (corresponding to real samples), but then the curvature peaks can no longer be resolved. As a result, the Q of hard-clamped modes such as VE1 cannot be computed accurately. We choose to prioritize accurate computations of Q for defect modes, and therefore a value of Λl representative of real samples, with $\Lambda l \approx 1$ μm and $\sigma_0 = 1$ GPa, is taken for all subsequent simulations.

As mentioned above numerically computing the quality factor of these modes requires a finer meshing in the regions where the curvature is at its highest. For PnC membranes there are two such regions: near the central defect and in the border. For numerical efficiency, we therefore divide the COMSOL modes into three areas, meshed separately, labeled R1 (the inner region), R2 (the inner defect region), and R3 (the border region), as shown in fig. 3.13a.

By progressively reducing the mesh size of these regions we can converge towards the predicted value of Q_b for D1. In fig. 3.13b we find that for D1 Q_b converges to approximately 1.5×10^7, for a frequency of 1.436 MHz. As expected, R2 is the region which is most important to computing this value, and Q_b remains almost constant when varying R1 and R3. For comparison, the quality factor of VE1, with

[11] Λl only depends on the parameters σ_0 and h. In principle, h could be varied, but in practice this causes the 2D approximation to break down in COMSOL, and nonphysical results are obtained.

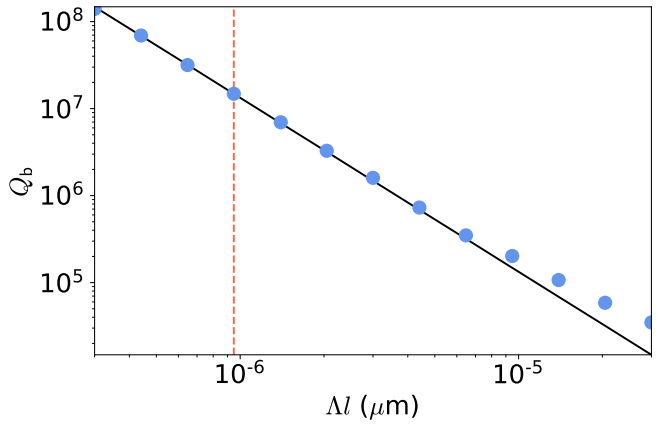

Figure 3.14: Variation of Q_b with the dissipation dilution factor Λl, for D1. The simulation was run by varying σ_0, keeping all other parameters. The blue points are the simulated data while the black line represents a fit with $1/\Lambda^2$. The dashed red line represents typical sample parameters.

a frequency of 1.415 MHz, is also computed. For that mode, no mesh refinement causes significant changes in Q. We note that even for the smallest mesh sizes considered in the R3 region, corresponding to the limits of the computer memory used for these simulations, the curvature profile near the membrane borders was poorly resolved. Thus, the computed value of $Q_b \approx 4 \times 10^6$ can only be considered as an upper estimate for the quality factor of VE1–the same applies to all VEMs studied in the following sections.

With this we have obtained a principal parameter for PnC membrane modes: for D1,

$$Qf \approx 2 \times 10^{13} \text{ Hz}, \tag{3.30}$$

which is a factor 10 improvement over the fundamental mode of plain membranes. By varying the tensile stress in the simulation we can vary Λl and verify the induced variation in Q. In fig. 3.14, we check that in the vicinity of typical sample parameters (in which the variation in material deformation is negligible), Q indeed follows the ideal scaling

$$Q_b \propto \frac{Q_{intr}}{\Lambda^2} \propto \frac{\sigma_0 b^2}{h}, \tag{3.31}$$

as expected for a soft-clamped mode. Q_b has a stronger dependence on σ_0 and the typical mode confinement length b. It has furthermore acquired a dependence on h in the regime where Q_{intr} is dominated by surface losses.

With this modified scaling of Q, similar to a plain membrane (section 3.1.5), we can compute the variation of the minimal value of n_{eff} with the membrane geometry. Assuming that the mode frequency follows a similar scaling to a plain membrane

($\Omega_{\mathsf{m}} \propto 1/b$), we can find this scaling by following a similar derivation to the one shown in Appendix B. As a reminder,

$$n_{\mathsf{eff}} \propto \frac{\Omega_{\mathsf{m}} m_{\mathsf{eff}}}{Q}. \tag{3.32}$$

For a PnC membrane, compared to a plain membrane of the same frequency, Q is significantly higher (m_{eff} does not change substantially, see chapter 4). The minimal effective population is thus smaller by a factor 10 in PnC membranes; we note that for lower frequency plain membrane modes, that is not the case (see section 3.4). From eq. (3.31) we find that n_{eff} follows the scaling

$$n_{\mathsf{eff}} \propto \frac{h^2}{b}. \tag{3.33}$$

n_{eff} thus scales more favorably with the membrane thickness than before (before, $n_{\mathsf{eff}} \propto h$), and has acquired an additional dependence on the mode confinement length b. Thus, both the Qf-product and n_{eff} acquire a more favorable scaling with geometrical parameters which we can control. Comparing a PnC membrane ($\Omega_{\mathsf{m}} \approx 1.5$ MHz, $Q \approx 1.5 \times 10^7$) to the plain membrane studied in the last chapter ($\Omega_{\mathsf{m}} \approx 0.5$ MHz, $Q \approx 4 \times 10^6$), n_{eff} is expected to remain almost the same, provided the environment temperature does not change. For any significant improvement to be observed, h needs to be reduced, and at its minimal value of 10 nm, a hundredfold reduction in n_{eff} can be expected.

As a consistency check, to check that the PnC membrane behaves as expected, we ask a further question: does the quality factor depend on the number of PnC unit cells surrounding the defect? We might expect Q to increase monotonously, and eventually reach an asymptote in the limit of wide PnCs. However, this seemingly simple question reveals an important behavior of the PnC membrane. If it is not taken in account, this leads to a significant degradation of the defect mode Q.

3.2.5 A "final" consistency check

To check the dependence of Q with the phononic shield width, we sweep the horizontal length of the membrane. As the membrane size increases, an increasing number of unit cells of the PnC can be accommodated. The vertical length then is accordingly adjusted to create a membrane shape as close to a square as possible. It is always ensured that an odd integer number of unit cells can be fitted within the membrane (see fig. 3.15a).

The resulting values of Q_{b} are shown in fig. 3.15b. For clarity, two values are plotted: the total quality factor and $Q_{\mathsf{b,inner}}$, the computed quality factor by integrating the curvature only in the inner (R1 and R2) regions. This allows us to separate the contribution of edge loss from the total bending loss. Q_{b} does not seem to vary

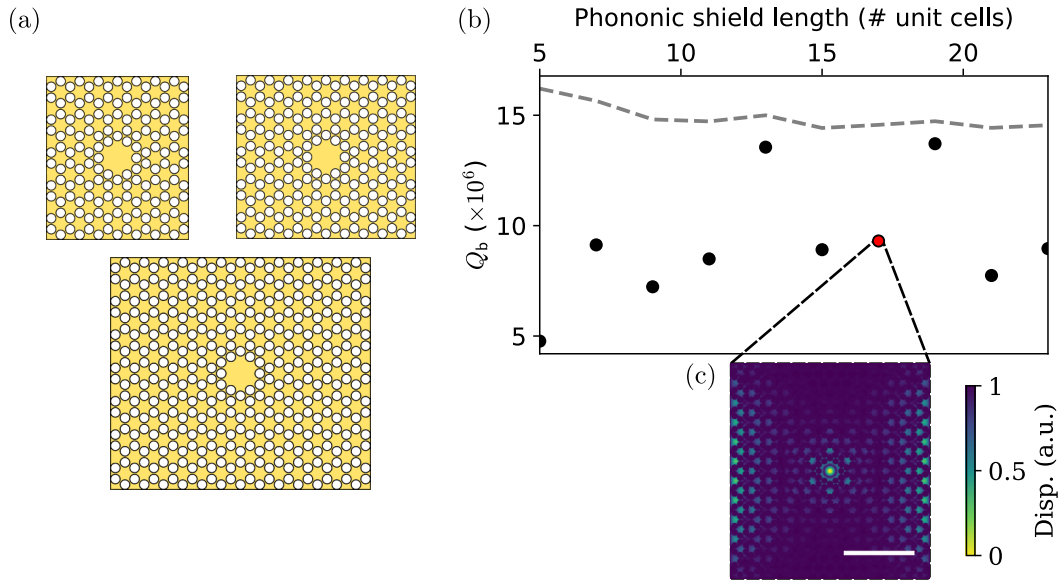

Figure 3.15: **a**, Examples of simulated membrane sizes for (from smallest to largest) 7, 9, and 13 unit cells either side of the defect. The number of unit cells in the $x-$direction is increased, and the unit cells in the $y-$direction are adjusted to ensure the membrane shape is as close as possible to a square. **b**, The mode profile and curvature are computed for different phononic shield length. The dashed gray line shows the value computed for $Q_{\mathrm{b,inner}}$. **c**, Displacement (Disp.) profile of the mode for the point highlighted in red. The white scale bar represents 1 mm.

with any discernible trend and almost always stays significantly below $Q_{\mathrm{b,inner}}$. Only punctually, e.g. for a length of 13 or 19 unit cells, does the quality factor approach the predicted value of 1.5×10^7. We note that at low n_x, $Q_{\mathrm{b,inner}}$ increases slightly because the distinction between inner and border regions becomes invalid.

Surprisingly, increasing the number of unit cells does not seem to increase Q_{b}. In fact, the answer as to why Q_{b} is much lower than $Q_{\mathrm{b,inner}}$ has a different origin: fig. 3.15c shows that when Q is low the D1 mode is not only vibrating near the center of the membrane, but also presents significantly displacement near the vertical borders of the membrane. In fact, we identify the mode shown here as a linear combination between D1 and (in this case) VE1. We note that the specific points at which this combination occurs is strongly dependent on a geometric parameter of the membrane called the margin M, discussed further in section 3.3.2. The figure shown here thus only serves to illustrate the mode combination effect, and is not meant to describe the general behavior of PnC membranes.

This linear combination of D1 and a VEM can be attributed to a coupling between defect and edge modes, resulting in a hybridization of the two. The origin of this coupling is that D1, despite being separated from the edge mode by the PnC,

still possesses finite overlap with the VEMs. We recall at this stage our observation in fig. 3.10b, where we found that D1 (along with D4 and D5) was split into two or more separate modes at distinct frequencies. This behavior is typical of mode hybridization and further supports the coupling hypothesis.

Following this logic, if the frequency of the edge mode were far from that of the defect mode, then no hybridization could occur and the coupling would no longer pose any problem. Failing to do so would result in a normal mode which would be hard clamped, and the benefit of the PnC would be lost. In fact, we see that the lower estimate on the simulated quality factor of D1 is similar to the predicted $Q_{\mathtt{b}} = 4\times10^6$ for hard-clamped modes. We study the coupling mechanisms of various modes further to test our hypothesis quantitatively. This will allow us to discern the circumstances in which the coupling results in hybridization, and propose a strategy to ensure that such an event can be deliberately avoided. This will guarantee an optimal operation of SiN membranes.

3.3 Mode coupling in PnC membranes

As we saw in fig. 3.10 the difference in frequency between defect and edge modes can be small, and in fig. 3.15 we found a mode which appears as a linear superposition of D1 and VE1. If such a hybridization occurs in a physical sample the entire purpose of the PnC would be defeated: the resulting modes would present non-negligible displacement near the border of the membrane, reintroducing the dominant edge loss in $Q_{\mathtt{b}}$. In this section we begin by studying the coupling mechanisms between different modes to verify in which conditions these events can occur, and which measures can be taken to prevent them. Finally, we show that these mechanisms can be applied to fabricate multi-defect high-Q modes which are localized at two distant location simultaneously.

3.3.1 Coupling of lossy harmonic oscillators

Let us consider two modes which are coupled at some finite rate γ. We model them as coupled point masses. Let x_1 and x_2 denote the positions with respect to equilibrium of the two oscillators, and let their respective natural frequencies and the energy dissipation rates be $\Omega_{1,2}$ and $\Gamma_{1,2}$. The equations of motion of these two oscillators read

$$\ddot{x}_1(t) + \Gamma_1\dot{x}_1(t) + \Omega_1^2 x_1(t) + \gamma^2 x_2(t) = 0, \tag{3.34}$$
$$\ddot{x}_2(t) + \Gamma_2\dot{x}_2(t) + \Omega_2^2 x_2(t) + \gamma^2 x_1(t) = 0. \tag{3.35}$$

In the regime where $\Gamma_{1,2} \ll \gamma \ll \Omega_{1,2}$, the normal mode frequencies $\Omega_\pm$ can be

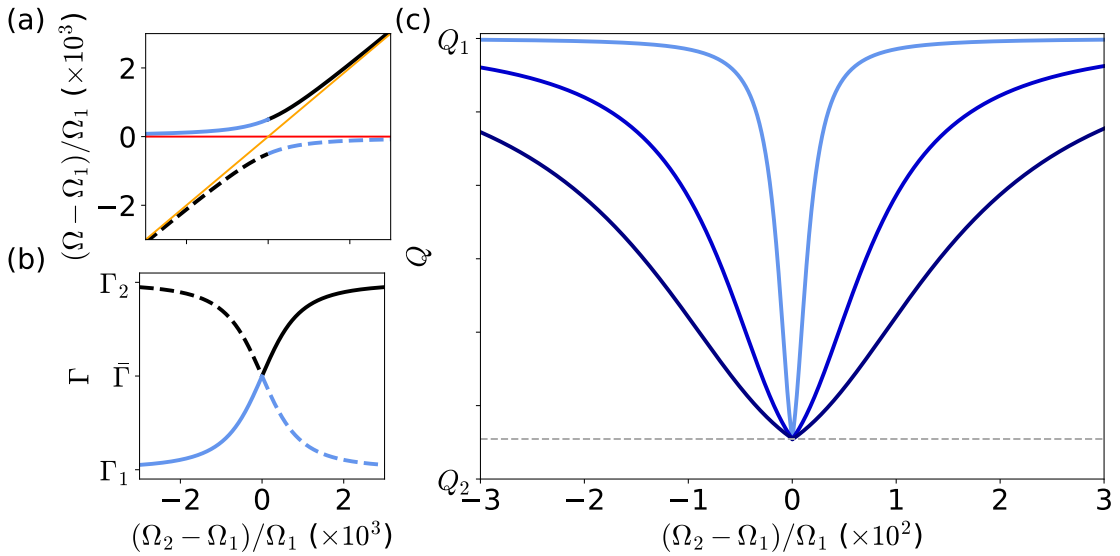

Figure 3.16: **a**, Variation of Ω_+ (full line) and Ω_- (dashed line) with respect to the detuning between the natural frequencies. The red and orange lines show $\Omega = \Omega_1$ and $\Omega = \Omega_2$, respectively. **b**, Similarly, variation of Γ_+ (full line) and Γ_- (dashed line). In blue, we show Ω_{sel} **(a)** and Γ_{sel} **(b)** for $\gamma/\Omega_1 = 10^{-3}$. **c**, Quality factor Q with respect to the detuning between the natural frequencies. From top to bottom, $\gamma/\Omega_1 = 10^{-3}$, 5×10^{-3}, and 10^{-2}. The dashed horizontal line indicates $\Omega_1/\bar{\Gamma}$.

written as

$$\Omega_{\pm}^2 = \frac{1}{2}\left(\Omega_1^2 + \Omega_2^2 \pm \sqrt{\left(\Omega_1^2 - \Omega_2^2\right)^2 + 4\gamma^4}\right). \tag{3.36}$$

See Appendix C for the derivation of this result. As simulated in section 3.3.2 and measured in chapter 4, $\Gamma_{1,2} \approx 10$ Hz and $\gamma > 1$ kHz. The variation of $\Omega_{\pm}$ with respect to the detuning between the natural frequencies in shown in fig. 3.16a.

Furthermore, we find in Appendix C that there are two possible regimes for the system depending on the relative magnitude of γ with respect to $|\Omega_1 - \Omega_2|$. When $\gamma^2 \gg |\Omega_1^2 - \Omega_2^2|$ we enter the small detuning regime and the modes become hybridized. In that case the energy is almost equally distributed between the two oscillators, and we must express the new normal modes in terms of a linear superposition of x_1 and x_2. In the basis $\{x_1, x_2\}$, the eigenvectors $\mathbf{x}_{\pm}$ read

$$\mathbf{x}_{\pm} \approx \frac{1}{\sqrt{2}}\begin{pmatrix}\pm 1\\ 1\end{pmatrix}. \tag{3.37}$$

Crucially, the dissipation rates $\Gamma_{\pm}$ of these hybridized mode are the same, and tend to the same average $\bar{\Gamma}$:

$$\lim_{(\Omega_1^2 - \Omega_2^2)/\gamma^2 \to 0} \Gamma_{\pm} = \bar{\Gamma} = \frac{1}{2}\left(\Gamma_1 + \Gamma_2\right), \tag{3.38}$$

Using the full expression for $\Gamma_{\pm}$, given in Appendix C and plotted in fig. 3.16b, we determine how the detuning between the defect and the edge mode affects losses, for various values of γ and assuming $\Gamma_1 < \Gamma_2$. We only consider the mode with the highest quality factor–in the limit of weak coupling, this is simply the defect mode. In fig. 3.16c we show how the quality factor Q can degrade by reducing the detuning between Ω_1 and Ω_2. We define the quality factor of the mode of interest as $Q = \Omega_{\mathsf{sel}}/\Gamma_{\mathsf{sel}}$, where Ω_{sel} and Γ_{sel} are its frequency and dissipation rate. The values of Ω_{sel} and Γ_{sel} are indicated in fig. 3.16a and b. The span over which the reduction in quality factor is significant increases with γ. Its minimum however does not, since it always tends to the limit of eq. (3.38). Thus, for any finite value of γ, when the detuning becomes sufficiently small, the modes hybridize and the coupling rate only affects the width of the dip.

With our damped harmonic oscillator model, we find that so long as there is a coupling rate $\gamma > 0$, normal modes can form and significantly degrade the quality factor of the highest-Q mode. This strong coupling only occurs when $\gamma^2 \gtrsim |\Omega_1^2 - \Omega_2^2|$. Regarding defect and edge modes, to quantify the magnitude of the hybridization problem, the coupling rate between the two must be extracted, to determine to which extent this parasitic effect can become a handicap. In the following we compute γ by numerical simulation and using the model derived here.

3.3.2 Numerical analysis of edge mode coupling

To extract the coupling rate γ between edge and defect modes by means of a numerical simulation, the frequency difference between the two must be varied. We accomplish this by varying the distance between the last row of holes of the PnC and the border of the membrane, i.e. the "margin" M of the membrane shown in fig. 3.17a. As M increases the size of the effective region in which edge modes are confined increases, lowering their frequency as shown in fig. 3.17b; conversely, the induced redistribution of static stress increases the stress in the defect region, thus raising the frequency of defect modes. We note that since a large amount of simulations were required to obtain these figures, the mesh was kept relatively coarse, resulting in a slight disagreement between the quality factor obtained here of $Q_{\mathsf{b}} \approx 10^7$ and the value quoted previously of 1.5×10^7. This discrepancy does not affect our conclusions for these results.

The presence of coupling between the modes is evidenced by the appearance of avoided crossings in the frequency. We conclude it to be at the origin of the unexpected variation in Q in fig. 3.15. We compute the coupling rate γ between D1 and the various nearby edge modes from these splittings. To do so, we assume that at the minimal distance between the frequencies at the avoided crossings, the frequency difference is equal to 2γ (cf. eq. (3.36)). The calculated values are given in table 3.2 and $\gamma/2\pi$ is always in the 4-12 kHz range, consistent with the findings of Ref. [4]. We note that crossings $5-7$ correspond to HEMs, which we see from fig. 3.17b to be more strongly influenced by variations in the margin that the VEMs.

Table 3.2: Estimated γ between the lowest frequency defect mode and the edge modes shown in fig. 3.17b, following the same mode indexing.

Mode index	$\gamma/2\pi$ (kHz)
0	5.4
1	4.1
2	6.2
3	8.6
4	11.5
5	4.7
6	5.0
7	5.9

The effect on the quality factor shown in fig. 3.17c is as predicted by the theory of coupled oscillators: the quality factor of D1 is strongly degraded at the avoided

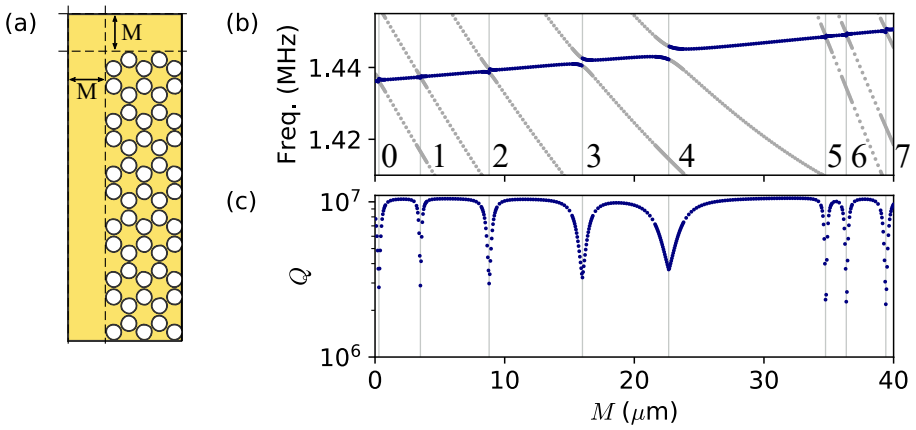

Figure 3.17: **a**, Illustration of part of a PnC membrane to illustrate the margin M. It is exaggerated here for clarity. **b**, As the margin M is increased the detuning between the defect mode frequency (shown in navy blue) and the edge mode frequencies (shown in gray) decreases. When the detuning becomes small with respect to the coupling rate, an avoided crossing can be observed, marked by the vertical gray lines numbered 0 to 7, in order of occurrence. **c**, At these crossing points the quality factor Q of the defect mode dips significantly. The figure is taken from Ivanov et al. [104]. The simulations were run with $\sigma_0 = 1$ GPa.

crossings. Since the edge mode quality factors are much lower that that of D1 at high stress, the quality factor of the resulting normal mode is essentially that of the edge modes.

To address this problem we suggest the following approach, which we proposed in Ref. [104]: "to maximize the defect mode Q, one could in principle fine-tune M to a specific value where the frequency difference between the defect mode and all VEMs is well above the coupling rate. This is a challenging and non-reproducible approach because of the high accuracy in M that is required, which exceeds the possibilities of the currently employed fabrication method [see chapter 4]. Furthermore, any off-centering of the PnC pattern with respect to the membrane window will multiply the number of edge modes as the symmetry is broken. Another option is to reduce the coupling between VEMs and the defect mode by increasing the size of the membrane, and, correspondingly, of the PnC. However, since the spectral density of edge modes is proportional to the membrane side length and the coupling never strictly cancels, the risk of hybridization scales poorly with the PnC size. For this reason, we suggest a third method, robust to errors in microfabrication, which will ensure reproducibly high quality factors for D1. Its principle is to engineer the frequencies of the VEMs to be far from that of D1, ensuring that even with micro-fabrication errors, they are always sufficiently separated." The modified membrane design we propose below is a way to bypass edge mode coupling problems.

3.3.3 Edge mode engineering

The second generation of membranes, illustrated in Fig. 3.18a, bypasses the problem of spectral crossings by engineering the frequencies of the VEMs. It possesses an "edge guard", i.e. its vertical borders are patterned with supplementary arrays of holes near the anti-nodes of the VEMs, to reduce their masses. This results in a shift toward higher frequencies of the VEMs, as shown in the simulated spectrum in Fig. 3.18b. As a result, D1 is no longer split into several peaks but appears as a single mode. Conversely, D2-D5 are spectrally adjacent to edge modes and do split–D4 and D5 are near the frequencies of HEMs, and are thus not influenced by the edge guard; they retain the same behavior as in our previous iteration of PnC membranes. We follow the same analysis as before to verify the properties of the edge guarded membrane.

First, we compute the dependence of the quality factor of D1 on the margin M. Since the VEMs are at higher frequencies, the first crossing event occurs at higher values of M in the second generation, as shown in fig. 3.18c. Accordingly, the quality factor of D1 is more robust to variations in M over a larger span, and for margins up to 25 μm, it remains at its maximal value (see fig. 3.18d). Note that the anti-crossings due to HEMs are still present at the same frequencies, as the edge guard does not affect them.

Next, the variation of the quality factor against the phononic shield length is computed, and we report our results in fig. 3.18e. As before we separate losses from the inner region and losses from the border or R3 region. From this data we find that the total quality factor is well fitted by the function:

$$Q_{\mathsf{b}}^{-1} = Q_{\mathsf{b,inner}}^{-1} + Q_0^{-1}\mathsf{e}^{-Cn_x}, \tag{3.39}$$

where n_x is the number of unit cells either side of the defect, and Q_0 and C are fit parameters. This heuristic equation is intended to be representative of the fact that edge losses become increasingly negligible with increasing n_x. From the fit we find $Q_{\mathsf{b,inner}} \approx 1.5 \times 10^7$, in agreement with our previous simulations, $Q_0 = 6.2 \times 10^5$, and $a = 0.47$ per unit cell. We furthermore verified that the dependence of Q_{b} on n_x was robust to variations in M, by repeating the simulation for $M = 10, 20, 30$ μm, producing good fits to eq. (3.39) with the same value for $Q_{\mathsf{b,inner}}$ each time.

We find from these tests that we recover the optimal quality of the soft-clamped PnC membrane, robust to micro-variations in the margin of the membrane. This robustness is required for the fabrication of PnC membranes because, as we discuss in the following chapter, the typical error in M makes it impossible to reproducibly fabricate a fist generation PnC membrane with high Q. We define our membrane side length based on these results: based on fig. 3.18c we choose $M = 20$ μm, and from fig. 3.18e we choose a PnC length of 17 unit cells. This ensures that we avoid edge mode coupling and are within 10% of the asymptotic value of $Q_{\mathsf{b,inner}}$. This

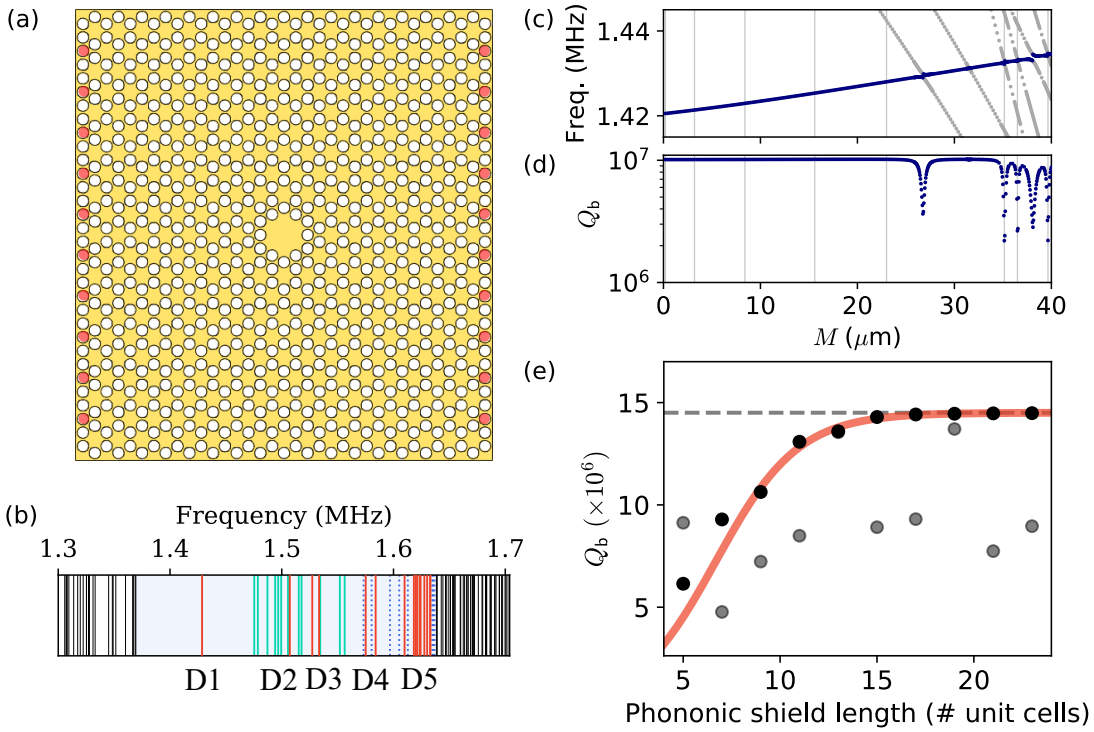

Figure 3.18: **a**, Illustration of an "edge guarded" membrane, featuring additional arrays of holes on the vertical sides of the membrane, colored in red. **b**, Spectrum of the second generation membrane. **c-d**, As we vary the margin M, we compute (**c**) the frequency and (**d**) the quality factor of the defect mode (in navy blue) and nearby edge modes (in light gray). These results, reproduced from Ref. [104], were computed with $\sigma_0 = 1$ GPa. The light gray vertical lines indicate the frequencies of the anti-crossing events in the absence of an edge guard. **e**, Estimated quality factor for varying length of the phononic shield. The red line represents a fit to the data with eq. (3.39), the black points are the computed data with edge guarding, the gray dashed line represents the fitted value for $Q_{\mathrm{b,inner}}$ using eq. (3.39), and the gray points are the computed data in the absence of an edge guard. For both simulations, $M = 30$ μm.

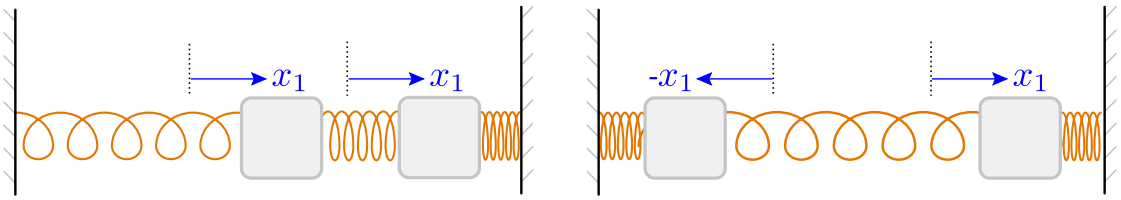

Figure 3.19: Schematic of the normal modes of two coupled spring masses. **(left)** The symmetric mode, and **(right)** the anti-symmetric mode.

results in a designed membrane size of 2.84 mm × 3.08 mm.

3.3.4 Double-defect membranes

Coupling dynamics have thus far been studied as a parasitic effect, which is detrimental to the reproducibility of high-Q PnC membranes. The flexibility of the PnC structure allows us to also draw a practical application from it: the embedding of identical defects within the PnC. Since two identical defects would the same spectrum of defect modes, coupling inevitably arises. In the small detuning regime, the modes would hybridize into symmetric and anti-symmetric normal modes which are delocalized over both defects. We can illustrate them in 1D for instance as in fig. 3.19. Crucially, these normal modes arise, in theory, even if the distance between the defects is large, as we found in section 3.3.1. Anti-symmetric mechanical modes have for example been used to couple to nonlinear circuit quantum electromechanics elements [16, 107] or to two photon cavities of different frequencies [33], or for scanning-force microscopy [5]. Having two distant antinodes can be practical, especially in hybrid systems where the samples must be protected from the probing beam; this is the case in electro-optomechanical systems for instance, where optical photons can be damaging to the superconducting circuity. To assess the practicality of this design, we numerically estimate the achievable coupling rates of the defect modes to gauge how close they must be to each other for significant mode hybridization to occur. The simulations which we did here were closely followed by a more detailed study published by the Schliesser Lab [4].

Here, we only focus on D1 modes: let $D1^+$ be their symmetric hybridization, and $D1^-$ the anti-symmetric hybridization, shown in fig. 3.20a. We create a distance between the two defects by displacing them in opposite directions along the $x-$axis of an edge guarded PnC membrane, as shown in fig. 3.20b. Note that there are two distinct configurations. For a distance corresponding to an odd number of unit cells, the system has a mirror symmetry. If that number is even, the symmetry is broken. For each separation distance we numerically extract the displacement profile and the frequency of $D1^+$ and $D1^-$ (shown in fig. 3.20c). Interestingly, the frequency can switch signs. We attribute this behavior to a phase flip of π of the coupling rate

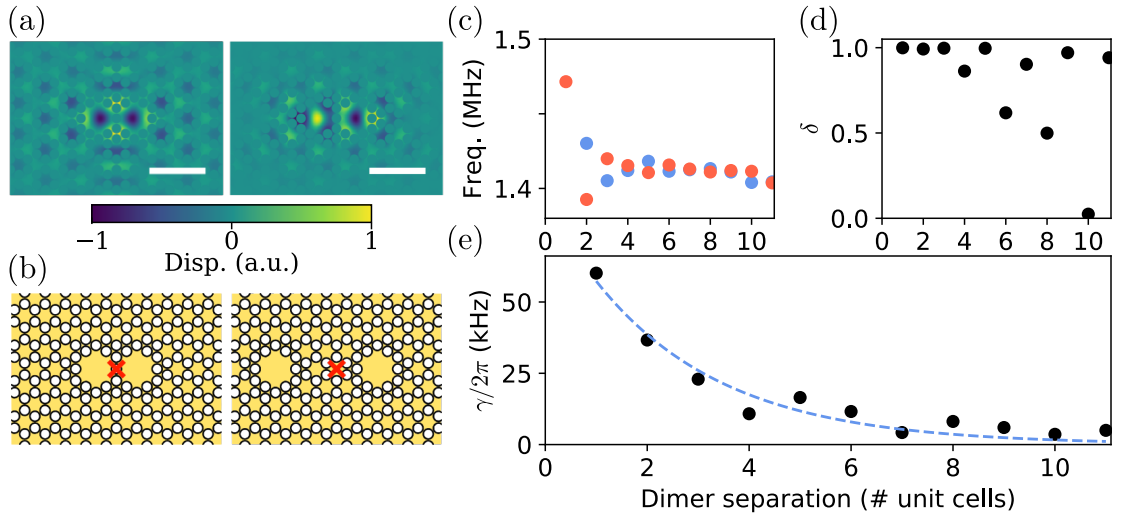

Figure 3.20: **a**, Simulated mode profiles of the D1$^+$ (left) and the D1$^-$ (right) modes. The white scale bars are 0.5 mm. **b**, Illustration of two possible configurations for the defects. The separation can be equivalent to an odd number of unit cells, shown left, with a separation of 1 unit cell. Alternatively, the separation can be even, shown right with a separation of 4 unit cells. In the latter case, the symmetry is broken, and the center of the membrane is indicated by a red cross. The membrane, with a total length of 17 unit cells, is here only shown partially. **c**, Frequency (Freq.) of the D1$^+$ (blue) and D1$^-$ (red) modes for varying dimer separation distances. **d**, Relative displacement of the center of the right defect with respect to the left defect, for D1$^+$. **e**, Extracted coupling rate γ , with an exponential fit to guide the eye (dashed blue line).

as the mode profile overlaps are varied. The file used for these simulations can be accessed in Ref. [83][12]. Let x_1 be the displacement at the center of the left defect, and x_2 the displacement at the center of the right defect. We quantify the hybridization of the D1 mode with the relative displacement δ of D1$^+$ at the center of one of the defects, compared to the other one. Let $\delta \equiv \min(x_1/x_2, x_2/x_1)$, which is plotted in fig. 3.20d. For even separations where the symmetry is broken, δ significantly dips. Still, even for a distance of 11 unit cells $\delta > 0.9$. This confirms the possibility of producing low-mass, high-Q hybridized modes with their two antinodes separated by several millimeters, in accordance with the findings of [4].

From this data the coupling rate can be determined: from eqs. (C.7) and (C.9), it can be shown that γ satisfies the equation

$$2\gamma^2\delta = |\Omega_+^2 - \Omega_-^2| - \sqrt{|\Omega_+^2 - \Omega_-^2|^2 - 4\gamma^2}, \tag{3.40}$$

[12]Found under the filename "SiN_PnC_Membrane_dimer.m'.

where Ω_+ and Ω_- are the frequencies of $D1^+$ and $D1^-$, respectively. This equation can be numerically solved, and we have employed the Newton method for doing so. The extracted values of γ are shown in fig. 3.20e, from which we find that for the lowest distance $\gamma/2\pi \approx 60$ kHz. The coupling rate as a function of distance is well described by an exponentially decreasing function.

3.4 Concluding remarks

In summary, we have verified the dependence of the key parameters of SiN nanomembranes, the Qf-product and the minimal value of n_{eff}, with the membrane geometry. To do so, we first described the main dissipation channels of loss in such resonators, namely bending and radiation loss. We have found that a plain SiN membrane is not an ideal mechanical resonator for a cryogenic sideband cooling experiment due to a poor scaling of the key parameters. The main limiting factor was found to be the hard-clamping condition, which induces a strong bending of the mode profile at the resonator borders and causes significant energy dissipation. We thus turned to an alternative approach: mode shape engineering, through which states of motion can be localized to a central defect embedded within a phononic crystal. In this manner, the hard-clamping condition was softened, and the resulting defect mode of interest was predicted to benefit from a tenfold increase of its Qf-product, for typical sample parameters. Furthermore, we checked that the scaling of Q for defect modes was more favorable with the dissipation dilution factor Λ than for plain membranes. As a result, Q can be increased by reducing the membrane thickness h, potentially increasing Qf by another factor 10. At those extreme aspect ratios, n_{eff} is also expected to decrease by up to a factor 100.

However, these improvements are limited by the fact that due to finite-size effects, spurious hard-clamped modes arise and can couple to the defect modes, thereby negating the benefit of the phononic crystal. We found that by engineering the frequencies of the parasitic edge modes with an "edge guard", such hybridization issues could be altogether bypassed, and we could ensure the defect modes remain softly clamped.

Finally, the possibility of mode coupling in a PnC membrane is taken advantage of for alternative membrane designs [4] to generate hybridized soft clamped modes. The two antinodes of the hybrid modes can be separated in a controlled manner over almost a millimeter The various PnC membrane designs presented and analyzed in this chapter were fabricated in our group, and the following chapter presents the characterization of those samples and the main conclusions we could draw from them.

Chapter 4

Membrane fabrication and characterization

In this chapter we present the fabrication and characterization of phononic crystal (PnC) membranes, introduced in chapter 3. They are distinguished from plain membranes by the addition of a hexagonal lattice of holes. This gives rise to a spectral band-gap, and when a geometrical defect is added to the PnC structure, to localized states of motion.

A large part of the work done during this thesis has been to develop a fabrication protocol for PnC membranes. Despite having been fabricated in the Schliesser Laboratory prior to this work [24], the transfer of recipes is seldom a trivial task. In addition, the LKB has historically little cleanroom fabrication expertise, requiring us to effectively work from scratch to develop the recipe. Section 4.1 summarizes this experience, presenting the main difficulties and success criteria for releasing PnC membranes. The limits to the fabrication precision are also emphasized, discussing to which extent they determine the reproducibility of high-Q defect modes.

To measure the properties of PnC membranes, there are different possible approaches. In chapters 1 and 2, we have described how to characterize a plain membrane by coupling it to a microwave circuit. In principle the same method could be applied to PnC membranes. However, the electromechanical device can only be characterized below 300 mK, which is prohibitively time-consuming: from its fabrication to its characterization, each device would require several days of work. This makes it cumbersome to incrementally vary the designs, as is often required when developing a fabrication procedure. Furthermore, we are here only interested in the properties of PnC membranes, which are the main topic of this chapter. Room temperature measurements are sufficient to obtain the necessary information. Section 4.2 presents an optical interferometry setup built during the course of this thesis. It is used for characterizing membranes accurately and conveniently. Three experiments are used to obtain the necessary information: the measurements of thermal spectra of the various modes, of their profiles, and of their quality factor.

Section 4.3 describes the methods used to perform these experiments.

In the analysis of chapter 3 we showed how a PnC structure could result in a spectral band-gap and in a set of localized high-Q defect modes. We further noted how due to finite-size effects, another set of localized modes we called edge modes arose, which could significantly degrade the quality factor of the defect modes. We proposed that the parasitic effects of the vertical edge modes (VEMs) could be negated by the implementation of an "edge guard": an additional array of holes placed along the vertical borders of the membrane. Section 4.4 verifies that the measured properties of the PnC membranes agree with our simulations. Due to fabrication micro-errors, defect and edge mode coupling is not expected to be a systematic effect. Rather, we expect to observe it as a reduction of the average defect mode quality factor. Several membranes of both types, with and without the edge guard, are measured to determine the net benefit of the edge guard.

As a practical application of mode coupling effects through the PnC, as in Ref. [4], we studied in the previous chapter how two localized defect states could become coupled to one another. We found that coupling rates as high as 60 kHz could be obtained. In such systems hybridized states could be formed even when the PnC defects were separated by approximately 2 mm. Section 4.5 presents these dimer membranes.

Section 4.6 review the results of this chapter.

4.1 Fabrication procedure

The addition of the PnC holes to the silicon nitride (SiN) membranes presents a significant challenge from a fabrication standpoint. It resulted in what would become more than a year of work to converge onto a recipe which could yield clean, high-Q membranes. In this section, we present our fabrication procedure for these PnC nanomembranes. We highlight in particular the lessons we drew from the (many) failed attempts and the essential steps we found necessary to obtain a fabrication yield of about 50%.

4.1.1 Wafer details

The samples presented in this work are fabricated from 4-inch Si wafers purchased from Si-Mat [108]. Nova [109] and Sil'Tronix [110] wafers were also bought at the start of this thesis for comparative tests, but eventually Si-Mat wafers were kept throughout for consistency. The surface of the wafers is parallel to the (100) crystal plane and is polished to ensure low roughness. On both sides of the wafers a thin layer layer of SiN is deposited by Si-Mat by low-pressure chemical vapor deposition (LPCVD). The Si substrate has a thickness of approximately 525 ± 25 μm and a resistivity superior to 10 kΩ.cm, while the SiN thickness is approximately 100 nm.

Tensile stress is generated during the LPCVD of SiN by using the difference in thermal expansion coefficients between SiN and Si to strain the former. Using this method, the maximally achievable stress is around 1.4 GPa. In this case it was specified to exceed 0.8 GPa.

4.1.2 Releasing free-standing PnC membranes

The fabrication of plain membranes is a procedure requiring only common cleanroom equipment. While they can be fragile, with sufficient experience one can obtain a yield so reproducibly close to unity that SiN membranes have become commerically available [21]. In our group, such membranes could be readily fabricated even prior to this thesis. While PnC membranes present significant challenges, and their fabrication requires a more sophisticated setup (detailed in the following section), the main fabrication steps remain generally speaking the same:

1. (Figure 4.1a) The wafers are diced into 3 cm × 3 cm chips for convenient handling, enabling the simultaneous fabrication of up to 9 membranes. The fabrication thus begins with a diced chip of Si coated with SiN on both sides. For further reference we define the side of the chip on which the membrane will lie as the "frontside", and the other one as the "backside".

2. (Figure 4.1b) A square of SiN is removed on the backside by UV lithography. This procedure involves coating the SiN with a photosensitive resist, can be removed by a developed if insolated with UV light. A focused laser beam is scanned over the chip's surface to recreate the design shown in fig. 4.1e (additional grooves are added to the chip for subsequent cleaving into smaller chips). The photoresist is developed, and the pattern is transferred to the SiN by etching the exposed part through reactive ion etching (RIE).

3. (Figure 4.1c, for PnC membranes only) The frontside is patterned with the PnC structure shown in fig. 4.1f by UV lithography .

4. (Figure 4.1d) A free-standing membrane is released on the fontside by etching the substrate through the backside. This is done in a hot potassium hydroxide (KOH) bath (see section 4.1.3). SiN is not etched by KOH, allowing it to act as a hard mask.

For a more detailed step-by-step fabrication procedures of plain and PnC membranes see Appendix D.

Steps 3 and 4 in particular present some challenges when fabricating PnC membranes because of their increased fragility. Below, we specify some additional details of the fabrication. Without taking them into consideration, it was found impossible to successfully and reproducibly release PnC membranes.

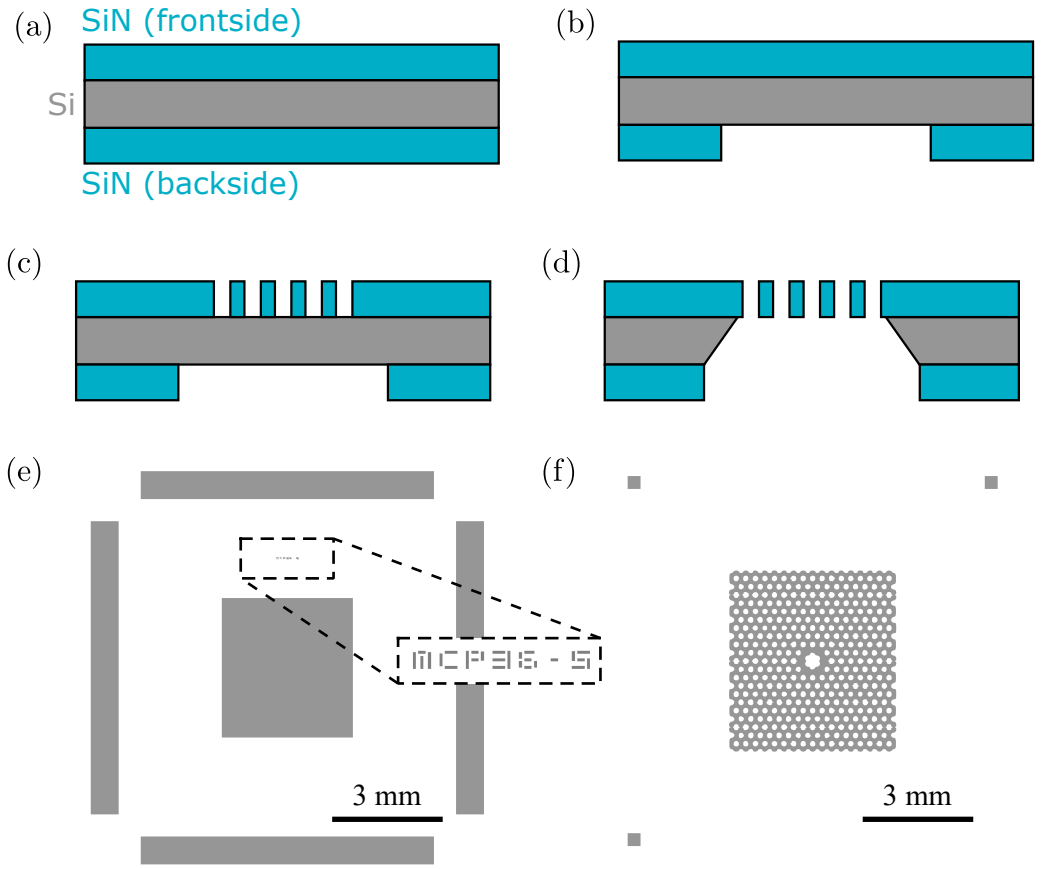

Figure 4.1: **a**, Illustrated side view of a typical Si chip used in fabrication. On both the "frontside" and the "backside" of it, a thin layer of SiN is deposited. The drawing is not to scale. **b**, After the RIE a window into the backside SiN is etched. **c**, For PnC membranes the frontside SiN is additionally patterned with the PnC structure by UV lithography and RIE. **d**, Plane cut illustration of a fully released PnC membrane. **e**, Illustration of the backside lithography pattern, featuring a central rectangle which will form the membrane, surrounding rectangles for cleaving grooves (not shown in **(b)**), and a label to ensure correct orientation. Inset is a zoom on the label. **f**, Illustration of the frontside lithography pattern, featuring the PnC with a defect and alignment squares. The alignment squares are to be used in electromechanical experiments.

4.1.3 Additional fabrication details

Frontside PnC pattern

An intuitive approach to fabricating PnC membranes could have been to structure a pre-released membrane with the array of holes, i.e. to follow the fabrication steps above in the order 1-2-4-3. In a paper published previously in our group [111] a similar procedure was successfully performed to partially pattern a pre-released SiN membrane with a photonic crystal of 300 nm holes by RIE (100 times smaller than the PnC holes). However, the samples in that work were fabricated at the C2N cleanroom, which was closed for the duration of this thesis. We attempted to reproduce the recipe in our own cleanroom as a first attempt, but this proved unsuccessful and the integrity of the membranes could not be preserved. One reason for this failed attempt may have been that we were not able to reproduce the fabrication parameters exactly as the machines were different. We therefore pattern the frontside with the PnC before the release, following the recipe of [24] based on which other groups fabricate PnC membranes as well [25, 112].

Anisotropic substrate etch

The etching of Si in liquid KOH is anisotropic: it is etched 400 times faster along the (100) crystal plane than along the (111)-plane [113]. We therefore select the substrate surface to be parallel to the (100) plane, ensuring that the net etch direction is normal to the surface. Due to the anisotropic etch the resulting Si block has a trapezoidal shape with a 54.7° angle between the (100) and the (111) planes, illustrated in fig. 4.2a.

In a bath of hot KOH diluted to a concentration of approximately 30% with deionized water and heated to 85°C, Si is etched at approximately 80 μm per hour. We measured the etch rate by using a profilometer by determining the depth of the etch after a few hours in the bath. During most of the KOH etch, the liquid is homogenized with a magnetic stirrer to minimize temperature and concentration gradients. We found that failing to do so would result in an asynchronous membrane release.

To ensure that only the backside of the substrate is etched by the KOH while avoiding its edges and fronstide, a Polytetrafluoroethylene (PTFE) holder is used, as shown in fig. 4.2b, sealing the chip with two stages of rubber O-rings. The edges are protected by the outermost O-ring, and the frontside is protected by rubber bands directly in contact with the chip, as shown in fig. 4.2c. A hole in the holder allows the KOH to etch the backside. As discussed below, some problems arose with such a holder which have led to a slight modification of the etching configuration.

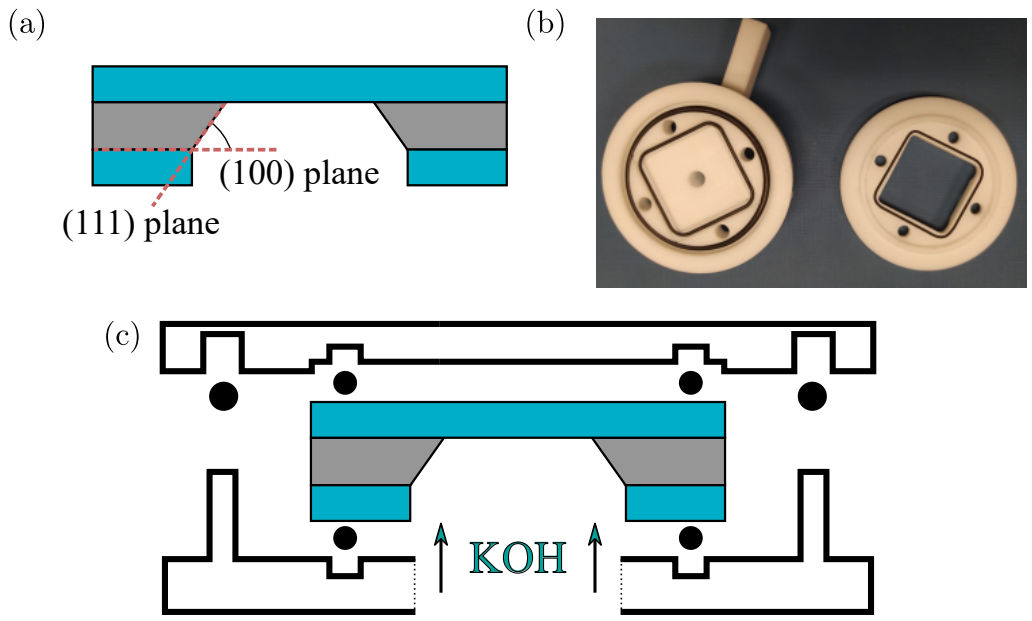

Figure 4.2: **a**, Plane cut illustration of a plain membrane indicating the (100) and the (111) etching planes. The angle between the two planes is 54.7°. **b**, Photograph of the PTFE holder used for etching plan SiN membranes. The lid is on the right. Black rubber bands ensure water-tightness at several stages. **c**, Schematic cross-section of the PTFE holder. The rubber bands are indicated as black circles. At the backside of the chip, a hole in the holder allows the KOH to etch the Si.

Holder troubles

Because of the elasticity of PTFE the holder warps over time, creating leaks which allow the KOH to reach the frontside. Interrupting the etch prematurely (after less than an hour) reveals that is this happens, the KOH etches the frontside Si as evidenced by the black marks shown in fig. 4.3a. After allowing the etch to reach near completion in such a case, we found that the membrane became released on both sides simultaneously. This resulted in a non-uniform etching front, shown in fig. 4.3b. This would eventually give rise to long isolated strips of Si which remained attached to the SiN (fig. 4.3c), parallel to which the latter would preferentially tear. In dozens of fabrication attempts we have never observed a case where this frontside etching successfully released a membrane[1]. We hypothesize that the reason for this is that the partial etching of the frontside Si releases some areas of the SiN before the rest. This redistributes the stress such that it locally exceeds the yield stress of SiN, tearing the membrane upon release.

When this problem is addressed by fabricating a new holder, a different problem arises: air pockets form between the chip and the holder, from which bubbles of air can escape and rupture the membranes, significantly reducing the yield. This happens in the span of a few seconds. Figure 4.3d-f show three snapshots of such an event. To prevent this the pressure conditions on both sides of the wafer need to be controlled to prevent any in- or outflow of liquid or air. An air channel can be installed in the PTFE holder to do so, maintaining an atmospheric pressure within the air chamber–this solution is seen in some commercial holders for thin-film release [114].

However, to avoid these issues altogether, we ultimately decided to etch the membranes by immersing them freely in the KOH bath without any particular PTFE protection of the frontside from the liquid. To do so, we coat the frontside with a resin called ProTEK PSB, marketed as a "spin-on replacement for silicon nitride or silicon oxide wet etch masks" [115]. The ProTEK plays the role of a hard mask during the KOH etch and is applied uniformly to the frontside prior to the wet etch. This coating is removed at the end of the fabrication procedure in a Piranha solution, a mixture of sulfuric acid and hydrogen peroxide. We note that Brewer, the provider for ProTEK, sells a removing agent for the coating but it could not be obtained in Europe.

We designed a new PTFE holder for this procedure, shown in fig. 4.4, intended only to prop the chip vertically with a set of v-grooves cut into the holder. The chips are kept upright to minimize viscous drag normal to the membranes as the holder is immersed into or removed from a bath. The sample chips are thus never removed from the holder prior to the end of the fabrication. A PTFE screw keeps

[1]Some PnC membrane release procedures do employ frontside etching [112], but this requires several phases of etching to ensure that only the last few μm of Si are etched through the frontside, and is not employed here.

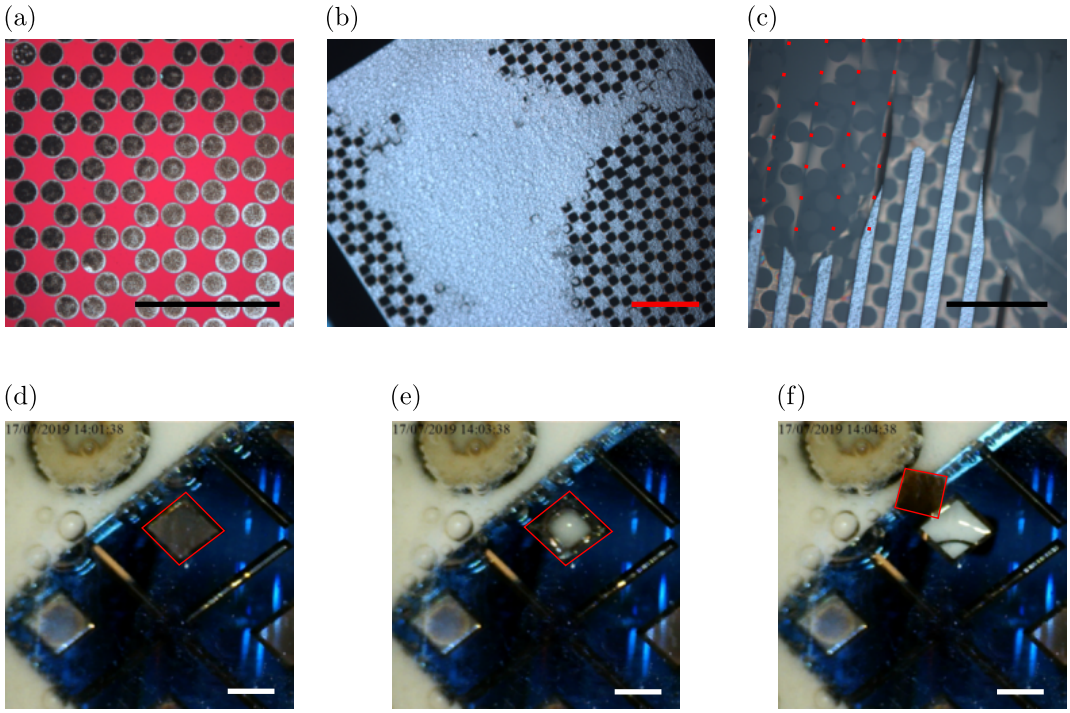

Figure 4.3: **a**, Frontside optical micrograph of a membrane after a prematurely interrupted etch. The Si surface, normally a reflective gray (as in the bottom right corner of the image) turns granular and black if the holder is not sufficiently waterproof. **b**, Backside optical micrograph of the etching front shortly before release. Non-uniformity is apparent and the openings at the PnC holes are evidence of frontside etching. **c**, Optical micrograph of a backside view of the etching front, at a later time than **(b)**. The Si remains attached to the SiN in long thin parallel stripes, along which the SiN preferentially tears. The most prominent tearing axes are highlighted with the red dotted lines. For **(a)-(c)**, the scale bar is 0.5 mm. **d-f**, Snapshots taken during a KOH etch of the backside of the sample chip. The partially etched membrane of interest is bordered with a red line in all pictures, showing how, within a few seconds a bubble escapes from its center and tears it away. The scale bars are approximately 3 mm.

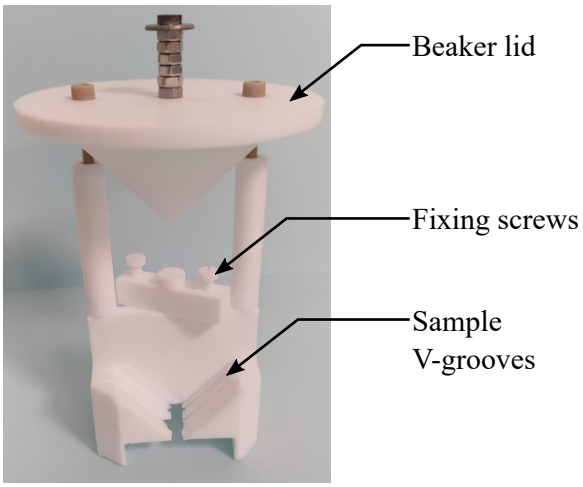

Figure 4.4: Photograph of the vertical sample holder. The samples are held upright by v-grooves, and fixed in place by a screw on the top.

the chips in place to prevent them from floating off due to the effervescence of KOH or piranha. A PTFE lid prevents the excessive evaporation of KOH. Note that the use of PTFE is necessary as it reacts neither with the strong bases (KOH) nor the acids (Piranha solution) involved in this fabrication procedure.

PnC membrane yield

A positive result is considered as a membrane with absolutely no tears. If as little as a single tether was torn, the sample was discarded. With the recipe provided here a yield of about 45% could be obtained–we note that due to the fragility of the membranes, there is a certain dependence on the experience of the manipulator. In fig. 4.5 we show the final product: PnC membranes made from SiN, both with and without an edge guard. In this chapter these two membrane designs will be primarily studied, changing only the configuration of the central defects in section 4.5. For further reference we will call the design shown on the left of fig. 4.5 a "generation 1" membrane, and the other one (with an edge guard) a "generation 2" membrane.

Estimated uncertainty in the geometrical parameters

Three parameters are systematically verified for which a good control is necessary: the lattice parameter b, the hole size r, and the membrane margin M (defined as the shortest distance from the outermost hole in the PnC to the border of the membrane). Errors in b and r originate solely from the laser lithography machine. A preliminary calibration was run to account for over-development. When correcting for this, a precision to less than 0.5 μm could be obtained in b and r.

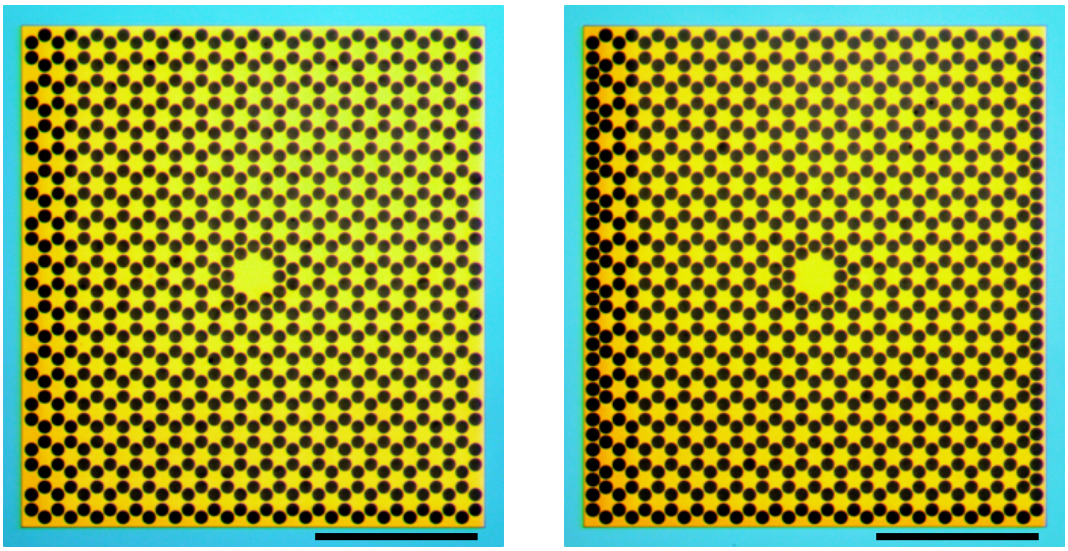

Figure 4.5: Optical micrographs of fabricated SiN membranes, structured with a hexagonal lattice PnC. **(Left)** The membrane has no additionnal patterning on its vertical edges, contrary to **(Right)**, where a series of holes is added.

On the other hand M is determined by two principal factors: the size of the membrane itself and the centering of the PnC structure within the membrane. Due to the etching angle during the etching of the KOH, any error in the estimation of the membrane thickness results in an error of the membrane size. Furthermore, a typical error of approximately 2 μm is found in the centering of the pattern, with an overall measured imprecision in M of approximately 5 μm. After these characterizations, the mechanical properties of the samples are measured in an optical interferometer.

4.2 Experimental Setup

An optical interferometry setup was developed over the course of this thesis, which needed to meet a series of requirements necessary for the complete characterization of PnC membranes:

1. **Vacuum**: The membranes must be placed in vacuum to ensure that residual gas damping does not significantly reduce the mode Q. The influence of pressure on Q is discussed further in section 4.4.3.

2. **Interferometer**: As derived in chapter 1, the detection must be shot-noise limited, i.e. the measured classical noise must be significantly lower than its quantum fluctuations. This is crucial for resolving the thermal motion of the membrane with high signal-to-noise and for measuring a mode's displacement profile (see section 4.4.2).

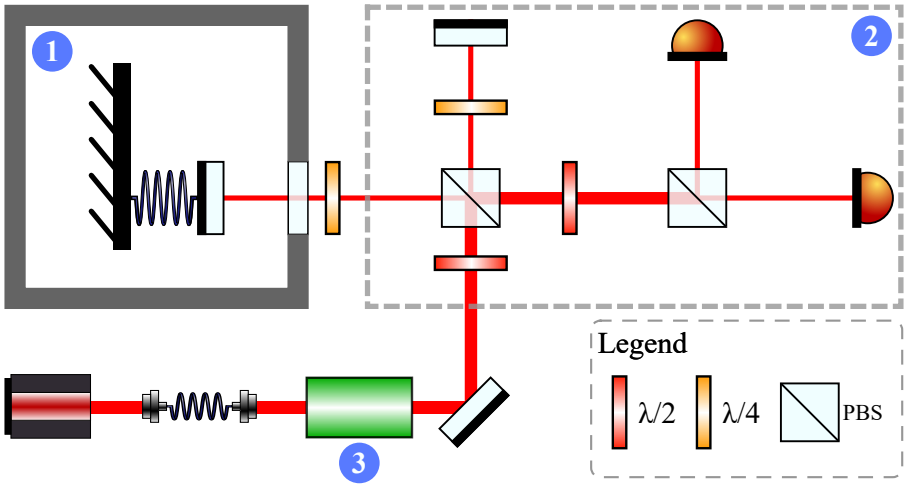

Figure 4.6: Schematic representation of the interferometer used in this work, comprising three main indicated parts: 1. the vacuum chamber in which the sample lies, 2. the interferometer stage, and 3. the laser intensity modulation stage.

In addition, the setup must allow for the measurement of more than one membrane without opening the vacuum chamber. Cycling the vacuum takes a significant amount of time and degrades the membrane performance. Several membranes are therefore fabricated on one chip in batches of up to 9 (varying with the yield). In practice, it must thus be possible cover a surface greater than 20 mm $\times$ 20 mm by sweeping the laser position.

3. **Mode driving**: A precise method for measuring the Q of a mechanical mode is the ringdown measurement (as shown in chapter 2). A resonant driving of the membrane modes is required for this.

Based on these considerations, we built the optical setup illustrated in fig. 4.6. It comprises three main parts: the vacuum chamber (discussed in section 4.2.1), the interferometer stage (section 4.2.2), and the laser intensity modulation stage (section 4.2.3). In the following, the important details concerning these three essential parts and how they address the requirements listed above, are discussed.

4.2.1 The vacuum chamber

The vacuum chamber consists of a simple aluminium cylinder with an optical viewport, illustrated in fig. 4.7a. Originally, the vacuum was formed by a single pumping bank consisting of a primary pump and a turbomolecular (turbo) pump. The pressure in this system can be reduced to less than 10^{-5} mbar in two steps: the primary pump first reduces the pressure to approximately 10^{-2} mbar, at which point the

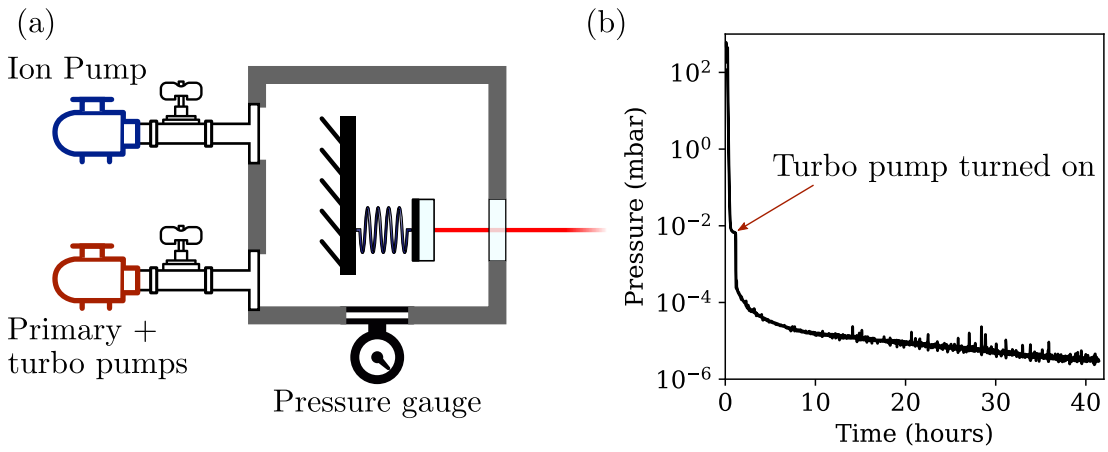

Figure 4.7: **a**, Schematic representation of the vacuum system, pumped in parallel by a primary and turbomolecular (turbo) pump bank, and an ion pump. The red beam indicates the optical access of the chamber to the sample. *Pump icon made by Freepik from www.flaticon.com.* **b**, Pressure evolution in a typical pumping cycle using only the primary and turbo pumps.

turbo pump is activated, further reducing the pressure. As seen in fig. 4.7b, reaching the necessary vacuum for measuring PnC membranes (see section 4.4.3) took up to two days of continuous pumping.

Furthermore, the turbo pump was suspected to be a significant source of mechanical noise. To prevent it from degrading the precision of our measurement, an additional vibrationless ion pump (Agilent Vaclon Plus 40 L/s, Diode) was installed. Ultimately, the turbo pump was not found to be problematic in terms of noise, but the ion pump was nevertheless kept as it significantly accelerated the pumping process. With this, pressures as low as 10^{-6} mbar could be reached by pumping overnight and samples could be characterized in rapid succession. We note that these pressures correspond to the upper boundaries of the ion pump's working range, significantly reducing its lifetime.

Thus, this vacuum setup successfully satisfies the first requirement of the system. However, it adds a complication: the translation stages required to scan an area of 20 mm$\times$ 20 mm take up much more space than available inside the vacuum chamber, making it impossible to move the samples themselves. Furthermore, it is difficult to displace the chamber as a whole, as it is heavy and rigidly connected to the ion pump (the latter condition is necessary for maximizing the pumping power). We thus take the approach of displacing the laser spot itself by setting the interferometer on a translation stage.

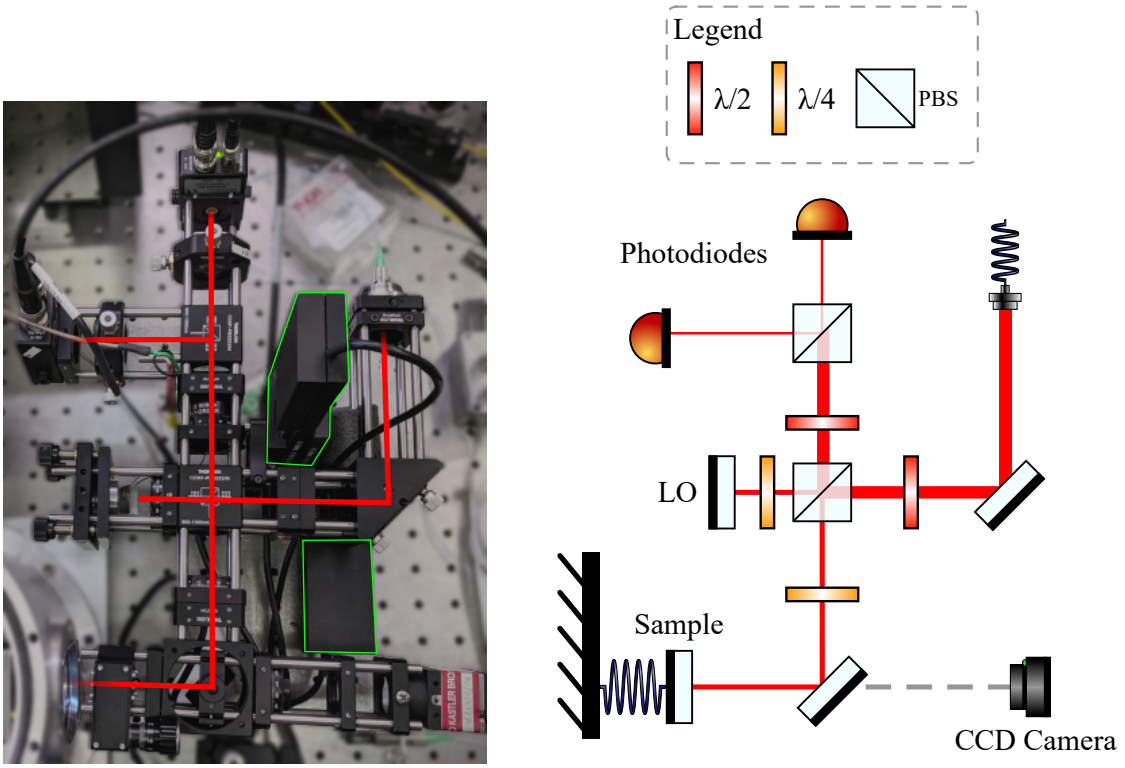

Figure 4.8: **(left)** Photograph of the monolithic interferometer. The beam path in drawn in red, and the visible parts of the translation stages are contoured in green. **(right)** Schematic representation of the interferometer shown left. Lenses have been omitted for clarity. Although this setup looks very similar to a Michelson interferometer, it can be shown to be formally equivalent to a Mach-Zehnder due to the $\lambda/4$ plates in front of the sample and the LO.

4.2.2 A shot-noise limited optical interferometer

Monolithic translation

If the interferometer is to be displaced as a whole, particular care must be taken to prevent the loss of the laser alignment. It was therefore constructed monolithically in a Thorlabs [116] cage system shown in fig. 4.8. The cage is held by a set of translation stages (Newport M-426 with LTA-HL actuator) which can displace the laser spot over up to 25 mm $\times$ 25 mm–these can be controlled remotely, for automatic data acquisition. To prevent excessive torque, the interferometer was designed to have its center to gravity placed as near to the translation stages as possible (see fig. 4.8). Note that since it is impossible to access the sample holder once the vacuum chamber is sealed, it is ensured that almost all alignment degrees of freedom for the optical path can be adjusted from the interferometer itself.

The setup shown here is formally identical to the Mach-Zehnder interferometer

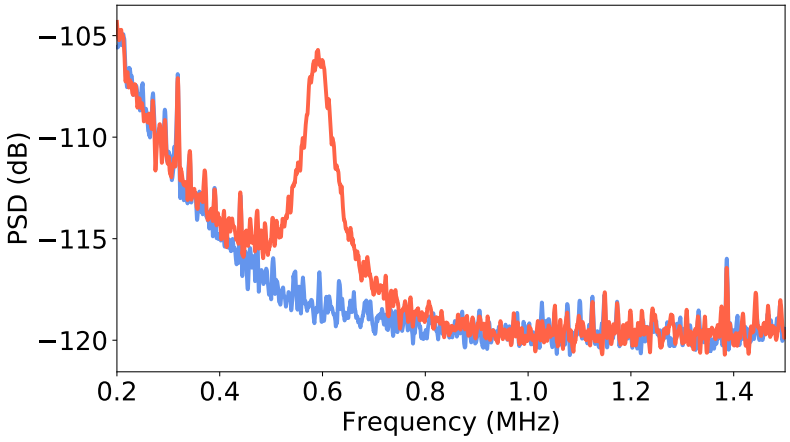

Figure 4.9: PSD of the laser noise with the noise eater off (red) and on (blue).

discussed in chapter 1, with the addition of a second photodiode at its output.

Balanced homodyne detection theory

At the output of the final beam splitter (BS) of a Mach-Zehnder interferometer, we showed in chapter 1 (section 1.2.2) that the spectrum of the laser power measured by the photodiode varies linearly with the position noise spectrum $\bar{S}_{xx}$ of the sample. Ultimately, we predicted that a shot-noise limited detection could readily resolve the mechanical noise peak with a signal-to-noise ratio $SNR \approx 45$ dB.

In this work, we use a Nd:YAG laser with a wavelength of 1064 nm. Bypassing the interferometer, we first characterize the power spectral density (PSD) of the laser, shown in fig. 4.9. We find a peak exceeding the noise floor by over 20 dB around 600 kHz, whose origin we attribute to relaxation oscillations of the laser. The laser itself has a noise eater feature which reduces this noise peak significantly. For the following the noise eater is in fact deactivated in order to have a clear classical noise source for reference.

To prevent a reduction in the *SNR* due to classical noise, a "balanced detection" scheme is used. It consists in rejecting the amplitude noise of the laser by exploiting the correlations that are maintained throughout the beam path. To do so, the light intensity from both output branches of the BS must be measured, as shown in fig. 4.8. As in chapter 1, a half-wave plate is added before the first polarizing beam splitter (PBS), to allow us to select the amount of power headed toward the sample.

It can be shown that the experimental scheme is formally equivalent to the Mach-Zehnder interferometer illustrated in fig. 4.10. In the following analysis both output branches of the final PBS are considered, labeled + and −. Their respective light

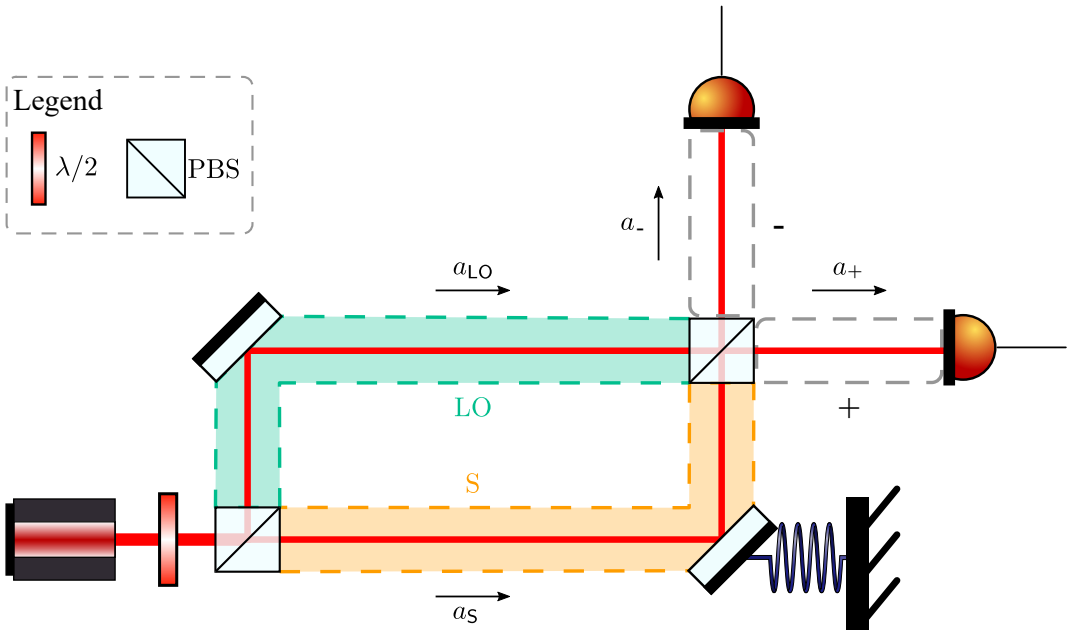

Figure 4.10: Schematic representation of a balanced homodyne detection, simplified to a Mach-Zehnder interferometer.

fields a_+ and a_- read

$$a_\pm(t) = \frac{1}{\sqrt{2}}\left(a_{\mathsf{LO}}(t) \pm a_{\mathsf{S}}(t)\mathrm{e}^{i\varphi}\right). \tag{4.1}$$

Note that $a_+ \equiv a_{\mathsf{PD}}$ as defined in chapter 1. To ensure the detection is maximally sensitive to mechanically-induced phase fluctuations, the static phase difference between the S and LO branches is kept at a half-integer multiple of pi. This is done by fixing the LO end mirror to a piezo-electric transducer (PZT). The static phase is thus locked around $\varphi \approx \pi/2$ with a feedback loop.

Similarly to the derivation in chapter 1 we find that the fluctuations of the light power $\delta P_\pm = \hbar\omega_{\mathsf{L}}\left(|a_\pm|^2 - \langle|a_\pm|^2\rangle\right)$ at the photodiodes read

$$\begin{aligned}\delta P_\pm[\Omega] \approx \pm P_0 p_{\mathsf{S}} p_{\mathsf{LO}} \frac{4\pi}{\lambda} x[\Omega] + \\ \sqrt{\hbar\omega_{\mathsf{L}} P_0}\left[\left(p_{\mathsf{LO}}\delta a^P_{\mathsf{LO}}[\Omega] + p_{\mathsf{S}}\delta a^P_{\mathsf{S}}[\Omega]\right) \pm \boxed{\left(p_{\mathsf{S}}\delta a^Q_{\mathsf{LO}}[\Omega] - p_{\mathsf{LO}}\delta a^Q_{\mathsf{S}}[\Omega]\right)}\right],\end{aligned} \tag{4.2}$$

where x denotes the fluctuations of the mechanical mode around its equilibrium position, δa^P and δa^Q are the fluctuations in the amplitude and phase quadratures of the fields in the LO and S branches (as indexed), ω_{L} is the laser angular frequency, and P_0 is the laser power at the input of the interferometer.

At this stage, to fully understand the contribution of noise to the signal, the field fluctuations must be expressed in terms of their classical and quantum components. Importantly, the classical noise of all field terms is correlated because it originates from the same laser noise. It therefore scales with the laser power of the corresponding branch. On the other hand, the quantum noises are uncorrelated; To express this, we write the quadrature fluctuation terms in general as:

$$\delta a^{P/Q}_{\mathsf{S/LO}}[\Omega] = \sqrt{P_0} p_{\mathsf{S/LO}} \delta a^{P/Q}_{\mathsf{class}}[\Omega] + \delta a^{P/Q}_{\mathsf{q,S/LO}}[\Omega], \tag{4.3}$$

where $\delta a^{P/Q}_{\mathsf{class}}$, of spectrum $\bar{S}^{P/Q}_{\mathsf{class}}$, is the classical field amplitude noise (common to S and LO) and $\delta a^{Q/P}_{\mathsf{q,S/LO}}$, of spectrum $\bar{S}^{P/Q}_{\mathsf{S/LO}}$, represents the fluctuations of the field of quantum origin. Note that $\delta a^{P/Q}_{\mathsf{class}}$ is the noise normalized for a flux of one photon per second; thus, $\bar{S}^{P/Q}_{\mathsf{class}}$ is made independent of the input laser power P_0. In the expression above, we have neglected the dephasing associated to the propagation of the beam along the S/LO path. This is a safe assumption for the typical Fourier frequency of 1 MHz considered here, given that a difference in length between S and LO of 300 m would be required to dephase the beam modulation by π.

With this, the readout signal can be expressed more succinctly. Upon arriving at the photodiodes the laser power becomes converted into a photocurrent $i_\pm \equiv \beta_\pm P_\pm$, where $\beta_\pm$ are the power-to-current conversion factors (assumed constant in the frequency range of interest) and $P_\pm = \hbar\omega_{\mathsf{L}}|a_\pm|^2$. The key step to a balanced detection comes from taking the difference between these two currents $\Delta i = i_+ - i_-$, which to the leading order of p_{LO} (we measure below that $p_{\mathsf{S}} \sim 10^{-2}$, while $p_{\mathsf{LO}} \sim 1$) reads

$$\begin{aligned}\Delta i[\Omega] =& \beta_\Sigma P_0 p_{\mathsf{S}} p_{\mathsf{LO}} \frac{4\pi}{\lambda} x[\Omega] + \\ & \sqrt{\hbar\omega_{\mathsf{L}} P_0} p_{\mathsf{LO}} \left(\boxed{\beta_\Delta \delta a^{P}_{\mathsf{LO}}[\Omega]} - \boxed{\beta_\Sigma \delta a^{Q}_{\mathsf{q,S}}[\Omega]} \right) + \\ & \delta i_{\mathsf{elec}}[\Omega],\end{aligned} \tag{4.4}$$

where $\beta_\Sigma = \beta_+ + \beta_-$, $\beta_\Delta = \beta_+ - \beta_-$, and δi_{elec} is the noise added by the electronic components of the measurement chain. If the detection is perfectly balanced ($\beta_+ = \beta_-$) the classical noise (boxed in red) is totally rejected. Al terms in this equation are assumed uncorrelated from one another.

For a laser with large classical amplitude noise, $\delta a^{P}_{\mathsf{LO}} \approx \sqrt{P_0} p_{\mathsf{LO}} \delta a^{P}_{\mathsf{class}}$. Since, in practice, β_+ and β_- are always slightly different, a residual amount of classical noise remains. Letting $\bar{S}_{\mathsf{elec}}$ be the added electronical noise spectrum, the noise spectrum $\bar{S}_{ii}$ of Δi reads

$$\bar{S}_{ii}[\Omega] = \beta_\Sigma^2 p_{\mathsf{LO}}^2 \left[\frac{16\pi^2}{\lambda^2} p_{\mathsf{S}}^2 \underbrace{P_0^2 \bar{S}_{xx}[\Omega]}_{\text{Signal}} + \hbar\omega_{\mathsf{L}} \underbrace{P_0 \bar{S}_{\mathsf{S}}^{Q}[\Omega]}_{\text{Quantum}} \right] + \beta_\Delta p_{\mathsf{LO}}^2 \hbar\omega_{\mathsf{L}} \underbrace{P_0^2 \bar{S}_{\mathsf{class}}^{P}[\Omega]}_{\text{Classical}} + \bar{S}_{\mathsf{elec}}[\Omega]. \tag{4.5}$$

Characterizing the interferometer

To vary β_+ and β_- finely, instead of tweaking the photodiode gain, the amount of light power that is sent in each photodiode is varied. This is done by rotating the half-wave plate that is placed just before the final PBS (see fig. 4.8)–note that this is impossible in a Mach-Zehnder scheme, but it works here. The effect of rotating the plate is shown in fig. 4.11: when the system in poorly balanced (i.e. most of the power is sent into one of the photodiode branches), the classical noise peak exceeds the noise floor over a large frequency interval; when β_Δ is minimized, the noise peak is suppressed by over 20 dB. In the frequency range 1.3-1.8 MHz (highlighted in fig. 4.11) relevant for the PnC membranes presented in this work, we may conclude that the classical amplitude noise lies well below the noise floor.

With the laser turned off $\bar{S}_{\mathsf{elec}}$ is measured, shown in fig. 4.11. For $P_0 = 30$ mW, the electronic noise floor lies less than a factor 2 below the laser noise floor in the frequency interval of interest. This indicates that the *SNR* is reduced by approximately 3 dB compared to our theoretical estimates. *SNR* was still found sufficiently high for the purposes of this work.

We measure that if $P_0 = 30$ mW, 300 μW return from the sample. This includes the reflectivity of SiN, which is approximately 10% for a thickness of 100 nm. From this we extract $p_{\mathsf{S}} \approx 10^{-2}$. Conversely, we measure a return power from the LO of 25 mW, giving $p_{\mathsf{LO}} \approx 83$ %.

Equation (4.5) underlines that there is a fundamental difference between the scaling of the current noise induced by $\bar{S}_{\mathsf{class}}$ and the one induced by $\bar{S}_{\mathsf{S}}^{Q}$: the former scales with P_0^2, whereas the latter only scales with P_0. This gives us a means to verify whether the classical noise is sufficiently rejected: we measure how the noise-floor level scales with the laser power. For clarity, we normalize the data by the laser power such that a quantum-limited noise floor would not vary in height with P_0. This independence of the noise floor height is precisely what we observe in fig. 4.12a in the frequency interval of interest. Note that for all these spectra the "dark spectrum" at $P_0 = 0$ mW was subtracted, allowing us to only compare contributions to the PSD from the laser noise.

We use the residual classical amplitude noise to compare its scaling with the "test noise floor" in the frequency range of interest. In fig. 4.12b, we plot the variation both of the height of the classical noise and of the mean of the test noise floor. We find that the scaling of the classical noise with the laser power is in good agreement

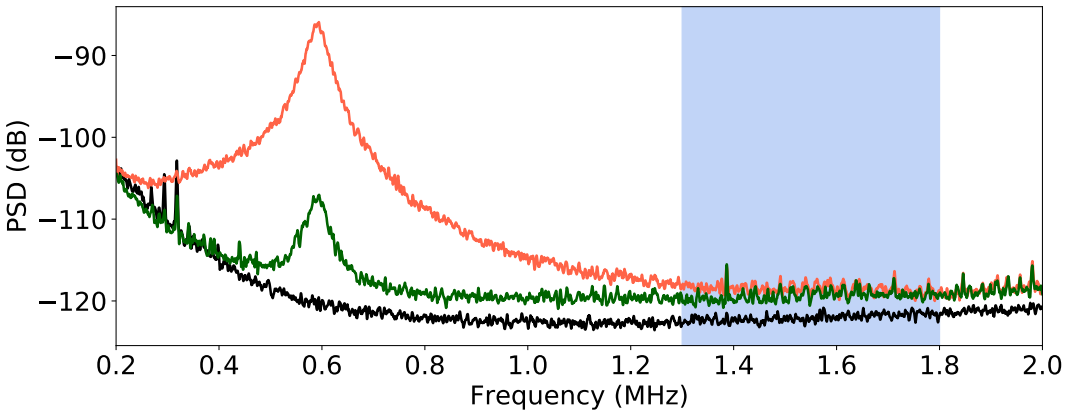

Figure 4.11: PSD of the interferometer when the balancing is poorly optimized (red), and when β_Δ is minimized (green). In addition, we show the electronic noise floor of the setup, measured with the laser turned off (black). The blue area indicates the frequency range of interest for characterizing the PnC membranes presented in this work. Here, $P_0 = 30$ mW.

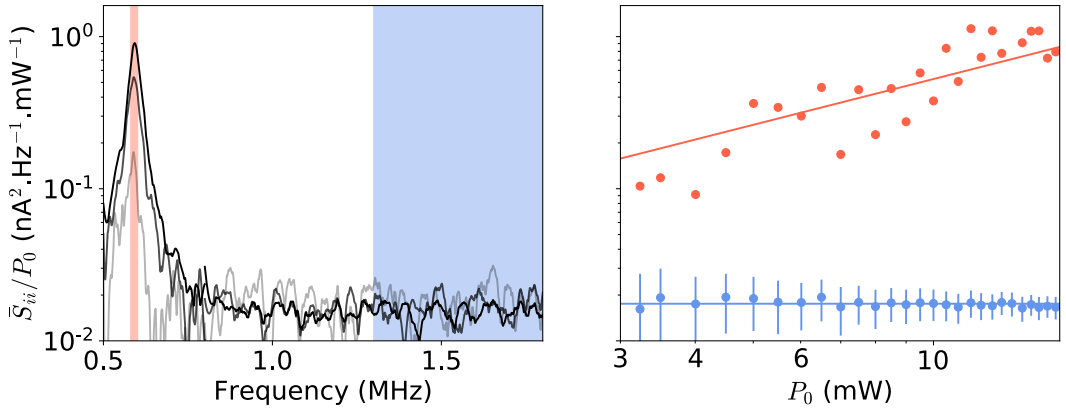

Figure 4.12: **a**, Laser noise spectrum per laser power, for varying optical power at the input of the inerferometer. From gray to black, $P_0 = 4$ mW, 7.5 mW, 16 mW. The red area highlights the classical noise peak, and the blue area represents the test noise floor, in the frequency interval of interest. **b**, Variation of the classical noise height (red) and of the mean of the test noise floor (blue). The the red line is a linear fit to the red points, and blue line is the mean of all the blue points. The error bars for the test noise floor data represent its standard deviation. For both figures, the spectrum at $P_0 = 0$ mW was subtracted.

with a linear fit $\bar{S}_{ii}/P_0 \propto P_0$. Conversely, we find the test noise floor $\bar{S}_{ii}/P_0$ to be independent of the laser power. We thus conclude that the detection in the interval of interest is shot-noise limited.

An additional advantage of this, as shown in chapter 1, is that the *SNR* increases with the laser power, which is not the case if classical noise is dominant. Here we found that a laser power of 5 mW in the S branch produced a sufficient *SNR* ($p_{\mathsf{S}} = 10^{-2}$); attempting to increase it further produced excessive detrimental effects such as mechanical frequency drifts. In this system, the thermal motion of SiN membrane can be resolved (see section 4.4.1). In some cases however, it is preferable to drive the mode, and strongly increase its amplitude of motion. That is particularly desirable for the measurements of the quality factor by ringdown, where the mode needs to be resonantly driven. To do so, we show in the following section that the laser itself can be used, using radiation pressure as a driving force.

4.2.3 Driving the mechanical motion

Optical driving of mechanical modes

In principle, a mode can be driven by any vibration source provided the drive is resonant with the mode frequency and coupled to it by some means. We can use the radiation pressure induced by the laser beam on the membrane by the reflection of photons off its surface. By modulating the laser power, radiation pressure can serve as a resonant drive. Here, we verify whether the induced amplitude of motion can be made to significantly exceed the thermal fluctuations for typical laser powers.

Suppose a laser of power P is reflected off dielectric of reflectivity R. The force exerted is then

$$F_{\mathsf{rad}} = 2\frac{RP}{c}, \tag{4.6}$$

where c is the speed of light in vacuum. If this force oscillates monochromatically at Ω_{m}, in resonance with a mechanical mode, the induced steady-state amplitude of oscillations is

$$\bar{x} = \frac{F_{\mathsf{rad}}}{\Gamma_{\mathsf{m}}\Omega_{\mathsf{m}} m_{\mathsf{eff}}}, \tag{4.7}$$

which we find directly from the equation of motion of a harmonic oscillator (eq. (1.4)).

As found in eq. (1.19), the RMS amplitude of thermal motion x_{th} at high temperatures is $x_{\mathsf{th}} \approx x_{\mathsf{ZP}}\sqrt{2n_{\mathsf{th}}}$, where x_{ZP} is the RMS amplitude of the zero-point motion of the mode. For typical resonator parameters ($m_{\mathsf{eff}} \sim 10$ ng, $\Omega_{\mathsf{m}} \sim 1.5$ MHz), $x_{\mathsf{th}} \approx 2$ pm at room temperature (in agreement with the measurements in section 4.4.2). For a thickness of 100 nm, the membrane has a reflectivity $R \sim 0.1$. Thus, for an incident power of 5 mW on the membrane, $\bar{x}/x_{\mathsf{th}} \sim 10^4$. Radiation pressure-induced ringdowns should thus be appropriate to obtain a precise measure of Q, provided the laser power can be modulated at MHz frequency with an

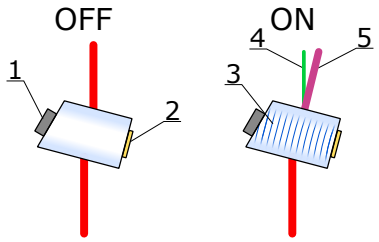

Figure 4.13: Principle of the AOM. The incident beam is shown in red 1: mechanical absorber. 2: Piezoelectric actuator. 3: Acoustic wave. 4: 0^{th} order beam (green). 5: 1^{st} order beam (violet). ©By Wikimedia Commons User:Ximeg / CC BY-SA 3.0

amplitude of several mW. There are several ways to do so; here, an acoutso-optic modulator (AOM) is used.

Acousto-optic modulation of the laser power

An AOM, schematically represented in fig. 4.13, essentially acts as a diffraction grating which can be switched on at will using an electric current. Using a piezoelectric actuator, a mechanical wave propagates through a transparent crystal. This produces a periodic modulation of the refractive index which diffracts the beam. If the incident beam is well aligned with respect to the crystal (the incidence angle is near the Brewster angle), then it is possible to get most of the power to go into the 1^{st} order and effectively cancel the 0^{th} order–for simplicity, we neglect other diffraction orders, as the power that goes into them is small. We can thus effectively turn the 0^{th} order beam off by switching all the power to the 1^{st} order.

The intensity of the 0^{th} order can be reduced further by passing twice trough the AOM. The experimental setup for the modulation stage is shown in fig. 4.14a, with a simplified schematic representation in fig. 4.14b. A strong current oscillating at 85 MHz is sent to the AOM, and a mixer further modulates the amplitude of those oscillations with a square signal. For a modulation at 10 kHz the power of the 0^{th} order is shown in fig. 4.14c. Note that the power does not follow the square modulation perfectly due to thermal effects; although this reduces the driving amplitude, ringdown measurements can still be successfully made, as shown in the following section.

With this, all of the main components of the measurement setup have been presented. They were found sufficient for the purposes of this work to fully characterize PnC membranes, namely to obtain the mode spectra, their profiles and to measure their quality factor. For this, we use the three methods presented below.

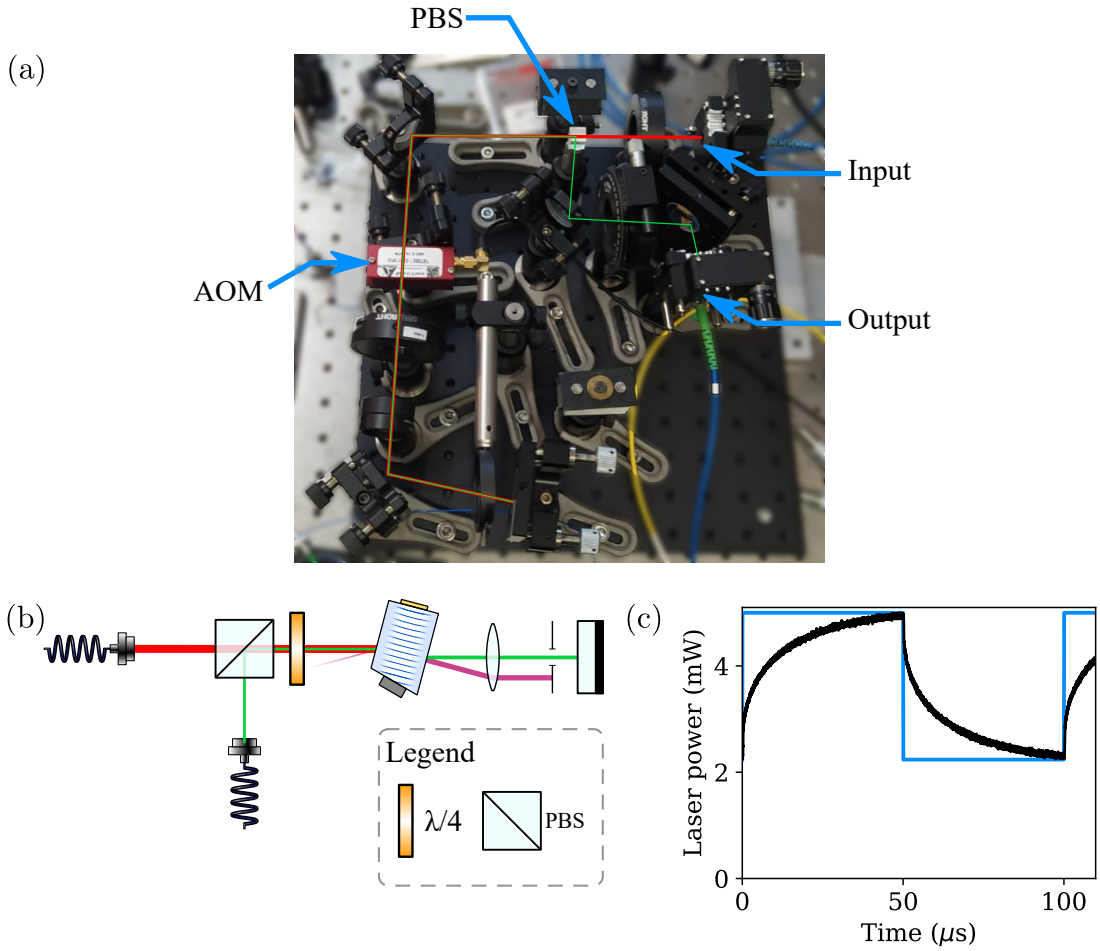

Figure 4.14: **a**, Picture of the modulation setup. The path of the incident beam is shown in red, and that of the 0^{th} order beam is shown in green, with the AOM turned ON. The 1^{st} order beam is not shown, for clarity. **b**, Schematic representation of the setup shown in **(a)**, when the AOM is turned ON (i.e. the laser beam is switched off). **c**, Power variation of the 0^{th} order, while varying the power of the electric current sent to the AOM Modulating at 10 kHz. The measured data is shown in black, and the ideal variation is shown in blue.

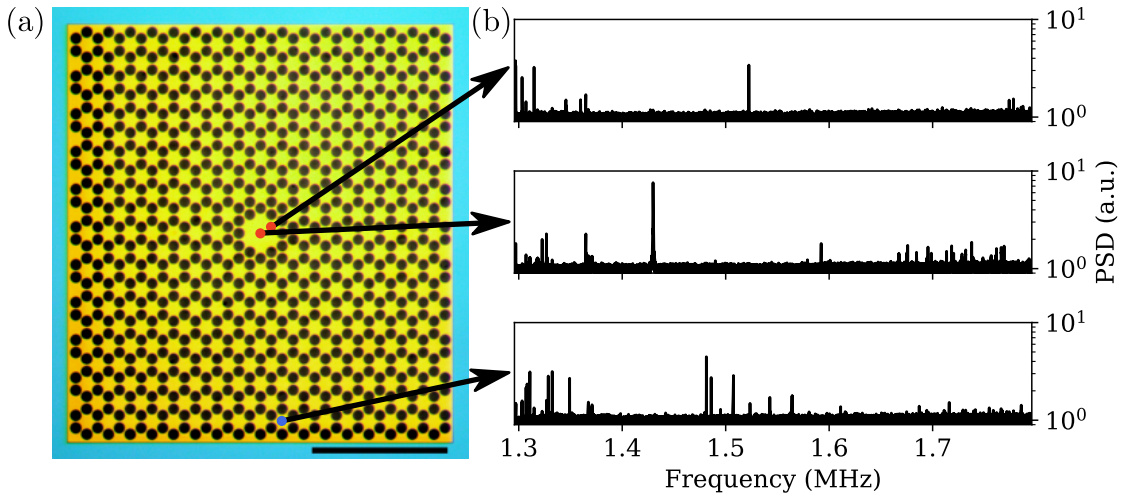

Figure 4.15: **a**, Optical micrograph of a PnC membrane of a generation 1 design. In yellow, the SiN is freely standing, and in light blue it is lying above Si. The points indicate the positions at which the spectra of **(b)** are measured. **b**, Three different spectra of the mechanical motion, taken at various points on the membrane.

4.3 Experimental methods

The output current from the interferometer i_Δ is here measured with a signal analyzer (SA, model MXA-N9020A). It takes the Fourier transform of i_Δ to obtain spectral information about the signal. In doing so, the continual thermal motion of the membrane can already be discerned with a shot-noise limited detection. However, to extract complete information about the system, a little more work is required. In particular, we wish to clarify what is meant by a membrane's thermal spectrum and how it can be used to reconstruct images of the mode profiles. Finally, with the SA, the quality factor of a mode can be measured, and the protocol used in this work, the ringdown, is detailed.

4.3.1 Measuring the spatially-dependent thermal spectrum

Let us consider a generation 1 membrane (without an edge guard), shown in fig. 4.15a. When we acquire a thermal spectrum with a bandwidth of 30 Hz, at different positions on the membrane (indicated on fig. 4.15a), significantly different results are obtained. For instance, fig. 4.15b shows the spectra at three points: two within the central defect, and one near the horizontal border; none of them are identical. The origin of this difference is attributed to the fact that the spectrum of a PnC membrane varies significantly with the position of the laser beam–there is no point at which all modes simultaneously present significant displacement.

It is particularly important in this work to find the full list of modes, as we wish to study the relationship between defect and edge modes. Several spectra must therefore be compiled. We do so by measuring spectra at various points on the membrane. They are grouped into 4 categories, based on their location: on the defect, along the horizontal borders, along the vertical borders, and within the PnC. For each measurement category, a single intermediary spectrum is produced by taking the maximal value of the displacement noise at each frequency. The intermediary spectra are finally superposed to produce the final "compiled" spectrum, discussed further in section 4.4.1.

The data of fig. 4.15b allow us to verify whether our prediction for *SNR* (estimated to be 45 dB) was correct. Its definition is the ratio of the height of the mechanical peak to the noise floor. A few points must be noted to compare theory and experiment:

- The measurement is taken with a bandwith of 30 Hz, much larger than the mechanical linewidth of 0.15 Hz (see section 4.4.3). This is done for conveniency to accelerate measurements, but comes at the cost of a 23 dB reduction of *SNR*.

- *SNR* was calculated assuming perfect interference contrast. In practice, the contrast is around 50%, which is equivalent to a reduction of p_{S} by a factor 2. From our definition of *SNR* (eq. (1.25)), this reduces it by a further 6 dB.

- Finally, the electronic noise floor lies at approximately 3 dB below the shot-noise floor, reducing *SNR* by that amount.

Overall, we would expect the mechanical peak to exceed the noise floor by approximately 13 dB. Here, our maximal *SNR* is closer to 10 dB. We attribute the remaining discrepancy to the detection inefficiency of the photodiodes.

For these measurements, having the interferometer on a translation stage is essential. The idea of compiled measurements and position-dependent spectra can be extended, as demonstrated in Ref. [117], to reconstruct the displacement profile of the various modes of the PnC membrane.

4.3.2 Measuring the mode profile

We image the profile of a mode by plotting the amplitude of the thermal motion of a mode as a function of the position by raster scanning over the desired surface. However, the high mode density of a PnC membrane can make it difficult to clearly identify the modes from their frequency. Mechanical frequency drifts caused by temperature fluctuations in particular make this process challenging.

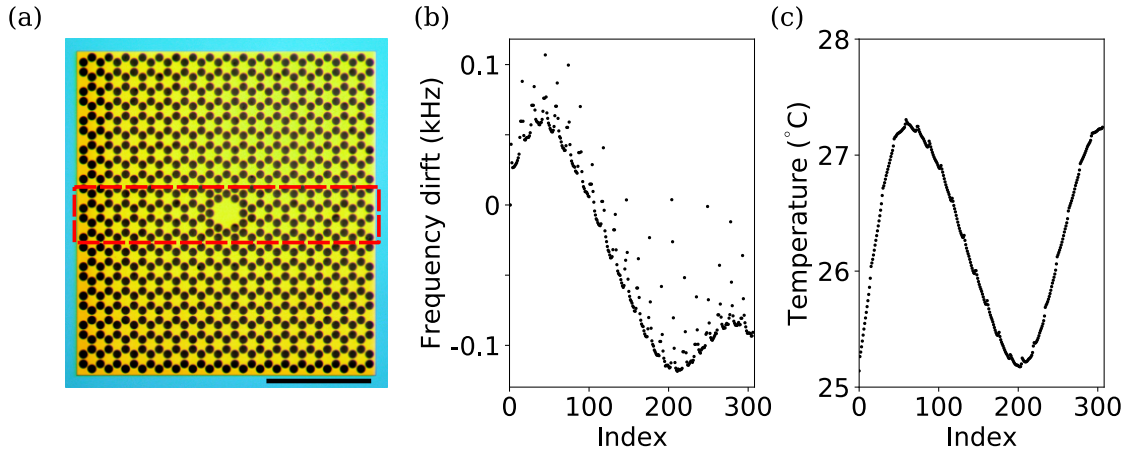

Figure 4.16: **a**, Optical micrograph of a generation 1 membrane, highlighting by the red rectangle the area over which the raster scan discussed in this section is performed. **b**, Frequency of the fundamental mode of a PnC membrane, at approximately 209 kHz, as a function of the laser position index. **c**, Temperature of the sample holder over the course of a scan.

Correcting thermal drifts

To illustrate this difficulty, we first track the frequency of a single membrane mode as we raster scan over the area indicated in fig. 4.16a–notice that the area slightly exceeds the membrane width. At each point of the grid we measure the thermal spectrum and extract its maximum near 209 kHz, the frequency of the (1, 1) mode of the PnC membrane. The result of this measurement is shown in fig. 4.16b.

The figure reveals a problem: the frequency of the mode can vary by more than 100 Hz over the course of the scan, exceeding the typical frequency difference between the bandgap modes. We furthermore distinguish two time scales: a slow drift present over the entire duration of the scan, and a rapid periodic drift. Using a thermistor attached to the sample holder, we find that its temperature follows that frequency drift closely, as shown in fig. 4.16c. Note that the two are not perfectly correlated. We attribute the slower frequency drift to changes in the room temperature as the scan can take upwards of ten hours (depending on the resolution). On the other hand, the faster drift is attributed to the fact that the membrane is not heated when the laser exceeds its borders, allowing the temperature to lower; when the laser returns on the membrane on the following pixels, the temperature increases again, and so on.

The problem caused by the temperature drift is clarified when considering modes within the PnC bandgap. Figure 4.17a shows the frequencies of three modes around 1.4 MHz (near the central frequency of the D1 mode). By eye it is relatively clear which mode is which, but for a computer the task is more complicated. Indeed,

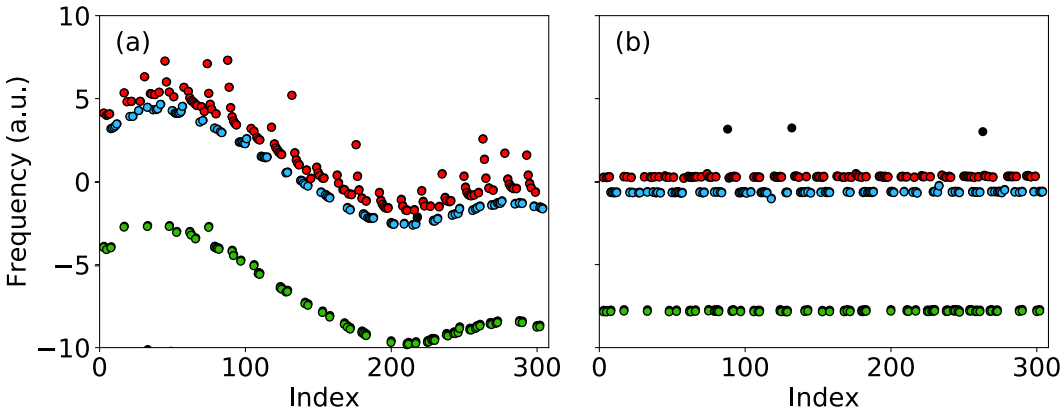

Figure 4.17: **a**, Frequency of three modes near 1.4 MHz as a function of the laser position index. Three modes were identified "by eye", and shown in red, green, and blue. **b**, Corrected frequency of the modes shown in **(a)**. The laser position dependence of the frequency is removed by dividing by the frequency of the fundamental mode, shown in fig. 4.16b.

they cannot be indexed by order of appearance as the modes are not systematically detected at each pixel (e.g. at nodes or outside of the membrane boundaries). More complicated forms of pattern recognition would be required.

On the other hand, we notice that they all drift in the same manner and, importantly, follow the same drift as the (1, 1) mode. We hypothesize that all modes have the same dependence on temperature which can be factored out by using a mode as the reference "thermometer mode". The (1, 1) mode here serves this purpose. We find that by normalizing all the modes by the position-dependent frequency of the thermometer mode, the drift is effectively canceled. They become easily identifiable, even by a computer (see fig. 4.17b). Note that both the slower and faster drifts have been rejected.

In fig. 4.17b, a straightforward frequency interval selection algorithm can be applied to identify which mode is which. The mode profile can then be reconstructed and the results of such measurements are discussed in section 4.4.2. From the measured current fluctuations the physical amplitude of the displacement can be obtained with some careful calibrations, as detailed below.

Calibrating the data to a physical displacement

If the position of the LO is swept over a large distance, we find from eq. (1.22) that the measured DC current varies sinusoidally with an amplitude

$$i_{\mathsf{amp}} = 2\beta_\Sigma P_0 p_{\mathsf{S}} p_{\mathsf{LO}}, \tag{4.8}$$

neglecting noise terms. From this, the quantity $\beta_\Sigma P_0 p_\mathsf{S} p_\mathsf{LO}$ can be readily solved for, and substituted in eq. (4.5) to find that

$$\bar{S}_{xx}[\Omega] = \bar{S}_{ii}[\Omega] \times \frac{\lambda^2}{8\pi^2 i_\mathsf{amp}^2}, \tag{4.9}$$

dropping again all noise terms. In practice, the high-frequency component of the signal is measured with the SA, while low-frequency component is measured on a separate branch of the measurement chain; thus, an additional conversion factor is needed. The electronics setup was often modified for the purpose of optimization and the conversion of the data to meters was not deemed crucial for its interpretation. For this reason, to conversion was only done once in section 4.4.2 to obtain am estimate of the RMS amplitude of the thermal fluctuations of the defect modes.

Finally, we measure the quality factor of the defect modes. In principle this can directly be done by measuring the thermal spectrum and extracting from it the linewidth of the mode of interest. For low mechanical linewidths, a more precise method is to drive the mode resonantly and to monitor the decay of the amplitude of motion over time. This is called a ringdown measurement, detailed below.

4.3.3 Ringdown measurement of the quality factor

The ringdown protocol is similar to the one presented for an electromechanical device in chapter 2: in the initial "driving phase" the mode is driven resonantly by modulating the laser power; in the following "readout phase" the modulation is turned off and the amplitude of the mechanical noise peak is monitored as a function of time. A typical ringdown curve obtained in such a manner is shown in fig. 4.18. The resulting measurement exceeds the noise floor by over 40 dB and the decay in mechanical amplitude can be readily distinguished. As in chapter 2, Q can be extracted by fitting this curve with a decaying exponential, following $x(t) \propto \exp(-\Omega_\mathsf{m} t/2Q)$.

With the presented setup, all requirements for the interferometric system are fulfilled: up to 9 membranes can be measured by pumping the vacuum chamber only once, and the full thermal spectrum, mode profiles, and quality factors can be extracted. In the following section, the results for a batch of PnC membranes of both generations are presented.

4.4 Results for defect and edge modes

In this section we demonstrate that, as predicted in chapter 3, the D1 mode hybridizes with one or more VEMs in a generation 1 membrane, but that this effect is negated in generation 2 membranes. This is achieved via the measurement of

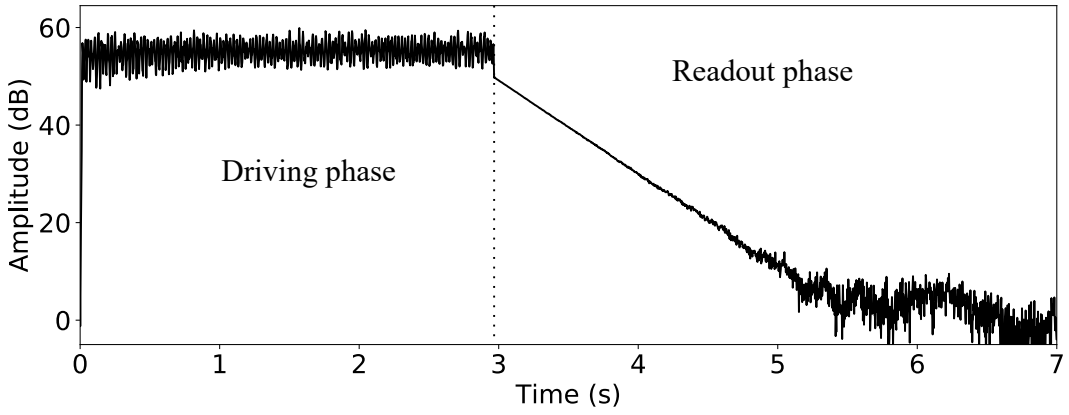

Figure 4.18: Ringdown measurements of a PnC membrane mode at 1.11 MHz following a forced resonant excitation with an AOM (driving phase). When the AOM is turned off, the resonator motion is left to naturally relax to a thermal state (readout phase).

thermal spectra and mode profiles.

Furthermore, the principal goal of canceling hybridization evens was to ensure that the bending quality factor $Q_{\mathfrak{b}}$ of the defect modes approaches its theoretically maximal value, with a particular emphasis on D1. Here, we verify that this goal is achieved and is in good agreement with numerical predictions. All membranes in this section have $b \approx 160$ μm, $r \approx 40$ μm, $M \approx 20$ μm.

4.4.1 Measured thermal spectra

We first consider the spectrum of a generation 1 membrane. Following the method described in section 4.3.1, thermal spectra are acquired at the 13 points indicated in fig. 4.19a. They are divided into the four specified categories: defect, vertical border, horizontal border, and PnC. This amount of points was found to be sufficient to include all modes of interest. We compared our results with the COMSOL simulation presented in chapter 3 (fig. 4.19b), and the compiled measured spectrum is shown in fig. 4.19c. The two are only in qualitative agreement; we attribute the discrepancies to microscopic differences in the geometry between the simulated model and the realized sample. However, they do not significantly affect the conclusions of this work.

We note that evidence of mode hybridization between defect and edge modes can already be discerned from the thermal spectra: around the frequency of the label D1 in fig. 4.19c we find several peaks in the spectrum of the defect category where there should be only one. Conversely, modes labeled D2 and D3 present no

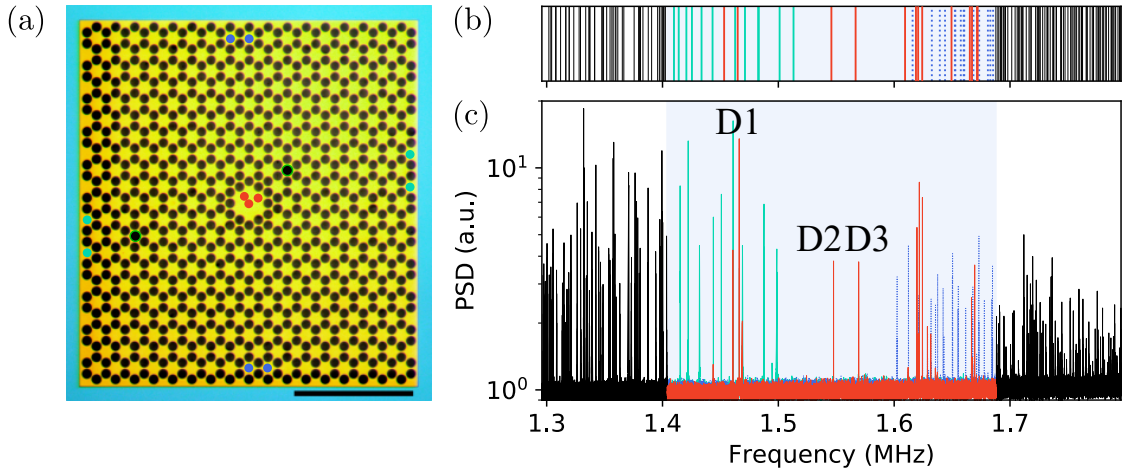

Figure 4.19: **a**, Optical micrograph of a PnC membrane of a generation 1 design. In yellow, the SiN is freely standing, and in light blue it is lying above Si. The points correspond to the various locations where the membrane spectra are measured, and their colors indicate their category: defect (red), vertical border (light blue), horizontal border (dark blue), and PnC (black). **b**, Simulated spectrum near the PnC bandgap. **c**, Compiled spectrum, consisting overall of 4 intermediary spectra, with colors corresponding to the measurement point category. In **(b)** and **(c)** the simulated bandgap is highlighted in light blue. Figure adapted from [118].

signs of such splitting.

Similarly, we characterize the spectrum of a generation 2 design, measuring the thermal spectra at the points indicated in fig. 4.20a. Numerical simulations predicted that the effect of an edge guard would be to push the frequencies of VEMs higher (see fig. 4.20b). Indeed, in the experimentally measured spectrum shown in fig. 4.20c this is precisely what we observe. Conversely, the frequencies of both defect modes and HEMs remain essentially unaffected. From this spectrum and in particular the central frequency of D1, we determine by comparison with numerical simulations that $\sigma_0 \approx 1.05$ GPa.

In generation 2 membranes D1 is spectrally isolated from all other modes. Now, only a single peak appears in the central defect. Thus, a correlation is observed between the splitting of a defect mode and the presence of VEMs in its spectral vicinity. However, we can also observe from fig. 4.20c that the defect mode splitting is not a systematic effect: modes D2 and D3 remain single peaks, although they are neighbored by VEMs. The stochasticity of hybridization events is discussed further in section 4.4.3. Before addressing this point we aim to conclusively demonstrate that the peak splitting is due to a hybridization of the defect modes with VEMs. We do this in the following by reconstructing the displacement profile of the membrane eigenmodes.

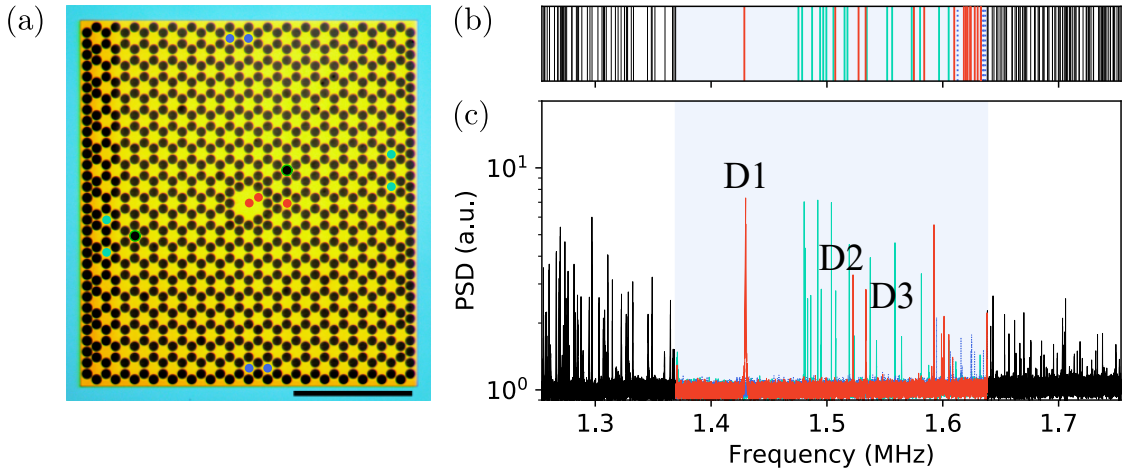

Figure 4.20: **a**, Optical micrograph of a PnC membrane of a generation 2 design. In yellow, the SiN is freely standing, and in light blue it is lying above Si. The points correspond to the various locations where the membrane spectra are measured, and correspond in color to the spectra in **(b)** and **(c)**. **b**, Simulated spectrum near the PnC bandgap. **c**, PSD spectrum of the membrane shown in **(a)**, consisting overall of 4 spectra, measured at the vertical borders (cyan), the horizontal borders (blue), the defect (red), and within the PnC (black). In **(b)** and **(c)**, the simulated bandgap is highlighted in light blue. Figure adapted from [118].

4.4.2 Measured mode profiles

We first consider a generation 1 membrane where the D1 mode and VEMs can become hybridized. We begin by measuring the tomographies of various modes in a small region around the central defect area. This allows us to image the defect mode profiles with high resolution (pixel size 10 μm $\times$ 10 μm) in one night of measurements. In fig. 4.21, the tomographies (converted to meters) of defect modes D1 to D4 are shown and found to be in good agreement with theory.

Interestingly, we can extract the effective mass of the various modes from this data. The RMS amplitude of the thermal motion is $x_{\mathsf{th}} = x_{\mathsf{zp}}\sqrt{2n_{\mathsf{th}}}$. By definition of the zero-point fluctuations the effective mass reads

$$m_{\mathsf{eff}} = \frac{k_{\mathsf{B}} T_{\mathsf{env}}}{\Omega_{\mathsf{m}}^2 x_{\mathsf{th}}^2}, \tag{4.10}$$

assuming $k_{\mathsf{B}} T_{\mathsf{env}} \gg \hbar\Omega_{\mathsf{m}}$. The extracted values for m_{eff}, extracting x_{th} from the point of maximal displacement, are given in fig. 4.21. They are in qualitative agreement with the results of [25]; Ref. [24] gives an effective mass for the D4 mode of 16 ng for a membrane thickness of $h = 35$ nm, which corresponds to an effective mass of 45 ng for $h = 100$ nm (assuming $m_{\mathsf{eff}} \propto h$), for an agreement of 71%. In comparison,

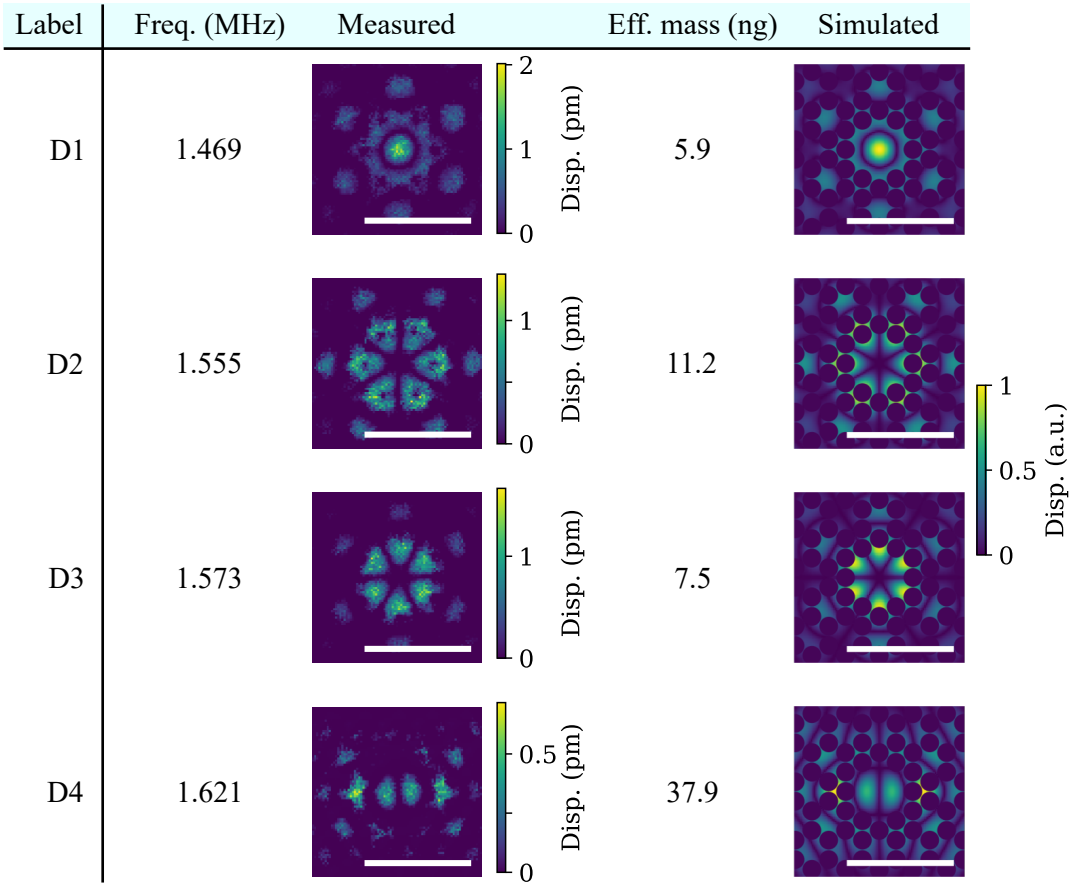

Figure 4.21: Mode shape tomographies of the first few defect modes of a generation 1 membrane. Each experimentally measured image is shown next to the simulated profiles computed in COMSOL, for comparison. From the maximal displacement of each mode, the effective (Eff.) mass can be calculated using eq. (4.10).

the mass of the fundamental mode of a plain membrane (of similar frequency to D1) is approximately 10 ng.

A mode profile scan was then repeated over a wider area (the same as in fig. 4.16a) to measure the displacement profiles over an entire strip of the membrane. We do this to simultaneously image defect modes and VEMs. In section 4.4.1 we found several frequencies around 1.42 MHz where significant displacement in the defect could be observed. With fig. 4.22 we confirm that those modes are linear superpositions of VEMs with D1. We note that the symmetry of the system is broken, as evidenced by the fact that hybridizations of D1 with a VEM on the left and right of the membrane are not degenerate. For reference, the profiles of the fundamental mode of the membrane, of a VEM mode on its own, of D2, and of D3 are also shown.

These mode profiles confirm that we have understood the behavior of the most

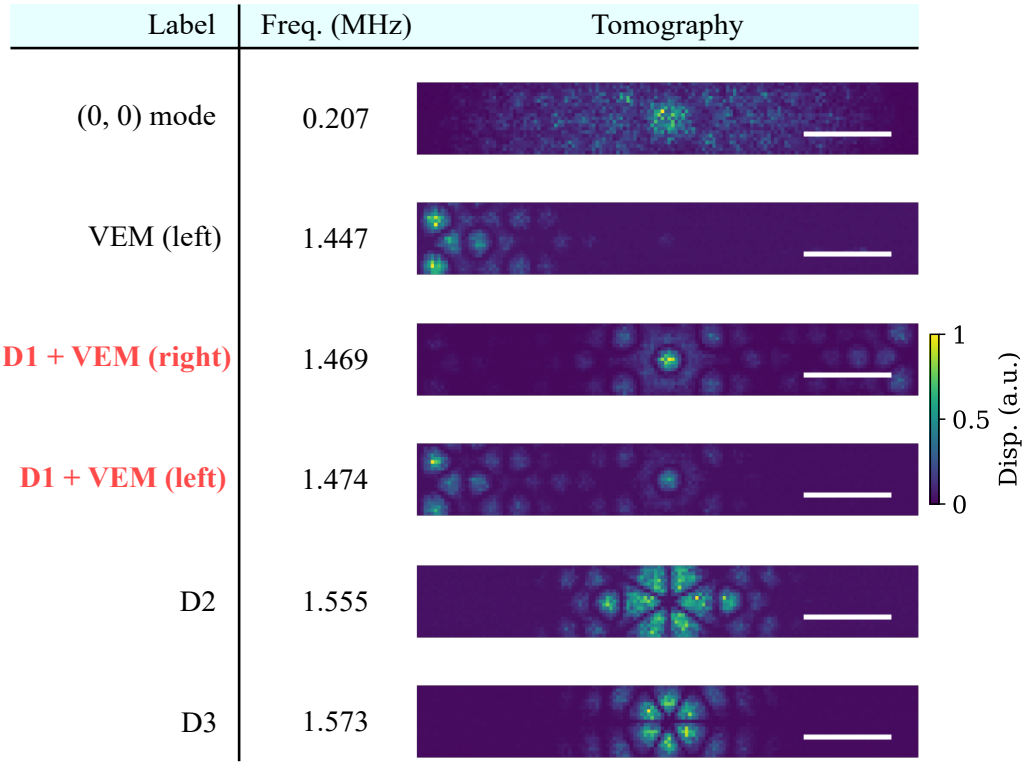

Figure 4.22: Mode shape tomographies for various modes of a generation 1 membrane. The scan is taken over the entire width of the resonator to measure the hyibridization between VEMs and D1.

relevant eigenmodes of PnC membranes. Furthermore, the appearance of mode hybridization has conclusively been observed. Following the analysis in chapter 3, non-negligible displacement of a mode near the border of the membrane is accompanied by a strong reduction in the bending quality factor Q_{b}. In the following we therefore measure its value to quantify the importance of border loss in physical samples of generation 1 and 2 membranes.

4.4.3 Measured Q_{b}

The total quality factor Q_{tot} is extracted with a ringdown. To determine Q_{b}, it must first be isolated from the other sources of loss such that $Q_{\mathsf{tot}} \approx Q_{\mathsf{b}}$. The other dominant loss channels are radiation loss and residual gas damping. We note that in principle, only edge modes are affected by the former since defect modes are protected by the phononic shielding. It has been shown that radiation loss can be minimized by leaving the chip to rest freely on its holder in the interferometer, without being fixed to it with any sort of glue or tape [87].

Residual gas damping on the other hand arises from elastic collisions with gaseous molecules (H_2O for instance), dissipating the mode energy. To ensure that this effect is negligible compared to bending loss, we verify the dependence of Q_{tot} on the chamber pressure. This will allow us to determine the pressure below which we must operate to ensure that bending loss is dominant. In that regime, results can be directly compared to simulations and the effect of an edge guard on the defect mode Q can be quantitatively studied.

Pressure dependence of the quality factor

Residual gas damping has an associated Q_{gas}, such that

$$Q_{\mathsf{tot}}^{-1} \approx Q_{\mathsf{b}}^{-1} + Q_{\mathsf{gas}}^{-1}. \tag{4.11}$$

Bianco et al [119] distinguish two regimes for gas damping: the free-molecule regime where the gas can be considered as an ensemble of non-interacting particles, and the viscous regime where molecule-molecule collisions occur more often than molecule-membrane interactions. In the free-molecule regime where the pressure is low, $Q_{\mathsf{gas}} \propto 1/p$, whereas in the viscous regime $Q_{\mathsf{gas}} \propto 1/\sqrt{p}$. We can thus identify which regime we are in based on the scaling of Q_{tot} with the pressure; it is necessary to be in the free-molecule regime to ensure that gas damping is minimal.

In fig. 4.23a, we record Q_{tot} as a function of the chamber pressure in a full cycle. We first raise then lower the pressure, cycling between a few nanobar and 10^{-2} mbar. The pressure is controlled by progressively manually closing or opening either the valve leading to the ion pump or to the turbo pump. A transition region around 10^{-4} mbar is found where the scaling of Q_{tot} changes: for lower pressures

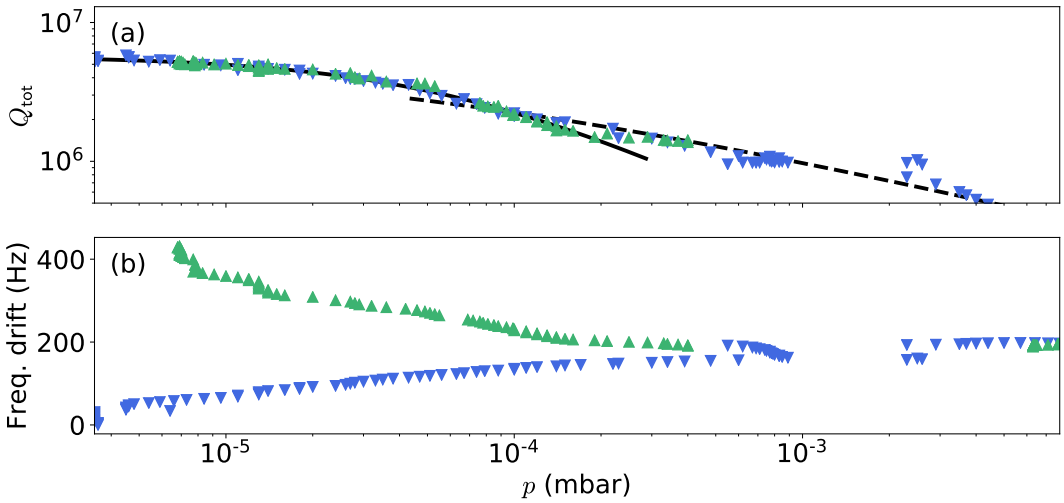

Figure 4.23: **a**, Variation of the quality factor Q_{tot} of D2 (at 1.53 MHz), when raising (green) and lowering (blue) the vacuum chamber pressure p. The lines represent fits to the data with eq. (4.11), for two regimes: the full line corresponds to the free-molecule regime, for $p \geq 10^{-4}$ mbar where $Q_{\text{gas}} \propto 1/p$; the dashed line follows the viscous regime model where $Q_{\text{gas}} \propto 1/\sqrt{p}$. **b**, Frequency (Freq.) drift of the mode, with the same color coding as **(a)**.

the variation of the quality factor is consistent with the free-molecule model ($Q_{\text{gas}} \propto 1/p$), while for higher pressures the scaling is in good agreement with the viscous model ($Q_{\text{gas}} \propto 1/\sqrt{p}$). With the free-molecule model we extract $Q_{\text{b}} = 5.7 \times 10^6$. At the lowest pressures reached by the vacuum chamber (5×10^{-6} mbar), residual gas damping contributes less than 10% to the total losses. We therefore conduct all measurements at a few nanobar, such that gas damping does not significantly affect our conclusions.

In principle, the mode frequency should also vary with the chamber pressure and scale differently in the two pressure regimes. We track these changes in fig. 4.23b, but find that the frequency monotonously decreases for the entire duration of the measurement cycle (which takes up to half an hour). This indicates that phenomena other than gas collisions are causing a frequency drift; from the short timescale of such a measurement and the magnitude of the drift, we attribute it mainly to heating by laser absorption rather than to room temperature fluctuations (which occur over several hours, and cause a drift of approximately 100 Hz.$^\circ$C^{-1}).

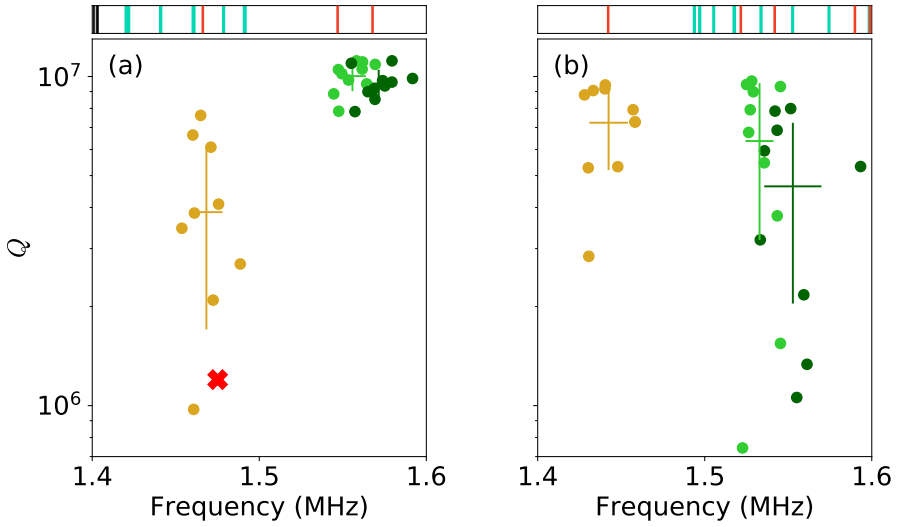

Figure 4.24: **a-b**, Collected values of Q from 10 different membranes of generation 1 **(a)** and 2 **(b)**, for D1 (yellow), D2 (light green) and D3 (dark green). The crosses of the corresponding color are centered at the mean frequency and quality factor and indicate their standard deviation. Above, the simulated spectrum of the corresponding design indicates the frequencies of the defect modes (red), VEMs (green), and PnC modes (black). The mode highlighted by the red cross was used for the mode profiling in fig. 4.22. Figure adapted from [104].

Edge guard vs no edge guard

The improvement of PnC membranes owed to the edge guard is quantified by comparing the quality factors of a generation 1 membrane to those of generation 2. However, as anticipated in section 4.4.1, there is a subtlety: edge modes are not systematically resonant with the nearby defect modes. We recall that in the numerical simulations of chapter 3, we found that the occurrence of hybridization strongly depends on the margin M. A given VEM and defect mode are only resonant at a specific value of M, with a tolerance inferior to 5 μm–the precision of our fabrication recipe. Consequently, micro-fabrication uncertainties can result in large sample-to-sample fluctuations of Q_b. We expect a good PnC membrane design to be robust to fabrication uncertainties, ensure that hybridization never occurs, and result in a high reproducibility of the defect mode Q_b. To verify this, we measure Q_b of the defect modes for 10 membranes of each generation.

The measured values for Q_b of the first three defect modes of generation 1 membranes are shown in fig. 4.24a. Note that the highlighted point in the figure, corresponding to the sample with one of the lowest Qs for D1, also corresponds to the sample for which hybridization with edge modes was observed in section 4.4.2. The

Table 4.1: Exctracted results from fig. 4.24, comparing the mean quality factor and its standard deviation (St. Dev.) for both membrane designs.

	Generation 1		Generation 2	
Label	Q ($\times 10^6$)	St. Dev. ($\times 10^6$)	Q ($\times 10^6$)	St. Dev. ($\times 10^6$)
D1	3.9	2.2	7.2	2.0
D2	10	1.0	6.4	4.6
D3	9.6	1.0	3.2	2.6

lowest measured quality factors, of the order of 10^6, are consistent with the upper estimate for Q_b of VE1 computed in chapter 3 (4×10^6). Ringdown measurements of Q were done for generation 2 membranes as well. They are shown in fig. 4.24b.

The extracted mean values for Q_b of defect modes from both generations are reported in table 4.1. For D1, the average value increases by almost a factor 2. In addition, while 1/10 generation 1 samples arrive within 50% of the simulated $Q_\mathsf{b} = 1.5 \times 10^7$, 5/10 samples achieve this for generation 2. The quality factors are also in good agreement with the values quoted in Ref. [24] (between 10^7 and 2×10^7). We note that this has the collateral effect of reducing the average Q for D2 and D3, which are not aimed to be optimized in generation 2. It could be suggested that depending on the defect mode of interest, the edge guard design could be tweaked to optimize the desired Q. For the D1 mode of a generation 2 membrane, the average Qf-product is

$$Qf \approx 1.0 \times 10^{13} \text{ Hz}. \tag{4.12}$$

We have been primarily interested in verifying that the fabricated design for PnC membranes is optimal, by studying in detail their thermal spectra and the coupling of defect modes to edge modes. As such, coupling was regarded as a parasitic effect. However, as shown by Catalini et al. [4] and as described in chapter 3, the fact that the PnC does not perfectly decouple the various modes from one another can be put to practical use. Indeed, a set of "dimer" modes (following the nomenclature of Ref. [4]) can be engineered by embedding several defects into the PnC. Hybrid modes separated by large distance can thus be engineered. In the following section, we present the experimental measurements of such dimer membranes and the comparison of these results with theory.

4.5 Results for dimer membranes

As described in chapter 3, the number of localized states of motion can be multiplied by increasing the number of defects in the PnC. Since there remains a finite overlap between the modes, they are coupled and become hybridized. This results in a new

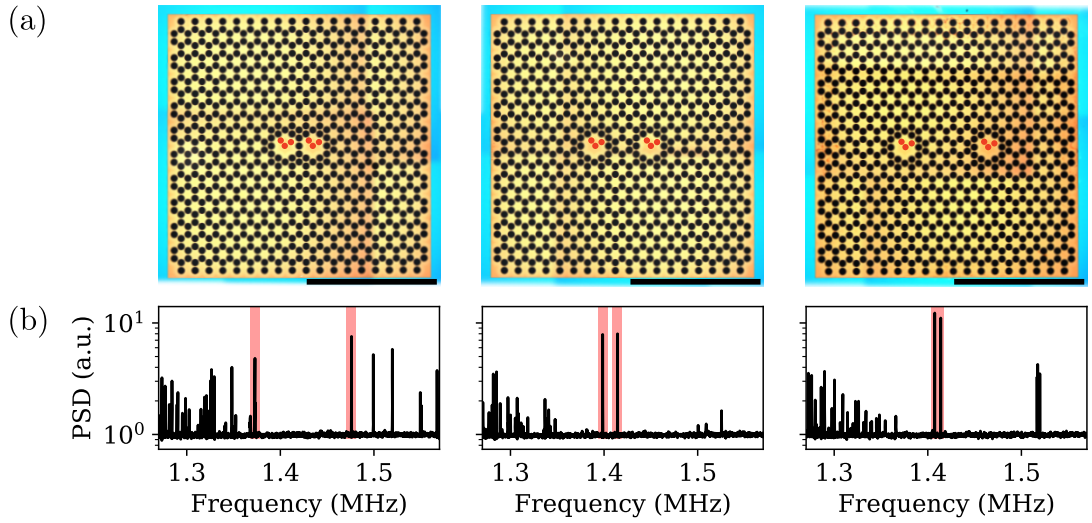

Figure 4.25: **a**, Optical micrographs of dimer membranes, for a dimer separation of 1, 3, and 5 unit cells (from left to right). The red points indicate the locations where the thermal spectra were measured. **b**, Measured compiled thermal spectra in the central defect area, for the membrane design which lies directly above them. The red area highlights the two D1 modes which become the $D1^+$ and $D1^-$ modes when hybridized.

set of normal modes localized to two distant defects. Here, we place the defects along a straight line on the membrane, varying their relative distance to vary the coupling rate, as shown in fig. 4.25a–of course, this distancing can be done along any axis, and could be used to fine-tune the coupling rate, as in Ref. [4]. Here, we wish to extract the coupling rate γ between the two fundamental defect modes, requiring us to measure their frequency and relative displacement amplitude. To do so, we already have all the tools at our disposal: by measuring the thermal spectra and the mode tomographies, all the necessary data can be extracted.

4.5.1 Measured thermal spectra and mode profiles

As before we measure the compiled thermal spectra. Since we do not consider edge modes for the purposes of this study, only the areas around the central defects are included. We show the compiled spectra for various dimer distances in fig. 4.25b. We restrict out study to the $D1^+$ and $D1^-$ modes, the symmetric and antisymmetric normal modes ensuing from a coupling between two D1 modes. As expected, the frequency splitting is reduced when the dimer distance increases.

Figure 4.26 shows the experimentally measured mode profiles for a dimer separation of 3 unit cells. We find them to be in good agreement with numerical simulation. With the current tomography method, the phase of the displacement

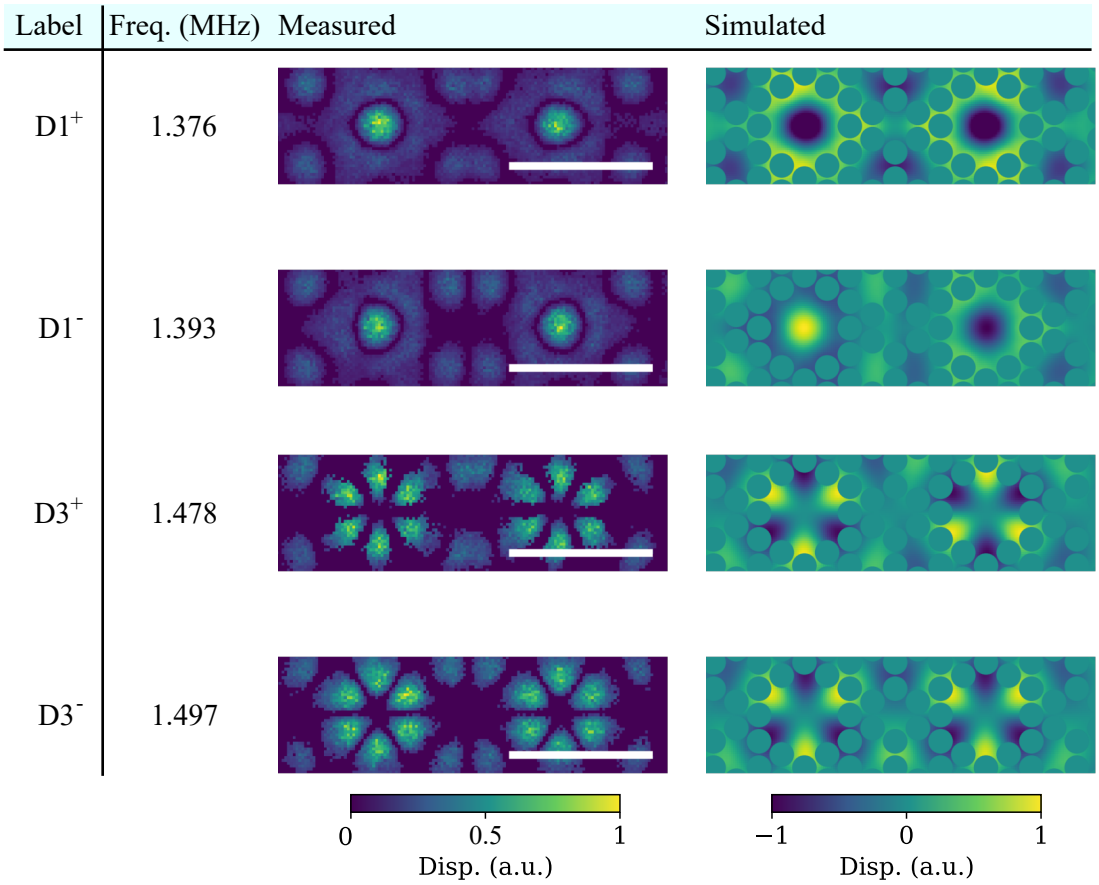

Figure 4.26: Mode profiles of a dimer membrane with a separation of 3 units cells, compared to their simulated profiles. Note that the absolute value of the displacement (Disp.) is measured for the mode profiles, while the simulated profiles take both positive and negative values to show the symmetry (or antisymmetry) of the modes.

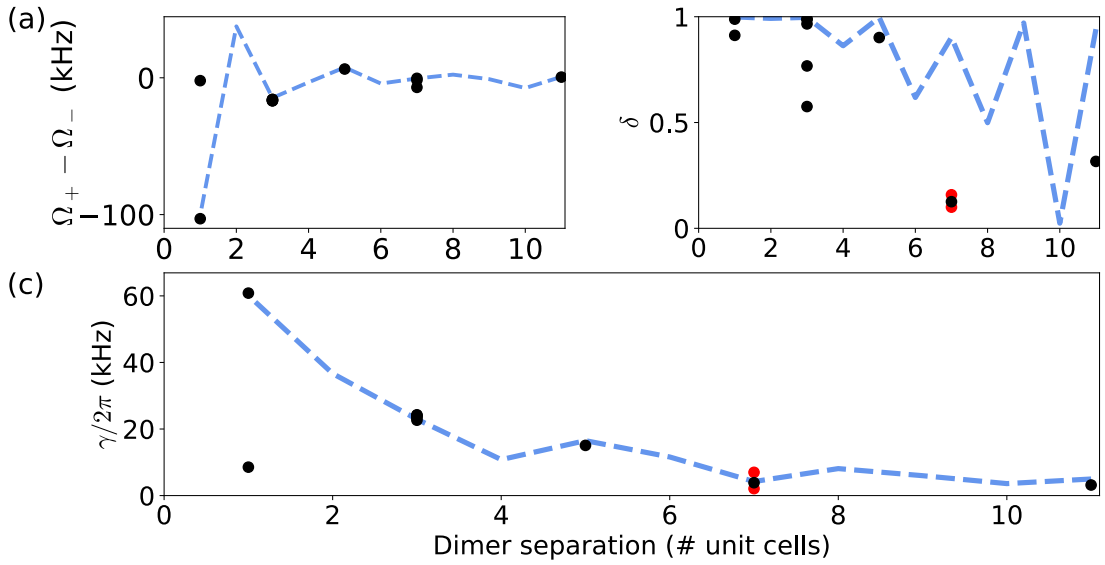

Figure 4.27: **a**, Difference between the frequency of the symmetric mode Ω_+ and the antisymmetric mode Ω_-. **b**, Measured values of δ for the highest frequency mode. For the points colored in red, an upper estimate on δ is given. **c**, Extracted values of the coupling rate γ based on the data in **(a)** and **(b)**. The red points represent an upper estimate on γ. In all plots the dashed blue lines indicate the simulated values from chapter 3.

cannot be determined as we can only measure its absolute value. Nevertheless, symmetric and antisymmetric modes can be still identified from their frequency. As seen in chapter 3, the dimer separation determines the mode order: for an odd number of unit cells separating the defects, the antisymmetric mode has the highest frequency, while the opposite is true for an even number. In phase-sensitive detection schemes (which would require separate readout and driving laser beams), such a comparison with numerical simulations would not be necessary. From these mode profiles, the relative displacement amplitude of the modes can be measured. This allows us to determine γ.

4.5.2 Determining the dimer coupling rate

As derived in Appendix C and discussed in the previous chapter, the coupling rate γ can be obtained from the frequencies of the normal modes of a system Ω_+ and Ω_-. We must also measure $\tilde{\delta}$, the ratio of the displacement on the center of one defect to the displacement on the center of the other. To always have a value below 1, we take $\delta = \min(\tilde{\delta}, 1/\tilde{\delta})$. These parameters verify the equation

$$2\gamma^2\delta = |\Omega_+^2 - \Omega_-^2| - \sqrt{|\Omega_+^2 - \Omega_-^2|^2 - 4\gamma^2}, \tag{4.13}$$

from which γ can be extracted.

We measure $\Omega_+ - \Omega_-$ and show the results in fig. 4.27a: good agreement is found with the numerical simulations of chapter 3. Odd distances between the dimers were here not measured as the coupling was predicted to be low. In addition to measuring the mode frequencies, we measure δ for the highest frequency mode only (it is identical for both modes), shown in fig. 4.27b. For some samples, the mode detuning was too high to measure δ, and each mode appeared localized to a single defect. In these cases we take as an upper estimate for the displacement on the other defect the noise floor, giving an upper estimate for δ. These are indicated by red points in fig. 4.27b. Note that for both $|\Omega_+ - \Omega_-|$ and δ, significant dips are occasionally measured which are not predicted by simulations. We attributed these departures from the ideal situation to microfabrication uncertainties. Larger dimer separations are expected to reduce the sample robustness to geometric fluctuations. Still, even for distances of 11 units cells (1.8 mm), the modes were hybridized with $\delta \approx 0.3$.

We evaluate γ for this data by solving eq. (4.13) with the Newton method. The extracted values are shown in fig. 4.27c: the maximal coupling rate is $\gamma/2\pi \approx 60$ kHz, in close agreement with the numerical simulation of chapter 3.

4.6 Concluding remarks

To summarize, we have shown how PnC membranes are fabricated and characterized in our group. With a monolothic and mobile interferometer, the full thermal spectra of PnC membranes were obtained and their mode profiles accurately measured. We have verified that the PnC membrane designs introduced in the previous chapter behaved as simulated: we were able to spectrally isolate the fundamental defect mode from all others through an edge guard; as a result, the average Q_{b} of the mode increased by a factor 2, arriving to within 50% of the simulated value. These results were published in [118].

The difference in nature between defect and edge modes makes this result all the more necessary due to the fact that edge modes are "hard-clamped". Here, an ideal setup ensured that radiation loss was negligible compared to bending loss. However, in a number of experiments this is not the case. The relative degradation in the quality factor of defect modes is then exacerbated if they become hybridized with edge modes. An example of this is the electromechanical device presented in chapter 2, where the membrane chip was fixed in place with droplets of epoxy–this was shown in Ref. [87] to increase radiation loss by up to a factor 10 compared to a design similar to the one used in this chapter.

With the current membrane parameters ($\sigma_0 = 1$ GPa, $b = 160$ μm, $h = 100$ nm), we have obtained $Qf \approx 1.0 \times 10^{13}$ Hz at room temperature. In comparison, the fundamental mode of a plain membrane is expected to have $Qf \approx 2 \times 10^{12}$ Hz ne-

glecting radiation loss, a factor 5 lower. Importantly, this value for PnC membranes is a lower bound: firstly, Qf can be increased by modifying the membrane aspect ratio, as discussed above; secondly, we measured in chapter 2 that, in a cryogenic environment, $Qf = 5 \times 10^{13}$ Hz for plain membranes, consistent with findings in the literature. With the same "cryogenic boost", the Qf-product of PnC membranes is expected to increase by another order of magnitude. In future work, PnC membranes should be measured in a cryogenic environment to verify this estimate.

Furthermore, such a measurement would help determine another key parameter, namely the minimal achievable value of n_{eff}, the effective population of a mode in a sideband cooling experiment. n_{eff} has no physical meaning in the interferometer discussed in this chapter. In future work it should be verified whether the optimized PnC membrane design has helped to reduce it, ideally to a value below 1. This can be achieved by cooling the mechanical mode in an electromechanical cavity.

Finally, we have studied an application of mode couplings in PnC membranes: the coupling of two separate defect modes. The non-zero overlap between the two resulted in defect modes, with coupling rates up to $\gamma/2\pi = 60$ kHz, and presenting significant hybridization even for distances exceeding 1.8 mm. As a result, symmetric and antisymmetric normal modes arose.

Both of the "practical" membrane designs, namely generation 2 membranes and dimer membranes, pave the road for further advances in the project, towards ground-state cooling of mechanical motion, and the preparation of non-classical phononic states. In the following and final chapter, we discuss the conclusions of this work, the outlook following from our results, and the partial progress made towards achieving these goals.

Chapter 5

Conclusion and outlook

Throughout the previous chapters, we have interested ourselves in developing a MHz-frequency mechanical resonator. Our aim was to assert its suitability first of all in an electromechanical sideband cooling experiment. We aimed in particular to increase the Qf-product and decrease the smallest achievable mode population n_{eff}, for any mode of our choosing. The minimal requirement for these values is $Qf > 10^9$ Hz (at 20 mK) and $n_{\mathsf{eff}} < 1$. Plain silicon nitride (SiN) membranes were found in chapter 2 to be suboptimal for this task, despite having $Qf \approx 5 \times 10^{13}$ Hz, because $n_{\mathsf{eff}} \gtrsim 100$ even at the highest cooling powers. The principal limitation in the presented experiment was that the membrane mode was being driven by external laboratory noise, raising the effective mode temperature to approximately 1.4 K.

In this final chapter, we summarize our findings and discuss the outlooks that are enabled by this work. In particular, section 5.1 discusses potential further progress on single-defect PnC membranes and how they may be incorporated in an electromechanical experiment. With such samples, the ground state for a SiN membrane mode appears to be within reach. The next goal after achieving this is to prepare highly non-classical states of motion, which can prove useful in a number of domains. Their applications range from precision sensing to quantum information or fundamental coherence studies. Finally, section 5.2 proposes possible approaches for generating such states with SiN membranes.

5.1 Single-defect PnC membranes

Chapter 3 demonstrated that in nanomembranes the quality factors of their eigenmodes could be increased significantly could be increased significantly by localizing them away from the membrane borders. Through numerical simulations, we found that in the absence of a specific mode engineering strategy, hybridization of the defect mode with a set of parasitic "edge modes" would in practice strongly limit the achievable quality factor. With this in mind, an "edge guard" was introduced

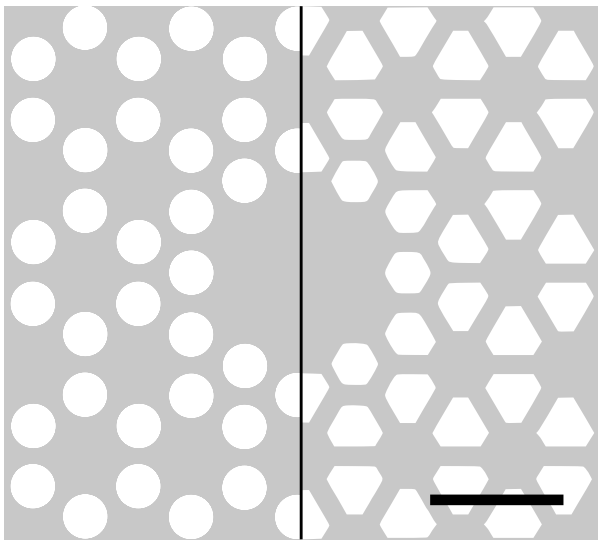

Figure 5.1: **(left)** Current design of the PnC membrane. **(right)** Optimized PnC membrane design, tweaking the shape of the central defect and of the PnC holes to optimize the mode profile. SiN is shown in gray, and the scale bar represents 200 μm. The author thanks L. Najera for his help with this figure.

to render the defect mode of interest robust to parasitic effects.

To experimentally verify the performance of the edge guard design, we characterized a large sample of PnC membranes by optical interferometry. We ensured the detection to be shot-noise limited to be able to measure the thermal motion of the various membrane eigenmodes. We thus reconstructed the spectrum of motion of the membrane, and asserted that the edge guard isolated the fundamental defect mode from any neighboring edge mode. Furthermore, by tracing the amplitude of motion of the defect mode as a function of position, we confirmed that in the absence of the edge guard, edge and defect modes hybridized. Ringdown measurements of Q demonstrated that this reduced the quality factor of defect modes by up to an order of magnitude. This also allowed us to verify that the measured values were in good agreement with numerical simulation. For edge-guarded PnC membranes the Qf-product exceeded that of plain membranes by a factor 10, for $h \approx 100$ nm. According to our estimations presented in chapter 3, this is still insufficient for reaching the ground state in an environment of temperature 1.4 K.

However, the phononic shielding around the defect modes should also serve to isolate them from technical noise, the cause of the excessively high environment temperature. We expect that this should help the mode thermalize with the cryostat's base temperature of 20 mK. Although we do not expect a reduction of n_{eff} with the presented samples, ground state cooling might still be made possible by this shielding.

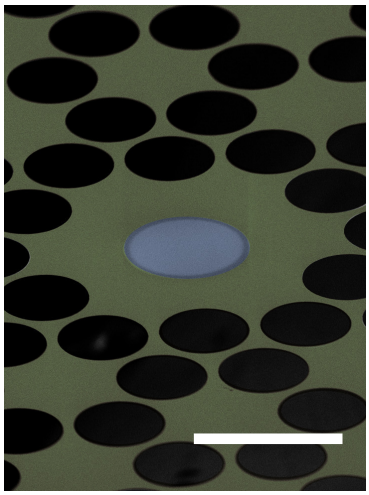

Figure 5.2: Scanning electron microscope image of a metalized PnC membrane. SiN is shown in dark yellow, and Nb is shown in blue. The scale bar represents 300 μm. Image courtesy of T. Capelle [43].

Two avenues are being considered to further improve the PnC membrane design. In essence, there are two elements of the membranes can be changed: the structure of the PnC itself (including the central defect) or the geometrical parameters of the membrane as a whole. Considering the former, the PnC was here chosen solely on the basis of matching the bandgap frequency to the resonance frequency of the central defect. However, further improvements can be made to optimize the mode shape, and reduce its curvature. As discussed in chapter 3, this would help improve on Qf or n_{eff}. A computer algorithm based on quadratic gradient-free optimization searches for the optima of these parameters by tweaking the shapes of the pads and tethers. For instance, n_{eff} is expected to decrease by a factor 2 with the optimized design shown in fig. 5.1.

The second avenue which can be explored is to increase membrane aspect-ratio. As found in chapter 3, Q_{b} for defect modes scales with the membrane geometry as $Q_{\mathsf{b}} \propto \sigma_0 b^2 h^{-1}$, where b is the PnC lattice parameter and σ_0 the tensile stress. Thus, even at a constant frequency (constant σ_0, b) Qf can still be increased by reducing h; in the literature, values as low as $h \approx 10$ nm have been employed [32]. With this modification, a hundredfold improvement in Q_{b} can be expected compared to plain membranes. As shown in chapter 3, reducing h by a factor 10 also reduces the minimal value for n_{eff} by a factor 100, making it in principle possible to reach the ground state even if the mode temperature is 1.4 K.

These suppositions can only be verified in a sideband cooling experiment. For this we need to couple a PnC membrane to a resonant microwave circuit, similar to the experiments of chapter 2. The work required to achieve this is substantial, in particular because a new fabrication protocol needs to be established. Prior to the

end of this thesis, some progress towards it had already been made: fig. 5.2 shows an image of a PnC membrane whose surface has been functionalized by the deposition of a Nb pad. Electromechanical cavities have already been fabricated with such samples but no microwave resonance could be measured. We suspect that polluting residues degraded the quality of the microwave resonance to an unmeasurable level. Further development on the fabrication protocol is required before positive results can be obtained. Once this has been achieved, an outstanding goal of the experiment will be to cool the fundamental defect mode and attempt to prepare it in its ground state.

While the zero-point motion of a harmonic oscillator is clearly a display of its quantum mechanical behavior, the resulting state can still be described with a purely positive Wigner function–this function can be interpreted as a classical probability distribution in phase space. Its interpretation no longer holds for non-Gaussian states, whose Wigner function can present some negativities [120]. Examples of such highly non-classical states include Fock states, containing exactly n phonons, or Schrödinger cat states (a superposition of two coherent states).

Preparing a mechanical resonator in non-Gaussian states is an important scientific milestone. Fundamentally, macroscopic quantum superpositions could be used to study gravitationally-induced decoherence mechanisms [121]. From a more applied perspective, non-Gaussian states are key for increasing the precision of force sensors beyond the standard quantum limit [122]; they could also be taken advantage of in quantum computing. In the following section we present some possible approaches to preparing an ultrahigh-Q SiN membrane mode in such a non-Gaussian quantum state.

5.2 Preparing non-Gaussian states of motion

Importantly, non-Gaussian states cannot be generated using only the electromechanical cavity presented in this work. The interaction is completely linear and the mechanical states produced by this system are always Gaussian if the initial state (here, thermal or vacuum) is Gaussian. A nonlinear element must be therefore introduced, and broadly speaking, there are two approaches to do so. The first one consists of coupling a mechanical element directly to a nonlinear resonator such as an artificial atom; the second requires the addition of an extrinsic nonlinearity, such as a single-photon emitter or detector. Both of these options are briefly presented below.

5.2.1 Direct coupling

This first approach lends itself well to the study of mechanical resonators fabricated with piezoelectric materials. Indeed, their intrinsic coupling to electric signals

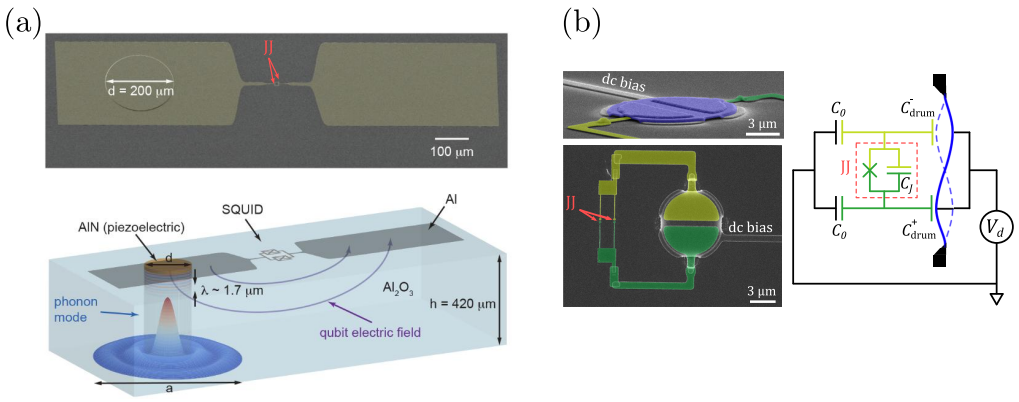

Figure 5.3: **a**, (Top) Optical micrograph of the top view of the BAR, on which the piezoelectric disk (diameter 200 μm) and the Josephson Junctions (JJ) of the qubit can be seen. (Bottom) Schematic of the BAR resonator. indicating the localization of the phonon mode (not to scale) energy. Images extracted from Chu et al. [15]. **b**, (Top left) SEM image of the aluminium plate and the DB bias line. (Bottom left) SEM image of the aluminium plate and the charge qubit, seen from the top. (Right) Electric diagram of the electromechanical device, showing the aluminium plate (blue) and the Cooper-pair box (red box). Images extracted from [16].

and their typically high frequencies allow a resonant coupling with superconducting qubits, with transition frequencies in the GHz range. A recent example of such a system came from the Schoelkopf Laboratory in Yale [15]: a frequency-tuneable qubit was strongly coupled to the phonon mode of a bulk acoustic resonator (BAR) using a piezoelectric disk. This device is illustrated in fig. 5.3a. When the qubit transition frequency was made resonant with the mechanical mode, single excitations were transferred from the former to the latter. In this manner, n-phonon Fock states were prepared [10].

Achieving the same kind of control over the state of an ultrahigh-Q mechanical resonator operating in the MHz range would have important consequences in quantum sciences and technologies. For instance, the lifetime of a quantum memory based on a high-Q SiN membrane such as the one described in chapter 2, if thermalized at 10 mK, would exceed 1 second[1]. Such low frequency resonators are also very effective in force sensing applications [4]. Finally, some collapse models predict that gravitationnal decoherence could become the dominant decoherence mechanism in low-frequency, ultrahigh-Q mechanical systems (see Chapter 6 of M. Gely's thesis [123] and Ref. [121]).

However, creating an interface between a superconducting qubit operating in the GHz range and a conventional mechanical resonator with a MHz resonance frequency is a significant challenge. A first experimental breakthrough in this direction has

[1]The thermal decoherence time is given by $(\Gamma_m n_{th})^{-1}$.

been demonstrated by the Lehnert laboratory [16]. In this experiment represented in fig. 5.3b, a thin aluminium plate is coupled to a superconducting qubit without resorting to the piezoelectric effect. A DC-bias needs to be applied to the vibrating plate to achieve this. By splitting the opposite electrode in two, the antisymmetric motion of the first-order mechanical mode gives rise to a differential charge offset across the qubit. By employing a highly non-linear qubit known as a Cooper-pair box, a sizable shift of the qubit transition frequency induced by the presence of a single phonon in the mechanical resonator could be observed. This effect was used to prepare mechanical states with sub-Poissonian probability distribution in the Fock basis. In principle, the dimer membrane presented in chapter 4 could be employed in a similar scheme, which would allow the use of mechanical resonators with significantly higher Qf-products. The principal limitations to the experiment of Ref. [16] were the low coherence properties of the Cooper-pair box caused by a high sensitivity to environmental charge noise. In the following section, we explore alternative approaches where a standard electromechanical system is employed in conjunction with a remote non-linear resource.

5.2.2 Extrinsic nonlinearity

Release-and-catch

Another strategy consists of keeping the electromechanical system linear, but connecting it via standard microwave transmission lines to a remote nonlinear resource. For instance, a single photon source was used by the Lehnert group [124] to excite a single-phonon state using the optomechanical interaction, with a state fidelity up to 83%. The advantage of such a modular approach is that the electromechanical and qubit systems can be packaged. Everything is only connected in the final stage of the experiment. However, the fidelity achievable in this "release-and-catch" approach is directly limited by losses in the transmission line between the photon source and the electromechanical system. In such a scheme, photon loss mixes the desired mechanical state with the initial Gaussian state. A "heralded state preparation" described in the following is an advantageous strategy which remains modular but is robust to photon losses.

Heralding

The principle of a detection-based preparation of non-Gaussian states is that instead of measuring the field quadrature with a homodyne detection (e.g. $\hat{a} + \hat{a}^\dagger$), the photon number $\hat{a}^\dagger\hat{a}$ is measured. Such a protocol was demonstrated to produce single-phonon states in the optical domain by the Gröblacher group [14]. A similar experiment could be performed in the microwave domain as well.

The principle of a heralded detection has been outlined e.g. in Ref. [14], and is summarized below. It is a detection-based protocol which uses the measurement to

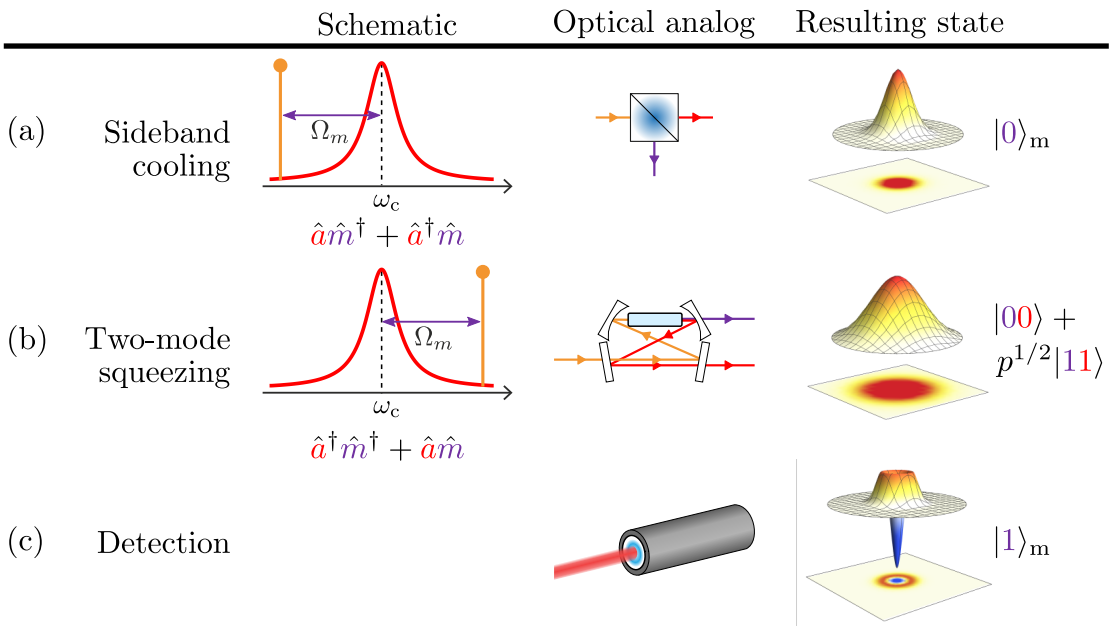

Figure 5.4: (More details in the main body) **a-c**, Principle of a herladed detection in electromechanics, in analogy to a purely optical system. The protocol is performed in three steps: **(a)** the sideband cooling interaction, **(b)** the two-mode-squeezing interaction, and **(c)** the detection of the output light field using a photon counter. For each step, the electromechanical interaction, the analogous optical component, and the resulting mechanical state (including the Wigner function) are shown. The index "m" after a ket indicates that it describes the Hilbert space of the phonon.

project the oscillator into the desired state using the measurement backaction. We propose to illustrate the protocol in analogy with a purely optical scheme, where a Fock-$|1\rangle$ state is prepared for a photon field.

The protocol starts by initializing the mechanical mode into the ground state. In electromechanics, this is achieved through the sideband cooling interaction; in the optical domain one would place a beamsplitter in front of the beam to ensure that its output is a vacuum state (fig. 5.4a). In chapter 1, we expressed the Hamiltonian of the electromechanical cavity in terms of the position $\hat{x}$ of the mode. This was consistent with the quadrature measurements presented throughout this thesis. Here, it will be more instructive to use the phonon ladder operator $\hat{m}$, with $\hat{x} \equiv x_{\mathsf{ZP}}\left(\hat{m} + \hat{m}^\dagger\right)$. In the presence of a pump, the interaction becomes linearized. The resulting effective Hamiltonian of the system depends on the frequency of the pump [20]: if it is on the blue mechanical sideband, we obtain what is known as the "two-mode-squeezing Hamiltonian" $\hat{H}_{\mathsf{tms}}$. In the interaction picture it reads

$$\hat{H}_{\mathsf{tms}} = \hbar g \left(\boxed{\delta\hat{a}^\dagger\, \hat{m}^\dagger} + \delta\hat{a}\hat{m} \right), \tag{5.1}$$

where $\delta\hat{a}$ represents fluctuations around the mean intracavity field.

Since the mechanical mode is in its ground-state, only the term boxed in red is permitted. It describes the simultaneous excitation of a photon on cavity resonance and of a phonon. If that interaction is applied, the mechanical state cannot be written independently of the intracavity field. We express the state of the electromechanical system as $|\psi\rangle_{\mathsf{em}}$, which initially reads $|\psi\rangle_{\mathsf{em}} = |00\rangle$ (both the mechanical mode and the cavity mode are in their ground states). If a short blue pulse (of duration $\tau \ll 1/g$) is sent into the cavity, the joint state reads

$$|\psi\rangle_{\mathsf{em}} \propto |00\rangle + p^{1/2}|11\rangle + p|22\rangle + \mathcal{O}\left(p^{3/2}\right), \tag{5.2}$$

where $p \ll 1$ is the excitation probability. The mechanical mode is still mostly in its ground state, but with a small probability a phonon has been excited; its creation is accompanied by the generation of a photon resonant with the cavity. In the optical domain, a weakly pumped optical parametric oscillator can be used to generate a similar state (fig. 5.4b). The generated photon travels down the measurement chain and can be measured with the "click" of a detector. Through this click the mechanical state is immediately projected onto the Fock-$|1\rangle$ state (fig. 5.4c). The protocol is probabilistic (there is a probability p of generating a phonon), but the "click" of the detector heralds the successful preparation of the system in the desired state.

The overall performance of this protocol can be characterized by the preparation fidelity of the Fock-$|1\rangle$ state on successful events. The overall fidelity is governed by three factors:

1. The probability of having one photon in the emitted wave packet, p. It is related to photon losses between the cavity and the detector.

2. The inefficiency $(1 - P[\text{click}|1])$. It gives the rate of false negative events: the probability of missing a click of the detector when a photon is emitted by the source. It is related to photon losses between the detector and the measurement apparatus.

3. The dark count ($P[\text{click}|0]$). It gives the rate of false positive events: the probability of measuring a click from the detector in the absence of an emitted photon. Its origin is discussed in section 5.2.3.

The infidelity $(1 - F)$ of the state is roughly given by the ratio of the noise to the signal. The signal is given by the probability of having a photon in the emitted wavepacket reduced by the inefficiency; the noise on the other hand is given by the dark count. Therefore, the infidelity reads

$$1 - F = \frac{P[\text{click}|0]}{pP[\text{click}|1]}. \tag{5.3}$$

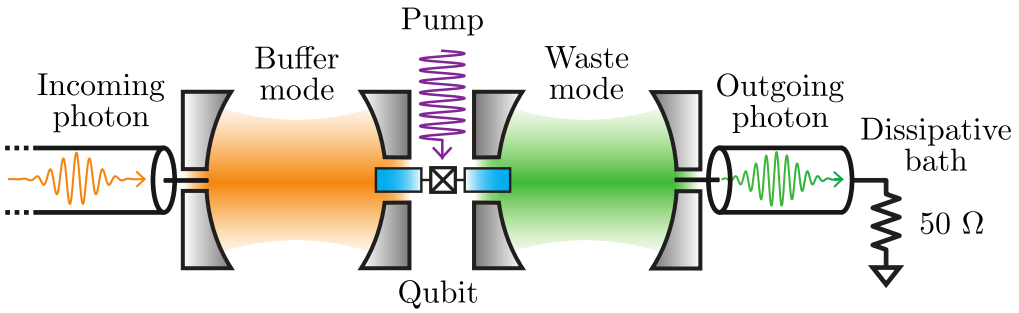

Figure 5.5: Illustration of the basic principle of the SMPD. The device comprises three elements: the buffer mode, the qubit, and the waste mode. A photon entering the buffer mode can be transduced into a photon in the waste mode, simultaneously exciting the qubit. The reverse is not possible due to the strong coupling of the waste mode to a lossy reservoir, preventing any spurious waste mode population. Figure adapted from [125].

Note the presence of the dark count rate $P[\text{click}|0]$ on the numerator. Even in the presence of finite photon losses ($pP[\text{click}|1] < 1$), the fidelity can be made arbitrarily large if the dark count rate is sufficiently low. In this sense, heralding schemes are said to be robust against photon losses.

Although low dark-count-rate photon detectors are available off-the-shelf in the optical domain, detecting the faint energy associated to microwave photons is much more challenging. Through a collaboration with the group of Zaki Leghtas at LPENS, a low dark-count single microwave photon detector (SMPD) based on superconducting qubits has been developed.

5.2.3 Counting single microwave photons

Several methods exist for counting single photons, but for brevity only the working principle of the SMPD developed with the group of Z. Legthas is discussed here. The interested reader is refered to Ref. [125] for further details.

The detector consists of three elements, shown in fig. 5.5: two harmonic oscillator modes, called the buffer and the waste, of frequency ω_b and ω_w; and a two-level-system (TLS) formed by an artificial atom of transition frequency ω_q. The Hamiltonian of such a system is highly nonlinear and contains many interaction terms. However, similarly to what we did for in the electromechanical Hamiltonian, specific terms can be amplified by pumping the qubit at the correct frequency. Here, the pump frequency is set to $\omega_\mathsf{L} = \omega_\mathsf{w} + \omega_\mathsf{q} - \omega_\mathsf{b}$. The pumped system is well described by the effective Hamiltonian

$$\hat{H}_{\mathsf{SMPD}} = \boxed{\chi \hat{b}\hat{\sigma}^\dagger \hat{w}^\dagger} + \chi^* \hat{b}^\dagger \hat{\sigma} \hat{w}, \tag{5.4}$$

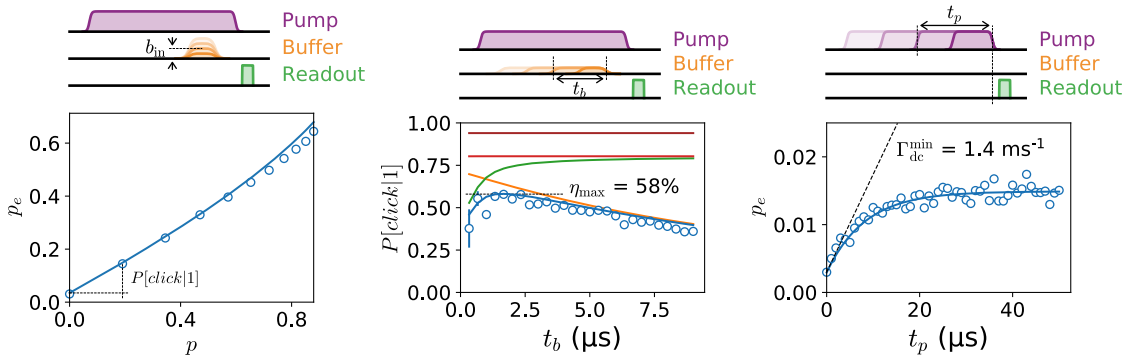

Figure 5.6: Three characterization experiments of the SMPD. **a**, The photon counting efficiency is tested by varying the amplitude b_{in} of the buffer pulse, and recording the average qubit population p_{e}. **b**, The duration of the buffer pulse t_{b} is varied and the variation of the efficiency of the detector is determined. **c**, The dark count of the detector is extracted by measuring p_{e} for varying pump pulse durations in the absence of a buffer pulse. Figure adapted from [125].

where $\hat{b}$ ($\hat{w}$) is the annihilation operator describing the buffer (waste) mode, $\hat{\sigma}$ is the annihilation operator for the qubit, and χ is the three-wave mixing rate. $\hat{H}_{\mathsf{SMPD}}$ can be interpreted in the following manner: if a photon enters the buffer cavity, then it can be transferred into the waste cavity by simultaneously exciting the qubit (as described by the term boxed in red). The qubit thus acts as the witness of the photon's passage. The state of the qubit can then be read at the end of the sequence by measuring the qubit-dependent shift of the waste cavity frequency. Note that this only works if the qubit is initialized in its ground state first. To prevent the reciprocal behavior ($\hat{b}^\dagger\hat{\sigma}\hat{w}$) which allows the qubit to relax, the waste cavity is strongly coupled to a dissipative bath. Thus, any incoming excitation is immediately damped in the environment, maintaining the waste in the ground state at all times.

The SMPD was characterized in the following manner:

- A "test run" of the detection is first made (fig. 5.6a). The SMPD is activated by the strong pump, and a short buffer tone of varying power b_{in} is sent into the buffer cavity. Afterwards, the pump is turned off and the state of the qubit is probed. For each value of b_{in}, the average population p_e of the qubit is recorded against the probability p of having a photon in the buffer pulse. The slope at the origin of the resulting curve is a measure of the efficiency $P[click|1]$.

- This experiment is repeated for varying buffer pulse duration t_{b} and the detector efficiency is recorded (fig. 5.6b). We find that the detector has an optimal functioning point for $t_{\mathsf{b}} \approx 2\ \mu$s. The corresponding maximal efficiency η_{max} is

$$\eta_{\mathsf{max}} \approx 0.58. \tag{5.5}$$

For shorter buffer pulse durations the detector efficiency is limited by the finite bandwidth of the buffer cavity, which doesn't accommodate for the spectral width of the incoming pulse. For longer t_{b} the buffer pulse duration exceeds the natural relaxation time of the qubit. The qubit eventually relaxes back into its ground state and reduces the measurement efficiency.

- Finally, the dark count of the SMPD is determined (fig. 5.6c). This is achieved by measuring whether or not the detector has "clicked" in the absence of a buffer pulse, for varying pump duration t_{p} (corresponding to the activation period of the detector). We find that the SMPD has a base dark count probability of 3×10^{-3} due to an improper ground-state initialization of the qubit. As t_{p} increases, so does the dark count, initially at a rate $\Gamma_{\mathsf{dc}}^{\mathsf{min}} \approx 1.4$ ms^{-1}. For short pump durations, the dark count probability reads

$$P[\text{click}|0] = 3 \times 10^{-3} + \Gamma_{\mathsf{dc}}^{\mathsf{min}} \mathrm{t}_{\mathsf{p}}. \tag{5.6}$$

  We attribute the increase of the dark count over time to thermal excitations of the qubit. This rate is an order of magnitude lower than comparable devices reported prior to this publication [126–129].

For a pump duration of the order of the microsecond and an optimal buffer pulse duration, assuming $p \sim 10^{-1}$, a state fidelity above 90% can be expected.

5.3 Concluding remarks

To summarize, in this thesis we have developed phononic engineering techniques for SiN nanomembranes. These will prove crucial for reaching the quantum regime of an electromechanical resonator with unprecedented coherence properties; we showed them to significantly outperform the non-optimized resonators measured in chapter 2. Since we measured plain SiN membrane modes to have lifetimes of the order of 30 s at cryogenic temperatures, we can expect ultralong coherence times for PnC membrane modes. The assembly of the electromechanical device with patterned membranes is ongoing. It will be measured in a dedicated dilution cryostat which arrived in the laboratory towards the end of 2020. In this manner, we will also be able to verify if the phononic shielding of PnC membrane modes helps them thermalize closer to the cryostat temperature.

Such a hybrid system is ideally suited for leveraging superconducting qubits as a nonlinear resource. It will allow us to prepare the membrane modes in non-Gaussian states characterized by negativities in the Wigner function. Heralding protocols, which exploit the backaction of the field measurement in the Fock-state basis, constitute a reliable method to prepare such nonclassical states. By developing a low dark-count-rate single-photon detector in collaboration with LPENS, we have demonstrated all the groundlaying elements to perform such an experiment.

These experiments are of interest for fundamental physics, as they could lead to the first study of gravitational decoherence mechanisms. Beyond this they can be used for quantum information technologies, where the mechanical resonator can play the role of highly sensitive force probes or quantum memories with long storage times.

Bibliography

[1]H. Cavendish, "Experiments to determine the Density of the Earth", Philosophical Transactions of the Royal Society of London **88**, 469–526 (1798).

[2]D. Rugar et al., "Single spin detection by magnetic resonance force microscopy", Nature **430**, 329–332 (2004).

[3]R. Fischer et al., "Spin detection with a micromechanical trampoline: towards magnetic resonance microscopy harnessing cavity optomechanics", New Journal of Physics **21**, 043049 (2019).

[4]L. Catalini, Y. Tsaturyan, and A. Schliesser, "Soft-Clamped Phononic Dimers for Mechanical Sensing and Transduction", Physical Review Applied **14**, 014041 (2020).

[5]D. Hälg et al., "Membrane-based scanning force microscopy", (2020).

[6]R. W. Andrews et al., "Bidirectional and efficient conversion between microwave and optical light", Nature Physics **10**, 321–326 (2014).

[7]A. Vainsencher et al., "Bi-directional conversion between microwave and optical frequencies in a piezoelectric optomechanical device", Applied Physics Letters **109**, 033107 (2016).

[8]W. Jiang et al., "Efficient bidirectional piezo-optomechanical transduction between microwave and optical frequency", Nature Communications **11**, 1166 (2020).

[9]M. Forsch et al., "Microwave-to-optics conversion using a mechanical oscillator in its quantum ground state", Nature Physics **16**, 69–74 (2020).

[10]Y. Chu et al., "Creation and control of multi-phonon Fock states in a bulk acoustic-wave resonator", Nature **563**, 666–670 (2018).

[11]A. D. O'Connell et al., "Quantum ground state and single-phonon control of a mechanical resonator", Nature **464**, 697–703 (2010).

[12]J. Chan et al., "Laser cooling of a nanomechanical oscillator into its quantum ground state", Nature **478**, 89–92 (2011).

[13]J. D. Teufel et al., "Sideband cooling of micromechanical motion to the quantum ground state", Nature **475**, 359–363 (2011).

[14]S. Hong et al., "Hanbury Brown and Twiss interferometry of single phonons from an optomechanical resonator", Science **358**, 203–206 (2017).

[15]Y. Chu et al., "Quantum acoustics with superconducting qubits", Science **358**, 199–202 (2017).

[16]J. J. Viennot, X. Ma, and K. W. Lehnert, "Phonon-Number-Sensitive Electromechanics", Physical Review Letters **121**, 183601 (2018).

[17]C. F. Ockeloen-Korppi et al., "Stabilized entanglement of massive mechanical oscillators", Nature **556**, 478–482 (2018).

[18]R. Riedinger et al., "Remote quantum entanglement between two micromechanical oscillators", Nature **556**, 473–477 (2018).

[19]J. Chen et al., "Entanglement of propagating optical modes via a mechanical interface", Nature Communications **11**, 943 (2020).

[20]M. Aspelmeyer, T. J. Kippenberg, and F. Marquardt, "Cavity optomechanics", Reviews of Modern Physics **86**, 1391–1452 (2014).

[21]B. M. Zwickl et al., "High quality mechanical and optical properties of commercial silicon nitride membranes", Applied Physics Letters **92**, 1–4 (2008).

[22]R. Riedinger et al., "Non-classical correlations between single photons and phonons from a mechanical oscillator", Nature **530**, 313–316 (2016).

[23]G. S. MacCabe et al., "Nano-acoustic resonator with ultralong phonon lifetime", Science **370**, 840–843 (2020).

[24]Y. Tsaturyan et al., "Ultracoherent nanomechanical resonators via soft clamping and dissipation dilution", Nature Nanotechnology **12**, 776–783 (2017).

[25]C. Reetz et al., "Analysis of Membrane Phononic Crystals with Wide Band Gaps and Low-Mass Defects", Physical Review Applied **12**, 044027 (2019).

[26]C. M. Caves, "Quantum-mechanical noise in an interferometer", Physical Review D **23**, 1693–1708 (1981).

[27]O. Arcizet et al., "Radiation-pressure cooling and optomechanical instability of a micromirror", Nature **444**, 71–74 (2006).

[28]S. Gigan et al., "Self-cooling of a micromirror by radiation pressure", Nature **444**, 67–70 (2006).

[29]A. Schliesser et al., "Radiation pressure cooling of a micromechanical oscillator using dynamical backaction", Physical Review Letters **97**, 1–4 (2006).

[30]S. Weis et al., "Optomechanically Induced Transparency", Science **330**, 1520–1523 (2010).

[31]A. H. Ghadimi et al., "Elastic strain engineering for ultralow mechanical dissipation", Science **360**, 764–768 (2018).

[32]I. Galinskiy et al., "Phonon counting thermometry of an ultracoherent membrane resonator near its motional ground state", Optica **7**, 718 (2020).

[33]A. P. Higginbotham et al., "Harnessing electro-optic correlations in an efficient mechanical converter", Nature Physics **14**, 1038–1042 (2018).

[34]U. Delić et al., "Cooling of a levitated nanoparticle to the motional quantum ground state", Science **367**, 892–895 (2020).

[35]A. A. Clerk et al., "Introduction to quantum noise, measurement, and amplification", Reviews of Modern Physics **82**, 1155–1208 (2010).

[36]D. T. Gillespie, "The mathematics of Brownian motion and Johnson noise", American Journal of Physics **64**, 225–240 (1996).

[37]H. B. Callen and T. A. Welton, "Irreversibility and Generalized Noise", Physical Review **83**, 34–40 (1951).

[38]G. J. M. Warwick P. Bowen, *Quantum Optomechanics* (OSA, London, 2015).

[39]F. Elste, S. M. Girvin, and A. A. Clerk, "Quantum Noise Interference and Backaction Cooling in Cavity Nanomechanics", Physical Review Letters **102**, 207209 (2009).

[40]T. J. Kippenberg et al., "Analysis of Radiation-Pressure Induced Mechanical Oscillation of an Optical Microcavity", Physical Review Letters **95**, 033901 (2005).

[41]H.-K. Lau and A. A. Clerk, "Ground state cooling and high-fidelity quantum transduction via parametrically-driven bad-cavity optomechanics", (2019).

[42]M. Brunelli et al., "Stroboscopic quantum optomechanics", Physical Review Research **2**, 023241 (2020).

[43]T. Capelle, "Ground state cooling of a mechanical oscillator and electromechanical parametric amplification", PhD thesis (2020).

[44]L. G. Villanueva and S. Schmid, "Evidence of Surface Loss as Ubiquitous Limiting Damping Mechanism in SiN Micro- and Nanomechanical Resonators", Physical Review Letters **113**, 227201 (2014).

[45]I. Marinković et al., "Optomechanical Bell Test", Physical Review Letters **121**, 220404 (2018).

[46]I. Shomroni, L. Qiu, and T. J. Kippenberg, "Optomechanical generation of a mechanical catlike state by phonon subtraction", Physical Review A **101**, 033812 (2020).

[47]I. C. Rodrigues, D. Bothner, and G. A. Steele, "Coupling microwave photons to a mechanical resonator using quantum interference", Nature Communications **10**, 5359 (2019).

[48]S. S. Verbridge et al., "High quality factor resonance at room temperature with nanostrings under high tensile stress", Journal of Applied Physics **99**, 10.1063/1.2204829 (2006).

[49]A. Zarka and F. Bastien, "Physical limitation on the quality factor of quartz resonators", Journal of the Acoustical Society of America **94**, 917–922 (1993).

[50]P. F. Cohadon, A. Heidmann, and M. Pinard, "Cooling of a Mirror by Radiation Pressure", Physical Review Letters **83**, 3174–3177 (1999).

[51]D. Rugar and P. Grütter, "Mechanical parametric amplification and thermomechanical noise squeezing", Physical Review Letters **67**, 699–702 (1991).

[52]A. H. Safavi-Naeini et al., "Observation of Quantum Motion of a Nanomechanical Resonator", Physical Review Letters **108**, 033602 (2012).

[53]M. Wu et al., "Microwave-to-Optical Transduction Using a Mechanical Supermode for Coupling Piezoelectric and Optomechanical Resonators", Physical Review Applied **13**, 1 (2020).

[54]G. A. Peterson et al., "Ultrastrong Parametric Coupling between a Superconducting Cavity and a Mechanical Resonator", Physical Review Letters **123**, 247701 (2019).

[55]B. Lassagne et al., "Ultrasensitive Mass Sensing with a Nanotube Electromechanical Resonator", Nano Letters **8**, 3735–3738 (2008).

[56]S. Blien et al., "Quantum capacitance mediated carbon nanotube optomechanics", Nature Communications, 1–6 (2019).

[57]X. Song et al., "Graphene optomechanics realized at microwave frequencies", Physical Review Letters **113**, 1–5 (2014).

[58]A. B. Shkarin et al., "Quantum Optomechanics in a Liquid", Physical Review Letters **122**, 153601 (2019).

[59]R. Riedinger et al., "Remote quantum entanglement between two micromechanical oscillators", Nature **556**, 473–477 (2018).

[60]M. Rossi et al., "Observing and Verifying the Quantum Trajectory of a Mechanical Resonator", Physical Review Letters **123**, 163601 (2019).

[61]J. M. Fink et al., "Quantum electromechanics on silicon nitride nanomembranes", Nature Communications **7**, 12396 (2016).

[62]F. Hoehne et al., "Damping in high-frequency metallic nanomechanical resonators", Physical Review B **81**, 1–5 (2010).

[63]B. D. Hauer et al., "Two-level system damping in a quasi-one-dimensional optomechanical resonator", Physical Review B **98**, 10.1103/PhysRevB.98.214303 (2018).

[64]M. Hamoumi et al., "Microscopic Nanomechanical Dissipation in Gallium Arsenide Resonators", Physical Review Letters **120**, 1–6 (2018).

[65]X. Zhou et al., "On-chip Thermometry for Microwave Optomechanics Implemented in a Nuclear Demagnetization Cryostat", Physical Review Applied **12**, 044066 (2019).

[66]M. Yuan et al., "Large cooperativity and microkelvin cooling with a three-dimensional optomechanical cavity", Nature Communications **6**, 8491 (2015).

[67]Q. P. Unterreithmeier, E. M. Weig, and J. P. Kotthaus, "Universal transduction scheme for nanomechanical systems based on dielectric forces", Nature **458**, 1001–1004 (2009).

[68]S. A. Fedorov et al., "Generalized dissipation dilution in strained mechanical resonators", Physical Review B **99**, 1–8 (2019).

[69]A. Noguchi et al., "Ground state cooling of a quantum electromechanical system with a silicon nitride membrane in a 3D loop-gap cavity", New Journal of Physics **18**, 103036 (2016).

[70]K. Geerlings et al., "Improving the quality factor of microwave compact resonators by optimizing their geometrical parameters", Applied Physics Letters **100**, 1–4 (2012).

[71]S. Kuhr et al., "Ultrahigh finesse Fabry-Pérot superconducting resonator", Applied Physics Letters **90**, 1–4 (2007).

[72]E. Wu, Y. H. Ma, and X. G. Han, "Observation of electromagnetically induced transparency in a ring cavity", Central European Journal of Physics **10**, 1216–1220 (2012).

[73]F. Massel et al., "Microwave amplification with nanomechanical resonators", Nature **480**, 351–354 (2011).

[74]M. L. Gorodetsky et al., "Determination of the vacuum optomechanical coupling rate using frequency noise calibration", Optics Express **18**, 23236 (2010).

[75]P. L. Yu et al., "A phononic bandgap shield for high-Q membrane microresonators", Applied Physics Letters **104**, 2–6 (2014).

[76]A. H. Ghadimi, D. J. Wilson, and T. J. Kippenberg, "Radiation and Internal Loss Engineering of High-Stress Silicon Nitride Nanobeams", Nano Letters **17**, 3501–3505 (2017).

[77]P.-L. Yu, T. P. Purdy, and C. A. Regal, "Control of Material Damping in High-Q Membrane Microresonators", Physical Review Letters **108**, 083603 (2012).

[78]A. W. Leissa, *Vibration of Plates* (Scientific, Technical Information Division, National Aeronautics, and Space Administration, 1969).

[79]C. Zener, "Internal friction in solids II. General theory of thermoelastic internal friction", Physical Review **53**, 90–99 (1938).

[80]Q. P. Unterreithmeier, T. Faust, and J. P. Kotthaus, "Damping of Nanomechanical Resonators", Physical Review Letters **105**, 027205 (2010).

[81]S. Timoshenko, *Vibration problems in engineering*, Vol. 207, 2 (1928).

[82]K. Yasumura et al., "Quality factors in micron- and submicron-thick cantilevers", Journal of Microelectromechanical Systems **9**, 117–125 (2000).

[83]E. Ivanov, "Edouard Ivanov Thesis: Comsol scripts.", Zenodo, `10.5281/zenodo.4090417`.

[84]A. Jöckel et al., "Spectroscopy of mechanical dissipation in micro-mechanical membranes", Applied Physics Letters **99**, 143109 (2011).

[85]I. Wilson-Rae, "Intrinsic dissipation in nanomechanical resonators due to phonon tunneling", Physical Review B **77**, 245418 (2008).

[86]I. Wilson-Rae et al., "High-Q nanomechanics via destructive interference of elastic waves", Physical Review Letters **106**, 1–4 (2011).

[87]S. Schmid et al., "Damping mechanisms in high-Q micro and nanomechanical string resonators", Physical Review B **84**, 165307 (2011).

[88]T. M. Karg et al., "Light-mediated strong coupling between a mechanical oscillator and atomic spins 1 meter apart", Science **369**, 174–179 (2020).

[89]M. Underwood et al., "Measurement of the motional sidebands of a nanogram-scale oscillator in the quantum regime", Physical Review A - Atomic, Molecular, and Optical Physics **92**, 1–5 (2015).

[90]G. D. Cole et al., "Phonon-tunnelling dissipation in mechanical resonators", Nature Communications **2**, 231 (2011).

[91]C. Reinhardt et al., "Ultralow-noise SiN trampoline resonators for sensing and optomechanics", Physical Review X **6**, 1–8 (2016).

[92]R. A. Norte, J. P. Moura, and S. Gröblacher, "Mechanical Resonators for Quantum Optomechanics Experiments at Room Temperature", Physical Review Letters **116**, 147202 (2016).

[93]M. Rossi et al., "Measurement-based quantum control of mechanical motion", Nature **563**, 53–58 (2018).

[94]M. M. Sigalas and E. N. Economou, "Elastic waves in plates with periodically placed inclusions", Journal of Applied Physics **75**, 2845–2850 (1994).

[95]J. D. Joannopoulos, P. R. Villeneuve, and S. Fan, "Photonic crystals", Solid State Communications **102**, 165–173 (1997).

[96]S. Bittner et al., "Observation of a Dirac point in microwave experiments with a photonic crystal modeling graphene", Physical Review B **82**, 014301 (2010).

[97]M. Sigalas and E. Economou, "Elastic and acoustic wave band structure", Journal of Sound and Vibration **158**, 377–382 (1992).

[98]P. Soltan-Panahi et al., "Multi-component quantum gases in spin-dependent hexagonal lattices", Nature Physics **7**, 434–440 (2011).

[99]T. Jacqmin et al., "Direct Observation of Dirac Cones and a Flatband in a Honeycomb Lattice for Polaritons", Physical Review Letters **112**, 116402 (2014).

[100]S. A. Fedorov et al., "Fractal-like Mechanical Resonators with a Soft-Clamped Fundamental Mode", Physical Review Letters **124**, 025502 (2020).

[101]S. Mohammadi et al., "Complete phononic bandgaps and bandgap maps in two-dimensional silicon phononic crystal plates", Electronics Letters **43**, 898 (2007).

[102]V. V. Zalipaev et al., "Elastic waves and homogenization in oblique periodic structures", Proceedings of the Royal Society of London. Series A: Mathematical, Physical and Engineering Sciences **458**, 1887–1912 (2002).

[103]S. A. Fedorov et al., "Thermal intermodulation noise in cavity-based measurements", Optica **7**, 1609 (2020).

[104]E. Ivanov et al., "Edge mode engineering for optimal ultracoherent silicon nitride membranes", Applied Physics Letters **117**, 254102 (2020).

[105]C. Brendel et al., "Pseudomagnetic fields for sound at the nanoscale", Proceedings of the National Academy of Sciences of the United States of America **114**, E3390–E3395 (2017).

[106]B. Xia, H. Fan, and T. Liu, "Topologically protected edge states of phoxonic crystals", International Journal of Mechanical Sciences **155**, 197–205 (2019).

[107]X. Ma et al., "Nonclassical energy squeezing of a macroscopic mechanical oscillator", arXiv:2005.04260 (2020).

[108]*Silicon Materials. url: https://www.si-mat.com/*, 2020.

[109]*NOVA Electronic Materials, LLC. url: http://www.novawafers.com/*, 2020.

[110]*Sil'tronix Silicon Technologie. url: https://www.sil-tronix-st.com.*

[111]X. Chen et al., "High-finesse Fabry-Perot cavities with bidimensional Si3N4photonic-crystal slabs", Light: Science and Applications **6**, 1–8 (2017).

[112]A. Beccari, "High aspect ratio Si3N4 nanomembranes", NanoFab-Net, `10.5281/zenodo.3898901` (2020).

[113]K. E. Petersen, "Silicon as a mechanical material", Micromechanics and MEMS: Classic and Seminal Papers to 1990 **70**, 58–95 (1997).

[114]*AMMT. url: https://www.ammt.com/products/wet-etching/*, 2020.

[115] *Brewer Science, Inc. url: https://www.brewerscience.com/products/protek-psb/*, 2020.

[116] *Thorlabs, Inc. url: https://www.thorlabs.com/*, 2020.

[117] A. Barg et al., "Measuring and Imaging Nanomechanical Motion with Laser Light", in *Exploring the world with the laser* (Springer International Publishing, Cham, 2018), pp. 71–85.

[118] E. Ivanov, "Fabrication of patterned silicon nitride nanomembranes at the LKB", NanoFab-Net, `10.5281/zenodo.4120417` (2020).

[119] S. Bianco et al., "Silicon resonant microcantilevers for absolute pressure measurement", Journal of Vacuum Science & Technology B: Microelectronics and Nanometer Structures **24**, 1803 (2006).

[120] A. Kenfack and K. Yczkowski, "Negativity of the Wigner function as an indicator of non-classicality", Journal of Optics B: Quantum and Semiclassical Optics **6**, 396–404 (2004).

[121] D. Kleckner et al., "Creating and verifying a quantum superposition in a micro-optomechanical system", New Journal of Physics **10**, 095020 (2008).

[122] F. Wolf et al., "Motional Fock states for quantum-enhanced amplitude and phase measurements with trapped ions", Nature Communications **10**, 1–8 (2018).

[123] M. F. Gely, "Measuring and controlling radio-frequency quanta with superconducting circuits", PhD thesis (Apr. 2020).

[124] A. P. Reed et al., "Faithful conversion of propagating quantum information to mechanical motion", Nature Physics **13**, 1163–1167 (2017).

[125] R. Lescanne et al., "Irreversible Qubit-Photon Coupling for the Detection of Itinerant Microwave Photons", Physical Review X **10**, 021038 (2020).

[126] A. Narla et al., "Robust Concurrent Remote Entanglement Between Two Superconducting Qubits", Physical Review X **6**, 031036 (2016).

[127] K. Inomata et al., "Single microwave-photon detector using an artificial Λ-type three-level system", Nature Communications **7**, 1–7 (2016).

[128] A. Opremcak et al., "Measurement of a superconducting qubit with a microwave photon counter", Science **361**, 1239–1242 (2018).

[129] S. Kono et al., "Quantum non-demolition detection of an itinerant microwave photon", Nature Physics **14**, 546–549 (2018).

[130] T. C. Mele, "Selective and anisotropic reactive ion etch of LPCVD silicon nitride with CHF3 based gases", Journal of Vacuum Science & Technology B: Microelectronics and Nanometer Structures **2**, 684 (1984).

Appendix A

Calibrating the resonator population

Here, we derive the method for calibrating the PSD of the probe sidebands based on a reference noise quantity, following the principles described in [35]. Specifically, we compare the magnitude of the mechanical noise to the measurement noise floor, assumed known. It is added to the signal by the amplification chain.

In the sideband cooling experiment of chapter 2, a phase-insensitive amplification chain is used to directly amplify the amplitude of the complex field $\delta\hat{a}$. Both quadratures of the field are thus amplified and it naturally follows from quantum mechanics that the amplifier must also contribute a minimal amount of noise [35]. In practice, the added noise from the amplification chain is some 20 times higher than this minimum. The amplification noise can be calibrated separately (see Ref. [43]), and we will use that fact to link the measured current noise spectrum $\bar{S}_{ii}$ to the mechanical noise spectrum $\bar{S}_{xx}$. Quantum noises in $\bar{S}_{\hat{x}\hat{x}}$ are here neglected since they are significantly smaller than the classical noise added by the amplifier.

We model the measurement chain as a three-step process, illustrated in fig. A.1.

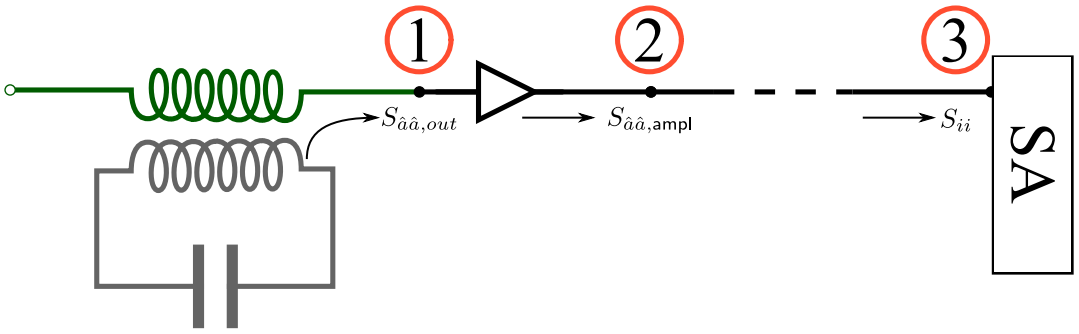

Figure A.1: Simplified measurement chain of the electromechanical signal until it reaches the spectrum analyzer (SA). The steps 1-3 are described in the main body.

The steps indicated in the figure represent key transitions in the signal, and are as follows:

1. *The signal leaves the cavity.* We find from eq. (1.50) that the intracavity field fluctuations, for $\bar{\Delta} = -\Omega_{\mathsf{m}}$ and for frequencies Ω near the mechanical resonance frequency Ω_{m}, reads

$$\delta\hat{a}[\Omega] \approx \frac{2i\alpha G}{\kappa}\hat{x}[\Omega], \tag{A.1}$$

   where the input field terms have been neglected. From the input-output formalism for a hanger cavity (as applicable to section 2.3), $\delta\hat{a}_{\mathsf{out}} = \sqrt{\kappa_{\mathsf{c}}/2}\delta\hat{a}$. The output field noise spectrum $\bar{S}_{\hat{a}\hat{a},\mathsf{out}}$ then reads

$$\bar{S}_{\hat{a}\hat{a},\mathsf{out}} = \frac{\eta\Gamma_{\mathsf{m}}C}{2}\frac{\bar{S}_{\hat{x}\hat{x}}[\Omega]}{2x_{\mathsf{ZP}}^2}. \tag{A.2}$$

2. *The signal is amplified.* We assume that, before reaching the first amplifier, the signal is attenuated by a factor $\mathcal{A}$. The amplifier then amplifies $S_{\hat{a}\hat{a}}$ and adds a certain amount of noise to the signal, which can be described in terms of an added amount of noise quanta n_{ampl}. The expression for the amplified noise spectrum $S_{\hat{a}\hat{a},\mathsf{ampl}}$ reads

$$\bar{S}_{\hat{a}\hat{a},\mathsf{ampl}}[\Omega] = \mathcal{G}\left(\mathcal{A}\bar{S}_{\hat{a}\hat{a},\mathsf{out}} + n_{\mathsf{ampl}}\right), \tag{A.3}$$

   where $\mathcal{G}$ is the gain of the amplifier.

3. *The signal reaches the measurement device.* From the amplifier to the measurement device (which is in this case a spectrum analyzer), the total signal may be additionally amplified or attenuated. Finally, we measured a current, which is related to the amplified field by

$$\bar{S}_{ii}[\Omega] = K(\Omega) \times \left(\mathcal{A}\frac{\eta\Gamma_{\mathsf{m}}C}{2}\frac{\bar{S}_{\hat{x}\hat{x}}[\Omega]}{2x_{\mathsf{ZP}}^2} + n_{\mathsf{ampl}}\right), \tag{A.4}$$

   where K is a transfer function encompassing the effect of any subsequent attenuation or amplification, as well as the conversion factor from the light field noise to the current noise.

Note that eq. (A.4) is valid so long as no significant amount of noise is added to the system after the first amplifier. This is usually true, as in a measurement chain, if $\mathcal{G}$ is sufficiently large the noise added by any subsequent device is negligible.

Considering the noise spectrum at a frequency $\Omega_{\mathsf{ref}} \neq \Omega_{\mathsf{m}}$, such that $\bar{S}_{\hat{x}\hat{x}}[\Omega_{\mathsf{ref}}] \approx 0$,

then $\bar{S}_{ii}[\Omega_{\mathsf{ref}}] \approx K(\Omega_{\mathsf{ref}}) n_{\mathsf{ampl}}$. Assuming that $K(\Omega_{\mathsf{ref}}) \approx K(\Omega_{\mathsf{m}})$, we can write

$$\bar{S}_{ii}[\Omega] \approx \frac{\bar{S}_{ii}[\Omega_{\mathsf{ref}}]}{n_{\mathsf{ampl}}} \times \left(\mathcal{A} \frac{\eta \Gamma_{\mathsf{m}} C}{2} \frac{\bar{S}_{\hat{x}\hat{x}}[\Omega]}{2x_{\mathsf{ZP}}^2} + n_{\mathsf{ampl}} \right), \tag{A.5}$$

which can be readily solved for $\bar{S}_{\hat{x}\hat{x}}[\Omega]$.

Appendix B

Scaling of the effective population

Based on the derived scaling of losses in chapter 3, we derive in this appendix how the effective membrane population n_{eff} in a sideband cooling experiment depends on the membrane parameters. We consider the tensile stress σ_0, the side length l, and the thickness h. In particular, we wish to find how n_{eff} can be reduced for a given intracavity field amplitude α. For simplicity, we neglect all quantum effects since the ground state is not reached. n_{eff} can then be taken as the effective thermal population derived in eq. (1.68). For $C \gg 1 + \eta_{\mathsf{rsf}}^{-1}$, the effective population reads

$$n_{\mathsf{eff}} \approx \frac{n_{\mathsf{th}}}{C}. \tag{B.1}$$

Recalling that $n_{\mathsf{th}} \approx k_{\mathsf{B}} T_{\mathsf{env}}/\hbar\Omega_{\mathsf{m}}$, $C \equiv 4g_0\alpha^2/\kappa\Gamma_{\mathsf{m}}$, we obtain the following expression:

$$n_{\mathsf{eff}} \approx \frac{k_{\mathsf{B}} T_{\mathsf{env}}}{\hbar\Omega_{\mathsf{m}}} \times \frac{\kappa\Gamma_{\mathsf{m}}}{4g_0^2\alpha^2}. \tag{B.2}$$

The vacuum coupling rate implicitly depends on the resonator geometry as well, since $g_0 \equiv \sqrt{\hbar/2m_{\mathsf{eff}}\Omega_{\mathsf{m}}}\,(\partial\omega_{\mathsf{c}}/\partial x)$. The resonator population then reads

$$n_{\mathsf{eff}} \approx \frac{k_{\mathsf{B}} T_{\mathsf{env}}\kappa}{2\hbar^2\alpha^2} \times \boxed{\Gamma_{\mathsf{m}} m_{\mathsf{eff}}} \times \left(\frac{\partial\omega_{\mathsf{c}}}{\partial x}\right)^{-2}. \tag{B.3}$$

In eq. (B.3), only the terms boxed in red depend on the relevant parameters. Indeed, if we model the capacity of the microwave circuit as a parallel plate capacitor, $\omega_{\mathsf{c}} \propto \sqrt{x}$, and $\partial\omega_{\mathsf{c}}/\partial x = \omega_{\mathsf{c}}/2x$. Since ω_{c} is defined independently of the membrane design, $\partial\omega_{\mathsf{c}}/\partial x$ is independent of the geometric parameters.

In chapter 3, we derived the following scalings:

- $\Gamma_{\mathsf{m}} \propto l^{-2}$. We obtain this scaling from the relation $\Gamma_{\mathsf{m}} = \Omega_{\mathsf{m}}/Q$. Considering only bending losses, $Q \propto l\sqrt{\sigma_0}$, and $\Omega_{\mathsf{m}} \propto \sqrt{\sigma_0}/l$.

- $m_{\mathsf{eff}} \propto l^2$.

In terms of geometric parameters, we can thus write

$$n_{\mathsf{eff}} \propto h. \tag{B.4}$$

This follows from the fact that a thinner membrane is lighter, and has a higher susceptibility to the cavity backaction.

Appendix C

Coupled damped harmonic oscillators

In this Appendix, we derive the eigenvectors, eigenfrequencies, and losses for two coupled harmonic oscillators, modeled as point masses. Let Ω_1 (Ω_2) denote the frequency of the first (second) oscillator, and Γ_1 (Γ_2) denote the energy dissipation rate of the first (second) oscillator. Furthermore, let X_1 (X_2) be the position of the first (second) oscillator. Let γ be the rate at which the two oscillators exchange energies. The equations of motion of the system, derived from Newton's second law, are

$$\ddot{X}_1(t) + \Gamma_1 \dot{X}_1(t) + \Omega_1^2 X_1(t) + \gamma^2 X_2(t) = 0, \tag{C.1}$$

$$\ddot{X}_2(t) + \Gamma_2 \dot{X}_2(t) + \Omega_2^2 X_2(t) + \gamma^2 X_1(t) = 0. \tag{C.2}$$

We assume that the two masses undergo harmonic oscillations. We hence take the following Ansatz for their solutions: $X_{1,2}(t) = \bar{X}_{1,2} e^{i\tilde{\Omega}t}$, where $\tilde{\Omega}$ is a complex eigenfrequency. The equations of motion can be then be written in the following matrix form:

$$\underline{\underline{M}}\bar{\mathbf{X}} = \mathbf{0}, \tag{C.3}$$

where $\bar{\mathbf{X}} = \left(\bar{X}_1, \bar{X}_2\right)^{\mathsf{T}}$. The 2x2 matrix $\underline{\underline{M}}$ is given by:

$$\underline{\underline{M}} = \begin{pmatrix} -\tilde{\Omega}^2 + \Omega_1^2 + i\Gamma_1\tilde{\Omega} & \gamma^2 \\ \gamma^2 & -\tilde{\Omega}^2 + \Omega_2^2 + i\Gamma_2\tilde{\Omega} \end{pmatrix}. \tag{C.4}$$

The system admits nontrivial solutions (i.e. $\mathbf{X} \neq \mathbf{0}$) if $\det\left(\underline{\underline{M}}\right) = 0$.

C.1 Eigenfrequencies

To solve this equation, we explicitly separate the eigenfrequency into its real and imaginary components: $\tilde{\Omega} = \Omega + i\Gamma/2$. Because high quality factor resonators are exclusively studied throughout this work, we assume that $\Omega > \gamma \gg \Gamma$, and treat Γ as a perturbation parameter. Separating the equation $\det\left(\underline{\underline{M}}\right) = 0$ into its real and imaginary terms yields the two following equations:

$$\Omega^4 - \Omega^2\left(\Omega_2^2 + \Omega_1^2\right) + \Omega_1^2\Omega_2^2 - \gamma^4 \approx 0 \tag{C.5}$$

$$\Gamma\left(2\Omega^2 - \Omega_2^2 - \Omega_1^2\right) - \Gamma_2\left(\Omega^2 - \Omega_1^2\right) - \Gamma_1\left(\Omega^2 - \Omega_2^2\right) \approx 0. \tag{C.6}$$

In eq. (C.5), only the terms of $\mathcal{O}\left(\Omega^4\right)$ were kept; in eq. (C.6), only terms of $\mathcal{O}\left(\Gamma\Omega^2\right)$ were kept. From eq. (C.5), two eigenfrequencies are found:

$$\Omega_\pm^2 = \frac{1}{2}\left(\Omega_1^2 + \Omega_2^2 \pm \sqrt{(\Omega_1^2 - \Omega_2^2)^2 + 4\gamma^4}\right). \tag{C.7}$$

From the terms inside the square root, two regimes stand out which are distinguished by the relative weight of γ with respect to the difference between the two natural frequencies. In the large detuning regime where $\gamma^2 \ll |\Omega_1^2 - \Omega_2^2|$, the eigenfrequencies are restored to the natural frequencies Ω_1 and Ω_2. On the other hand, in the small detuning regime where $\gamma^2 \gg |\Omega_1^2 - \Omega_2^2|$, the eigenfrequencies are separated symmetrically around the average of the natural frequencies, with $\Omega_+^2 - \Omega_-^2 = 2\gamma^2$.

Substituting eq. (C.7) into eq. (C.6), the dissipation rates of the normal modes can be found. They read

$$\Gamma_\pm = \frac{\Gamma_1\left(\Omega_\pm^2 - \Omega_2^2\right) + \Gamma_2\left(\Omega_\pm^2 - \Omega_1^2\right)}{\left(\Omega_\pm^2 - \Omega_2^2\right) + \left(\Omega_\pm^2 - \Omega_1^2\right)}. \tag{C.8}$$

In the small detuning regime, Γ_+ and Γ_- converge to the same value, which is the average of the natural dissipation rates: $2\Gamma_\pm \to \Gamma_1 + \Gamma_2$. In the large detuning regime, the two values tend to the natural dissipation rates, here $\Gamma_+ \to \Gamma_1$ and $\Gamma_- \to \Gamma_2$.

C.2 Eigenvectors

The eigenvectors can be found by substituting eq. (C.7) into eq. (C.3). For this calculation, we neglect any term $\mathcal{O}(\Gamma)$ and above, as they add minimal corrections to the result. Let $\mathbf{X}_\pm$ denote the eigenvectors of the system, which read

$$\mathbf{X}_\pm = N_\pm\begin{pmatrix} \pm 2\gamma^2 \\ \sqrt{(\Omega_1^2 - \Omega_2^2) + 4\gamma^4} \mp (\Omega_1^2 - \Omega_2^2) \end{pmatrix} \tag{C.9}$$

where N_+ and N_- are normalization factors ensuring that the norms of the eigenvectors are 1. In the small detuning limit, the modes become hybridized and the eigenvectors can in that case be written as

$$\mathbf{X}_\pm = \frac{1}{\sqrt{2}} \begin{pmatrix} \pm 1 \\ 1 \end{pmatrix}, \tag{C.10}$$

In the large detuning coupling, the modes become independent and can be written as

$$\mathbf{X}_+ = \begin{pmatrix} 1 \\ 0 \end{pmatrix} \tag{C.11}$$

$$\mathbf{X}_- = \begin{pmatrix} 0 \\ 1 \end{pmatrix}. \tag{C.12}$$

Appendix D

Fabrication recipes

D.1 Plain SiN membrane fabrication

Here, we present the detailed step-by-step fabrication procedure for releasing plain SiN membranes. The relevant fabrication steps are illustrated in fig. D.1, and referred to below.

- The entire 4-inch wafer is coated with a lithography resist (AZ 5214), serving as a protective mask, and baked at for 1'30" ($T = 110$°C).
- (Figure D.1a) The wafer is diced into individually handled 3 cm × 3 cm chips.

For each chip:

- (Preliminary cleaning) Ultrasound acetone bath for 10' ($T = 50$°C), followed by a rinse in isopropanol (IPA) and drying with a nitrogen gun.
- The side of the chip on which the membranes will be fabricated is chosen and labeled as the "frontside". The other side is the "backside" (see fig. D.1a). The frontside is typically the side of the wafer which is coated in the protective resist, although an optical inspection is made to ensure that there are no apparent defects.
- (Figure D.1b) AZ 5214 E (positive UV lithography resist) is spun on the frontside (4000 rpm, acceleration 1000 rounds.min^{-2}).
- The sample is baked on a hot plate for 1'30" ($T = 110$°C).
- The previous two steps are repeated for the backside.
- Backside lithography on an MJB4 mask aligner to define the windows (see figure D.1b). In soft contact mode, exposition for 10'.

- The resist is developed in AZ 726 MIF for 30'.
- Rinsing in deionized (DI) water and drying with a nitrogen gun.
- (Figure D.1c) Dry etching of SiN using reactive ion etching (RIE). A combination of O_2 and CHF_3 is used to etch the SiN with high selectivity to Si (10:1) [130], with an etch rate of about 31 nm/min.
- (Figure D.1d) Ultrasound acetone bath for 10' ($T = 50$°C), followed by a rinse in isopropanol (IPA), and drying with a nitrogen gun.
- (Figure D.1e) KOH dip ($T = 85$°C, concentration 30%) with stirring at 200 rpm, in the waterproof holder. The etch rate is approximately 80 μm/hour.
- When approximately 50-40 μm of Si remain, the stirring is halted.
- The end of the etch is marked by the end of the effervescent release of H_2 bubbles. The sample is transferred to a DI water bath of the same temperature as the KOH and rinsed.
- Rinsing in IPA and drying with a nitrogen gun.
- (Final cleaning) Dip in 3:1 piranha ($3H_2SO_4 + H_2O_2$) for 20'.
- (Figure D.1f) Rinsing in DI water, then IPA and drying with nitrogen gun.

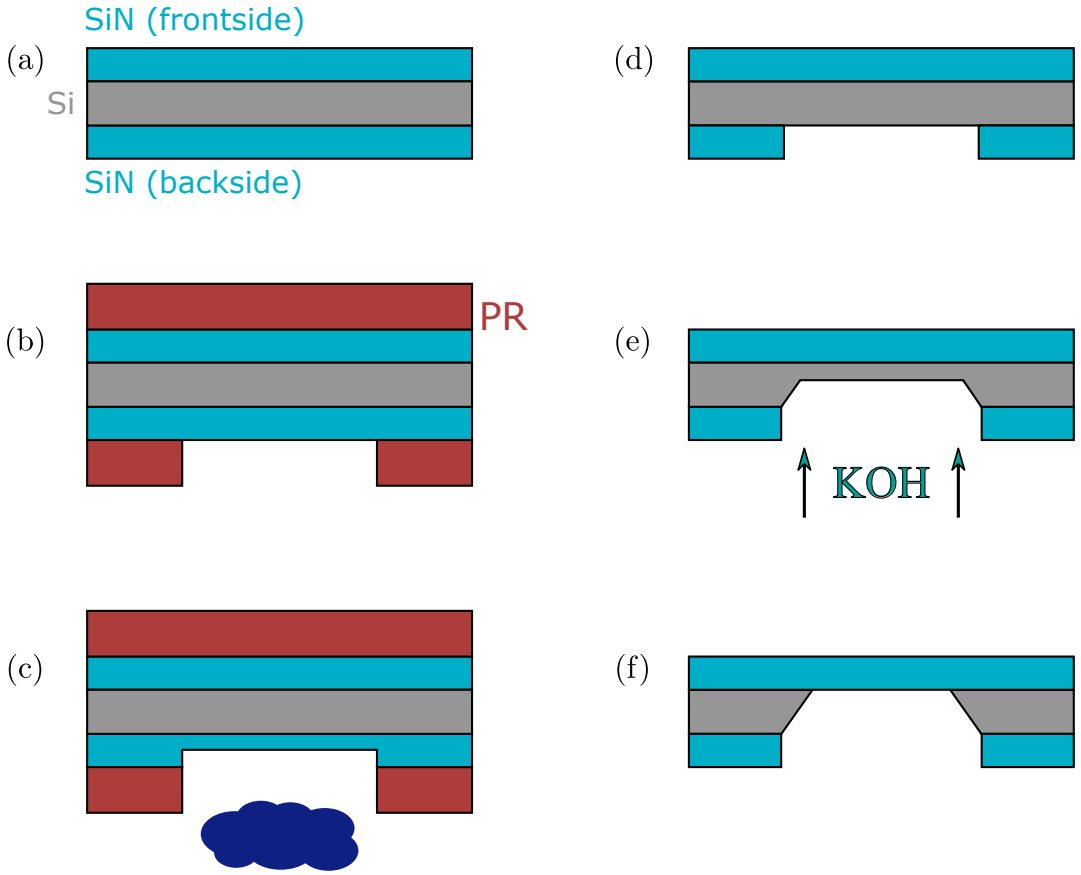

Figure D.1: (See the main body for additional details) Illustration of the key steps of the plain membrane fabrication. Blue: SiN; gray: Si; red: photoresist (PR).

D.2 Patterned SiN membrane fabrication

The text included in the following was published by the author in an open-source journal for sharing cleanroom fabrication recipes [118]. It details the fabrication of a PnC nanomembrane made from SiN.

Fabrication of patterned silicon nitride nanomembranes at the LKB

Edouard Ivanov[1], Thibault Capelle[1], Thibaut Jacqmin[1], Samuel Deléglise[1], and Antoine Heidmann[1]

[1] *Laboratoire Kastler Brossel, Sorbonne Université, CNRS, ENS-Université PSL, Collège de France, 75005 Paris, France*

Thin silicon nitride nanomembranes are attracting growing attention following a novel fabrication method which consists in patterning them with a phononic crystal. In engineering the vibrational mode profile, the dominant mechanisms of loss, radiation loss and intrinsic material loss, are simultaneously addressed and mitigated. The fabrication method employed by the optomechanics group at the Laboratoire Kastler Brossel is presented here; in particular, we only employ basic lithography techniques and wet etching processes.

Keywords: lithography, soft clamping, phononic crystal, silicon nitride, wet etch, KOH

FABRICATION PROCESS

In this report, we present the process used by the optomechanics group at the Laboratoire Kastler Brossel for fabricating 'soft-clamped' silicon nitride (SiN) membranes [1]. The (100) Si wafers were bought from Si-Mat [2], with stoichiometric SiN deposited on both sides of the Si by low-pressure chemical vapor deposition. Two kinds of wafers are currently used in our work, and the method described below has been tested on both kinds: the first is a 500 µm thick Si wafer, with intrinsic resistivity ($\rho > 10\,000\ \Omega$.cm), and layers of 100 nm of SiN; the other is a 300 µm tick Si wafer, with a resistivity of $\rho \approx 1 - 30\ \Omega$.cm, and a SiN thickness of 35 nm.

As with most fabrication methods reported by other groups for SiN membranes, patterned or otherwise, the fabrication process is based on the wet etching of the Si frame in a warm KOH bath. KOH possesses a high selectivity of SiN to Si, and SiN can thus be used as a hard mask to locally etch the Si at a high rate. This property can be used for fabricating various shapes of anchored membranes or strings of SiN [1,3-5].

Releasing an unpatterned SiN membrane by itself is a relatively straightforward process, with high yield and high margin of error. Conversely, it has repeatedly been observed that the release of a membrane patterned in such a way than thin structures exist within it requires more meticulous handling of the samples [3,6]. Moreover, the addition of air holes in the SiN membrane (see Figure 1) adds another channel for the KOH to etch the Si, which must absolutely be blocked for the release to be successful. Several approaches involve the use of watertight PEEK holders, protecting the membrane side [1,3].

Here, we present an alternative etching process which differs slightly from the usual approach to release these PnC structures; the membrane side is protected, rather than by an external holder, by a thick layer of photoresist lying on the surface on the chip for the duration of the KOH etch.

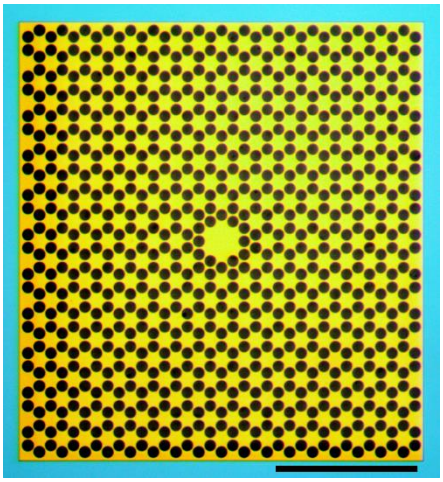

Figure 1- Optical micrograph of a patterned SiN membrane.
In yellow, the freely standing SiN; in blue, the SiN above Si; in black, air holes. The black scale bar represents 1 mm.

The bought wafers are initially diced into 3 cm × 3 cm chips, before being bathed in an ultrasound bath of hot acetone, at 50°C. After each acetone bath, a chip is systematically rinsed in isopropanol before drying with N_2. The procedure is then as follows, illustrated in figure 2:

- Step 1: a single chip is rinsed as above.
- Step 2: before any further procedure, the side of the chip on which the membrane will be fabricated (the *frontside)* is covered with a protective coating of photoresist AZ 5214 E. The frontside is chosen based on best surface cleanliness. The resist is then spun onto the other side of the chip (the *backside)*, and a window is patterned by h-line laser lithography (on the Microtech Laserwriter LW405C). The developer used is AZ 726 MIF.
- Step3: the SiN window on the backside is etched by reactive ion etching (RIE) involving a mixture of CHF3 and SF6 gases.
- Step 4: the sample is cleaned in a hot ultrasound acetone bath, followed by a dip in IPA.
- Step 5: resist is spun onto the frontside, which is patterned with the phononic crystal structure by laser lithography.
- Step 6: the SiN on the frontside is etched by RIE
- Step 7: another acetone/IPA cleaning cycle is undergone.
- Step 8: for the duration of the KOH etch, the frontside is protected with a thick photoresist unaffected by KOH: ProTEK PSB [7].
- Step 9: the Si is etched in a KOH bath, with a concentration of approximately 30%. The etch consist of two phases: first, the KOH is heated to 85°C, into which the sample is dipped, held by a Teflon holder keeping it vertical during the duration of the etch (see Figure 3). To ensure homogeneity throughout the liquid, the KOH is stirred with a magnetic stirrer at 200 rpm. When an estimated less than 50 µm of Si remain, the temperature is decreased to 75°C to reduce the amount of H_2 bubbles generated, and the stirring is interrupted.
- Step 10: after the KOH etch is fully finished and the SiN membranes are fully released (which can be judged by eye), the samples are transferred to a in a piranha solution (with a H_2O_2:H_2SO_4 ratio of 1:4) in order to remove the ProTEK. The process is finalized by a dip in deionized (DI) water, and IPA.
- (Optional) Step 11: in case the piranha etch was not successful in fully etching the Protek, a second, stronger piranha etch is undergone, with a H_2O_2:H_2SO_4 ratio of 1:1.

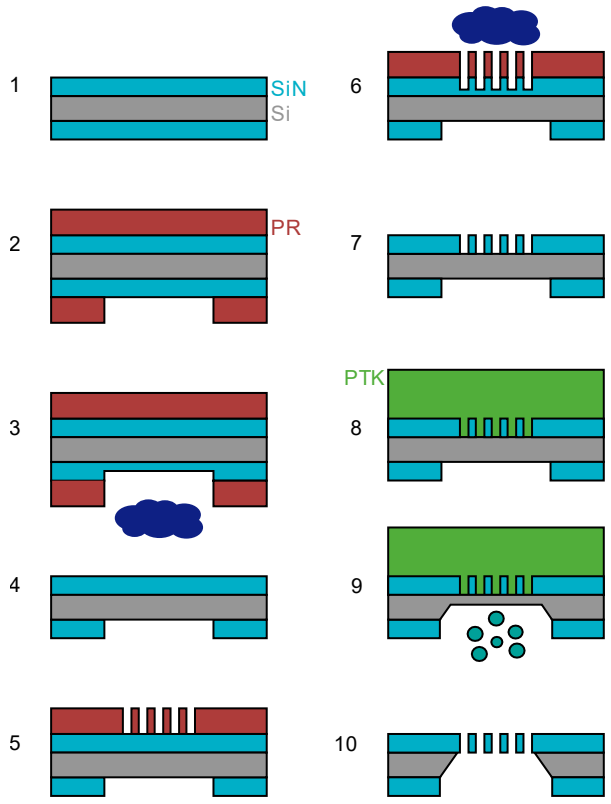

Figure 2- Illustrated fabrication process.
Blue: SiN; gray: Si; red: photoresist (PR); green: ProTEK PSB (PTK)

The precision in the width and height of the membrane window was of the order 1 µm, with an accuracy of the order of 1 µm, and good reproducibility from one bath to another. The centering of the PnC pattern was also determined, by measuring the distance of an outermost hole to the membrane border and comparing that to its design value. We found a precision in that distance of 2 µm, with an accuracy of 2 µm.

ADITIONNAL REMARKS

- Step 9: the empty Teflon holder is heated in the KOH until the temperature of 85°C is reached, to prevent a temperature dip when the sample is inserted. When 85°C are reached, the holder is removed from the solution, the chip is loaded, and the holder is finally returned to the solution.
  The verticality of the Teflon holder is employed to minimize viscous drag normal to the membrane surface during manipulations in the KOH; it serves as a way to ensure that the H_2 bubbles generated by the KOH etch do not affect with excessive force onto the membranes as well. Once the chip is loaded onto the holder, it is never removed until the process is fully terminated.
- Step 10: After the membranes are released, the sample is treated as delicately as possible. Any dip in a solvent or DI water simply consists of gently lowering down the holder into the solution, and letting is clean by diffusion for approximately 10 minutes.

REFERENCES

1. Tsaturyan, Y. *et al*. (2017) Nat. Nano. **12**, 776 783.
2. URL: https://www.si-mat.com/.
3. Beccari, A. *(2020) 10.5281/zenodo.3898901.*
4. Reinhardt, C. *et al*. (2016) PRX **6**, 201001.
5. Norte, R. A. *et al*. (2016) PRL **116** 147202.
6. Thesis of Norte, R. A.
   URL:https://thesis.library.caltech.edu/8718/
7. URL:
   https://www.brewerscience.com/products/protek-psb/

Appendix E

Symbol list

Table E.1: List of the most important symbols found throughout this manuscript.

Symbol	Meaning
General terms	
$S_{\mathcal{O}\mathcal{O}}$	Noise spectral density of $\mathcal{O}$
$\bar{S}_{\mathcal{O}\mathcal{O}}$	Symmetric noise spectral density, $\bar{S}_{\mathcal{O}\mathcal{O}}[\Omega] = S_{\mathcal{O}\mathcal{O}}[-\Omega] + S_{\mathcal{O}\mathcal{O}}[\Omega]$
Mechanical resonator	
$\hat{x}$, x	Position operator or variable
$\hat{p}$, p	Momentum operator or variable
m_{eff}	Effective mass of a continuous mode
Γ_{m}	Energy dissipation rate
Ω_{m}	Natural angular frequency
χ_{m}	Mechanical susceptibility, $\chi_{\mathsf{m}}^{-1}(\Omega) = m_{\mathsf{eff}}\left[(\Omega^2 - \Omega_{\mathsf{m}}^2) - i\Gamma_{\mathsf{m}}\Omega\right]$
T_{env}	Temperature of the resonator's environment
n_{th}	Mean number of thermal quanta, $n_{\mathsf{th}}(\Omega) = 1/\left(\exp\left(\hbar\Omega/k_{\mathsf{B}}T_{\mathsf{env}}\right) - 1\right)$
x_{zp}	RMS displacement of the zero-point motion, $x_{\mathsf{zp}} = \sqrt{\hbar/2m_{\mathsf{eff}}\Omega_{\mathsf{m}}}$
$\hat{H}_{\mathsf{m}}$	Hamiltonian of the mechanical resonator, $\hat{H}_{\mathsf{m}} = \hat{p}^2/2m_{\mathsf{eff}} + m_{\mathsf{eff}}\Omega_{\mathsf{m}}^2\hat{x}^2/2$
Silicon nitride membrane	
E	Young's modulus
$\tilde{E}$	Generalized Young's modulus, $\tilde{E} = E - iE_2$
σ_0	In-plane stress
$\boldsymbol{\sigma}$	Stress vector
$\boldsymbol{\epsilon}$	Strain vector
ρ	Density

h	Membrane thickness
l	Membrane side length
ν	Poisson's ratio
u	Displacement profile of a mode
Λ	Dissipation dilution factor, $\Lambda = \sqrt{Eh^2/3(1-\nu^2)\sigma_0 l^2}$
$\mathcal{U}$	Total energy of a mode
$\mathcal{U}_{\mathsf{bend}}$	Bending energy of a mode
$\mathcal{U}_{\mathsf{elong}}$	Elongation energy of a mode
Q	Quality factor, $Q = 2\pi\mathcal{U}/\Delta\mathcal{U}$ or $Q \approx \Omega_{\mathsf{m}}/\Gamma_{\mathsf{m}}$
Q_{intr}	Intrinsic quality factor, $Q_{\mathsf{intr}} = E/E_2$
Q_{b}	Quality factor associated to bending losses
Q_{rad}	Quality factor associated to radiation losses
$\Delta\mathcal{U}$	Energy loss per cycle of a mode, $\Delta\mathcal{U} = 2\pi\mathcal{U}_{\mathsf{bend}}/Q_{\mathsf{intr}}$

Phononic crystal membrane

b	Lattice parameter of the phononic crystal
r	Radius of the holes
M	Margin, distance between the last hole in the phononic crystal and the membrane border
γ	Coupling rate for dimers
$\Omega_{\pm}$	Frequency of the symmetric resp antisymmetric normal modes of a dimer membrane

Microwave circuits and optics

$\mathcal{C}$	Circuit capacitance
$\mathcal{L}$	Circuit inductance
$\hat{a}, a$	Resonant circuit ladder operator, or the intracavity light field
α	Average amplitude of the intracavity light field
ω_{c}	Circuit resonance frequency, $\omega_{\mathsf{c}} = 1/\sqrt{\mathcal{LC}}$
$\hat{H}_{\mathsf{c}}$	Circuit Hamiltonian, $\hat{H}_{\mathsf{c}} = \hbar\omega_{\mathsf{c}}\left(\hat{a}^\dagger\hat{a} + 1/2\right)$
ω_{d}	Driving frequency
κ_{i}	Internal dissipation rate
κ_{c}	Dissipation rate to the coupled readout port (coupling rate)
χ_{e}	Electrical susceptibility, $\chi_{\mathsf{e}}^{-1}(\omega) = i\omega + \kappa/2$
Δ	Detuning between the driving tone and the cavity resonance, $\Delta = \omega_{\mathsf{d}} - \omega_{\mathsf{c}}$
λ	Optical wavelength
f	Optical frequency
SNR	Signal-to-noise ratio of an interferometer
ε_0	Vacuum permittivity

Electromechanical device

G	Frequency shift per displacement, $G = \partial\omega_{\mathsf{c}}/\partial x$
g_0	Single-photon coupling rate, $g_0 = x_{\mathsf{zp}}G$

g	Dressed coupling rate, $g = g_0\alpha$
C_0	Single-photon cooperativity, $C_0 = 4g_0^2/\kappa\Gamma_\mathsf{m}$
C	Dressed cooperativity, $C = C_0\alpha^2$
$\hat{H}_\mathsf{em}$	Hamiltonian of the electromechanical device, $\hat{H}_\mathsf{em} = \hat{H}_\mathsf{c} + \hat{H}_\mathsf{m} - \hbar G\hat{a}^\dagger\hat{a}\hat{x}$
$\bar{\Delta}$	Corrected laser detuning, $\bar{\Delta} = \Delta - g^2/2\Omega_\mathsf{m}$
$\delta\Omega_\mathsf{m}$	Electromechanically-induced frequency shift of the mechanical mode
Γ_em	Electromechanically-induced mechanical dissipation
Γ_eff	Effective mechanical dissipation, $\Gamma_\mathsf{eff} = \Gamma_\mathsf{m} + \Gamma_\mathsf{em}$
χ_eff	Effective mechanical susceptibility, $\chi_\mathsf{eff}^{-1}(\Omega) = m_\mathsf{eff}\left[-\left(\Omega^2 - (\Omega_\mathsf{m} + \delta\Omega_\mathsf{m})^2\right) + i\Omega\Gamma_\mathsf{eff}\right]$
η_rsf	Resolved sideband factor, $\eta_\mathsf{rsf} = (4\Omega_\mathsf{m}/\kappa)^2$
n_cn	Added mechanical population by the dynamical backaction
n_eff	Effective mean mechanical population, $n_\mathsf{eff} = \left(\Gamma_\mathsf{m} n_\mathsf{th} + \Gamma_\mathsf{em} n_\mathsf{cn}\right)/\Gamma_\mathsf{eff}$

Edouard Ivanov **Janvier 2021**

Optimization of silicon nitride membranes for hybrid superconducting-mechanical circuits

Abstract: In this thesis, we study an engineered mechanical oscillator coupled to a microwave cavity. In a preliminary experiment, microwave photons were used as a cold bath to reduce the temperature of the mechanical oscillator by a factor 500. We present several improvements to the membranes which should enable us to cool them down to their quantum ground state. In particular, we explore the rich physics of phononic bangaps to isolate an ultrahigh-quality-factor membrane mode from decoherence channels, a technique known as "soft-clamping". Using a quantum-limited interferometer able to resolve the membrane's Brownian motion, we reconstruct the profiles of the membrane modes. Thanks to this setup we identify a set of parasitic membrane modes which significantly degrade the quality factor of the soft-clamped modes. Specific mode engineering strategies are therefore implemented to ensure the optimal performance of the softly-clamped membranes. Once integrated in an electromechanical cavity, the optimized membranes developed over the course of this thesis should operate deep in the quantum regime. We discuss the perspectives of preparing nonclassical states of motion by exploiting superconducting qubits as a nonlinear resource. In particular, we propose a scheme which could achieve this using a single microwave-photon detector, developed in collaboration with LPENS. This hybrid electromechanical system could be used to store fragile quantum states on the scale of seconds, to measure minute forces with unprecedented precision, or to study the boundary between the quantum and the classical worlds.

Keywords: electromechanics, silicon nitride, MEMS, cryogenics, electromechanical cooling, ground state, nonclassical state, non-Gaussian, mechanics, spectral engineering, phononic crystal, decoherence, interferometry

Résumé : Dans cette thèse, nous étudions un résonateur mécanique optimisé qui est couplé à une cavité micro-ondes. Au cours d'une expérience préliminaire, des photons micro-ondes sont employés comme bain froid pour réduire la température de l'oscillateur mécanique d'un facteur 500. Nous introduisons plusieures améliorations à ces membranes dans l'optique de les refroidir jusqu'à leur état quantique fondamental. En particulier, nous explorons la physique riche des bandgaps phononiques pour isoler

un mode de facteur de qualité ultra-élevé de ses canaux de décohérence, une méthode connue sous le nom de “soft-clamping”. Avec un interféromètre limité quantiquement et capable de résoudre le mouvement Brownien des membranes, nous reconstruisons le profil des modes de la membrane. Grâce à cette expérience, nous identifions un groupe de modes parasitiques qui dégradent fortement le facteur de qualité des modes “soft-clamped”. Des stratégies d'optimisation du profil spectral sont donc implémentées pour assurer la performance optimale des membranes “soft-clamped”. Une fois intégrées dans une cavité électromécanique, les membranes optimisées qui ont été développées au cours de cette thèse devraient opérer profondément dans le régime quantique. Nous discutons des perspectives pour préparer des états de mouvement non-classiques qui exploitent la nonlinearité des qubits supraconducteurs. Nous proposons en particulier une méthode pour réussir cela en utilisant un détecteur de photons micro-ondes uniques, qui a été développé en collaboration avec le LPENS. Un tel système electromécanique hybride pourrait être utilisé pour stocker des état quantiques fragiles à l'échelles des secondes, pour mesurer avec une précision sans précédent des forces infimes, ou encore pour sonder la frontière entre les mondes classiques et quantiques.

Mots clés : electromécanique, nitrure de silicium, MEMS, cryogénie, refroidissement electromécanique, état fondamental, état non-classique, état non-Gaussien, mécanique, optimisation spectrale, crystal phononique, décohérence, interférométrie.